STEAM EFFECTS ON OXIDATION BEHAVIOR OF ALUMINA-SCALE FORMING NICKEL-BASED ALLOYS AND A KINETICS ANALYSIS OF COMPLEX SCALE EVOLUTION DURING ISOTHERMAL OXIDATION

by

Wei Zhao

BS in Materials Science and Engineering, Tsinghua University, 2004

MS in Materials Science and Engineering, Tsinghua University, 2006

Submitted to the Graduate Faculty of

The Swanson School of Engineering in partial fulfillment

of the requirements for the degree of

Doctor of Philosophy

University of Pittsburgh

2012

UNIVERSITY OF PITTSBURGH

THE SWANSON SCHOOL OF ENGINEERING

This dissertation was presented

by

Wei Zhao

It was defended on

January 24th, 2012

and approved by

Gerald H. Meier, PhD, William Kepler Whiteford Professor,

Department of Mechanical Engineering and Materials Science

Anthony J. DeArdo, PhD, William Kepler Whiteford Professor,

Department of Mechanical Engineering and Materials Science

Götz Veser, PhD, Professor,

Department of Chemical and Petroleum Engineering

Dissertation Director: Brian M. Gleeson, PhD, Harry S. Tack Chair Professor,

Department of Mechanical Engineering and Materials Science

STEAM EFFECTS ON OXIDATION BEHAVIOR OF ALUMINA-SCALE FORMING NICKEL-BASED ALLOYS AND A KINETICS ANALYSIS OF COMPLEX SCALE EVOLUTION DURING ISOTHERMAL OXIDATION

Wei Zhao, PhD

University of Pittsburgh, 2012

The first part of this study investigated steam effects on the oxidation behavior of Al_2O_3-scale forming Ni-based alloys. This effect was assessed in the context of Giggins and Pettit's oxidation map [1] for the Ni-Cr-Al system, which was determined under dry oxidizing conditions. Of particular relevance to the design of high-temperature alloys and coatings is the location in the oxide map of the kinetically-dictated critical Al content (N_{Al}^*) in a given alloy to form a continuous Al_2O_3-scale. It was found that N_{Al}^* increases when the air contains 30% steam. A rigorous quantitative analysis based on Maak's modification[2] of Wagner's theory[3] was carried out to determine the key parameter affecting an increase in N_{Al}^* under wet oxidizing conditions. By checking the sensitivity of N_{Al}^* with respect to each parameter in the theory, it was deduced that the only parameter which can give the necessarily large change in N_{Al}^* found in wet-air oxidation is the critical volume fraction of internal oxide, f_v^*, a parameter that is usually assumed to be a constant and independent of the reacting conditions.

From experimental observation, it was found that the surface of NiO scale became unstable in wet oxidizing conditions. Unlike the dense and uniform surface formed scale in dry air, finger-like protrusions or a powder-like porous structure could form under wet conditions. The experimental conditions and possible mechanisms for this observed instability were assessed.

In the second part of this study, a novel kinetics analysis method was established to quantify the kinetics of scale evolution based on analyzing the instantaneous growth rate constant k^i and the time exponent n^i determined from thermogravimetric (TG) data. A methodology is proposed to ascertain whether the oxidation kinetics has come to a steady state from a transient stage, and to accurately determine the growth rate constant. Both a fundamental analysis and an experimental validation of this methodology are presented. This kinetics analysis method was further extended to quantify the scale evolution during the initial oxidation stage. Specifically, a method to track the extent and kinetics of the metastable → stable Al_2O_3 phase transformation in thermally formed alumina scales was established.

TABLE OF CONTENTS

LIST OF TABLES

LIST OF FIGURES

PREFACE

This work is dedicated to my parents, **Rong Wei** and **Xifu Zhao**, who motivated me to study abroad at the first place, who shared all my feelings these are bitter and sweet, who gave me all their patience and love throughout the journey and who celebrated with me to “laugh to the end”.

I would like to thank Prof. Brian Gleeson for his supervising and support during the course of this work. I have learned and benefited a lot from his abundance of knowledge, smart ideas and the art of good leadership.

I would like to thank all my committee members, the course lecturers, the technicians and my colleges for their sincerely help with my academic advances. They helped me build up each single step to today’s achievement.

Finally, I would like to thank all my friends. They are the real ones to spend their everyday life with me. With them, I felt that I was not alone in the path of taking the professional training, seeking self-improvement and pursuing happiness.

1.0 INTRODUCTION

1.1 HIGH TEMPERATURE OXIDATION OF METALS

At high temperature, most metals are not thermodynamically stable. They will usually react with the oxidant (typically oxygen) in the environment to form a solid scale product on the surface. The scale formed by thermal oxidation is different from a thin film generally used in the processing of electronic semiconductor devices and optical coatings. For a general definition, a thin film is a layer of material ranging from fractions of a nanometer (monolayer) to several micrometers in thickness, while a scale is several micrometers to hundreds of micrometers in thickness. In scales, the chemical activity profiles of the components and the growth kinetics are typically controlled by mass diffusion rates through the scale. Figure 1.1 shows typical scale morphology formed at high temperature. This is an SEM cross-sectional image of pure Ni (99.99%) after oxidation in air at 1000^{o}C for 20 hours. It is seen that the scale is not fully dense. Rather it tends to contain some voids, shown as the dark region in figure 1.1. These voids are formed by the annihilation of vacancies in the vicinity of metal/scale interface[4,5], which is a reflection of the Kirkendall effect.

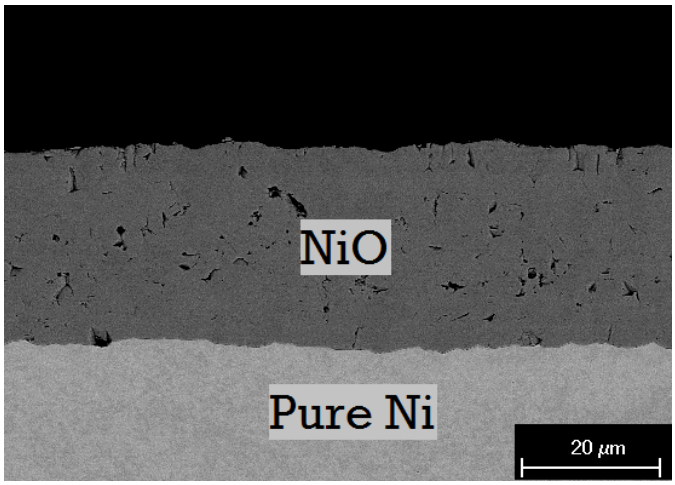

Figure 1.1 Cross-sectional SEM image of oxide scale formed on pure Ni (99.99%) after oxidation in air at 1000°C for 20hours

1.1.1 Thermodynamics of metal oxidation

A typical chemical reaction for gaseous oxidation is given by equation 1.1:

$$M + \frac{\upsilon}{2} O_2 = MO_\upsilon \tag{1.1}$$

Since the conditions most often encountered in high-temperature reactions are constant temperature and pressure, the combination of 1st and 2nd law of thermodynamics is most conveniently written in terms of the Gibbs free energy [6]. The Gibbs free energy change associated with equation 1.1 is:

$$\Delta G_{1.1} = \Delta G^o + RT \ln \frac{a_{MO_\upsilon}}{a_M \cdot \left(a_{O_2}\right)^{\upsilon/2}} \tag{1.2}$$

where ΔG^o is the free-energy change when all species are present in their standard states; a_i is the thermodynamic activity of *i*, which describes the deviation from the standard state for a given species and may be expressed as:

$$a_i = \frac{p_i}{p_i^o} \tag{1.3}$$

where p_i is either the vapor pressure over a condensed species or the partial pressure of a gaseous species and p_i^o is the same quantity corresponding to the standard state of *i*. If the Gibbs free energy change is smaller than zero ($\Delta G < 0$), the oxidation reaction is thermodynamically favored, i.e. the metal will be oxidized. If the Gibbs free energy change is equal to zero ($\Delta G = 0$), the reaction is in equilibrium, i.e. the forward reaction and backward reaction in equation 1.1 is in balance so that no more oxide will form; if the Gibbs free energy change is greater than zero ($\Delta G > 0$), metal is stable and oxidation will not take place. If the activities of metal and metal oxide are taken as unity, equation 1.2 may be used to derive the oxygen partial pressure at which the metal and oxide coexist, i.e., the dissociation pressure of the oxide (P_{MOv}^*). When the metal and oxide coexist, equation 1.1 is in equilibrium so the Gibbs free energy change for this reaction is zero ($\Delta G_{1.1} = 0$). Taking this value into equation 1.2 and replacing the oxygen activity by oxygen partial pressure in the unit of atm gives:

$$P_{MO_v}^* = \exp\left(\frac{2 \cdot \Delta G^o}{vRT}\right) \tag{1.4}$$

Therefore, thermodynamic stability of the metal can be determined by comparing the oxygen partial pressure in the environment and the dissociation pressure of the metal oxide: If oxygen partial pressure in the environment is greater than the dissociation pressure of the metal oxide ($P_{O_2} > P_{MO_2}^*$),metal will be oxidized; if oxygen partial pressure in the environment equals the dissociation pressure of the metal oxide ($P_{O_2} = P_{MO_2}^*$), metal and its oxide can co-exist; if oxygen partial pressure in the environment is smaller than the dissociation pressure of the metal oxide ($P_{O_2} < P_{MO_2}^*$), metal is stable, i.e. no metal will be oxidized. The dissociation pressure of metal

oxide can be read from the Ellingham diagram shown by Figure 1.2 by drawing a straight line from the origin marked O through the free energy line at the temperature of interest and reading the oxygen partial pressure from its intersection with the scale at the right side labeled P_{O_2}. In this diagram, each line corresponds to a reaction for a metal to react with 1 mole oxygen to form metal oxide. The lower the line is, the more stable the oxide is. For example, the line for Al_2O_3 is below the line for Cr_2O_3 at all temperatures. This means Al_2O_3 is more stable than Cr_2O_3 at all those temperatures. Since more stable oxide can be formed below a continuous less stable oxide, for a Cr_2O_3-scale forming alloy containing Al as a component, Al_2O_3 may be formed below the Cr_2O_3 scale. It is worthwhile to note that most of the lines on this diagram have positive slopes. This is because the slope of those lines is the derivative of Gibbs free energy with respect to temperature, which is the negative entropy change of the reaction. Since most of the reactions contain 1 mole of oxygen gas as a reactant while contain only solid metal oxide as product, and the entropy of gas phase is usually larger than solid phase, the entropy change of most of the reactions are negative. Therefore, the slope, the negative entropy change of the reaction, is mostly positive. In practice, the oxygen partial pressure is usually controlled by H_2/H_2O or CO/CO_2 buffer gases. The equilibrium H_2/H_2O or CO/CO_2 ratio with a metal at certain temperature can also be found in this diagram by extending a line from the H or C point on the left with the point on the metal reaction line at that temperature to the corresponding H_2/H_2O or CO/CO_2 ratio axis on the right.

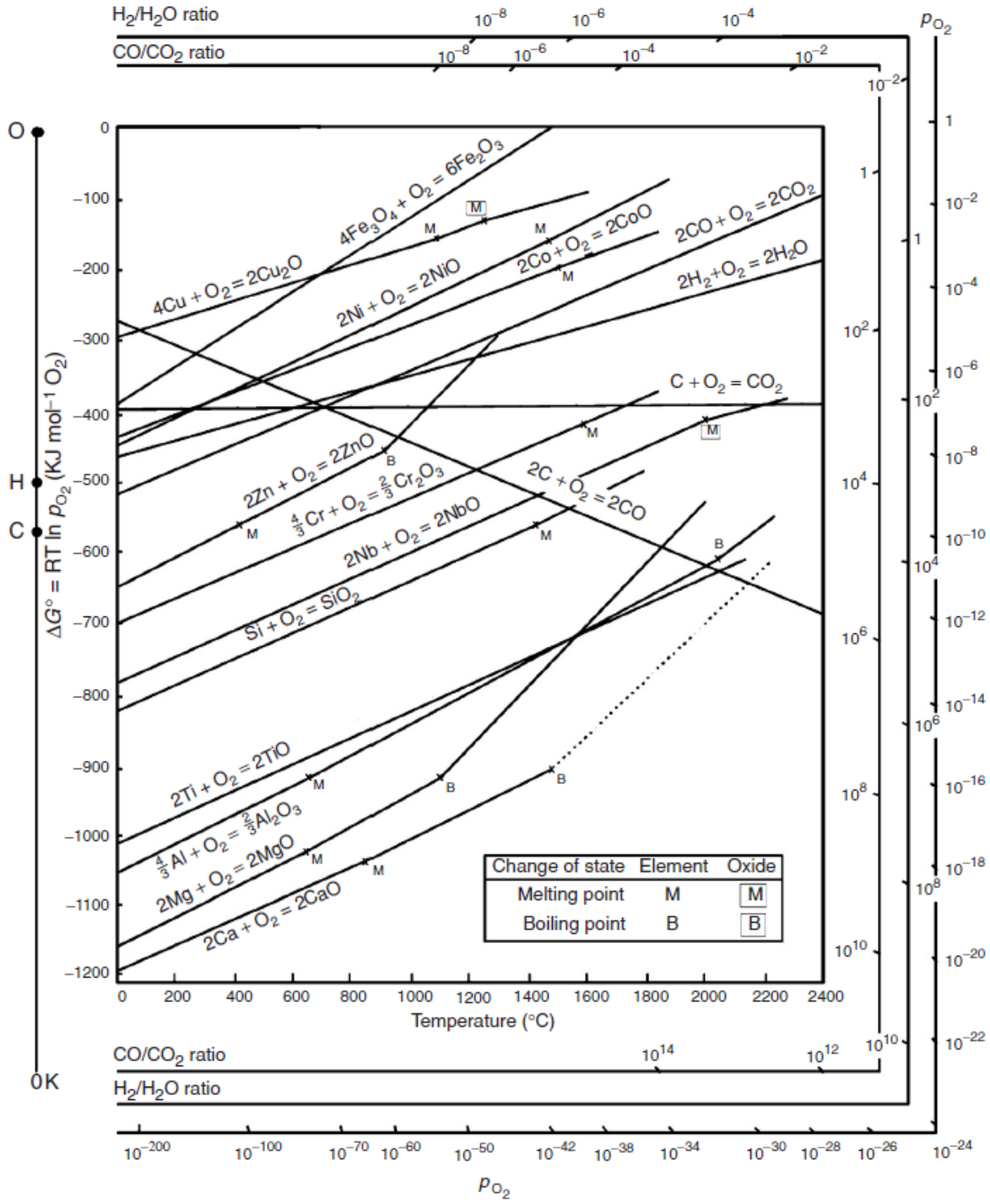

Figure 1.2 Ellingham diagram of oxide stability at different temperature and oxygen pressure

If the metal element has more than one valence, multi-layer oxide scale may form during the oxidation process. A good example can be found by oxidation of pure iron, for there are three common types of iron oxide, FeO (wustite), Fe_3O_4 (magnetite) and Fe_2O_3 (hematite), which are shown by the iron-oxygen phase diagram in Figure 1.3. On this diagram, there is an important division line at 570°C. Below this temperature, FeO is not a stable phase and is therefore absent from the oxide scale during oxidation; however, above this temperature, all three oxides can be stable.

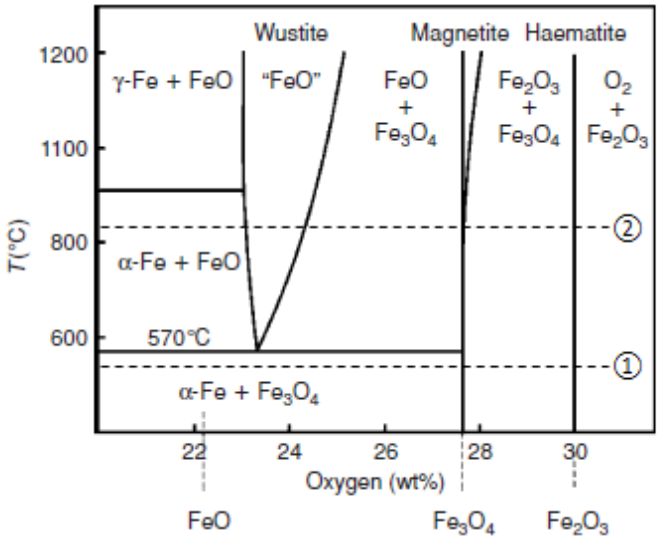

Figure 1.3 Iron oxygen phase stability diagram

Figure 1.4 shows a cross sectional image of pure iron oxidized above 570°C[7]. The occurring oxides from the surface to the bulk metal are Fe_2O_3, Fe_3O_4 and FeO in sequence. Mapping this sequence onto the phase diagram yields a line termed “diffusion path”. On a phase diagram, a diffusion path shows the path of the concentration changes, which drive diffusion within the reacting system. The dash line #2 on Figure 1.3 is a typical diffusion path corresponds to the oxide sequence of oxidation of pure Fe above 570°C. Going from the right side of the line #2 to the left, the line encounters a series of regions on the phase diagram in the sequence of O_2+

Fe_2O_3, Fe_2O_3, Fe_2O_3+ Fe_3O_4, Fe_3O_4, Fe_3O_4 + FeO, FeO, FeO+α-Fe and α-Fe. However, only the single-phase regions can be observed on the cross section of oxidized sample at this temperature and this sequence is exactly the same as the sequence shown in Figure 1.4. Two-phase regions only exist at the interfaces so that they cannot be observed. According to the Gibbs phase law, the degrees of freedom *F* is determined by:

$$F = C - P + 2 \tag{1.5}$$

where C is the number of components and P is the number of phases. If the temperature and total pressure are fixed, equation 1.5 becomes:

$$F = C - P \tag{1.6}$$

Since there are two components Fe and O (C = 2), the degrees of freedom for the two phase region (P = 2) is zero. It means that the two-phase region cannot have a concentration gradient which requires at least one degree of freedom for the change of concentration. Therefore, the two-phase region is invisible on the cross-sectional image.

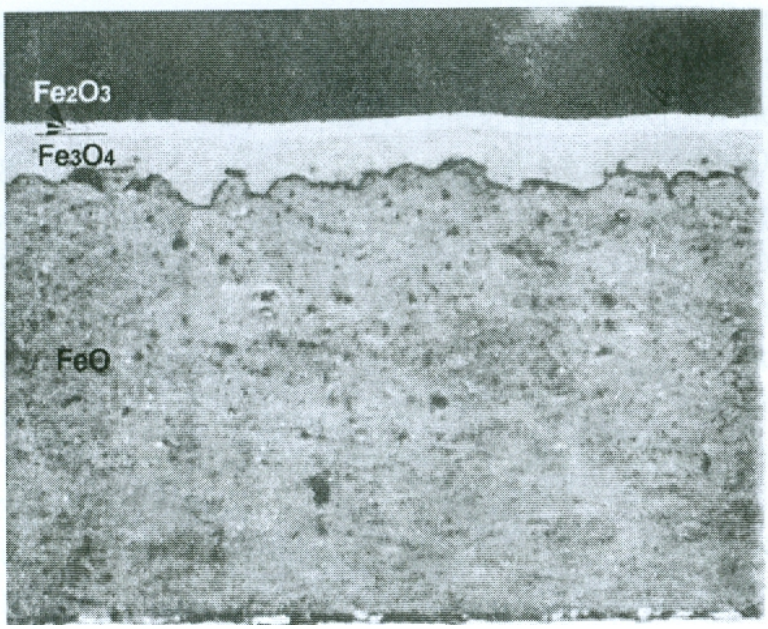

Figure 1.4 Cross-sectional SEM image of scales formed on pure Fe oxidized at 620°C[7]

1.1.2 Kinetics of oxidation of metals forming single-phase oxide scale

Although thermodynamics predicts the stability of a metal against oxide formation at a certain temperature, it is very rare that the metal is completely oxidized within a time range of practical interest, even if the metal is not the stable phase. This is because the growth kinetics are usually limited by the diffusion rates of the reactant species. For such diffusion controlled relations, parabolic growth kinetics are the most commonly encountered. At high temperature, suppose there is no volatile species, the overall oxidation rate is controlled by the flux of the principal diffusing species, which is dictated by Fick's first law: the flux is proportional to the composition (indeed chemical potential) gradient of the principle diffusing species, which is reflect by:

$$J = -D\frac{\partial C}{\partial x} \tag{1.7}$$

where J is the flux of diffusion species, C the composition of the diffusion species and x the distance the species need to move. Neglecting the lateral diffusion near the edges, the flux is linearly proportional to the growth rate of the scale. Assuming local equilibrium is established[6], the activities of the reactants and production follow:

$$\frac{a_{MO_v}}{a_M \cdot \left(a_{O_2}\right)^{v/2}} = \exp\left(-\frac{\Delta G^o}{RT}\right) = K_{ox} \tag{1.8}$$

Therefore, the boundary condition, the compositions (chemical potentials) of species at the gas/scale interface and scale/metal interface are fixed. By assuming the compositions (chemical potentials) gradient is linear, this gradient is inversely proportional to the distance that the species need to move x. In this case, the growth rate of the scale follows:

$$\frac{dx}{dt} = \frac{k'}{x} \tag{1.9}$$

where k' is a constant. Integrating equation 1.9 and assuming the thickness of the scale is 0 when *t* is 0 gives the widely used parabolic growth kinetics:

$$x^2 = k_p t \tag{1.10}$$

where k_p is usually defined as parabolic growth rate constant of the scale. This parabolic growth rate constant is determined by a variety of factors such as temperature and defect concentration[6, 8]. The oxidation of nickel gives a good example of the effect of defect concentration on the growth rate constant. NiO is a p-type semiconductor that has a predominance of cation deficiency[6]. Accordingly, oxidation of nickel proceeds is dominated by the outward migration of cations through cation vacancies. Figure 1.5 shows a typical defect structure of p-type, metal-deficit NiO with cation vacancies and electron holes[6].

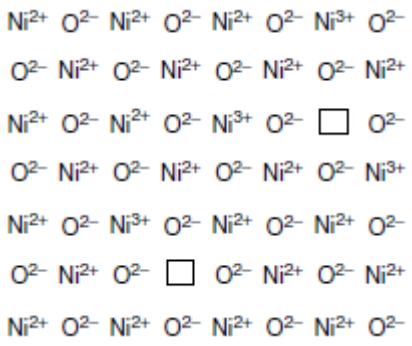

Figure 1.5 Defect structure of p-type, metal-deficit nickel oxide[6]

The formation of this defect structure can be visualized if one considers the interaction of the NiO lattice with oxygen shown in Figure 1.6[6]. In step (b) the oxygen chemisorbs by attracting an electron from a Ni site thus forming Ni^{3+} or an electron hole. In step (c) the chemisorbed oxygen is fully ionized forming another hole and Ni^{2+} enters the surface to partner with the O^{2-}, thus forming a vacancy in the cation sub-lattice.

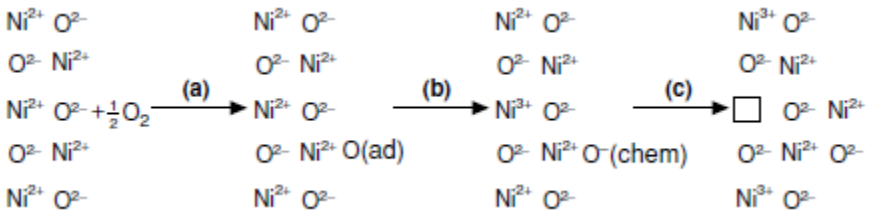

Figure 1.6 Formation of Ni vacancies and electron holes in NiO[6]

The overall defect reaction for this process can be written in Kröger-Vink notations as:

$$\frac{1}{2}O_2 = O_O + V_{Ni}^{''} + 2h^{\bullet} \tag{1.11}$$

The equilibrium constant for this reaction is:

$$K_{1.11} = \frac{p^2 \cdot \left[V_{Ni}^{''}\right]}{p_{O_2}^{1/2}} \tag{1.12}$$

where p is the concentration of electron holes and [V_{Ni}''] is the concentration of nickel vacancies. From the conservation of electrical neutrality, p=2[V_{Ni}''], it is derived that the Ni^{2+} vacancy concentration is a function of the oxygen partial pressure shown by:

$$\left[V_{Ni}^{''}\right] = \left(\frac{K_{1.11}}{4}\right)^{1/3} \cdot p_{O_2}^{1/6} \tag{1.13}$$

Assuming the diffusion coefficient is linearly proportional to the vacancy concentration, it is expected that growth rate constant will increase with increasing oxygen partial pressure to the 1/6 power.

Under some circumstances[9], the Ni vacancy may be single charged V_{Ni}'. In such a case, the defect reaction is:

$$\frac{1}{2}O_2 = O_O + V_{Ni}^{'} + h^{\bullet} \tag{1.14}$$

Thus, the vacancy concentration has the relation with oxygen partial pressure shown by:

$$\left[V_{Ni}^{'}\right] = K_{1.14}^{1/2} \cdot p_{O_2}^{1/4} \tag{1.15}$$

where $K_{1.14}$ is the equilibrium constant for this reaction 1.14.

Fueki and Wagner[9] oxidized nickel over a range of oxygen partial pressures from the dissociation pressure of NiO to 1 atm at temperatures between 900 and 1400^{o}C. Their results showed that the observed parabolic rate constant did vary with the oxygen partial pressure of the atmosphere to the 1/n power: the value of n varies from lower than 6 at 1000^{o}C to 3.5 at 1400^{o}C. They also determined the self-diffusion coefficient of nickel ions in nickel oxide as a function of oxygen partial pressure. The values of the self-diffusion coefficients were independent of oxygen partial pressure in the low oxygen-pressure range and proportional to $p_{O2}^{1/6–1/3.5}$ in the intermediate oxygen-pressure range. These experimental results indicate the dominating type of vacancies is determined by oxygen pressure.

Since the defect concentration significantly influences the growth rate constant, it is expected that impurities which may affect the defect concentration can also affect the growth kinetics. Indeed, early measurements of the oxidation of nickel over the temperature range 700-1300^{o}C showed a surprising variation of the parabolic rate constant over four orders of magnitude[10,11,12]. Later determinations, using nickel of significantly improved purity[13,14] showed that the parabolic rate constant for nickel containing 0.002% impurity was reliably reproducible and was lower than that for the less-pure nickel samples used earlier. Since the majority of impurity elements found in nickel are either divalent or trivalent, they will, when dissolved in the oxide, either have no effect on or increase the mobility of cations in NiO. An example of this dopant effect on defect concentration by trivalent impurity can be represented as follows:

$$M_2O_3 \xrightarrow{NiO} 2M_{Ni}^{\bullet} + 3O_o + V_{Ni}^{''} \tag{1.16}$$

When the impurity level is high, to the extent that the NiO becomes an extrinsic semiconductor, the Ni vacancy concentration is determined by the impurity concentration rather than the intrinsic reactions. It is, therefore, understandable that the impure nickel specimens were found in general to oxidize more rapidly than pure nickel. The activation energy of the process remained fairly constant regardless of impurity level indicating that the rate-determining step remained unchanged.

1.1.3 Kinetics of oxidation of metals forming a multi-layered oxide scale

From Figure 1.4, it is seen that the oxidation kinetics of each layer of a multi-layered oxide scale can be significantly different. For example, the wustite phase, FeO, is a p-type metal-deficit semiconductor which can exist over a wide range of stoichiometry, from $Fe_{0.95}O$ to $Fe_{0.88}O$ at 1000^oC according to Engell[15,16]. With such high cation-vacancy concentrations, the mobility of cations and electrons (via vacancies and electron holes) is extremely high. The much greater mobility of defects in FeO causes this layer to be very thick compared with the Fe_3O_4 and Fe_2O_3 layers when the oxide is formed above 570^oC. In fact the relative thicknesses of FeO : Fe_3O_4 : Fe_2O_3 are in the ratio of roughly 95 : 4 : 1 at 1000^oC[17]. Contrary to the oxidation kinetics of single-layer oxide, the growth kinetics for inner layers of multi-layer oxides shows little oxygen partial pressure dependence. It is because the boundary conditions for the diffusion of principal diffusing species are fixed by the equilibrium established at the interfaces between oxide layers or between oxide scale and the alloy. For example, the scale formed on iron above 570^oC is predominantly FeO, growth of this layer controls the overall rate of oxidation. However, since the defect concentrations in FeO at the Fe/FeO and FeO/Fe_3O_4 interfaces are fixed by the equilibria achieved there, for any given temperature, the parabolic rate constant will be relatively

unaffected by the external oxygen partial pressure. Increasing the oxygen partial pressure in the gas phase should, theoretically, lead to an increase in the relative thickness of the out-most Fe_2O_3 layer. However, since this layer only accounts for about 1% of the metal-scale thickness, any variation in rate constant with oxygen partial pressure will be difficult to detect.

1.2 HIGH TEMPERATURE OXIDATION OF ALLOYS

1.2.1 Thermodynamics of alloy oxidation

Typical oxidation mechanisms of binary alloy systems are shown schematically in Figure 1.7 and Figure 1.8. For the case that the alloy based on noble metal, such as Ag, Au, Pt etc., which does not form a stable oxide, and alloyed with reactive elements such as Al, Cr, Ni, Fe, Co etc., which form stable oxides, there are two possible oxidation pathways[18] shown in Figure 1.7 (a) and (b). If both of the alloy elements form stable oxide, there are generally four different types of oxidation mechanisms, shown in figure Figure 1.8. The first three types are differentiated by solubility of the two oxides. They are when the two oxides have unlimited solubility (a), the solubility is limited (b) and no solubility (c). When the concentration of the element (e.g. B) which can form the more stable oxide is high enough, its scale is almost exclusively present, as shown in Figure Figure 1.8 (d). In general, many of the factors described for the oxidation of pure metals also apply to the oxidation of alloys, but alloy oxidation is much more complex due to some, or all, of the following factors[6]:

- *The metals in the alloy will have different affinities for oxygen reflected by the different free energies of formation of the oxides.*

- *Ternary and higher oxides may be formed.*
- *A degree of solid solubility may exist between the oxides.*
- *The various metal ions will have different mobilities in the oxide phases.*
- *The various metals will have different diffusivities in the alloy.*
- *Dissolution of oxygen into the alloy may result in sub-surface precipitation of oxides of one or more alloying elements (internal oxidation).*

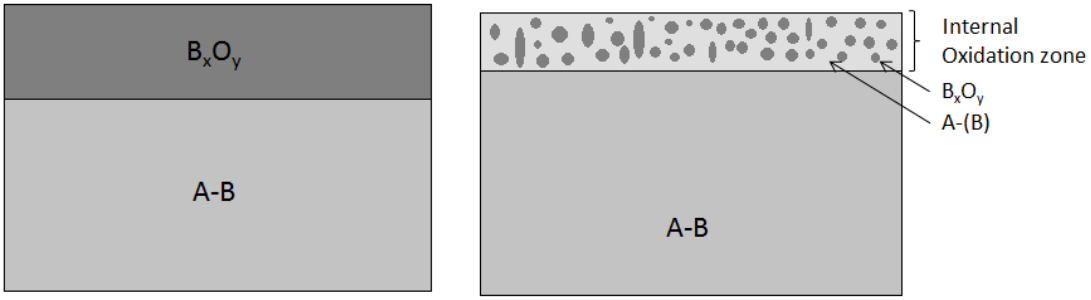

(a) (b)

Figure 1.7 Schematics of oxidation pathways for alloys which are based on a noble metal alloyed with a reactive element

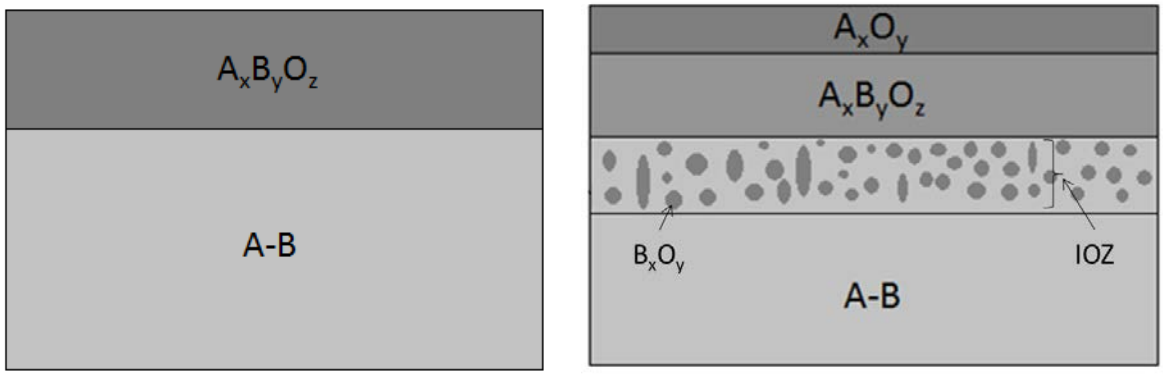

(a) (b)

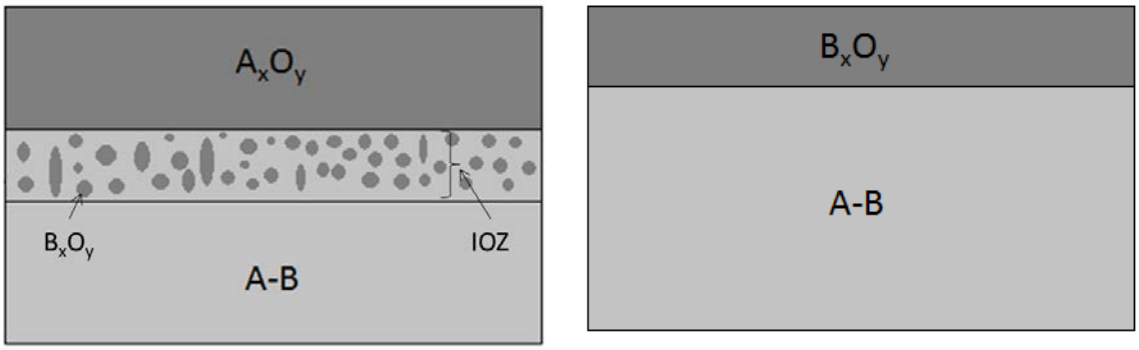

(c) (d)

Figure 1.8 Schematics of oxidation pathways for alloys in which both of the alloy elements form stable oxide (IOZ stands for internal oxidation zone)

1.2.2 Kinetics of alloy oxidation

1.2.2.1 Initial competitive nucleation

As discussed at the end of last section, alloy oxidation is more complex than pure metal oxidation in both thermodynamics and kinetics aspects. One major difference is when both of the alloy elements can form stable oxide under the oxidizing environment, there is a transient stage when both of the oxides are nucleating and growing before steady-state scaling behavior can be established[19]. The establishment of a protective scale on an initially bare alloy exposed to a high P_{O_2} is a time-dependent process. Virtually, all the thermodynamically stable products are formed during the transient stage[20,21]. With the reaction proceeds, a gradient develops in the oxidant activity, such that the least stable products dissociate or are displaced, leaving only the most stable product(s) closest to the alloy. The steady-state scales formed on alumina- and chromia-formers are predominantly Al_2O_3 and Cr_2O_3, respectively, because these oxides are very stable and the diffusivities of the base-metal cations are low. As a consequence of the latter, the continued growth of the less-stable transient products above the established Al_2O_3 and Cr_2O_3 scale layer is essentially terminated and, they may be eventually detached or dissolved. The duration of the transient stage can vary significantly from alloy to alloy. For some alloys it can be of the order of seconds, while for others it can be the order of days. The duration generally decreases with increasing content of the protective-scale-forming element.

The interfacial composition of the protective-scale-forming element, e.g. Al or Cr, changes during the transient stage from its bulk content to a time-invariant, steady-state value. According to a treatment by Gesmundo et al.[22] this change in the interfacial composition should be gradual and regular (assuming no phase change), without an intermediate decrease below and then increase to the steady-state value, as was predicted by Whittle et al[23]. The steady-state

interfacial composition of B in a binary alloy A-B forming an exclusive BX_v scale layer is given by[24]:

$$N_B^i = \frac{N_B^o - F(u)}{1 - F(u)} \tag{1.17}$$

where N_B^i is the interfacial composition of B, N_B^o the bulk concentration of B and

$$F(u) = \pi^{1/2} u \cdot \exp(u^2) \cdot erfc(u) \tag{1.18}$$

where

$$u = \left(\frac{V_m}{\nu M_X} \right) \left(\frac{k_p}{2D_B} \right)^{1/2} \tag{1.19}$$

where V_m is the molar volume of the alloy, ν the stoichiometry factor in BX_v, M_x the atomic weight of X and k_p the growth rate of the scale. F(u) is referred to as the auxiliary function and it has limiting values from F(u=0)=0 to F(u=∞)=1. Wagner[24] derived equation 1.17 by assuming recession of the alloy-scale interface, parabolic thickening kinetics of the BX_v scale, composition independence of D_B, and no solubility of A in BX_v. The change in the interfacial composition of B will determine whether a protective scale can be form or not.

1.2.2.2 Steady-state diffusion kinetics

The steady-state defined in oxidation is different from the general definition in kinetics. In general kinetics, steady-state means the flux is constant with respect to time. However, with the oxide scale thickening during oxidation, the flux of diffusing species is always decreasing with time. Therefore, steady-state in oxidation can be defined as the oxide constitution and boundary conditions do not change with time. During steady-state diffusion, the kinetics of external oxide scale growth on an alloy has a similar parabolic form to the case on the metal in equation 1.10.

However, the concentration of the secondary alloying element plays an important role on the growth rate of the external scale[6]. Taking the oxidation of Ni-Cr alloys as an example, Figure 1.9 shows a dependence of the parabolic growth rate on Ni-Cr alloys with various Cr concentrations[25,26]. When the Cr concentration is low in the alloy, the chromium dissolves in the NiO scale. The trivalent Cr^{3+} can change the defect structure of NiO and increases the concentration of Ni^{2+} vacancies. The parabolic rate constant increases with increasing Cr concentration in the alloy. After passing a critical value, the chromium in the alloy forms discontinuous chromia precipitates which block the outward diffusion of Ni^{2+}. The more chromium in the alloy, the larger volume fraction of precipitates it will have and the less flux of Ni^{2+} there will be. Therefore the parabolic growth rate decreases with increasing chromium concentration. Furthermore, when the chromium concentration is high enough, the chromia precipitates can be continuous and a layer of chromia will form. Under this case, the outward diffusion of Ni^{2+} will be completely blocked and only chromia will grow. Therefore, there is a dramatic drop in parabolic growth rate with further increasing chromium concentration. Further increasing chromium concentration does not influence the growth rate of chromia very much.

Besides the difference in external scale growth rate, formation of an internal oxidation zone (IOZ) is another possible distinguishable feature for alloy oxidation. Internal oxidation is the process in which oxygen diffuses into an alloy and causes sub-surface precipitation of the oxides of one or more alloying elements. The typical morphology of the IOZ is shown in Figure 1.8 (b) and (c). The growth kinetics of IOZ varies with oxidation mechanism; however, it can be quantified for the simplest case where there is no external oxide formation.

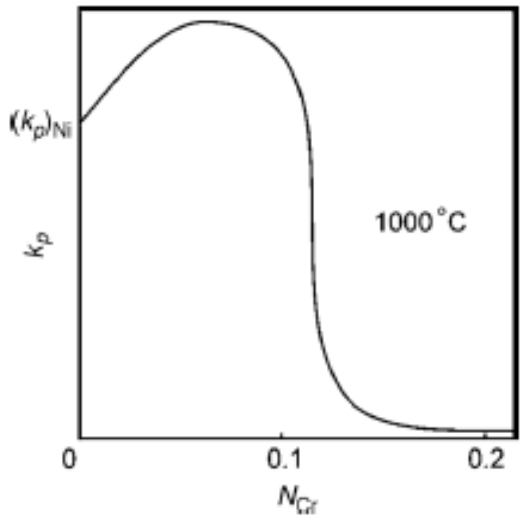

Figure 1.9 Dependence of the parabolic oxidation rate of Ni-Cr alloys with varies Cr concentration[6]

Suppose the concentration profiles of oxygen and solute B are linear, as shown by Figure 1.10. The concentration of oxygen and solute B at the internal oxidation front is assumed to be zero. Therefore, the flux of oxygen diffusing to the internal oxidation front is given by the Fick's first law,

$$J_o = D_O \frac{N_O^S}{XV_m} \tag{1.20}$$

where N_O^S is the oxygen solubility in A (atom fraction), V_m is the molar volume of the solvent metal (cm^3/mole), and D_O is the diffusivity of oxygen in A (cm^2/sec).

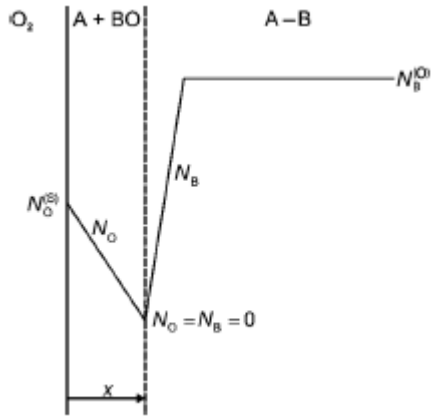

Figure 1.10 Simplified concentration profile of oxygen and solute in the alloy

Suppose all the supplying oxygen flux is consumed by forming BO_v in the internal oxidation front, the amount of oxygen consumed is:

$$\frac{dm}{dt} = \frac{N_B^o v}{V_M}\frac{dX}{dt} \tag{1.21}$$

where N_B^o is the initial solute concentration. Since the supply is equal to the consumption, it yields

$$D_O \frac{N_O^S}{XV_m} = \frac{N_B^o v}{V_M}\frac{dX}{dt} \tag{1.22}$$

Rearranging the terms provides,

$$XdX = \frac{N_O^S D_O}{v \cdot N_B^o} dt \tag{1.23}$$

Integrating of equation 1.23 and using the initial condition that X=0 when t=0, a parabolic growth rate is derived in equation 1.24,

$$X = \left[\frac{2N_O^S D_O}{N_B^o v} t\right]^{1/2} \tag{1.24}$$

From this equation, the growth rate of internal oxidation increases with increasing the product of oxygen solubility N_O^S and oxygen diffusivity D_O, which is also defined as oxygen permeability.

The rate is also seen to decrease with increasing solute concentration. Although a more complex form of growth kinetics can be obtained from a more rigorous derivation, the general growth rate dependence on those terms remains the same.

1.2.3 Transition from internal to external oxide formation

From Figure 1.9, it can be seen that there is a critical concentration of solute element, above which the outward diffusion of solute will be rapid enough to form a continuous blocking layer of BO_v and stop the growth of solvent oxide as well as internal oxidation. This transition to external oxidation is the basis for the design of Fe-, Ni-, and Co-base engineering alloys. These contain a sufficiently high concentration of a solute (e.g., Cr, Al, or Si) to produce an external layer of a stable, slowly growing oxide (e.g., Cr_2O_3, Al_2O_3, or SiO_2), which prevents oxidation of the parent metal. This process is also known as selective oxidation. Quantificational determination of the critical concentration of solute N_B^* has been carried out by Wagner[3]. It was assume that A-oxide would not form as an external scale. in this case, the concentration profile used for calculation of this critical concentration of solute N_B^* is shown by Figure 1.11. Since the thickness of the IOZ has been found to be proportional to the square root of time, it is written in the form of:

$$X = 2\gamma\left(D_O t\right)^{1/2} \tag{1.25}$$

where D_o is the diffusion coefficient of oxygen in the alloy and γ is a dimensionless factor to account for the proportional coefficient.

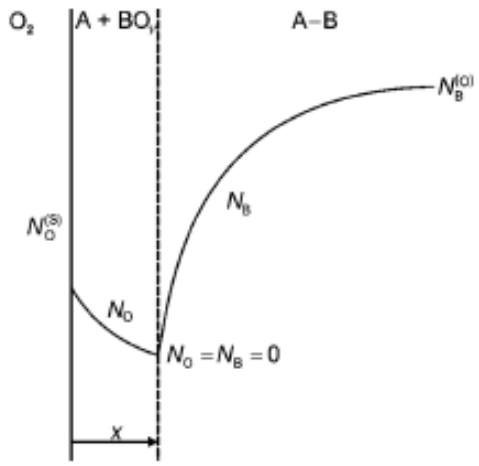

Figure 1.11 Concentration profile used for the calculation of critical concentration of solute in alloy

From Fick's 2nd law, the diffusion of solute element B from alloy is determined by

$$\frac{\partial N_B}{\partial t} = D_B \frac{\partial^2 N_B}{\partial x^2} \tag{1.26}$$

with initial conditions $t = 0$, $N_B = 0$ for x < 0 and $N_B = N_B^{(o)}$ for x > 0, and boundary conditions t = t, $N_B = 0$ for x = X and $N_B = N_B^{(o)}$ for $x = \infty$. The solution for equation 1.26 is given by

$$N_B(x,t) = N_B^{(o)}\left[1 - \frac{erfc\left(\frac{x}{2\left(D_B t\right)^{1/2}}\right)}{erfc\left(\theta^{1/2}\gamma\right)}\right] \tag{1.27}$$

where $\theta = D_O/D_B$. There is a mass balance in the model that the amount of solute B consumed by forming BO_v as an internal oxidation must be equal to the amount of solute B supplied by diffusion from the bulk alloy. Assume the mole fraction of BO_v in the IOZ is f and V_m is the molar volume of the alloy, from the mass balance,

$$\frac{fdX}{V_m} = \left[\frac{D_B}{V_m}\frac{\partial N_B}{\partial x}\right]dt \tag{1.28}$$

Substituting equation 1.25 and 1.27 into equation 1.28 yields

$$\alpha = \frac{f}{N_B^{(o)}} = \frac{1}{\gamma\pi^{1/2}}\left(\frac{D_B}{D_O}\right)^{1/2}\frac{\exp\left(-\gamma^2\theta\right)}{erfc\left(\gamma\theta^{1/2}\right)} \tag{1.29}$$

As presented by Rapp[27], for a realistic assumption that $N_O^{(s)}D_O << N_B^{(o)}D_B$, which is $\gamma\theta^{1/2} << 1$, equation 1.29 can be simplified as

$$\alpha \approx \frac{2\nu}{\pi}\left[\frac{N_B^{(o)}D_B}{N_O^{(s)}D_O}\right] \tag{1.30}$$

According to Wagner, when the volume fraction of oxide, g = f (V_{ox}/V_m), reaches a critical value, g*, the transition from internal to external scale formation should occur. Insertion of f, in terms of g*, in α in Equation 1.30 then gives the criterion for external oxidation

$$N_B^{(o)} > \left[\frac{\pi g^*}{2\nu}N_O^{(s)}\frac{D_O V_m}{D_B V_{ox}}\right]^{1/2} \tag{1.31}$$

Equation 1.31 enables prediction of how changing exposure conditions will affect the concentration of solute required to produce an external scale. Those conditions that decrease the inward flux of oxygen, e.g., lower N_O^S (i.e. lower p_{O2}) and those that increase the outward flux of B, e.g., cold working the alloy (increasing D_B by increasing the contribution of short-circuit diffusion) will allow the transition to external oxidation to occur at lower solute concentrations. Rapp[27] tested this Wagner theory using Ag-In alloys. It was found that at p_{O2} =1 atm and T=550^{o}C the transition occurred for g*=0.3 (N_{In}=0.15). Rapp then used this value to predict the effect of reduced p_{O2} (reduced N_O^S) on the N_{In}^* value at 550^{o}C. This is shown in Figure 1.12, in which the dash and solid lines are calculated N_{In}^* with and without pre-oxidation and the circles and crosses are experimental for N_{In}^* samples with and without pre-oxidation. Despite some scattering of the data, the agreement between experiment and Equation 1.31 was excellent. Rapp's experiments also gave an indirect verification of the effect of increased D_B, caused by cold work, on the transition. Specimens containing only 6.8 at% In were observed to undergo the

transition to external In_2O_3 formation around scribe marks under exposure conditions that required 15 at% In to produce the transition on un-deformed surfaces.

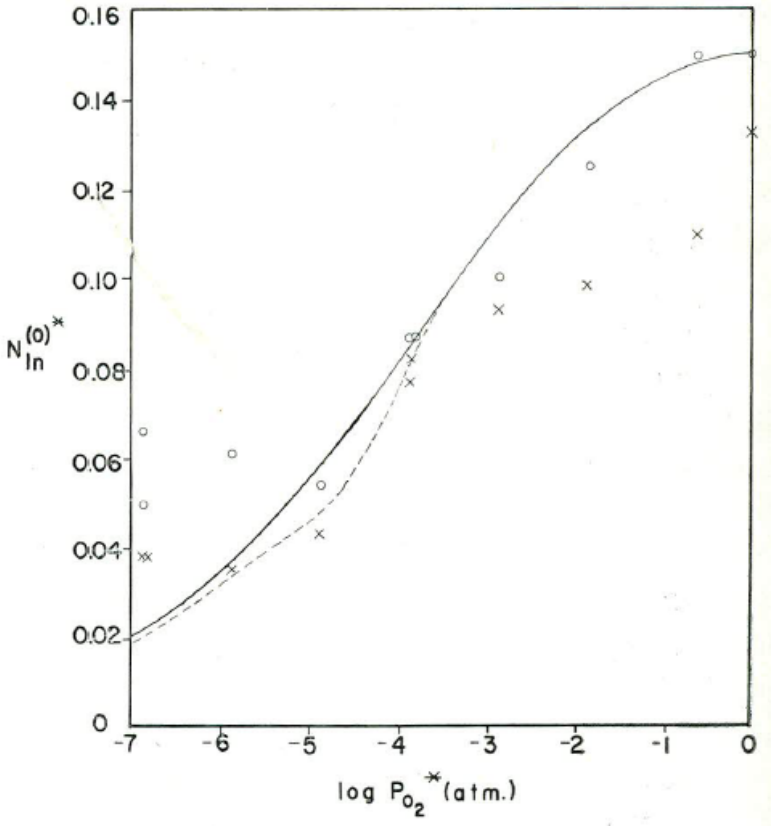

Figure 1.12 The critical concentration of N_{In}^{*} to form a continuous external In_2O_3 scale at different oxygen partial pressure at 550°C. The dash and solid lines are calculated N_{In}^{*} with and without pre-oxidation and the circles and crosses are experimental for N_{In}^{*} samples with and without pre-oxidation

However, in Rapp's study[27], the critical volume fraction g^{*} was determined by a single experimental observation that the critical mole fraction of In to form an external In_2O_3 scale at 1atm O_2 at 550°C was 0.15. Since molar volume of $InO_{1.5}$ is twice as much as molar volume silver, the critical volume fraction of $InO_{1.5}$ to form an external In_2O_3 scale (g^{*}) is 0.3. There was no theoretical foundation to determine this g^{*} for other alloy systems at different conditions accurately.

Maak[2] modified the above model to taking into account the effect by the growth of an external AX_v scale. In this modified model, equation 1.29 remains the same but the parameter γ is calculated using

$$\frac{N_O^{(s)}}{vN_B^{(o)}} = \frac{\left[erf\left(\gamma\right) - erf\left\{\left(\frac{V_m}{vM_O}\right)\left(\frac{k_p(AX_v)}{2D_O}\right)\right\}\right]\exp\left(\gamma^2\right)}{\phi^{1/2}\exp\left(\gamma^2\phi\right)erfc\left(\gamma\phi^{1/2}\right)} \tag{1.32}$$

Despite the complex form of this equation, it gives important information that the value of the critical concentration N_B^* tends to be higher for the case when AX_v scale formation can occur.

1.2.4 The third element effect on forming a protective external scale

This third element effect can be seen on oxidation maps[1, 28] where oxidation data are superimposed on the ternary composition triangle, as illustrated in Figure 1.13. These maps are not thermodynamic diagrams, but are based upon kinetic processes which take place during scale development. Three primary regions of oxidation can be seen corresponding to (I) NiO external scales +Al_2O_3/Cr_2O_3 internal oxides, (II) Cr_2O_3 external scale + Al_2O_3 internal oxides, and (III) external scales of only Al_2O_3. The boundary between the NiO- and Al_2O_3-scale forming regions is indicates the critical Al concentration N_{Al}^* to form a protective Al_2O_3 scale. The addition of Cr to Ni-Al alloys results in a remarkable synergistic effect. Specifically, chromium additions of about 10wt% can enable external Al_2O_3 formation on alloys having aluminum levels as low as 5wt%. Wagner observed the similar effect for Cu-Zn-Al alloys[30] and Pickering obtained similar results for Ag-Zn-Al alloys[29]. In the latter experiments Ag-3 at% Al alloys were found to oxidize internally while, under the same conditions, an Ag-21at%Zn-3at%Al alloy produced an external Al_2O_3 scale.

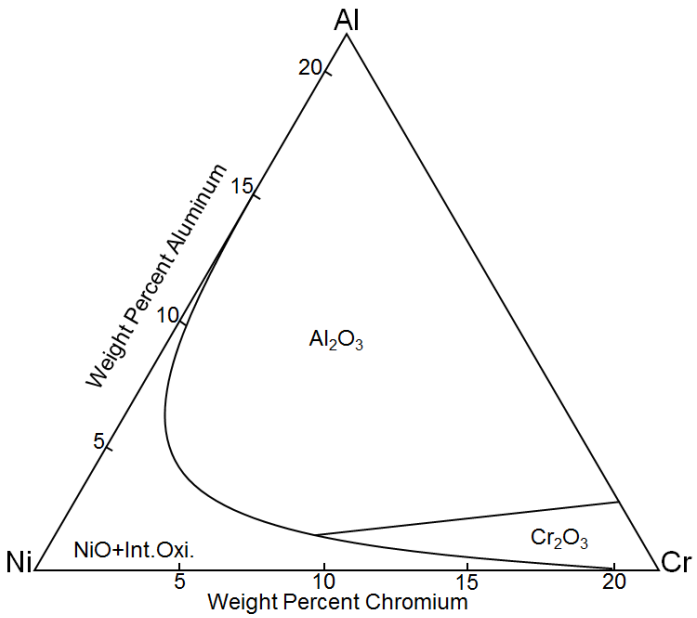

Figure 1.13 Oxidation map for Ni-Cr-Al oxidized in Ar+10% oxygen at 1000°C for 20h (Re-plot from Giggins and Pettit's work[1])

An often-cited mechanism for the third element is that if the third element oxide has a stability intermediate between that of A and B and if the p_{O2} is great enough to form the oxide of the third element, this will, in effect, decrease the inward flux of oxygen and allow external formation of BO_v at lower concentrations of B[30]. This concept is often referred to as "secondary gettering" [31]. However, not all ternary additions that form oxides of intermediate stability have the desired effect[32,33]. For example, the addition of Mn to Fe-Al alloys does not facilitate the establishment of an Al_2O_3 scale when present in high concentration even though the stability of MnO is intermediate to FeO and Al_2O_3[34,35]. Nevertheless, the concept has proved useful in the design of high-temperature alloys since the element which provides protection by selective oxidation (e.g., Al) often has detrimental effects on other alloy properties, particularly mechanical properties, and should, in these cases, be held at as low a concentration as is feasible. This concept has led to the development of the M-Cr-Al (M = Fe, Ni, or Co) alloys. For example, the addition of Cr to

reduces the critical concentration N_{Al}^{*} in Ni-Al alloys. This behavior has allowed the design of more ductile alloys and coatings.

1.2.5 Sustaining the growth of protective external scale

As was discussed in the previous section, formation of a continuous BO_v scale layer on an alloy of a given B content can be more easily facilitated by exposure to a lower oxidant pressure or by apparently effecting a decrease in the D_O/D_B ratio. If a continuous BO_v scale is established under a particular set of conditions, it might be necessary to determine if its growth can be sustained under a different set of conditions. An example of this could be the pre-oxidation of an alloy at a low P_{O2} followed by in-service exposure to a higher P_{O2} and/or different temperature. Clearly, the sustained growth of a continuous BO_v scale requires a sufficient supply of B from within the alloy to the alloy/scale interface. The maximum possible rate of supply of B in the alloy can be imposed by setting the concentration of B at alloy/scale interface to zero, thereby producing the steepest possible diffusion gradient of B. Under steady-state conditions, this maximum rate of supply of B would have to equal the rate of consumption of B as a result of BO_v scale growth. Determination of the minimum B content $N^{o}_{B(min)}$ necessary for the sustained exclusive growth of a BO_v scale on an A-B alloy was originally considered by Wagner[24], who further assumed that D_B is independent of concentration, that the BO_v scale obeys parabolic thickening kinetics, that solvent metal A is insoluble in BO_v, that concentration of B at the interface is negligible and that the recession of the alloy/scale interface can be neglected. With these assumptions, the minimum concentration of B in the alloy to sustain the growth of BO_v is:

$$N^{o}_{B(\min)} > \frac{V_m}{vM_O}\left(\frac{\pi \cdot k_p}{2D_B}\right)^{1/2} \tag{1.33}$$

1.3 STEAM EFFECTS ON THE OXIDATION BEHAVIOR OF ALLOYS

Kofstad[8] called the influence of steam on alloy oxidation a "forgotten" problem as it was not until the 1990s when the study of steam effects on oxidation behavior of alloys was significant. Most of the studies were done on Fe-based systems, while some of them were done on Ni-based and other alloy systems. A variety of phenomena have been found in steam oxidizing conditions. Even though, the mechanism of the steam effects is poorly understood[36, 37] because of the diversity of scale-steam interactions possible. The steam effects on the oxidation behavior of alloys are summarized as follows:

1.3.1 Oxide stability in steam

The conditions under which the oxides of interest are thermodynamically stable can be assessed from the equilibrium oxygen partial pressures at which they dissociate. If the effective oxygen partial pressure in the steam is lower than the equilibrium dissociation partial pressure for an oxide, then that oxide would not be expected to form. In the pure steam, the effective oxygen partial pressure comes from the dissociation of steam as:

$$H_2O(g) = H_2(g) + \frac{1}{2}O_2(g) \tag{1.34}$$

From law of mass reaction, the following equilibrium condition must be hold

$$K_{1.34} = \frac{p_{H_2} \cdot p_{O_2}^{1/2}}{p_{H_2O}} \tag{1.35}$$

where the equilibrium constant is given by:

$$K_{1.34} = \exp\left(\frac{-\Delta G^{o}_{1.34}}{RT}\right) \tag{1.36}$$

and from Kubaschewski and Alcock[38]

$$\Delta G^{o}_{1.34} = -230000 - 8.14T\ln(T) + 9.25T \tag{1.37}$$

Assuming that the dissociation goes to equilibrium at the metal/steam interface and partial dissociation of x mole steam is assumed to give x moles H_2 and x/2 moles O_2, then the effective oxygen partial pressure can be calculated as a function of partial pressure of steam. Figure 1.17 shows the calculated equilibrium dissociation oxygen partial pressure–temperature relationships for steam over a range of pressures, and for Cr_2O_3 and the other oxides of iron. It can be seen that, even at a total pressure of 1 bar, the oxygen partial pressure from the equilibrium dissociation of steam is two orders of magnitude higher than the dissociation oxygen partial pressure needed to form the least stable iron oxide, Fe_2O_3. Therefore, it would be expected that all the oxides would be present in scales grown at all the steam pressures shown in Figure 1.14, provided that the steam was equilibrated on the metal-oxide surfaces, and the steam flow rate was sufficient to prevent oxygen depletion (or hydrogen accumulation).

Another issue related with the stability of oxide in steam is chromium volatilization. For Cr-containing alloys there is the possibility that formation of volatile species in steam which can reduce the service life of the alloys affected through loss of scale protectiveness. The volatile chromium oxy-hydroxide $CrO_2(OH)_2$ is formed via

$$\frac{1}{2}Cr_2O_3(s) + H_2O + \frac{3}{4}O_2 = CrO_2(OH)_2(g) \tag{1.38}$$

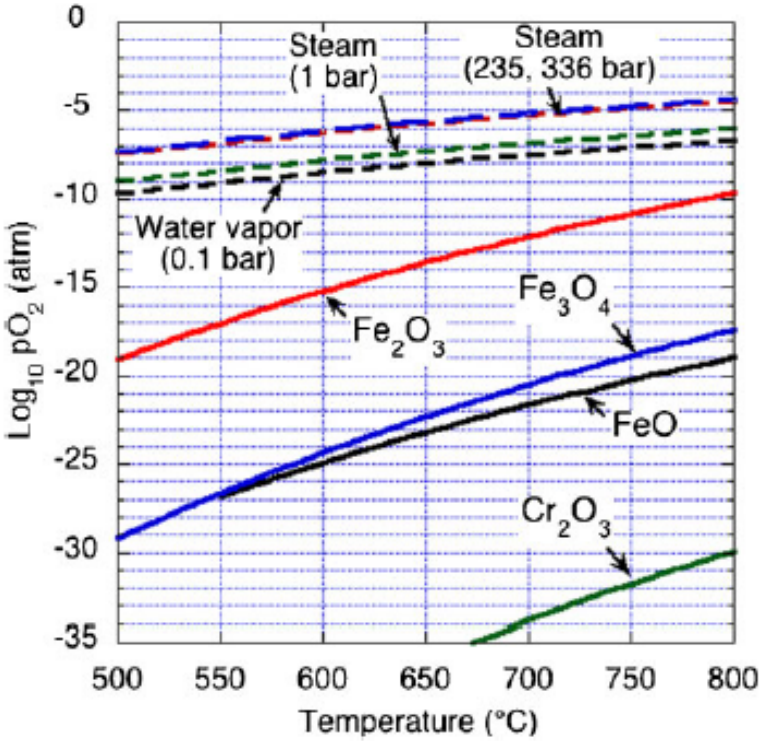

Figure 1.14 Partial pressure of oxygen from dissociation of steam[39]

The source of oxygen is assumed to be the dissociation of steam via the reaction shown in equation 1.34. Figure 1.15 compares the vapor pressure of $CrO_2(OH)_2$ as a function of temperature under different steam pressures using thermodynamic data from the work of Opila et al.[40]. Table 1.1[41] shows the results of calculated mass loss of Cr (metal) from the surfaces of laboratory-sized alloy coupons oxidized at 650°C to 800°C in air+10%H_2O, based on a low steam flow rate (low flow rate means gas transport theory in the viscous flow regime can be used). These data suggest that the loss of Cr would be small at 650°C. However, since the Cr loss is linear proportional to the vapor pressure of $CrO_2(OH)_2$ which is linear proportional to the steam pressure, the Cr loss could become significant at the higher temperatures at 240 bar. These data also indicate that the vapor pressure of $CrO_2(OH)_2$ in steam at the temperatures and pressures used in laboratory tests (1-17 bar) would be much lower at all temperatures than under current (241 bar, 541°C) and future boiler operating conditions (340 bar, 760°C).

Table 1.1 Calculated Cr loss rate at different temperatures in air+10%H_2O [41]

		J_{Cr} (Cr metal)	
Temperature, ^oC	$pCrO_2(OH)_2$, atm	g/cm^2sec	mg/cm^2year
650	$5.0x10^{-8}$	$1.4x10^{-12}$	0.04
700	$1.6x10^{-7}$	$4.2x10^{-12}$	0.13
800	$1.2x10^{-6}$	$3.0x10^{-11}$	0.95

It is notable that, if the oxygen required in the reaction shown in equation 1.38 is supplied by a source other than by dissociation of steam (such as in an air-steam mixture), a significantly higher vapor pressure of $CrO_2(OH)_2$ is generated. As indicated in Figure 1.15, over the temperature range of interest the vapor pressure in an ambient-pressure air+10% H_2O is estimated to be similar to that in steam at 240-340 bar. Calculated losses of Cr from a high-Cr austenitic steel (alloy NF709) in an air+10% H_2O environment showed excellent agreement with those measured experimentally as shown in Table 1.2[41].

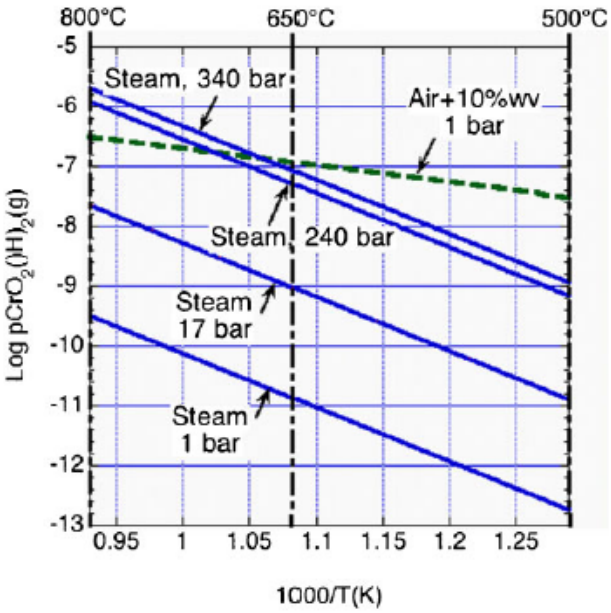

Figure 1.15 Vapor pressure of $CrO_2(OH)_2$ at different temperatures and steam pressure[39]

Table 1.2 Loss of Cr from evaporation in wet air condition [41]

Temperature ^{o}C	J_{Cr} (Cr metal) g/cm^{2}sec	
	Calculated	Measured
650	$(2.1\pm0.2)\times10^{-11}$	$(1\text{-}2)\times10^{-11}$
800	$(1.2\pm0.1)\times10^{-10}$	1.5×10^{-10}

1.3.2 Effect of steam pressure on oxidation kinetics

As a general conclusion, the growth kinetics for almost all oxides has been found to be increased with the presence of steam[8,42,43,44,45,46]. Besides the enhanced growth rate of individual oxide, the steam can elongate the transient stage in which all oxides are growing before a protective Cr_2O_3 layer can be established[52]. However, it has been reported by Hayashi et al.[47] that for the oxidation of Ni-Al binary alloy at around 800^{o}C, the oxidation rate of NiO may be decreased by the presence of steam, along with a thick metallic Ni layer forming at the NiO/alloy interface. Detailed steam effects on the growth kinetics will be shown in the following sections.

1.3.3 Oxidation of commercial Fe-based alloys in steam

1.3.3.1 Oxidation of Fe-based alloys

Steam in the atmosphere is well known to accelerate oxidation of Fe-based alloys at high temperatures[48]. Early work[49] shows that the scaling rate of Fe rises by a factor of 1.2 at 850^{o}C and by 1.6 at 950^{o}C by steam. The following summarizes the steam effects on steam oxidation of pure Fe and Fe-based alloy and its mechanism if it was provided.

Change in iron oxide scale morphology[49]

According to the oxidation conditions, there are three types of iron oxide scale structures:

- Oxidized in dry oxygen. The scale is characterized by loss of contact between scale and metal over about half the surface.
- Oxidized in oxygen with steam. The scale is continuous and contact between scale and metal is maintained over the entire surface for the whole oxidation period.
- Oxidized in oxygen with steam. The scale forms an inner porous layer.

Figure 1.16 shows the change of scale structures from dry oxygen to oxygen with 69% steam.

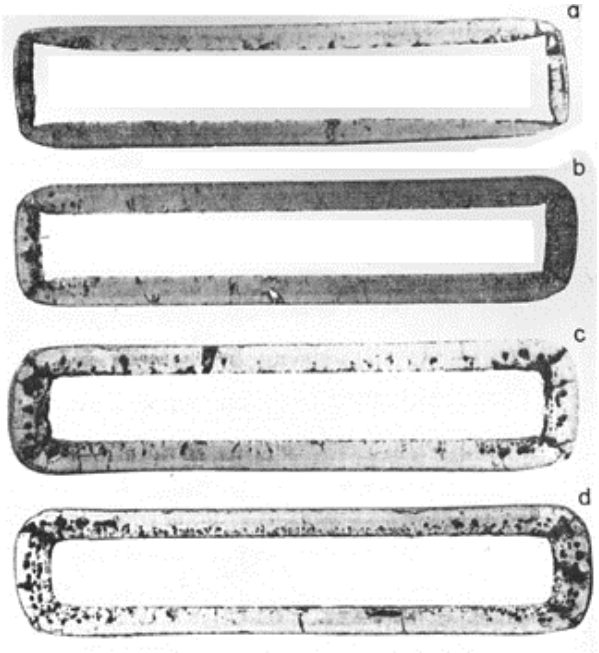

Figure 1.16 Change of scale structures with different levels of steam content. (a) 100% oxygen (b) 98% oxygen +2% steam (c) 88% oxygen + 12% steam (d) 31% oxygen + 69% steam[49]

Enhanced Growth Kinetics

The presence of steam with oxygen has been found to accelerate the oxidation rate of mild steel and two grades of pure iron of varying purity[49]. Associated with the enhanced growth

rate, inert makers[8] were found at the iron/wustite interface after oxidation in dry oxygen at 950°C, while after oxidation in mixtures of oxygen and steam, the markers were found to be present in the FeO. At the same time, the FeO layer becomes very porous. To explain this result, it was supposed that pores occur at the iron/wustite interface during the oxidation. In the presence of steam, a H_2/H_2O mixture is formed in these pores, which transports oxygen to the iron/scale interface by an oxidation/reduction mechanism. Therefore, oxide bridges are built up from the metal to the scale, which enables the further oxidation of the metal without substantial inhibition. A schematic is shown in Figure 1.17 to illustrate this mechanism[44,49,50]. For this mechanism to occur, pores must exist in the oxide scale. However, it has been found[51] that the growth kinetics were increased without the formation of pores. This is explained by hydrogen in the scale enhanced the creep ability. Therefore, the loss of contact if oxidized in dry oxygen could be filled by creep or flow within the scale if oxidized in oxygen with steam. By this mean, the contact was maintained so that the outward diffusion of iron is enhanced.

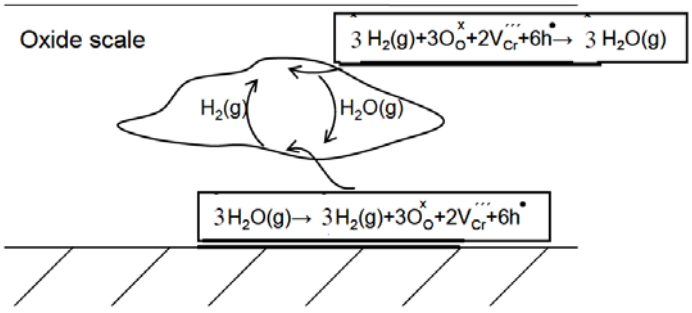

Figure 1.17 Schematics of the transport mechanism by oxidation/reduction of H_2/H_2O mixture[50]

Breakaway oxidation

Besides enhancing the scale growth rate, steam has also been reported to promote breakaway oxidation[46,52]. In this case, the alloy loses its ability to form a protective scale and starts to form a non-protective scale of the base metal either locally or entirely on the surface. Figure 1.18 shows an example of the morphology of the breakaway oxidation. Several

hypothesizes have been proposed to explain the mechanism for breakaway oxidation[53,54]. It may be due to the enhanced Cr depletion as a consequence of formation of volatile species $CrO_2(OH)_2$ by:

$$Cr_2O_3 + 3/2O_2(g) + 2H_2O(g) = 2CrO_2(OH)_2(g)$$

However the enhance Cr depletion due to formation of volatile $CrO_2(OH)_2$ cannot explain the experimental finding that the tendency for occurrence of breakaway oxidation is increased by H_2O/O_2 ratio. Another possibility is the steam may penetrate through the scale to the scale/alloy interface. Reaction of the steam with the alloy may result in formation of rapid growth of hematite beneath the chromia scale, leading to a separation between the chromia scale and the matrix and the destruction of the initial protective scale[53,54]. A more well-accepted mechanism considers the increased tendency for Cr to be oxidized internally, rather than forming an external scale[43]. It was inferred the oxygen permeability into the alloy was enhanced in wet oxidizing conditions. Formation of a protective Cr_2O_3 scale requires more Cr content in the alloy when it is oxidized in wet oxidizing conditions.

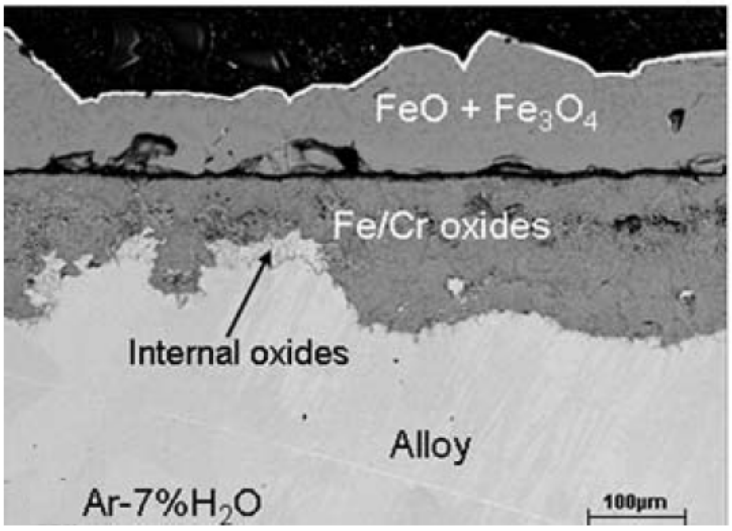

Figure 1.18 The morphology of the breakaway oxidation of Fe-10Cr after oxidation in Ar-7%H_2O for 72h at 900^{o}C

Enhanced spallation in cyclic oxidation

Steam can also enhance the extent of scale spallation during thermal cycling[55, 55]. This is shown in Figure 1.19 by the thermogravimetric experiment carried on 304SS and 310SS samples[55]. Increasing Ni and Cr contents has beneficial effect to prevent the spallation under cyclic oxidation in wet oxidizing conditions[55].

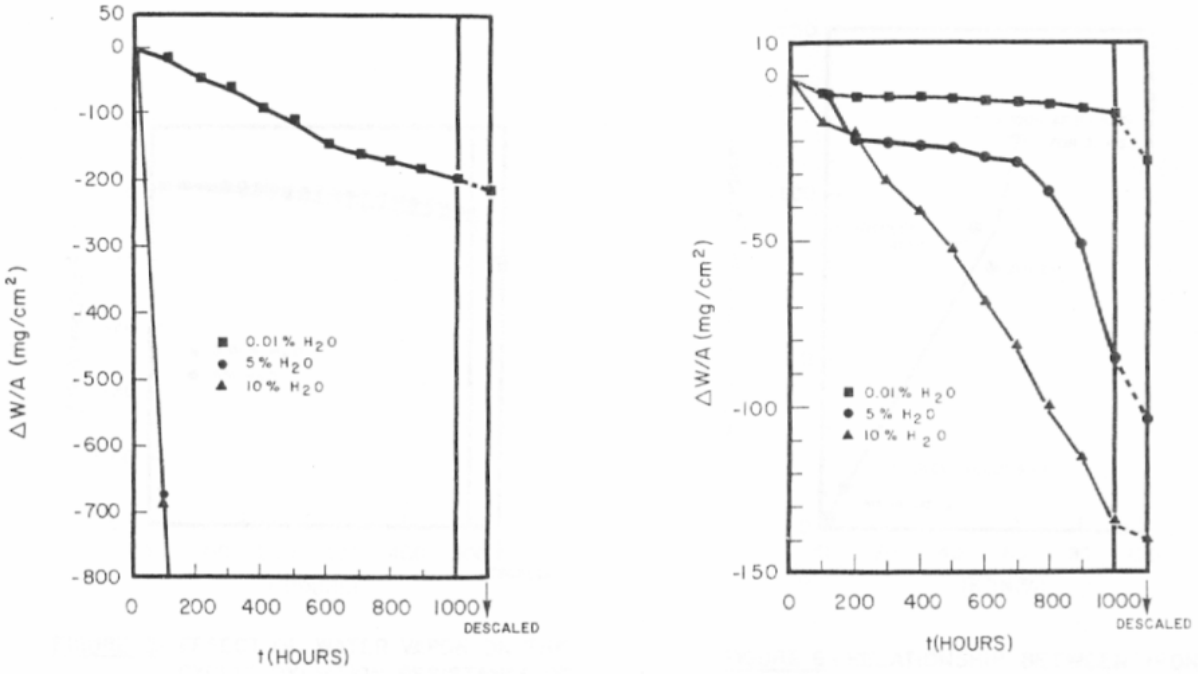

Figure 1.19 Weight gain curves to show the enhanced spallation after cyclic oxidation of (a) 304SS and (b) 310SS at 1000^{o}C[55]

Promote transient oxidation

It was found[56] for an Fe-based alloy oxidized at 1000^{o}C under dry oxidizing condition, the scale was composed mainly of γ-Al_2O_3, at the initial stage and then transformed to α-Al_2O_3. By contrast, under wet oxidizing conditions, the transient oxides was found to be as $(Mg,Fe)(Cr,Al)_2O_4$, $MgAl_2O_4$ (orthorhombic), Al_2O_3 and these oxides transform to $MgAl_2O_4$ (cubic), Cr_2O_3, Fe_2O_3, α-Al_2O_3 with time.

1.3.4 Oxidation of Ni-based alloys in steam

Steam effects on the oxidation of Ni-based alloys were not studied as much as on Fe-based alloys. Studies on alumina-forming Ni-based alloys were even less. Even though, the steam effects on oxidation behavior of Ni-based alloys are summarized in the following:

- The presence of steam permits a H_2/H_2O mixture to be formed in voids, which facilitates a rapid inward transport of oxygen across the pores via dissociative gas transport and thus increases the growth rate of the scale[44,49]. This is a similar effect as the one shown in Figure 1.17.
- The scales spalls more profusely during cyclic oxidation in wet air than in dry air, particularly for those alloys with alumina scales which are only moderately adherent under dry oxidizing conditions[57]. Comparatively, steam has little effect to promote cracking and spalling on the alloy with extremely adherent Al_2O_3 scale[58]. This trend can be seen by Figure 1.20[57]. From this figure, the spallation of Al_2O_3 scale becomes more severe with increasing steam pressure on Rene N5 with regular amount of sulfur and sulfur is usually considered to be detrimental to adhesion of the scale[57]. This trend indicated that steam enhances cracking and spalling of Al_2O_3 scale with moderate adhesion. However, if sulfur is removed from that alloy, the cyclic oxidation behavior of that alloy in wet air becomes similar to the same alloy oxidized in dry air. This means steam does not cause substantial cracking and spalling for alloy with adherent Al_2O_3 scale.
- Steam may change the plasticity of the oxide scales, although it can either be decreased[55] or increased[44] depending specific cases. It was proposed that steam decreases the plasticity of the scale and caused enhanced spallation during cyclic oxidation[55]. By

contrast, other research proposed[44] that steam can increase the oxidation rate of the scale because the cracks formed within the scale can be healed due to enhanced oxidation.

- Steam can cause the vaporization of some oxides to be increased because of the formation of hydrated species with high vapor pressures[59]. This issue is very important for Cr_2O_3-scale forming alloys used at high temperature (above ~800^{o}C) or under high steam and oxygen pressure[41].
- Steam causes the concentration of proton defects to be increased, which can influence defect-dependent properties such as high-temperature creep and diffusion[60,61]
- Thicker oxides are formed during oxidation in wet air than dry air. This was found due to primarily extended transient meta-stable Al_2O_3 formation during in the initial stage. Metastable Al_2O_3 has orders of magnitude greater oxidation rate over α-Al_2O_3. Extended metastable Al_2O_3 growth produces thicker Al_2O_3 scale. Meanwhile, spinel was also found to form on top of the alumina scale during long-term exposure[57].

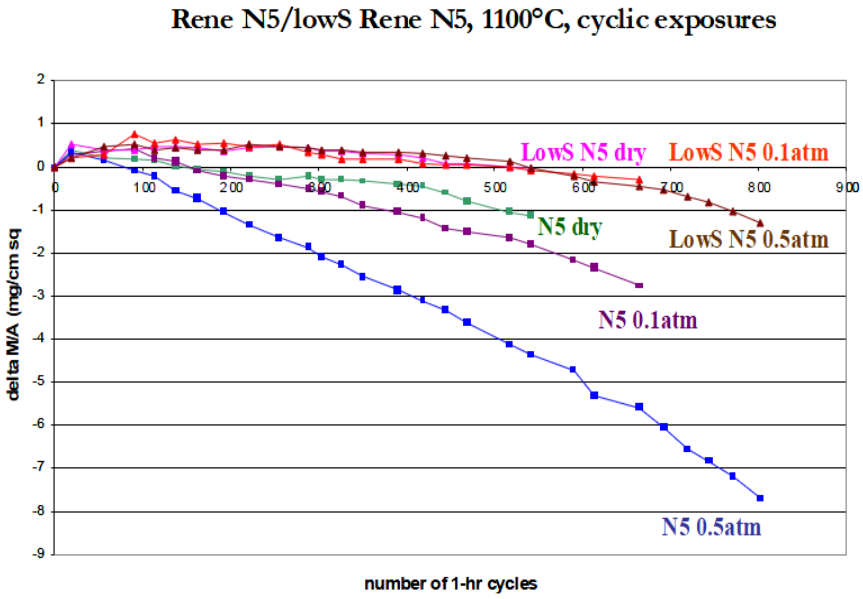

Figure 1.20 Weight change versus time measurements for René N5 specimens - low S (< 1ppm) and regular S (3-5ppm) - cyclically oxidized in dry and wet air at two water vapor pressures (0.1atm and 0.5atm)[57]

1.4 KINETICS ANALYSIS OF THE SCALING BEHAVIOR OF ALLOYS

1.4.1 Types of kinetics of alloy scaling

Systematic investigation of the kinetics of oxidation of metals and alloys were undertaken by Tammann[62,63], Pilling and Bedworth[64] and Evans[65] in the early twentieth century. Their studies, in conjunction with experimental investigations by other researcher, have established several relations between the reaction time and the degree of metal consumption. These relations have been found to be linear, parabolic, linear-parabolic, cubic and logarithmic[18] (at low temperature). In most of the cases, the growth kinetics of the scale is assumed to be parabolic. Under this assumption, the parabolic growth rate constant is calculated by plotting the weight gain per unit area versus square root of time or the square of the weight gain per unit area versus time. Then, the parabolic growth rate constant is determined by the slopes of the linear part of the curves. However, this conventional method can be inaccurate under certain cases such as the oxidation process with an initial faster-growing stage. Taking oxidation of Ni-7.5Cr-20Al-3Si-3Pt-0.1Hf-0.05Y alloy in air at 1150^{o}C as example, the parabolic growth rate constant k_p calculated by the two plots is shown in Figure 1.21. From Figure 1.21 (a), the growth rate constant k_p is 1.2×10^{-12} g^2/cm^{4}sec, while the growth rate constant k_p is 0.6×10^{-12} g^2/cm^{4}sec from Figure 1.21 (b). It is clear that this conventional method is not accurate for this case, because the two growth rate constants are not identical. By the same time, the conventional method cannot characterize the kinetics changes during the initial stage, which is shown by the non-linear part of the curves on the left side of the dash lines in Figure 1.21. Therefore, a rigorous method that can determine the real growth rate constant for the steady-state oxidation and a method that can characterize the instantaneous kinetics changes during the initial stage are needed.

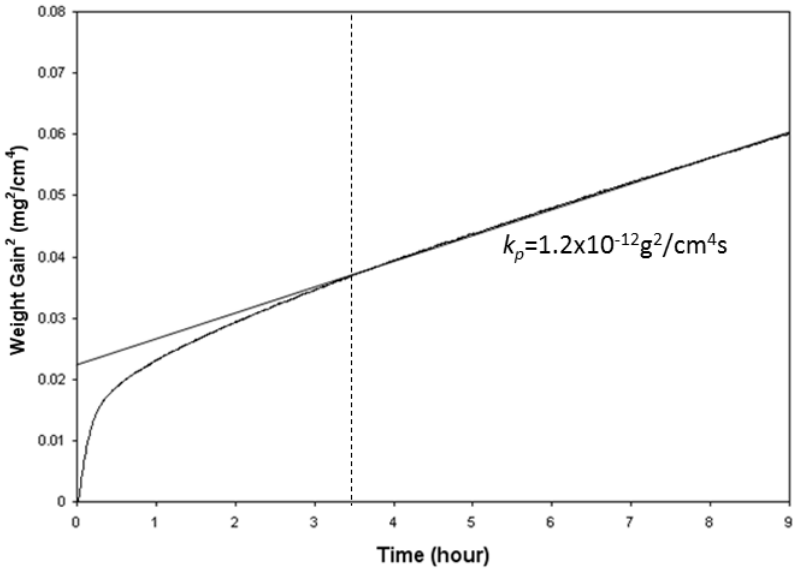

(a)

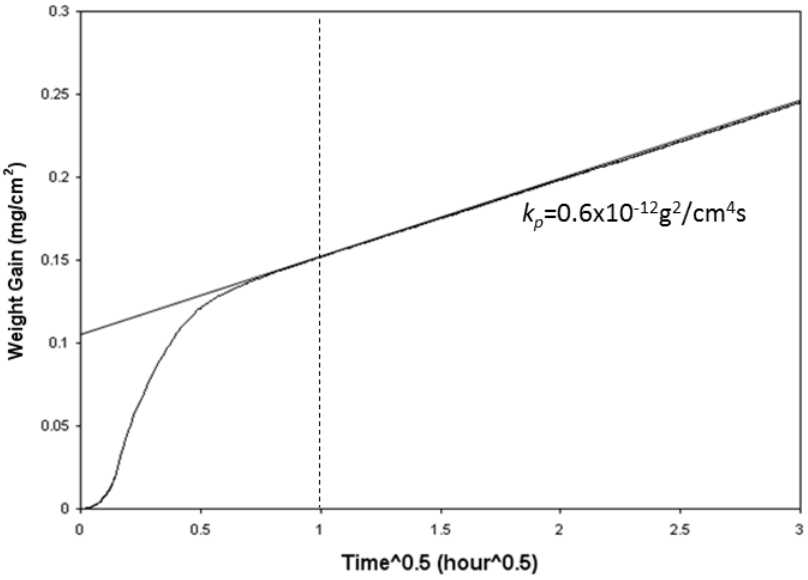

(b)

Figure 1.21 Calculation of parabolic growth rate constant for oxidation of Ni-7.5Cr-20A-l3Si-3Pt-0.1Hf-0.05Y alloy in air at 1150^{o}C. (a) k_p is the slope of the later part of the curve and (b) k_p is the square of the slope of the later part of the curve

1.4.2 Deviation from perfect parabolic law

Pieraggi[66] has pointed out that when the weight gain or scale thickness produced during the initial stage of oxidation is not negligible, the steady state parabolic law is given by:

$$\Delta m^2 - \Delta m_i^2 = k_p \left(t - t_i \right) \tag{1.39}$$

or:

$$\left(\Delta m - \Delta m_i \right)^2 = k_p \left(t - t_i \right) \tag{1.40}$$

In this case, the growth kinetics are already not in complete accordance with the perfect parabolic law. In other words, if the growth kinetics are written in the form of

$$\Delta m = k \cdot t^n \tag{1.41}$$

the instantaneous time exponent *n* is not 0.5 at all times during the oxidation. Direct evidence for the deviation from idea parabolic law has been shown in Figure 1.21. Another example of the deviation is the case when the growth kinetics are found to be cubic. In this case, the scaling may involve a predominance of grain-boundary diffusion through the scale coupled with a large extent of grain growth during the oxidation process[67,68,69]. The effective diffusion coefficient D_{eff} in the scale can be calculated as contributions from both lattice diffusion and grain boundary diffusion in the form of:

$$D_{eff} = f_l D_l + f_{gb} D_{gb} \tag{1.42}$$

where D_l and D_{gb} are lattice and grain-boundary diffusion coefficients and the f_l and f_{gb} are is the area fraction of the lattice and grain-boundary. When grain-boundary diffusion is dominating, the effective diffusion coefficient D_{eff} is approximately equal to $f_{gb}D_{gb}$. Since the average grain size is found to increase linearly with the total scale thickness *x*, the area fraction of grain boundary f_{gb} is approximately inversely proportional to the scale thickness *x*, and therefore so is the

effective diffusion coefficient D_{eff}[69]. Thus, the differential equation established for the instantaneous scale thickness growth is:

$$\frac{dx}{dt} \cong \frac{\left(\frac{k''}{x}\right)}{x} = \frac{k''}{x^2} \tag{1.48}$$

Integration of this equation produces the cubic growth kinetics. Indeed, when the average grain size is large enough, the effective diffusion coefficient D_{eff} will eventually be dominated by lattice diffusion. By this time, the effective diffusion coefficient D_{eff} will be independent of the average grain size and the growth kinetics will go back to parabolic thereafter. It is important to realize that many assumptions need to be met for well-behaved parabolic growth kinetics to occur, i.e. equation 1.47 to hold. In reality, deviation from idea parabolic is usually found. The deviation may be small and negligible, but in some cases it can be significant and it carries information of the mechanism of scaling behavior.

1.5 EXISTING MODELS FOR NON-IDEAL OXIDATION BEHAVIOR

The simplest treatment for non-ideal oxidation behavior is to employ equations 1.39 and 1.40 when calculating the growth rate constant, instead of the ideal equation 1.10. Indeed, when Δm^2-t and Δm-$t^{1/2}$ plots are used to calculate the growth-rate constant and the slope is found to not go through the origin, it implies the real case is different from equation 1.10 and is better expressed by equation 1.39 and 1.40. Furthermore, Pieraggi[66] pointed out that for the case with a transient period of faster kinetics, a plot of Δm-$t^{1/2}$ is inherently superior to the Δm^2-t plot. The merit for this concept is that it is convenient to use and may provide a good estimation of the steady state

k_p; however, the limitation is that it confines the growth kinetics to be parabolic, and it is not valid if there is any deviation from the steady-state assumption after the initial transient stage.

Monceau and Pieraggi[70] proposed a local analysis method to calculate parabolic rate constants. In this method, they assumed all the weight gain vs. time curve can be fitted to a parabola:

$$t = A + B\Delta m + C\Delta m^2 \tag{1.49}$$

and the kinetics parameters can be evaluated from the coefficients A, B and C obtained from such a fit. They also claimed that k_p does not depend on the values of Δm_i and t_i, which fits the initial condition for integrating the rate law. On the contrary, the coefficient B and A would permit the determination of k_l and of the characteristic elements of the transient period for only some cases. In the "local parabolic fitting", a window of data is fitted by equation 1.49 and the "real" parabolic growth rate constant k_p=1/C for this period. After one fitting, the window is moved with a certain translation step to cover data from another period and another k_p is calculated in the same way. After the window covers all the data from experiment, the "real" k_p as a function of time is produced. Figure 1.22 shows an illustration of this method applied to an experimental curve.

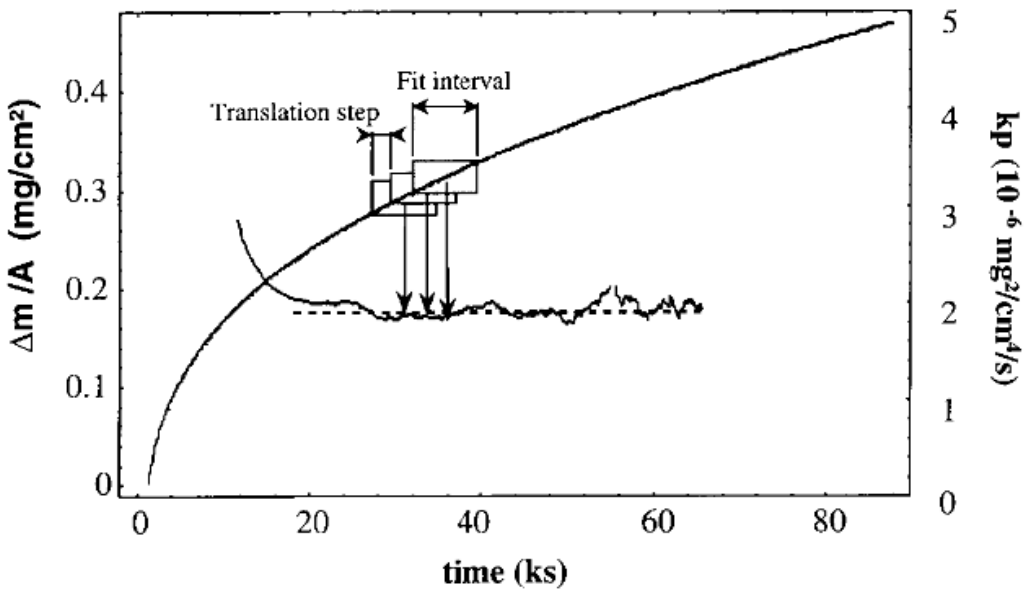

Figure 1.22 An illustration of local analysis method to calculate k_p

The merit of this method is that it takes into consideration the change of growth rate constant as a function of time. In this aspect, it has an advantage over equations 1.39 and 1.40 in which the growth-rate coefficient is constricted to be a constant for all the testing time. Meanwhile, with more fitting parameters A and B, the method allows impacts from oxidation history (e.g. initial stage) to be reduced by adjusting A and B. However, the usefulness of this method is still limited. Firstly, this method still confines the growth kinetics to be parabolic. Although an adjustment can be made to accommodate cubic growth kinetics such as adding another parameter D for the cubic term, the real kinetics can be more complex than simple polynomial behavior. For example, if there is a transition from formation of a faster growing oxide to a slower growing oxide, and this transition is slow to the extent that none of the oxide is dominating during the transition period, the growth kinetics are neither parabolic, nor cubic or any form of polynomial. Secondly, this method requires a fitting of A,B and C from the experimental data. Due to the nature of the diffusion-controlled process, the weight gain increase for a unit of time always becomes smaller with increasing time. Therefore, the coefficients for higher-order terms (e.g. C

or D) quickly become overwhelmed by noise for longer oxidation time. Qualitatively, this error increases exponentially, making it almost impossible to use this method for long-term analysis.

Some researchers[71,72] have employed the concept of instantaneous time exponent n^i and instantaneous growth rate constant k^i to characterize the growth kinetics. In general, these two instantaneous values are calculated by:

$$n^i = \frac{\partial(\log \Delta m)}{\partial(\log t)} \tag{1.50}$$

$$k^i = 2\Delta m \frac{\partial \Delta m}{\partial t} \tag{1.51}$$

Indeed, equation 1.51 is actually the same as:

$$k^i = \frac{\partial \Delta m^2}{\partial t} \tag{1.52}$$

Therefore, using equation 1.51 implies that the growth kinetics are parabolic. It has been pointed out that using these instantaneous values without careful consideration may lead to erroneous conclusions[73]. Indeed, the values calculated by equations 1.50-1.51 are not "instantaneous" as they are named. The oxidation history may have significant impacts on the calculated "instantaneous" values. This point will be illustrated in details in the discussion section. In conclusion, the "instantaneous" values may be used to provide detailed information on scaling kinetics; however, the correct way to use them has not been thoroughly determined.

2.0 OBJECTIVES

This study will consist two parts. In the first part, steam effects on the oxidation behavior of alumina-scale forming Ni-based alloys will be investigated. In particular, the oxidation map for the model Ni-Al-Cr system in wet oxidizing conditions will be established. The mechanistic reason for steam shifting the N_{Al}^{*} boundary to form a protective Al_2O_3 scale will be analyzed quantitatively based on Maak's modification[2] of Wagner's theory[3]. The relevance of the findings will be applied to a number of commercial Al_2O_3-scale forming alloys. The surface instability found from experimental observation of NiO scale formed in wet oxidizing conditions will also be studied. A series of experiments will be carried out to confirm the environmental conditions for the unusual surface instability to form. Based on the observations, obtained possible mechanisms will be proposed to account for the occurrence of the irregular structures formed particularly in wet oxidizing conditions.

In the second part, a detailed kinetics analysis method based on thermogravimetric measurement and its associated instantaneous n-value curve will be presented. This method can be used to accurately determine accurate growth-rate constants of steady-state oxidation and help to analyze the structural evolution dynamics of a thermally-grown scale. An example of this analysis will be quantifying the extent of θ-$Al_2O_3 \rightarrow \alpha$-$Al_2O_3$ phase transformation during the transient-stage oxidation of Al_2O_3-scale forming alloys.

2.1 STEAM EFFECTS ON THE OXIDATION OF Ni-BASED ALLOYS

As detailed in the literature survey of this thesis, most of the current studies on steam effects focus on chromia-scale forming systems. However, materials used at higher temperature often rely on formation of a protective alumina scale. Some research has been carried out to study the effects of steam on alumina-scale forming Ni-based alloys; although, those studies focused mostly on commercial alloys, which contain a variety of alloying elements. Such highly alloyed systems bring much complexity to clearly ascertaining the fundamental oxidation mechanism(s) associated with the steam effects. Therefore, a thorough study using model alloy systems such as pure Ni, Ni-Al binary alloys and Ni-Al-Cr ternary alloys is needed. Several mechanisms[53,74,75] have been proposed to explain the increased critical concentration of chromium in Cr_2O_3-scale forming Fe-based system. The most accepted one was that the increased critical chromium concentration is due to the enhanced oxygen permeability[43]. However, this mechanism has not been validated. Moreover, the same mechanism may not be valid for Al_2O_3-scale forming Ni-based alloys. Therefore, a rigorous quantitative analysis is needed to determine the key reason for any shift of the critical aluminum concentration in Al_2O_3-scale forming Ni-based system.

Based on the review presented, the scientific objectives for the first part of this study can be formulated as follows:

- Determine the 1000^{o}C oxidation map for the model Ni-Cr-Al system in wet oxidizing conditions by assessing the oxidation behavior of alloys with different Cr and Al contents.
- Estimate the extent of the shift, if any, of the boundary to form a protective Al_2O_3 scale when changing from dry to wet oxidizing conditions.

- Assess whether the hypothesis that the increased critical concentration is due to the enhanced oxygen permeability into the alloy is applicable to Al_2O_3-scale forming Ni-based alloys.
- More rigorously determine the mechanistic reason for steam shifting the boundary for critical aluminum concentration (N_{Al}^*) by quantitatively applying Maak's modification[2] of Wagner's theory[3].

Our preliminary works found that surface instability occurred on NiO scale formed in wet oxidizing conditions. Rahmel et al.[76] oxidized Ni at 1000 and 1100°C in atmospheres containing water vapor, however they did not report any effect of water vapor on the oxidation of Ni. On the contrary, Auchi et al.[77] confirmed the present find of surface instability on the pure Ni oxidized in wet oxidizing condition at 1000°C. It seems the conditions in which the surface instability can form are very specific. Those conditions may include, but are not limited to, temperature, steam content and composition of the alloy. The study of the NiO surface instability in wet oxidizing conditions is a good complement to the study of steam effects on the oxidation of Ni-based alloys. The objectives of this section will be to investigate the conditions for the surface instability to occur and to provide experimental validation and theoretical analysis to address the possible mechanisms for the formation of surface instability.

2.2 KINETICS ANALYSIS OF SCALING BEHAVIOR OF ALLOY OXIDATION

Generally, quantification of the rate of alloy oxidation is reported in terms of a parabolic growth rate constant k_p and an activation energy Q for that growth-rate constant. However, these two factors can only be used to characterize the kinetics of steady-state oxidation. During the course

of oxidation, the nature of the scale can be time variant. In such cases where the nature of the scale is changing with time, the growth rate constant determined by conventional methods will be affected and become inaccurate. Thus, a quantification method that can assess the progress towards steady-state oxidation kinetics are needed. A related purpose of this study is to establish a kinetics analysis scenario that can be used to more accurately determine the growth-rate constant and estimate the extent of scale evolution during the course of oxidation.

Based on the literature review provided in the previous section, the scientific objectives for the second part of this study can be formulated as follows:

- Assess the extent to which the conventional method of kinetics analysis can be inaccurate if the growth kinetics are not a single-stage steady-state.
- Illustrate by simulated examples that the instantaneous time exponent n^i and the instantaneous growth rate constant k^i are not accurate immediately after the oxidation kinetics are changed from one trend to another.
- Discuss the situation under which the instantaneous time exponent n^i and the instantaneous growth rate constant k^i can be used to determine the oxidation kinetics for a steady-state oxidation.
- Establish a standard procedure to more accurately determine oxidation kinetics from thermogravimetric experiment data.
- Develop a kinetics analysis method that can be used to quantifying the extent of $\theta \rightarrow \alpha$ phase transformation in a thermally grown Al_2O_3 scale. Other conditions for this kinetics analysis method to apply will be addressed.

3.0 EXPERIMENTAL PROCEDURES

Two commercial alloys AM1 and Rene N5 were used to illustrate the steam effects on commercial superalloys. Their compositions are shown in Table 3.1. To study the oxidation behavior of Al_2O_3-scale forming Ni-based alloy fundamentally, seven model Ni-Cr-Al alloys were produced. The nominal compositions of those alloys are shown in Table 3.2 and their positions on the oxidation map[1] are shown on Figure 3.1. These alloys were designed to have two aluminum levels, 5 at% and 8 at% and for each aluminum level, there are three chromium levels. There is one composition sitting exactly on the borderline of the 1000^{o}C kinetics boundary to form Al_2O_3 scale in 0.1atm oxygen[1]. The alloys were designed in this way to determine the possible shift of the boundary when steam is present. All the alloys are single phase γ-Ni(Cr,Al) according to the Ni-Cr-Al phase diagram[78].

Table 3.1 Nominal composition of commercial superalloy AM1 and Rene N5

Alloy	Ni	Cr	Co	Mo	W	Ta	Ti	Al	Hf	Y	B	C	Re
Rene N5	Bal	7	8	2	5	6	0	6.2	0.2	0.01	0.004	0.05	3
AM1	Bal	7.5	6.5	2	5.5	8	1.2	5.3	0	0	0	0	0

The processing route for each of the alloy was the same as that used by Giggins and Pettit[1], which is described in the following. All alloy ingots were prepared by argon arc-melting followed by drop-casting to form 25mm diameter rods. The Ni-Cr-Al alloys were cut into 5 mm

thick disks and were given a preliminary vacuum anneal at 1000^{o}C for 48h. Each disk was cold-rolled to 1mm thickness and then annealed in vacuum at 1000^{o}C for 48h to promote homogeneity. All samples were polished through to a 600-grit finish using SiC grinding paper and ultrasonically cleaned in acetone immediately before oxidation. The oxidized samples were cold-mounted, cut in cross-section and polished using standard metallographic techniques. The cross-sectional morphology of the mounted samples was analyzed using scanning-electron microscopy (SEM). All the cross-sectional images were taken by back-scattering electrons in SEM since it is sensitive to the element distribution (volumetric density of nuclei). The composition of phases was measured by the energy-dispersive X-ray spectroscopy (EDS).

Table 3.2 Nominal composition of the Ni-Cr-Al alloys in at% and wt%

	Ni(at%)	Al(at%)	Cr(at%)	Ni(wt%)	Al(wt%)	Cr(wt%)
#1	90	8	2	94.3	3.9	1.8
#2	87	8	5	91.5	3.9	4.6
#3	82	8	10	86.7	3.9	9.4
#4	92	5	3	94.9	2.4	2.7
#5	90	5	5	93.0	2.4	4.6
#6	85	5	10	88.4	2.4	9.2
#7	88.3	6.26	5.42	92	3	5

Figure 3.2 shows a schematic of the apparatus setup to produce wet air as well as hanging the samples[58]. Compressed air with steam concentration less than 2ppm was used for dry oxidation test, while, air+30% steam was produced by flowing compressed air through one water baths at 70^{o}C (P_{H2O}=0.32atm) to saturate the air with steam and a condenser with temperature set at 69^{o}C (P_{H2O}=0.3atm). After switching from tests in dry air to tests in wet air, air+30% steam was flown through the whole system for 24 hours to purge the residue dry air. Prior to each test, samples

were hung on a rod and put into the cold zone, followed by purging the furnace for 2 hours. Then, the samples were inserted to the hot zone by pushing a piece of magnet at the other end of the rod.

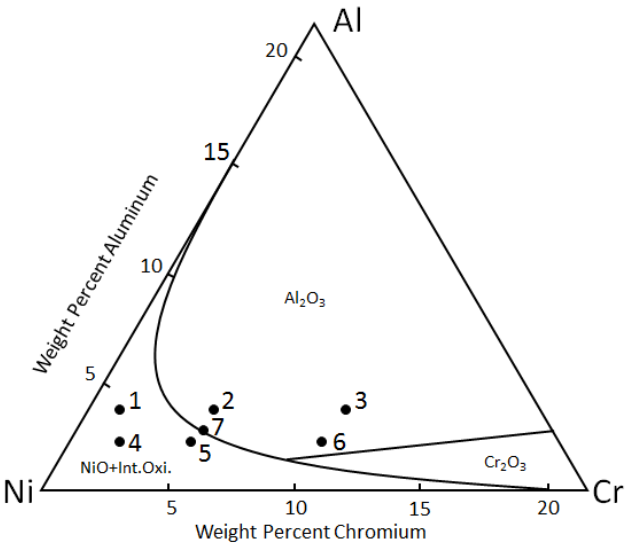

Figure 3.1 Oxidation map for Ni-Cr-Al alloy oxidized in dry 0.1atm oxygen at 1000°C for 20h[1]

To reveal the steam effects on the oxidation map, all the samples were oxidized in dry air and in air+ 0.3atm steam at 1000°C for 20h. The cross-sectional morphology was used to determine which region the samples belong to on the oxidation map.

A study on oxygen permeability was carried out using a Ni-3at%Al alloy. The sample preparation procedure and oxidation method were the same as those used for the Ni-Cr-Al alloys. The oxygen permeability was assessed by measuring the thickness of internal oxidation zone measured from cross-sectional SEM images. The tests were carried out for different oxidation times of 1h, 4h, 24h, 64h and 98h. These alloys were also used to study the NiO growth in the environment with and without steam.

A study on the activation energy of NiO grown in dry air and wet air was performed on pure Ni 99.99% oxidized at temperatures from 900°C to 1050°C with a 50°C interval. The

growth rate constants of NiO grown in those conditions were plotted in an Arrhenius diagram. Expressing the growth rate constant in the form of:

$$k_p = \exp\left(\frac{-Q}{RT}\right) \tag{3.1}$$

where k_p is the growth rate constant, Q the activation energy, R the idea gas constant and T the temperature. The activation energy was determined by a linear fitting of k_p as a function of 1/T.

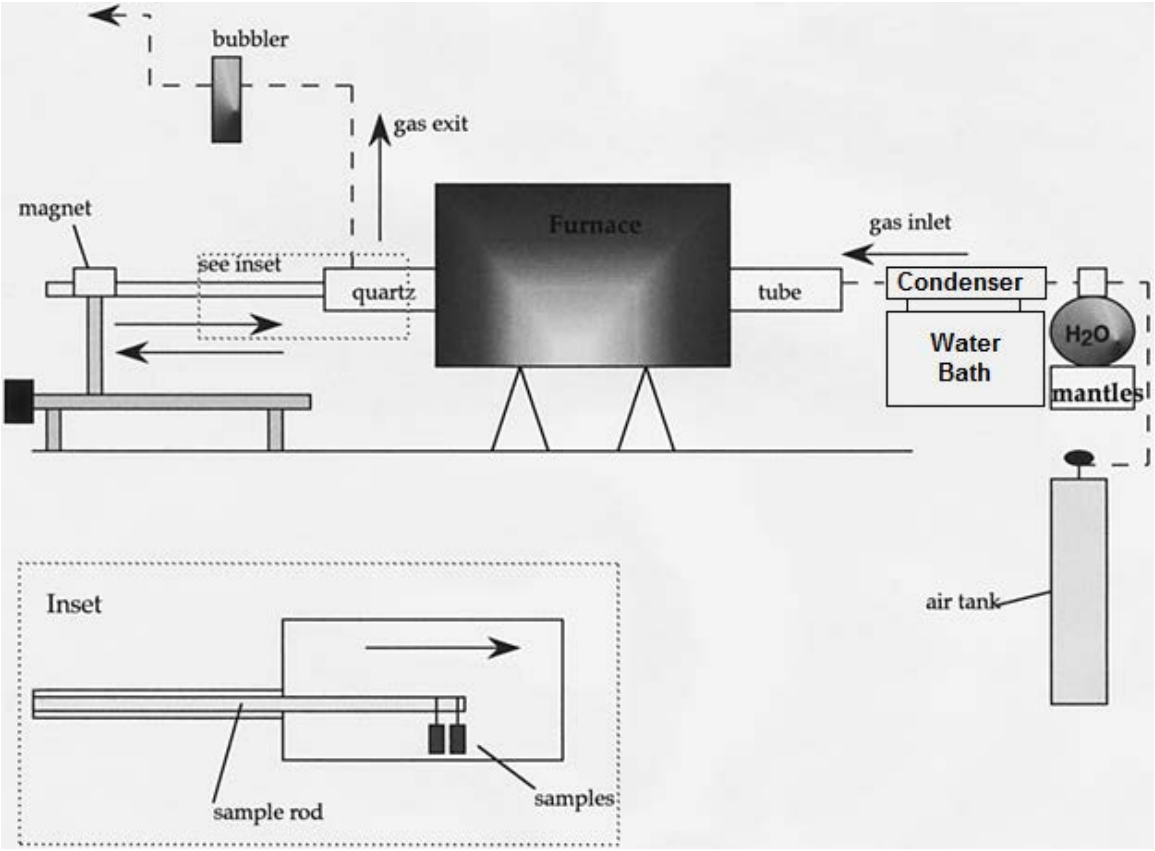

Figure 3.2 Apparatus for oxidation experiment in dry and wet air (Re-plot from Janakiraman et al.'s work[58])

Surface instability was investigated using three types of pure Ni metal with three different purity levels: Ni 99.99%, Ni 99% and Ni200 (>98%). All purities were produced from Goodfellow. The experiment apparatus was the same as that shown in Figure 3.2. Oxidation had been carried out at 1000^{o}C and 1100^{o}C and three steam levels 6%, 20% and 30%. After oxidation, surface images were taken by secondary electron (SE) detector of SEM, which is sensitive to the morphology of

the sample. The phases and texture formed on the samples were determined using X-ray diffraction (XRD) method with standard $\theta/2\theta$ geometry and Cu Kα radiation. Electron backscatter diffraction (EBSD) was used to map the orientation of the grains and grain boundaries.

All the thermogravimetric experiments were conducted using a Setaram TAG 1750. The resolution of this equipment is around $2x10^{-7}$g. Alloy samples were disks with around 1mm in thickness and 10mm in diameter with a surface finish condition the same as previous. The samples were hung from sapphire hooks and were heated in air from room temperature to the target temperature at a rate of 99^{o}C/min. After each test, the weight change during the heating stage was excluded by setting the zero time and zero weight gain point. The XRD pattern for thin Al_2O_3 scales formed at 1100^{o}C was determined by a glancing-angle XRD technique. The phase constitution of those Al_2O_3 scales was calculated by conventional XRD quantitative method.

4.0 RESULTS AND DISCUSSIONS

4.1 STEAM EFFECTS ON OXIDATION BEHAVIOR OF Ni-BASED ALLOYS

4.1.1 Effects of steam on the Ni-Al-Cr oxide map

4.1.1.1 Steam effects on isothermal oxidation of some commercial alloys

Since commercial alloys have a variety of compositions, the steam effects on the oxidation behavior can be significantly different for different alloys[55]. Figure 4.1 show the cross-sectional SEM images of AM1 and Rene N5 oxidized in dry air and air+30%H_2O at 1000^{o}C for 20h. The compositions of those two superalloys are shown in Table 3.1. Since those images were taken by the back-scattering electrons (BSE), lighter elements give darker contract on BSE images while heavier elements give brighter contract. When AM1 superalloy was oxidized in dry air, it formed a light grey layer on the top, which was identified as $Ni(Cr,Al)_2O_4$ spinel by EDS analysis under SEM. This layer was embedded with a discrete layer of "white" particles which were identified as heavy-metal oxides such as tungsten oxide or tantalum oxide. Below the spinel layer, there was a continuous Al_2O_3 scale shown as the black layer below the light grey layer on the image. From Table 3.1, AM1 superalloy has relatively lower Al concentration. It also has very low amount of other elements which may promote the Al_2O_3-scale formation. Therefore, AM1 has only marginal ability to form a protective Al_2O_3 scale in dry air at 1000^{o}C. When this superalloy

was oxidized in wet air, it could not form a continuous Al_2O_3 scale. Instead, it formed some NiO on the top of surface and a layer of spinel phase which was locally non-continuous. The Al_2O_3 only formed as discrete internal oxide islands. By contrast, Rene N5 is a good Al_2O_3-scale forming alloy. It could form a uniform and continuous Al_2O_3 scale in dry air at 1000°C. When it was oxidized in wet air, it could also form a continuous Al_2O_3 scale although some nodules were formed locally and a thick and continuous spinel layer was formed above the Al_2O_3 scale.

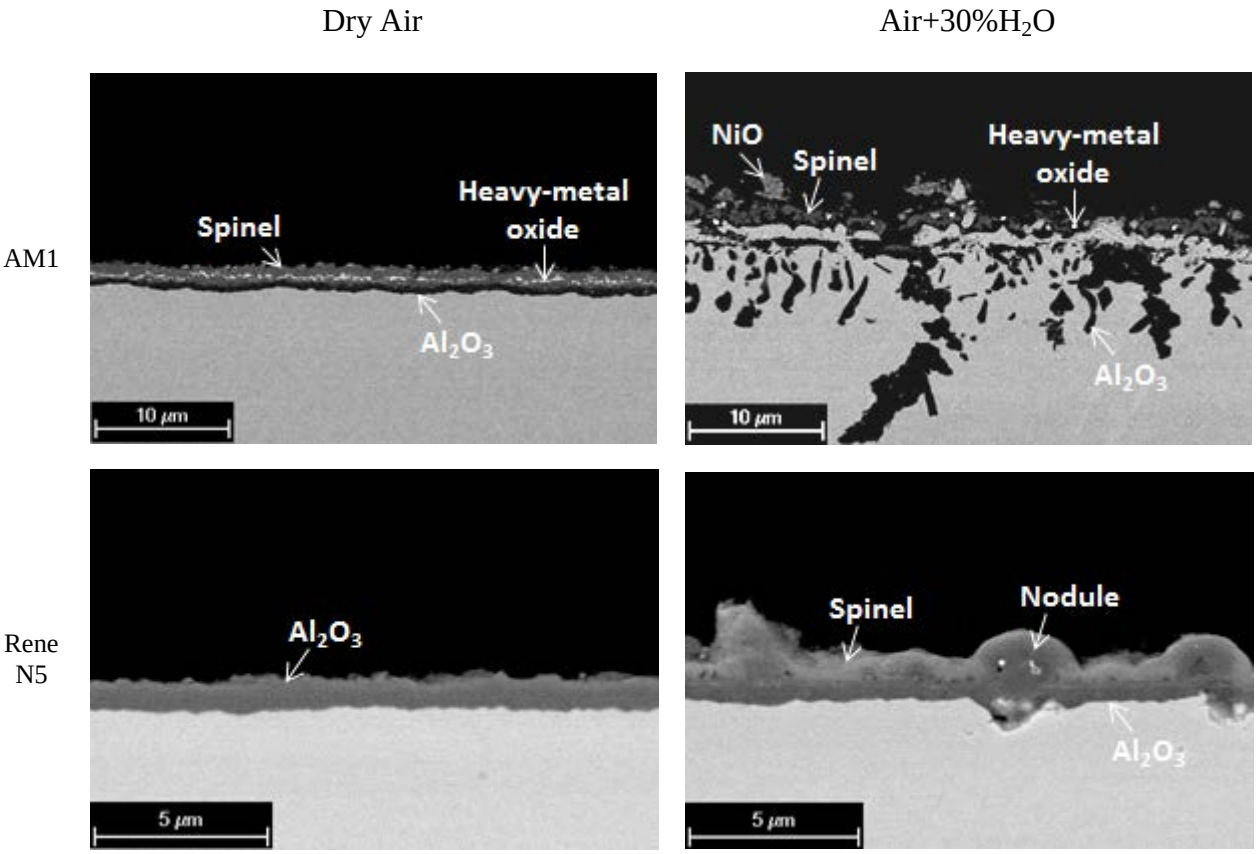

Figure 4.1 Cross-sectional BSE images of commercial alloy AM1 and Rene N5 oxidized in dry air and air+30%H_2O at 1000°C for 20h

Therefore, steam could be very detrimental to the isothermal oxidation behavior of commercial alloy (e.g. AM1). It increased the critical concentration of Al (N_{Al}^{*}) to form a continuous Al_2O_3 scale. However, not all commercial alloys were such vulnerable to the oxidation in steam (e.g. Rene N5). It is not easy to draw a conclusion whether the better oxidation behavior of Rene N5

was due to the slight higher Al concentration or due to the synergistic effect by other elements. To study the steam effect on the N_{Al}^{*} for Al_2O_3-scale forming Ni-based alloy, model alloys will be used instead of commercial alloys.

4.1.1.2 Determination of N_{Al}^{*} boundary in the oxidation map for Ni-Cr-Al system

From the oxidation map established by Giggins and Pettit[1], there are three groups of oxidation behavior that can be found from oxidation of Ni-Cr-Al alloys at 1000^{o}C: (I) forming NiO + internal oxidation, (II) forming Al_2O_3-scale or (III) forming Cr_2O_3-scale. Since this study focuses on Al_2O_3-scale forming alloys, all the tested samples are in the regions I and II, or on the boundary between those two regions. Figure 4.2 shows a typical morphology of the NiO scale and internal oxidation precipitates. Although the NiO scale is fairly protective at high temperatures (e.g. above 900^{o}C), the growth kinetics of NiO is orders of magnitude greater than that of Al_2O_3 scale. Therefore, high temperature application of alloys still relies on the formation of a continuous Al_2O_3 scale. In this study, all the oxidation behaviors that are not forming a continuous Al_2O_3 scale will be called non-protective. In Figure 4.2, there are four obverse interfaces, which are labeled as 1 to 4 on the side of the image. The interface 1 is the sample surface between the scale and gas. From interface 2, internal oxidation precipitates started to form. This interface is considered as the original surface of the alloy because internal oxidation precipitates can be used as intrinsic marks. The interface 3 is between the external scale and the alloy. The interface 4 is where internal oxidation precipitates stop to form, which is also called internal oxidation front. From interface 1 to 3, the matrix was identified as NiO by the EDS analysis under SEM. This layer is the external NiO scale. The region between interfaces 2 and 3 is called metal consumption zone (MCZ). The MCZ is formed since Ni diffused out to form NiO

so that the base metal was consumed. Therefore, the alloy surface recessed back and formed this MCZ.

Figure 4.2 Typical morphology of non-protective scale formed on Ni-Cr-Al alloy oxidized in dry air at 1000^{o}C

From interface 2 to 4, internal oxidation precipitates were formed. This region was the internal oxidation zone (IOZ). The contract of the internal oxidation precipitates changed with the depth, indicating that the compositions of the internal oxidation precipitates were changed. The lighter grey precipitates embedded within the NiO and in the adjacent region below the scale/alloy interface were mostly $NiAl_2O_4$ spinel phase, while the black precipitates formed deep in the alloy were Al_2O_3. Cr was not found to be enriched in any of the morphology by EDS analysis. It either stayed in the alloy matrix as a component at its nominal composition or mixed with other internal oxidation precipitates in the adjacent region below the scale/alloy interface. Therefore, the changes in composition for the majority phases were shown as a schematic diffusion path on Ni-Al-O phase diagram shown in Figure 4.3. From the gas environment to the alloy matrix, the

sequence of occurring phases was NiO, spinel + NiO, spinel + γ-Ni, γ-Ni + Al_2O_3. All three-phase regions are invisible on the morphology since the three-phase region cannot have a concentration gradient so that they can only exist at the interface.

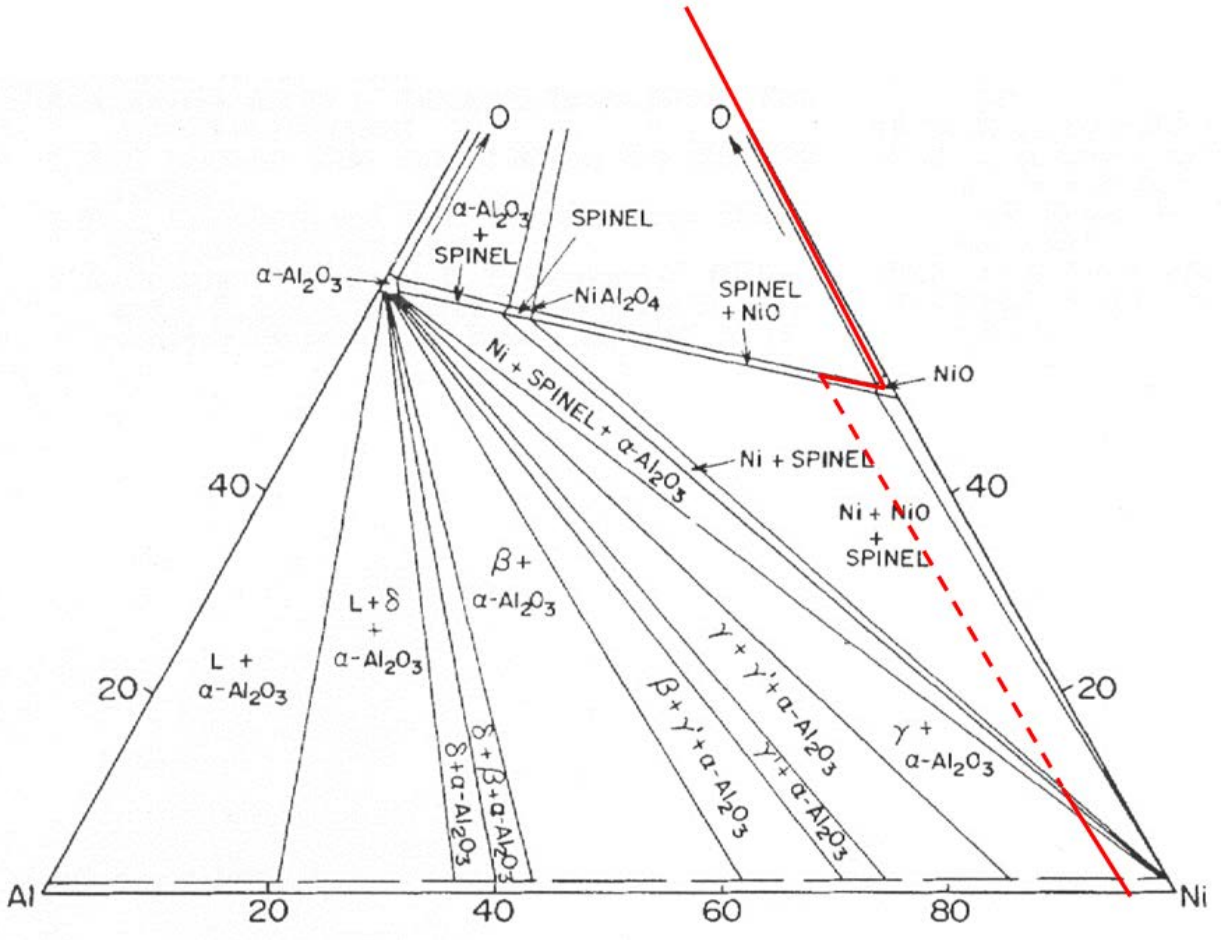

Figure 4.3 Ni-Al-O phase diagram with superimposed schematic diffusion path (red line). The dash line means the three-phase region cannot be seen on the cross section.

A comparison of the oxidation behavior of a series of Ni-Cr-Al alloys oxidized in air and air+30% steam for 20 hours is shown in Figure 4.4. The compositions of those alloys are shown in Table 3.2. Since the NiO scale on alloys #4 and #5 had completely spalled off during cooling, those alloys are not discussed in the following. Alloy #1, which is in NiO-forming region in dry oxidizing condition, showed similar oxidation behavior after oxidized in air+30% steam. A NiO

scale formed on the surface of that alloy. An IOZ was formed below the NiO scale. Although the alloy formed a similar three-layered structure in dry air and air+30% steam, the presence of steam changed the growth rate of the external scale. The total thickness of NiO was enhanced with steam in the atmosphere. Especially, the thickness of MCZ was significantly increased.

Alloy #2 is in the Al_2O_3-scale-forming region in dry oxidizing conditions. By contrast, it showed localized protective oxidation behavior when it was oxidized in wet oxidizing condition. Most of the surface became non-uniform and formed internal oxidation pits. However, it is seen that a fairly continuous Al_2O_3 layer formed beneath the internal pits. If this layer became continuous, it would block the further internal oxidation.

Alloy #3 has the highest Al and Cr contents. It was protective both in air and air+30% steam. Comparatively, the scale formed in wet oxidizing condition has thick spinel layer formed on surface. Steam-enhanced spinel formation has been found in other research as well[57]. Although the reason for this phenomenon is not very clear.

Alloy #6 was able to form a protective Al_2O_3 scale when it was oxidized in air, however, it failed to form such a protective scale when it is oxidized in air+30% steam. The non-protective scale formed in the wet oxidizing condition is not similar to it formed on alloy #2. This alloy formed a relatively dense but not continuous Al_2O_3 layer below the NiO scale, which means that this alloy composition is subcritical to a protective composition for wet oxidizing condition.

Alloy #7 was on the borderline to form protective Al_2O_3 scale in dry oxidizing condition. The oxidation of alloy #7 in dry oxidizing condition manifests localized behavior. Part of the oxidized surface was protected by Al_2O_3 scale, while there are locally non-protective patches. On the contrary, after oxidized in wet conditions, the whole surface was non-protective NiO scale. This morphology was very similar to the non-protective alloy #1 oxidized in wet condition.

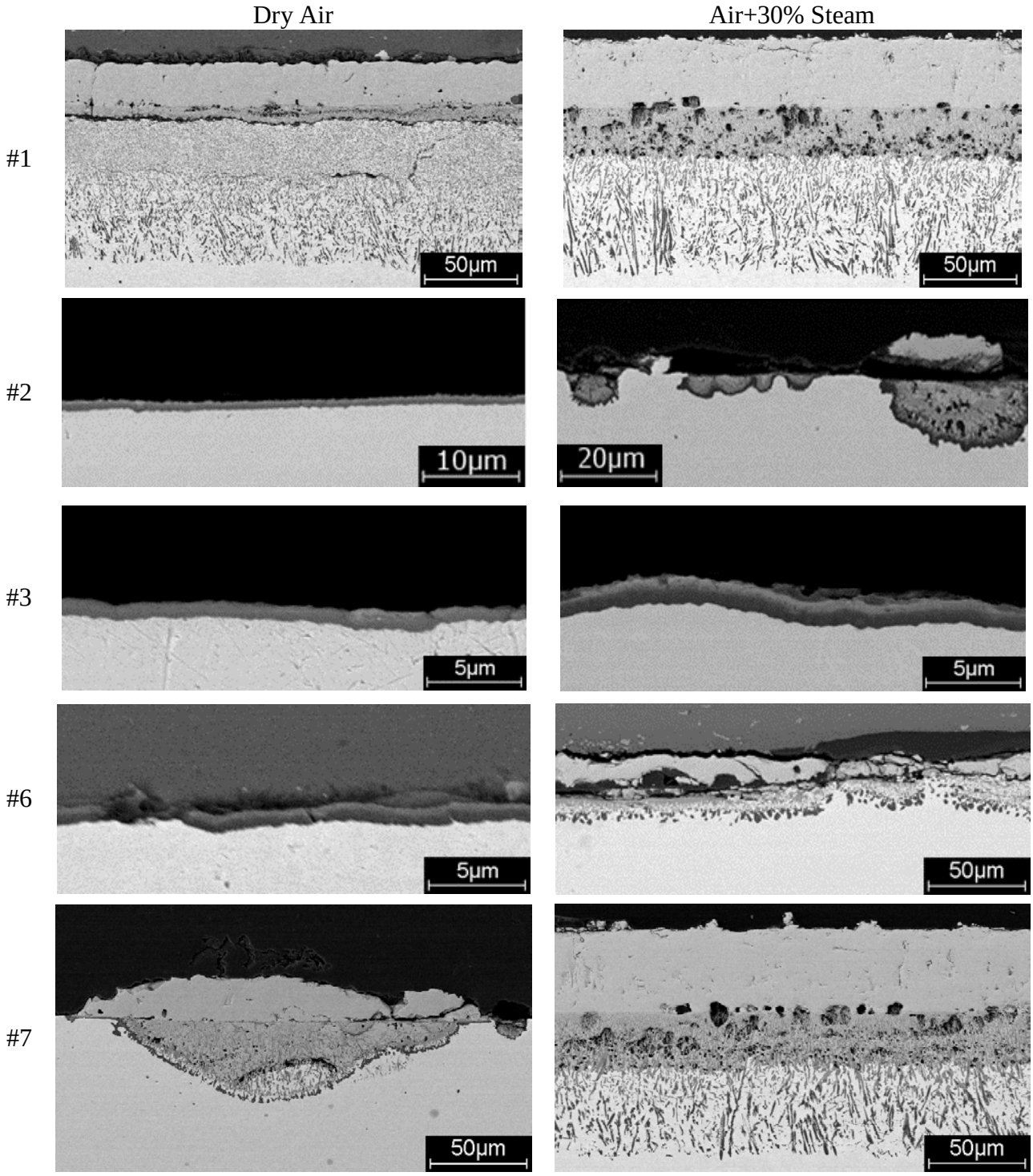

Figure 4.4 Comparison of oxidation behaviors of model Ni-Cr-Al alloys in dry air and air+30%H_2O atmosphere at 1000°C

The above results clearly show that steam is detrimental from the standpoint of inhibiting certain alloy from forming a protective Al_2O_3 scale. Specifically, the alloys need to contain more Al

and/or Cr to form a protective oxide scale when they are oxidized in wet oxidizing condition. In other words, the N_{Al}^{*}, i.e. the boundary to form a protective alumina scale on the oxidation map shifts towards higher Al/Cr region in wet oxidizing condition. This shift of N_{Al}^{*} boundary was shown by the oxidation map for Ni-Cr-Al system in air+30%H_2O at 1000^{o}C in Figure 4.5. In this figure, the blue area stands for the NiO-forming region, the yellow area stands for Al_2O_3-scale forming region and the green area stands for Cr_2O_3-scale forming region. In dry air, alloy #6 is super-critical to the N_{Al}^{*} boundary (dash line) while alloy #7 which has higher Al but lower Cr content is right on the N_{Al}^{*} boundary. This infers that alloy #6 may be just slightly super-critical to the N_{Al}^{*} boundary in dry air. Comparatively, alloy #2 is close to the N_{Al}^{*} boundary in wet air (solid line), while alloy #3 which has the same Al but higher Cr content is super-critical to this N_{Al}^{*} boundary. This infers that alloy #3 may be just slightly super-critical to the N_{Al}^{*} boundary in wet air. Therefore, as a rough estimation, the N_{Al}^{*} was increased by 60% as the difference in Al content between alloy #3 and #6.

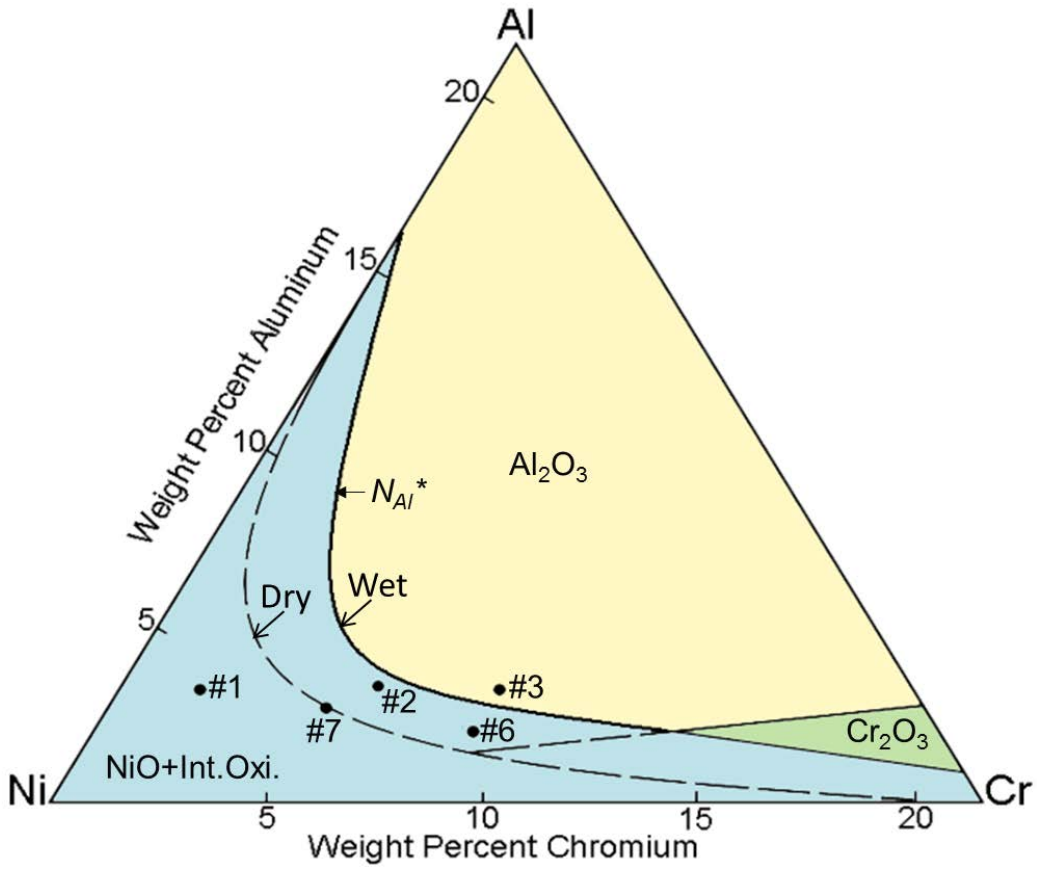

Figure 4.5 Schematic oxidation map for Ni-Cr-Al system in air+30% steam at 1000°C after 20h

Finally, based on the experimental observation that the steam increases the N_{Cr}^{*} in Cr_2O_3-scale forming Fe-based alloy[43], it is very likely that steam also increases the N_{Cr}^{*} in Ni-based alloy. Therefore, although the boundary between NiO-forming region and Cr_2O_3-scale forming region was not investigated in this study, it is expected that this boundary is also shifted towards higher Cr content region as shown in Figure 4.5.

4.1.1.3 Measurements of internal oxidation to assess oxygen permeability

The observed shift in the N_{Al}^{*} when the steam is present in the atmosphere may be explained by the increased oxygen permeability into the alloy. This hypothesis is based on a limiting condition of Wagner's theory to predict critical solute concentration for the transition from internal oxidation to external scale formation[27], i.e.

$$N_{Al}^{*} \propto \left(\frac{N_O^S D_O}{D_{Al}} \right)^{1/2} \tag{4.1}$$

where N_o^S is the concentration of dissolved oxygen on the surface, D_o the diffusion coefficient of oxygen in the alloy and D_{Al} the diffusion coefficient of Al in the alloy. If the oxygen permeability into the alloy is enhanced, a simultaneous phenomenon that must exist is that the IOZ thickness should be increased as well. The thickness of the IOZ is given by[27]:

$$\xi \approx \left[\frac{2N_O^S D_O t}{\nu N_{Al}^o} \right]^{1/2} \tag{4.2}$$

where ξ is the thickness of the IOZ and N_{Al}^o is the aluminum concentration in the bulk alloy. It is seen that the thickness of the IOZ is proportional to the square root of oxygen permeability $N_o^S D_o$. Therefore, the validity of this hypothesis for alumina-scale forming nickel-based alloy can be checked by measuring the thickness of the IOZ in Ni-3at%Al oxidized in dry air and in air+30%H_2O. Figure 4.6 shows an example of cross-sectional images of Ni-3Al after being oxidized in the two different environments at 1000^{o}C for 1h. Since part of the IOZ is incorporated into the metal recession zone in the NiO scale, the total thickness of the IOZ was equated to the combination of the metal recession zone (MCZ) in the NiO scale plus the precipitate zone in the subsurface of the bulk alloy. In the case of dry oxidizing conditions, some gaps formed during the cooling of the sample. The thickness of the gap was not included in the total IOZ thickness. Figure 4.7 summarizes the thicknesses of the IOZ in Ni-3at%Al oxidized in dry air and air+30%H_2O for a series of time. Each data on this figure is an average value measured at different sites on the same sample. No significant difference can be observed between the dry and wet oxidizing conditions. This comparison indicates that enhanced oxygen permeability into the alloy is not found for Ni-3Al in wet oxidizing conditions and it cannot be the reason to account for the increased N_{Al}^{*}.

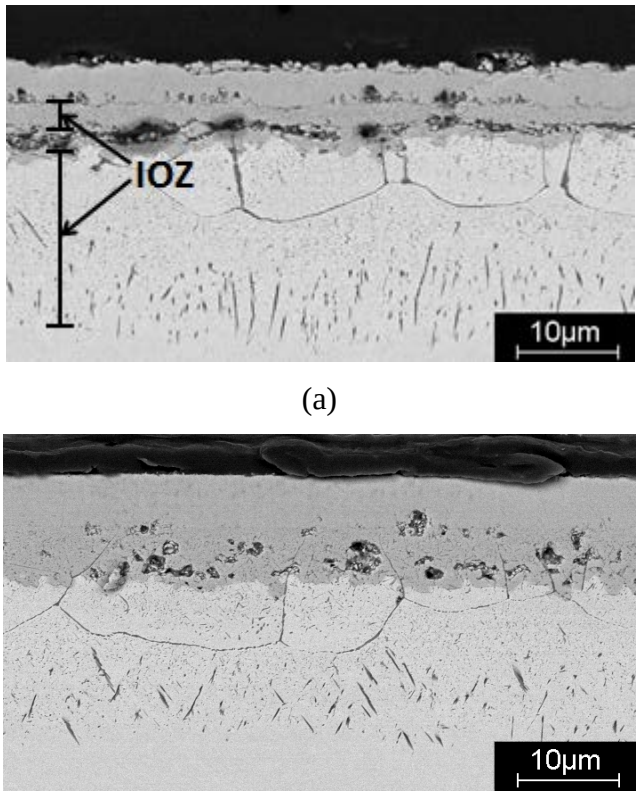

Figure 4.6 SEM cross-sectional images of Ni-3at%Al oxidized in (a) air and (b) air+30%H_2O for 1 hour

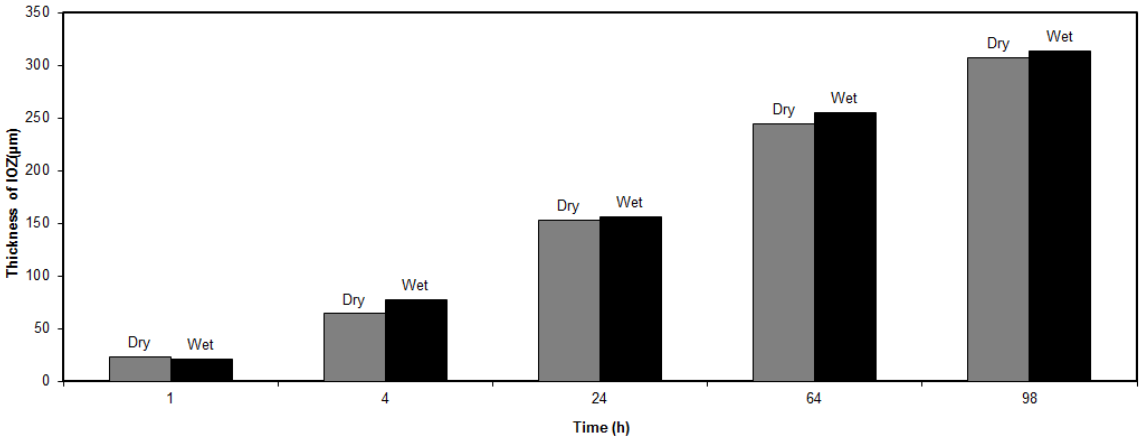

Figure 4.7 Thickness of IOZ of Ni-3at%Al oxidized in air (dry) and air+30%H_2O (wet) at 1000^oC

4.1.1.4 Accounting for enhanced NiO growth in wet oxidizing conditions

Figure 4.8 shows an example comparison of the NiO scale grown in dry and wet air. The NiO scale was completely separated from the base alloy on samples oxidized in dry air while no gap formed on samples oxidized in wet air. Although the gaps came from complete spallation during cooling, separation to some extent very likely existed at high temperature to initiate the spallation. Figure 4.9 summarizes the thicknesses of NiO scale grown in the two different environments for a series of times. It is clearly seen that the NiO growth was enhanced in the wet oxidizing conditions. To aid in deducing the rate-controlling process for NiO scale formation in both dry and wet oxidizing conditions, the activation energy for the NiO scale growth was measured. The activation energy can depend on a number of factors, such as whether the substrate is single- or poly-crystalline[79], surface orientation[80], processing procedure (i.e. cold work)[72], surface treatment[72] and purity[81]. Even so, for this study in which substrate variation was not a factor, the value of the activation energy can provide insights of the rate-controlling process in the scale growth. The Arrhenius plot for the NiO scale formed on Ni metal at different conditions is shown in Figure 4.10[82]. The growth-rate constants in dry air (red line) and wet air (blue line) measured in this study are also shown in this figure. Those lines are nearly parallel to each other, indicating that the activation energies for the NiO growth in those two conditions are similar. Indeed, the activation energy for NiO growth in dry air was found to be 200kJ/mol, while this energy for NiO growth in air+30%H_2O was found to be 190kJ/mol. Though there is a small difference, both values are in a very good agreement with 200kJ/mol reported by Haugsrud[83] for NiO grown in pure O_2. According to Elrefaie *et al.*[82], there is reasonable agreement when an average activation energy values are within the range of ±22kJ/mol. Therefore, although the growth rate constant of NiO is greater in the wet oxidizing condition, the

oxidation mechanism may still be dominated by outward diffusion of Ni cations[83,84] as in dry air. The differences in the kinetics are consequently inferred to be due to secondary effects[85] (i.e. kinetics effects that do not influence the rate-controlling step in the reaction process).

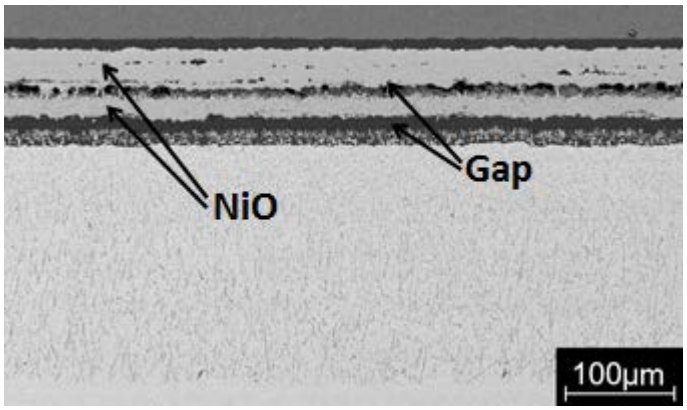

(a)

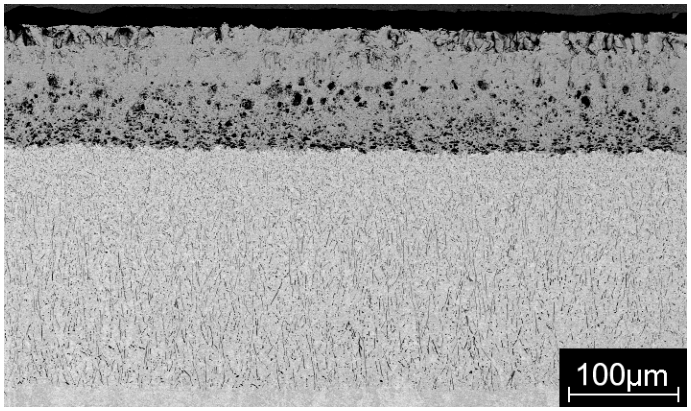

(b)

Figure 4.8 Cross-sectional images of Ni-3at%Al oxidized in (a) air and (b) air+30%H_2O at 1000°C for 64 hour

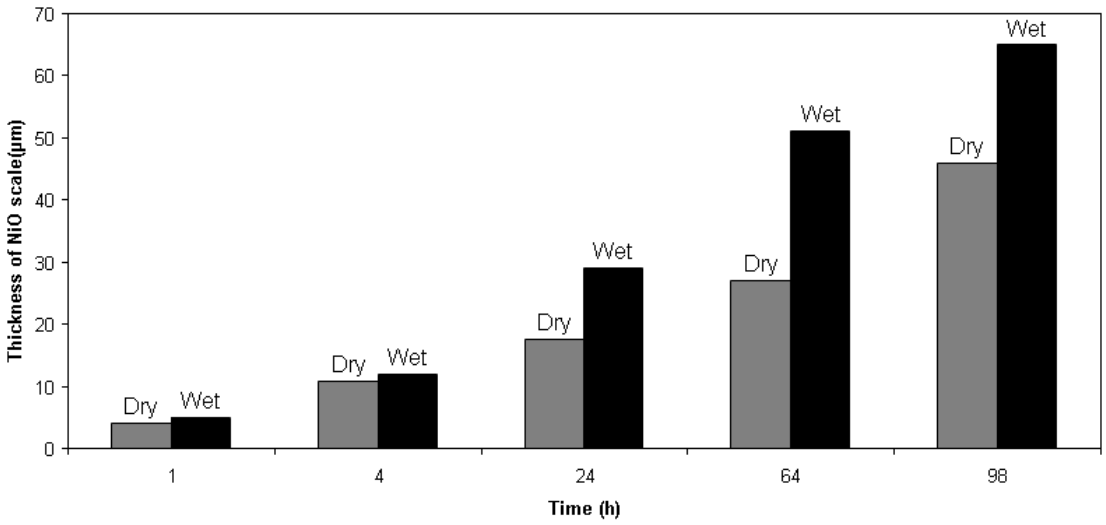

Figure 4.9 Thickness of NiO scale of Ni-3at%Al oxidized in dry air (dry) and air+30%H_2O (wet) at 1000°C

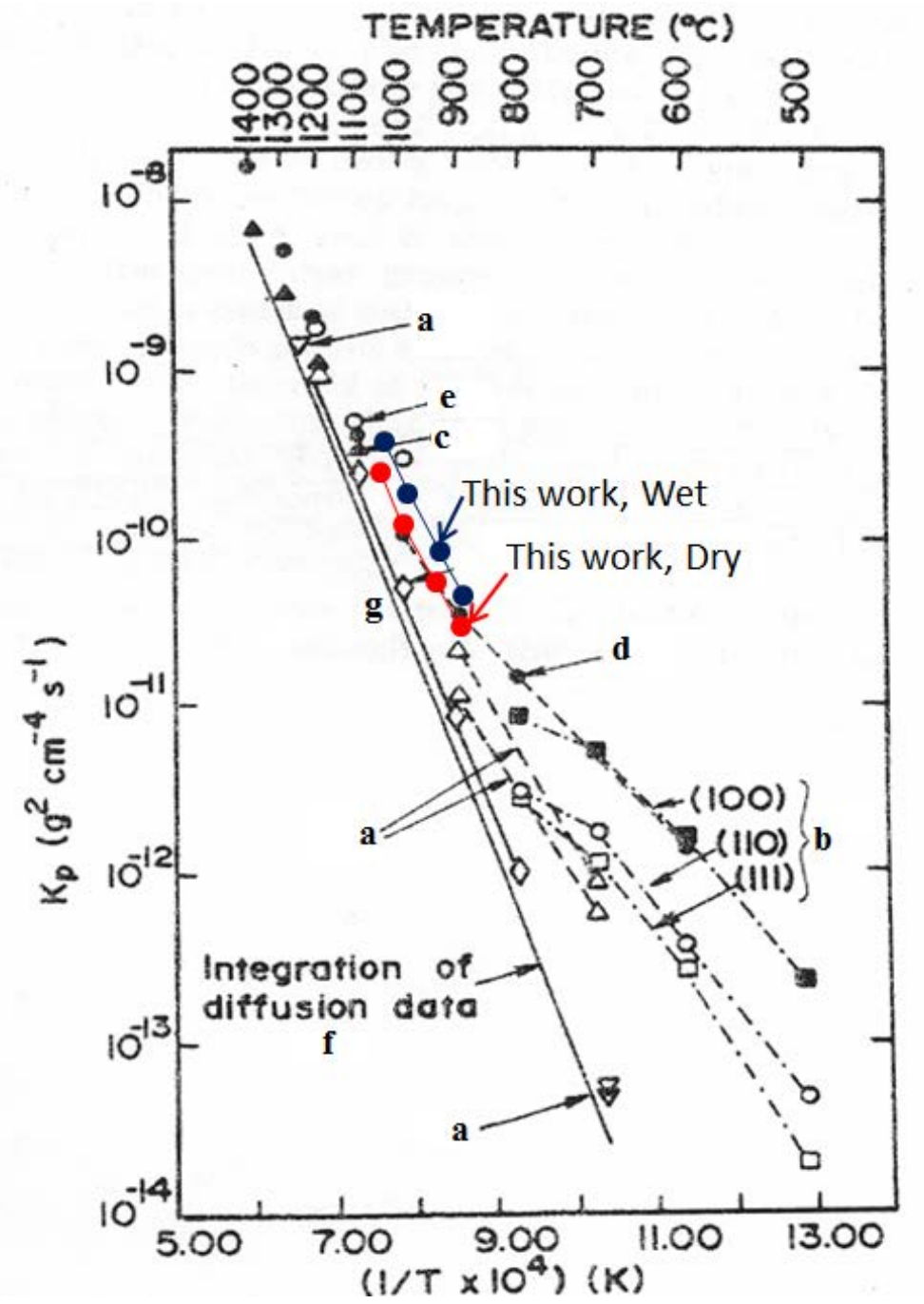

Figure 4.10 Arrhenius plot of NiO scale formed on Ni metal at different conditions[82]. The references have been labeled as (a) 72 (b) 80 (c) 86 (d) 87 (e) 88 (f) 89 (g) 82. The red line and blue line come from this work for dry and wet air respectively.

It was found that NiO scale formed on pure Ni oxidized at 1000°C in wet air has much finer grain sizes comparing to that formed in dry air[77]. Therefore, there was more grain boundary in NiO formed in wet oxidizing conditions. Diffusion through grain boundary is much faster over solid-state lattice diffusion, although the area fraction of grain boundary is much smaller than lattice. Since grain boundary diffusion has lower activation energy, NiO growth is dominated by grain boundary (or short-circuit diffusion) at lower temperature (<~1000°C) while by lattice diffusion at higher temperature (>1000°C) [84]. This trend can be seen by the slope change at around 1000°C in Figure 4.10. Moreover, the small difference in the activation energy for NiO formed in dry and wet air may also due to this effect.

Another mechanism for the enhance NiO in wet air is that the steam improves the adhesion of the NiO scale and therefore enhances the growth rate constant. This effect is shown schematically in Figure 4.11. During the course of oxidation, Ni cations diffuse outward to create vacancies at the oxide/metal interface. Condensation of these vacancies forms voids in the MCZ[4,90]. This is a representation of the Kirkendall effect. Those voids can be filled by oxidation of Ni within MCZ. Since oxygen ingress when in dry air is apparently very low, very limited MCZ space filling can occur. Therefore, the scale lost some of the contact with the alloy due to merging of voids to form a gap. By contrast, oxidation in air with steam allows for voids filling by enhanced oxygen ingress. The nature of this inward transport of oxygen is not well understood, it is likely due to direct molecular transport (O_2 and/or H_2O), diffusive transport (*e.g.*, OH^-) through the scale, or some combination of the two. There are several possible mechanisms may support the inward transport of oxygen-containing species. One mechanism is the one shown in Figure 1.17. In this mechanism[50], since there is an oxygen potential gradient in the scale, it tends to push the reaction $H_2O(g) = H_2 + O_O^X + V_{Ni}^{''} + 2h^{\bullet}$ to the left in upper part and

to the right in the lower part of a pore. Therefore, a gradient for $H_2O(g)$ is established and it drives $H_2O(g)$ to move inward through gas phase transport, which is expected much faster than solid phase transport. Another mechanism reported by Robertson and Manning[4] is shown in Figure 4.12. If a void is formed at the scale/alloy interface, it will reduce the local oxidation rate above the void. This allows the oxide at grain boundary to dissociate and open a pore. Then gases can penetrate the scale through those micro-pores. No matter through which mechanism, as long as the oxygen-containing species can transport to the scale/alloy interface, they will oxidize Ni from the base alloy to fill the space in MCZ. The inward growth of NiO due to inward transport of oxygen-containing species was also found in oxidation of pure Ni in dry air and air with steam[91]. In conclusion, the presence of steam enhanced the oxygen ingress though the NiO scale, which promotes the space filling within the MCZ. This effect maintains the adhesion of NiO scale and therefore increases the growth rate constant.

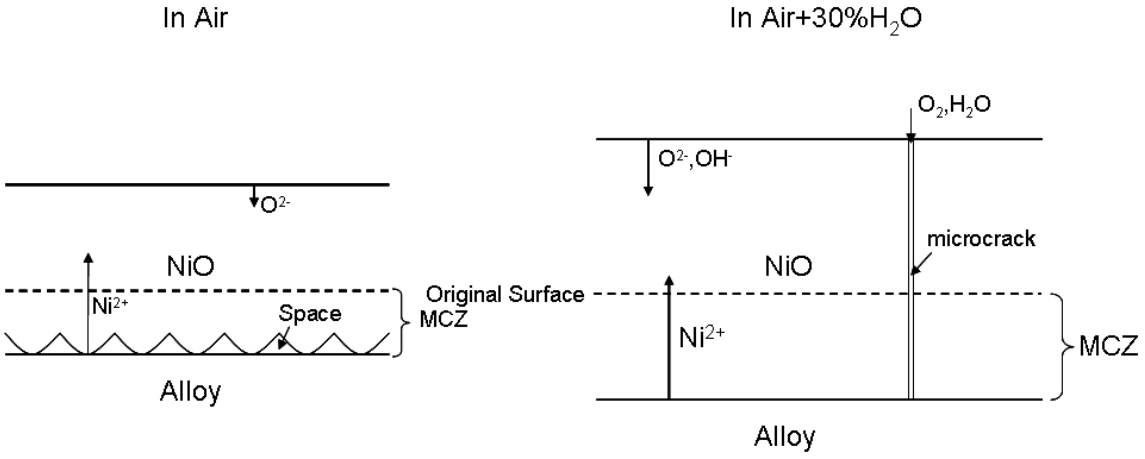

Figure 4.11 Schematic of transporting species when oxidizing in dry air and air+30%H_2O

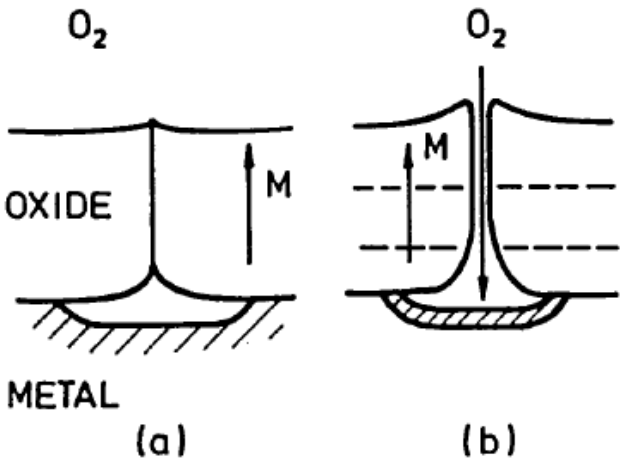

Figure 4.12 Schematic of a micro-pore forming above a void [4]

4.1.1.5 Comparison of steam effect at the early stage

As was shown in Figure 4.5, alloy #6 was able to form a continuous Al_2O_3 scale in dry air but formed a NiO scale in air+30%H_2O at 1000^oC at 20h. To study the oxidation mechanism, it is important to clarify whether this difference existed from the very early stage or if there was an initial stage in which this alloy formed a continuous Al_2O_3 scale in both atmospheres but this Al_2O_3 scale eventually broke down in air+30%H_2O. Figure 4.13 compares the surface morphology for alloy #6 oxidized in dry air (a) and (b) and in air+30%H_2O (c) and (d) at 1000 ^oC for 5min (a) and (c) and 30min (b) and (d). It is seen that the difference in the oxidation behavior of this alloy in the two environments existed right from the initial stages of oxidation. For the alloy oxidized in dry air, shown in Figure 4.13 (a) and (b), only Al_2O_3 formed. For the alloy oxidized in air+30%H_2O, NiO initially formed as discrete islands, shown in Figure 4.13 (c) and then became continuous with time, as shown in Figure 4.13 (d). Therefore, it is clear that the presence of steam resulted in very different (i.e. less protective) oxidation from the very early stage of reaction. In other words, alloy #6 did not initially form a continuous Al_2O_3 scale, which eventually broke down with continuous oxidation.

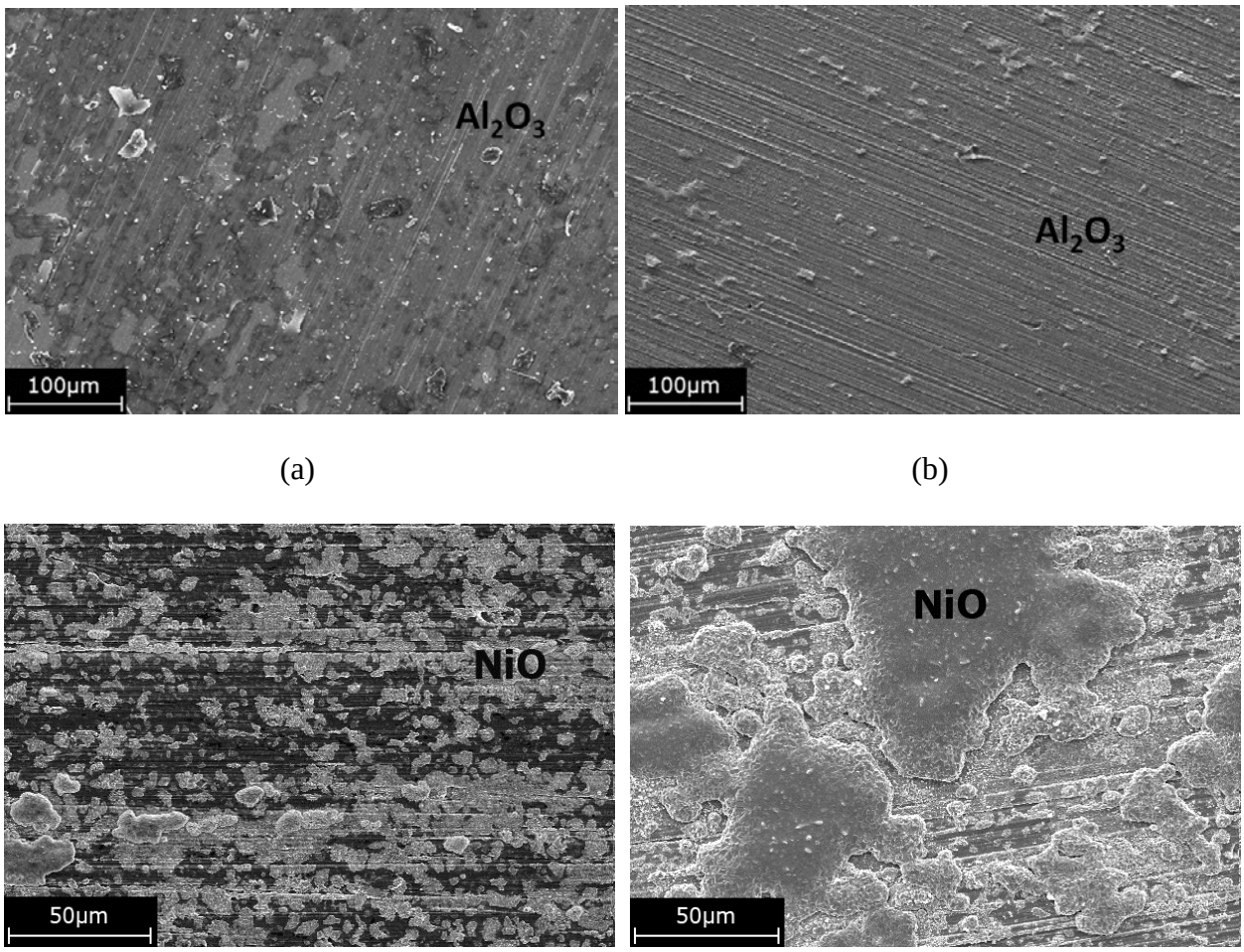

Figure 4.13 Comparison of steam effect on alloy #6 oxidized in dry air for (a) 5min (b) 30min and in air+30%H_2O for (c) 5min and (d) 30min. In (a) and (b), the dark area are Al_2O_3 scale.

4.1.1.6 Using theory to account for the increased critical concentration of Al

Two criteria have been proposed by Wagner[3,24] to determine the critical concentration of Al to form and maintain a protective alumina scale. In one criterion, which is shown by equation.1.33, the critical concentration must be large enough to sustain the growth of the external scale[24]. For this criterion to be applicable, the alloy must be able to initially form an Al_2O_3 scale. This criterion has been used for some Cr_2O_3-scale forming Fe-based alloys[43,48]. However, for certain Al_2O_3-scale forming Ni-based alloys oxidized in wet air in this study (e.g. alloy #6), initial

formation of an Al_2O_3 scale was not observed (Figure 4.13). Such a result leads to the inference that this criterion cannot be used in this situation.

At the same time, the metal consumption rate for alloys oxidized in the air+30%H_2O at 1000^{o}C was found to increase by a factor of two compared to that of alloys oxidized in dry air. The enhanced metal consumption rate, in turn, changes the boundary condition for the diffusion of oxygen from the alloy/scale interface to the internal oxidation front. Quantitatively, this effect must change the critical concentration of Al to form a protective scale to some extent. To estimate the extent to which the enhanced metal consumption rate can affect the critical concentration, a rigorous analysis based Maak's modification[2] of Wagner's theory[3] for the transition from internal oxidation to external scale formation will be carried out. This theory has been introduced in section 1.2.3, however, it was assumed that $N_O^s D_O << N_B^o D_B$ as a limiting condition to simplify the analysis. In this section, a more rigorous calculation without such an assumption will be presented. Therefore, for the completeness of this section, a detailed presentation of Maak's modification[2] of the Wagner's theory[3] will be given. Figure 4.12 shows the concentration profiles of oxygen and solute element B assumed in Wagner's theory. It is also assumed that the solvent A oxide does not form on the surface. The thickness of the IOZ (ξ) is assumed to proceed according to a parabolic law:

$$\xi = 2\gamma\sqrt{D_O t} \tag{4.3}$$

where ξ is the distance between the original alloy surface and the internal oxidation front, D_O is the diffusion coefficient of oxygen in the IOZ, γ is a dimensionless factor related to the parabolic rate constant for internal oxidation and t is time. The concentration profile for oxygen and solute B should follow Fick's second law. Since there is no external scale formation, the boundary

condition for oxygen diffusion is fixed. In this case, the solution of Fick's law for the concentration profile of the oxygen in the IOZ is given by[27]:

$$N_O = N_O^S \left\{1 - erf\left[x / 2(D_O t)^{1/2}\right] / erf(\gamma)\right\} \quad for\ 0 \le x \le \xi \tag{4.4}$$

where N_o^S is the oxygen solubility on the alloy surface, x is the distance from the alloy surface, *erf(r)* is the error function and N_O is the oxygen mole fraction at the distance x.

The concentration profile of the element B beneath the IOZ is given by:

$$N_B = N_B^O \left\{1 - erfc\left[x / 2(D_B t)^{1/2}\right] / erfc(\gamma\varphi^{1/2})\right\} \quad for\ x \ge \xi \tag{4.5}$$

where N_B^O is the mole fraction of B in the bulk alloy, D_B is the interdiffusion coefficient of B and the base metal in the vicinity beneath the internal oxidation front, *erfc(r)* is the complementary error function of r and φ equals D_O / D_B.

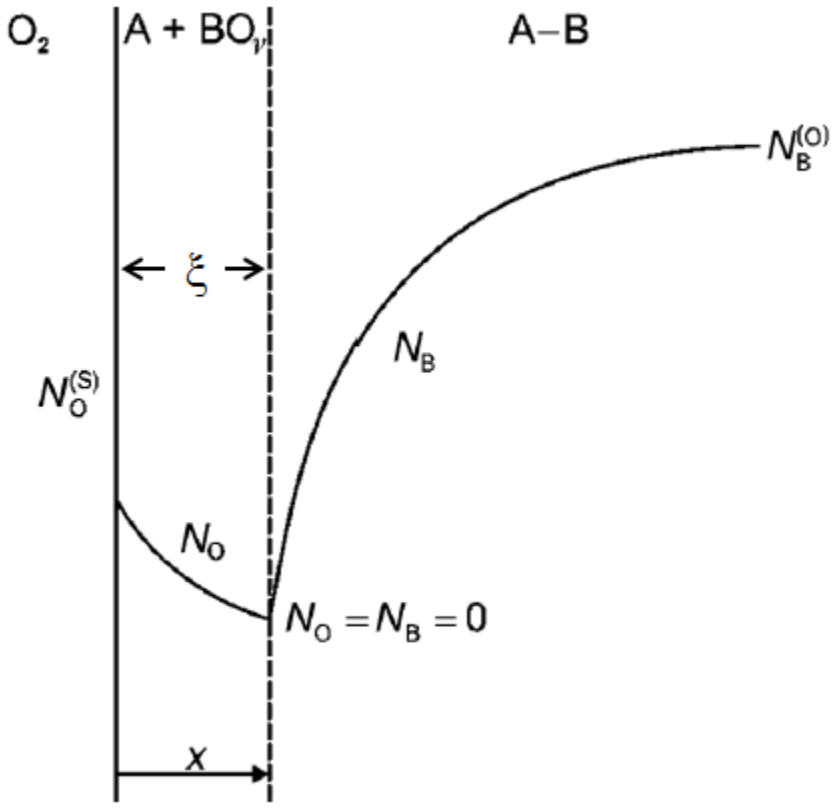

Figure 4.14 Concentration profile used for the calculation of critical concentration of solute in alloy[6]

Due to the outward diffusion of B from the interior of the alloy, B is enriched in the IOZ. The enrichment factor is defined as:

$$\alpha = \frac{f}{N_B^O} \tag{4.6}$$

where f is the mole fraction of the BO_v. At $x = \xi$, the amount of B arrived at this interface equals the amount of BO_v formed at the interface, which gives:

$$f\frac{d\xi}{dt} = D_B \frac{\partial N_B}{\partial x}\bigg|_{x=\xi} \tag{4.7}$$

Substituting equations 4.3 and 4.5 into 4.7, the enrichment factor is calculated as:

$$\alpha = \frac{1}{F\left(\gamma\varphi^{1/2}\right)} \tag{4.8}$$

where $F(r)=\pi^{1/2}r\exp(r^2)erfc(r)$. For the transition from internal oxidation to external oxidation, it is proposed[3] that if the volume fraction of the BO_v reaches a critical volume fraction f_v^*, the oxides will block the inward diffusion of oxygen so that the internal oxidation will be terminated. Therefore, BO_v will only form on the surface of the alloy as a continuous layer. Under this case, the critical mole fraction f^* corresponding to this critical volume fraction is given by:

$$f_v^* = \frac{V_{BO_v}}{V_{alloy}} \tag{4.9}$$

$$f^* = \frac{V_{BO_v}/V_{BO_v}^m}{V_{alloy}/V_{alloy}^m} \tag{4.10}$$

where V_{BOv}^m and V_{alloy}^m are molar volume of BO_v and the alloy. Substituting equation 4.9 into equation 4.10 yields:

$$f^* = \frac{f_v^*}{\rho} \tag{4.11}$$

where ρ is the ratio of the molar volume of BO_v to that of the alloy. Substituting equation 4.8 and equation 4.11 into the equation 4.6, the critical mole fraction of B to form an external B oxide scale can be calculated to be:

$$N_B^* = \frac{f_v^* F\left(\gamma\varphi^{1/2}\right)}{\rho} \tag{4.12}$$

To calculate this critical mole fraction, the values of ρ and φ can be found from literatures. In the case for Ag-In alloy[27], f_v^* was found to be 0.3 and this value has been used in many papers although the particular cases were different. There are two ways to determine the dimensionless parameter γ, one is by measuring the thickness of the IOZ and then calculating γ in accordance with its definition in equation 4.3; the other way is by analyzing the flux balance at the internal oxidation front by equating the flux of oxygen and B in the ratio that they can form stoichiometric BO_v. This flux balance gives:

$$\frac{N_O^S}{\nu N_B^o} = \frac{G(\gamma)}{F(\gamma\varphi^{1/2})} \tag{4.13}$$

where $G(r)=\pi^{1/2} r \exp(r^2) erf(r)$. If all other parameters in equation 4.13 are known, γ can be numerically solved.

However, this Wagner's theory assumes that the oxygen partial pressure is very low, to the extent that solvent-oxide cannot form on the surface. In more realistic cases, the base metal A should be able to form its oxide as well. Figure 4.15 shows a schematic of this more realistic morphology. This figure is a schematic reflection of the morphology shown in Figure 4.2. Maak[2] modified Wagner's theory to take into account the growth of an external scale. It is assumed that the IOZ still thickens according to the parabolic law in equation 4.3, and that the external scale growth also follows the parabolic rate law. Accordingly, the thickness of the MCZ is given by:

$$X^2 = 2k_c t \tag{4.14}$$

where X is the thickness of MCZ and k_c is the appropriate rate constant related to the growth of the external scale. To make the calculation convenient, a new variable u is defined as:

$$u = \left[k_c / (2D_o)\right]^{1/2} \tag{4.15}$$

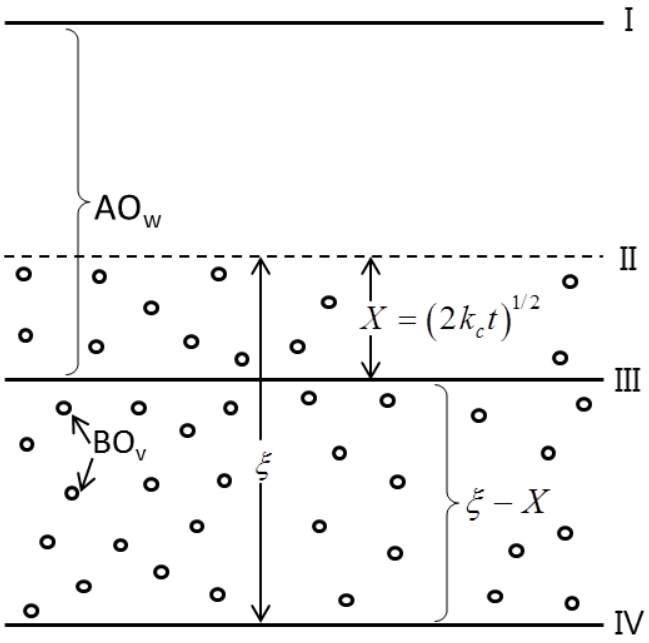

Figure 4.15 Schematic of the typical morphology of oxidized samples that forms a solvent-oxide scale (I to III), a metal consumption zone (II to III) and an internal oxidation zone (II to IV)[92]

Since the boundary condition for the diffusion of oxygen in the IOZ is changed, i.e. one boundary is moving due to the metal consumption, the concentration profile of oxygen no longer follows equation 4.4, but is instead given by:

$$N_O = N_O^S \left\{ \frac{1 - erf\left[x / 2(D_O t)^{1/2}\right]}{erf(\gamma) - erf(u)} \right\} \quad for\ X \le x \le \xi \tag{4.16}$$

while the concentration profile of B remains the same as in equation 4.5. Following Wagner's treatment, γ is calculated by:

$$\frac{N_O^S}{\nu N_B^o} = \frac{erf(\gamma) - erf(u)}{erf(\gamma)} \cdot \frac{G(\gamma)}{F(\gamma\varphi^{1/2})} \tag{4.17}$$

which is complementary to equation 4.13 in the previous case. It is worthwhile to note that equation 4.17 becomes identical to equation 4.3 when u=0. The equation to calculate the enrichment factor α should be the same as equation 4.8 because the mass balance at the internal oxidation front remains the same and the expression for ξ (equation 4.3) and N_B (equation 4.5) are also the same. Finally, the critical concentration of B for the transition from internal to external oxidation is given by the same expression as equation 4.12. However, the γ value used to calculate the enrichment factor α, as well as the N_B^*, is determined by equation 4.17 when the external scale is present, rather than equation 4.13 for the case without an external scale. Again, equation 4.13 can be solved numerically.

In practice, to determine the γ value by equation 4.17, there are several parameters that need to be found: the oxygen diffusivity in the IOZ D_o, the diffusion coefficient of Al in the alloy D_{Al}, the oxygen solubility N_o^S at the alloy/scale interface and the parameter u. The parameters v and N_B^o are fixed particular to the samples.

Determining the effective oxygen diffusivity in the internal oxidation zone

The alloy system we studied is Ni-Al alloy, in which Al is the more reactive element. Park and Altstetter[93] measured the oxygen diffusion coefficient in solid γ-Ni by a solid-state electrochemical method. It was found the diffusivity of oxygen in nickel is:

$$D_O = 4.9\times10^{-2}\exp\left(-\frac{164kJ/mole}{RT}\right)cm^2/\sec \quad (850^oC\ to\ 1400^oC) \tag{4.18}$$

This value corresponds to the oxygen diffusivity in a clean bulk γ-Ni matrix. At 1000^{o}C, this value is D_o=9.1x10^{-9}cm^2/sec. However, the microstructure of the oxidized alloy in the IOZ is different from that used in the electrochemical study. Figure 4.16 is a cross-sectional image of a deep-etched Ni-3at%Al sample oxidized in wet air at 1000^{o}C for 98h. In this figure, the internal

oxidation precipitates are those whisker-like continuous rods, which extend from the original surface to the internal oxidation front.

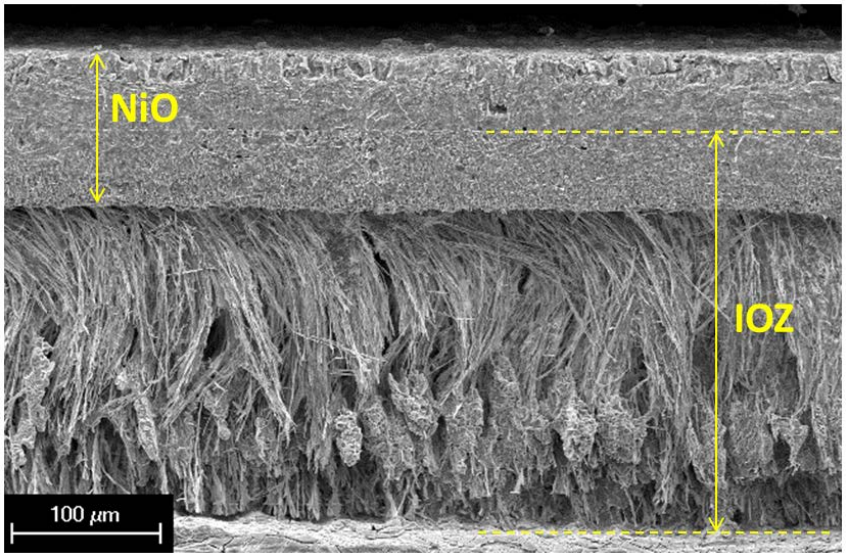

Figure 4.16 Cross-sectional image of a deep-etched Ni-3at%Al sample oxidized in wet air at 1000°C for 98h

Stott et al.[94] pointed out that the incoherent interfaces between the oxides and the alloy matrix are good diffusion paths for fast inward diffusion of oxygen from the surface to the internal oxidation front. Therefore, the effective diffusion coefficient of oxygen in the IOZ should consider the contribution from those interfaces. For such a case, the total inward oxygen flux is given by:

$$j_{eff} = j_m A_m + j_i A_i + j_{ox} A_{ox} \tag{4.19}$$

where j_m, j_i and j_{ox} are the fluxes through the matrix, the oxide/metal interface and the oxide particles respectively, and A_m, A_i and A_{ox} are the area fraction of the matrix, the oxide/metal interface and the oxide rods. Since the oxygen diffusivity through the oxide rods is very low, the third term in equation 4.19 can be neglected. Thus, the effective oxygen diffusion coefficient in the IOZ is approximated to be

$$D_{o,eff} = D_o A_m + D_{o,i} A_i \tag{4.20}$$

where the D_o is the oxygen diffusion coefficient in the nickel matrix and $D_{o,i}$ is the interfacial diffusion coefficient. For the case of continuous rods of radius r, the number of rods in unit cross-sectional area of the zone, Z is given by[94]:

$$N_{BO_v}\xi / V_{all} = Z\pi r^2 \xi / V_{BO_v} \tag{4.21}$$

where N_{BOv} is the mole fraction of oxide BO_v, V_{BOv} and V_{all} are the molar volume of the oxide and the alloy. Meanwhile,

$$A_i = 2\pi r Z \delta_i \tag{4.22}$$

where δ_i is the width of the interface, and

$$A_m = 1 - A_i - A_{ox} = 1 - 2\pi r Z \delta_i - \pi r^2 Z \tag{4.23}$$

Substituting equations 4.21-4.23 into equation 4.20 and simplifying gives:

$$\frac{D_{o,eff}}{D_o} = 1 + \frac{V_{BO_v} N_{BO_v}}{V_{all}} \left[\frac{2\delta_i D_{o,i}}{r D_o} - 1 \right] \tag{4.24}$$

Based on this relation, the effective oxygen diffusion coefficient has a linear relation with N_{BOv}, which equals to the mole fraction of B in the alloy. For the Ni-3at%Al alloy, it was found that the internal oxidation precipitates are $NiAl_2O_4$ up to a depth of 90% of the total depth and Al_2O_3 for a greater depth into the alloy[95]. Therefore, it is assumed that all the internal oxides are $NiAl_2O_4$. Therefore, $N_{Ni0.5AlO1.5}$=0.03. From Stott et al.[94], $V_{Ni0.5AlO1.5}$= 19.5cm^3/mole, V_{all} = 6.67cm^3/mole, δ_i is assumed to be 1nm, which is typically the width assumed for grain-boundary diffusion study, r is measured to be around 0.13μm and $D_{o,i}$ / D_o is found to be 8.0x10^3 at 1000^{o}C. Substituting all the parameters into equation 4.24, the effective oxygen diffusion coefficient in the IOZ for Ni-3at%Al alloy is calculated to be $D_{o,eff}$=1.0x10^{-7}cm^2/sec.

Determining the oxygen solubility N_o^S from thermodynamics

When there is an external NiO scale present, the oxygen solubility N_o^S is no longer determined by the exterior gas environment, but by the equilibria established at the alloy/scale interface. This equilibrium is not the one for the γ-Ni and NiO. Rather, because of the presence of the Al in the alloy, the equilibria are established by three phases: γ-Ni, NiO and the spinel $NiAl_2O_4$. This can be shown by a schematic of an isothermal cross section of the ternary phase diagram for Ni-Al-O at 1000°C, Figure 4.17. The oxygen activity corresponding to the three-phase equilibria should be the same on any point within the three-phase region on the ternary phase diagram.

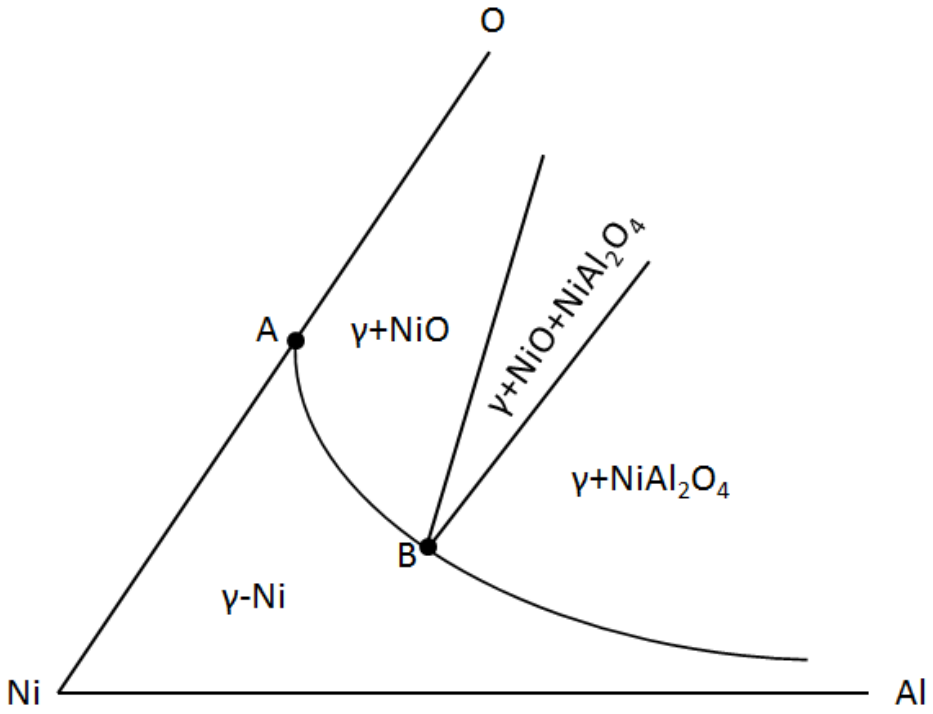

Figure 4.17 Schematic of the isothermal cross section of Ni-Al-O ternary diagram near the Ni-rich corner at 1000°C. Point A corresponds to the γ-Ni/NiO equilibrium and point B corresponds to a γ-Ni/NiO/$NiAl_2O_4$ equilibria

Elrefair and Smeltzer[96] determined the oxygen partial pressure corresponding to the three-phase equilibria between 1123 and 1423K based a electrochemical measurement on the cell of Ni,NiO,$NiAl_2O_4$|ZrO2(+CaO)|Ni,NiO and it follows the relation:

$$\log P_{O_2}(atm) = -\frac{24,478}{T} + 8.804\left(\pm\frac{60}{T}\right) \quad (1123-1423K) \tag{4.25}$$

At 1000°C, the oxygen pressure corresponding to γ-Ni/NiO/$NiAl_2O_4$ coexistence is $4.1x10^{-11}$atm. This oxygen partial pressure is a little smaller than the one corresponding to point A, $4.5x10^{-11}$atm, which is the dissociation pressure of oxygen for NiO equilibrated with Ni. Further, the Gibbs free energy change for the reaction:

$$\frac{1}{2}O_{2(g)} = \underline{O}_{(Ni,absorb)} \tag{4.26}$$

was found[97] to be:

$$\Delta G^o_{4.26} = -179300 + 67.6T \ J/mole \tag{4.27}$$

when $\underline{O}$ uses 1at% standard state, which equals 100 x N_o^S. Therefore, the Gibbs free energy change for this reaction at 1000°C is -93,235kJ/mol.

$$\frac{\underline{O}}{P_{O_2}^{1/2}} = K_{4.26} = \exp\left(\frac{-\Delta G^o_{4.26}}{RT}\right) \tag{4.28}$$

Substituting the oxygen partial pressure for three-phase equilibria at 1000°C into equation 4.28, the corresponding oxygen solubility is found to be N_o^S=$4.1x10^{-4}$.

Utilizing Maak's modification to calculate the oxygen solubility N_o^S

The N_o^S value can also be determined by using Maak's modification and comparing it with the value determined by thermodynamics. In equation 4.13, one other parameter that needs to be determined is $D_{Al.}$ This has been reported in several papers[98,99,100]. At around 1000°C, the

D_{Al} values from those papers are in fairly good agreement. An accurate temperature dependence is deduced to be[98]:

$$D_{Al} = 1.0 \exp\left(\frac{-260 kJ / mol}{RT}\right) cm^2 / \sec \tag{4.29}$$

Thus, at 1000°C, D_{Al} is $2.1 \times 10^{-11} cm^2/sec$.

The stoichiometry factor v determines the mass balance of oxygen and aluminum at the internal oxidation front. This internal oxidation front is shown as the interface at of x = ξ in Figure 4.14. At this interface, oxygen reacts with aluminum to form Al_2O_3. Therefore, v is 1.5 for Al_2O_3. This is taken to be the case even though it is known that IOZ is primarily comprised of $NiAl_2O_4$[95]. Indeed, the stoichiometry factor v should be different from 1.5 when considering the influence of forming both Al_2O_3 and $NiAl_2O_4$. Inferred from an analysis by Meijering[101], this effect could be estimated by replacing v by an effective stoichiometry factor v_{eff}, which depends on the ratio of the distances for the two internal oxidation fronts (for forming $NiAl_2O_4$ and Al_2O_3) and the oxygen potentials at those two internal oxidation fronts. In the case of internally oxidized for Co-Ti alloys, Megusar and Meier[102] found that the oxygen concentration profile and the oxygen flux to the internal oxidation front are changed by having internal zones of a different oxide. However, in the present case, the high stabilities of Al_2O_3 and $NiAl_2O_4$ are considered to allow for the simplification that v=1.5. Moreover, the experimental results showed no difference in the IOZ depth, ξ, in dry and wet oxidizing conditions. This suggests that the aluminum concentration profile beneath the IOZ is not changed by the presence of steam, and thus the mole fraction of Al_2O_3 formed in the internal oxidation zone is not changed. Therefore, assuming a constant v=1.5 does not affect the analysis of determining N_{Al}^* in the wet and dry oxidizing conditions.

The molar volume of oxide at the internal oxidation front was chosen to be the one for $AlO_{1.5}$. The N_B^o value is 0.03 for Ni-3at%Al alloy. u can be determined from the metal recession rate k_c=3.8x10^{-11} cm^2/sec measured in this study in dry air. This u value was found to be u_{dry}=0.0098. The γ value can be determined by the parabolic rate constant k_p for the IOZ, assuming the thickness of the IOZ follows the form of:

$$\xi^2 = k_p t \tag{4.30}$$

and γ can be calculated as:

$$\gamma = \sqrt{\frac{k_p}{4D_{o,eff}}} \tag{4.31}$$

In this study, k_p=2.7x10^{-9} cm^2/sec for dry air. Therefore, the experimental γ is γ_{dry} = 0.082. Substituting all the parameters into equation 4.17, the N_o^S value determined using Maak's modification is 5.4x10^{-4}. This value is in reasonable agreement with the value 4.1x10^{-4} determined by thermodynamics. Therefore, the use of Maak's modification in the present study is validated.

Determining the key parameter for the increased critical concentration of Al (N_{Al}^*)

By comparing the cross-sectional morphologies of the samples oxidized in dry air and wet air, (i.e., Figure 4.6), the nature of the three-layer structure is essentially identical in both dry and wet oxidizing conditions. All three layers thicken according to the parabolic rate law, indicating that the overall process is diffusion controlled. This implies that the dynamic situation to form this morphology is the same in both conditions. Therefore, Maak's modification of Wagner's criterion should also be valid in wet air. In other words, the effect of each parameter on the N_{Al}^* under wet oxidizing conditions can be quantified by this modified criterion. In

equations 4.12 and 4.17, ρ and D_{Al} are not expected to be different in dry and wet oxidizing conditions; whereas, the four parameters $D_{o,eff}$, N_o^S, u and f_v^* need to be considered.

The parameter u is related to the corrosion constant k_c, which is a measurement of the metal consumption rate. From present experiments, the metal consumption rate was enhanced in the wet oxidizing condition. Specifically, in dry air k_c=1.9x10^{-11}cm^2/sec while in wet air k_c=3.6x10^{-11}cm^2/sec. Substituting these two values into equations 4.12, 4.15 and 4.17 and keeping all other parameters constant, the N_{Al}^* values can be calculated for those two values. It was found that the increase in the metal consumption rate gives only a 0.1% increase in the N_{Al}^* value. Actually, this extent of change agrees with the theoretical analysis by Gesmundo and Viani[92]. They found that when u (0.0098 in dry air) is much smaller than γ (0.082 in dry air), the critical concentration is almost a constant versus u. On the basis of the experiments conducted in this study, the increase in the N_{Al}^* value is around 60%. This change is two orders of magnitude smaller than this experimental result. Therefore, the enhanced metal consumption rate is not the reason for the increased N_{Al}^*.

The sensitivity of N_{Al}^* to $D_{o,eff}$ and N_o^S is shown in Figure 4.18. Here, N_{Al}^* is plotted as a function of $D_{o,eff}$ (a) and N_o^S (b) when keeping all other variables constant. In this figure, the dashed line II corresponds to the determined $D_{o,eff}$ and N_o^S on the two curves, respectively. Dashed line I and III correspond to those values divided or multiplied by a factor of five. It is seen that even when these two parameters are separately changed by a factor of five, the changes in N_{Al}^* is no larger than 7%. Moreover, N_{Al}^* is not sensitive to any increase in $D_{o,eff}$ and N_o^S. A small decrease in either or both of these two parameters will not significantly decrease N_{Al}^* either; although, a large decreasing either or both of these two parameters can effectively

decrease N_{Al}^{*}. Even so, the values of $D_{o,eff}$ and N_o^{S} are such that even considering relatively large variations, they cannot cause the large change in N_{Al}^{*} that was experimentally determined.

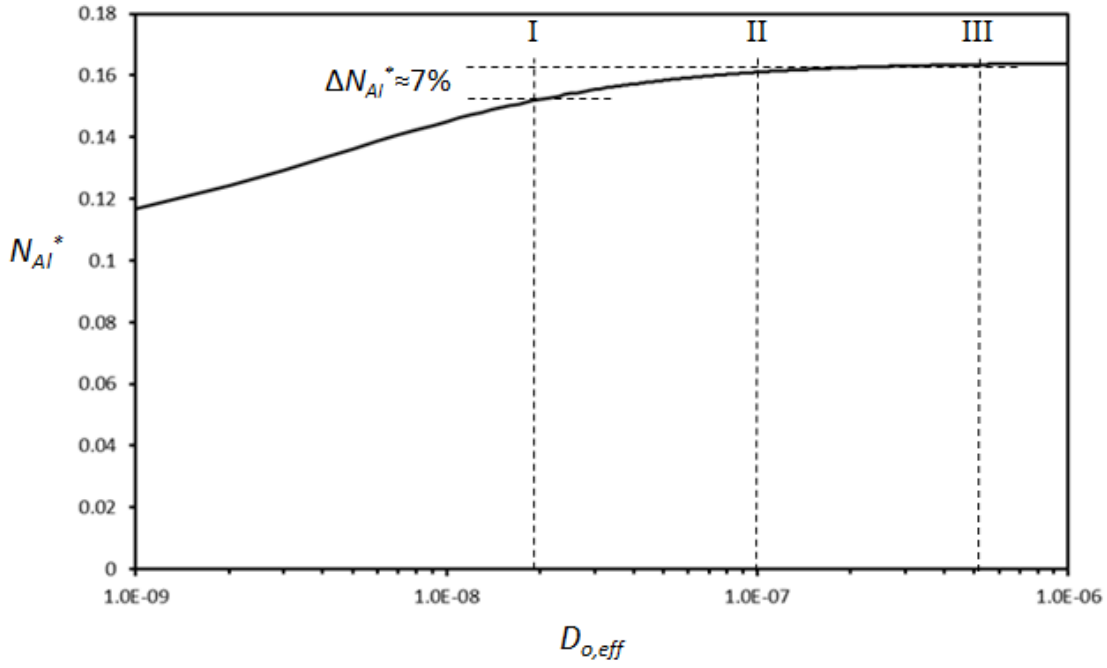

(a)

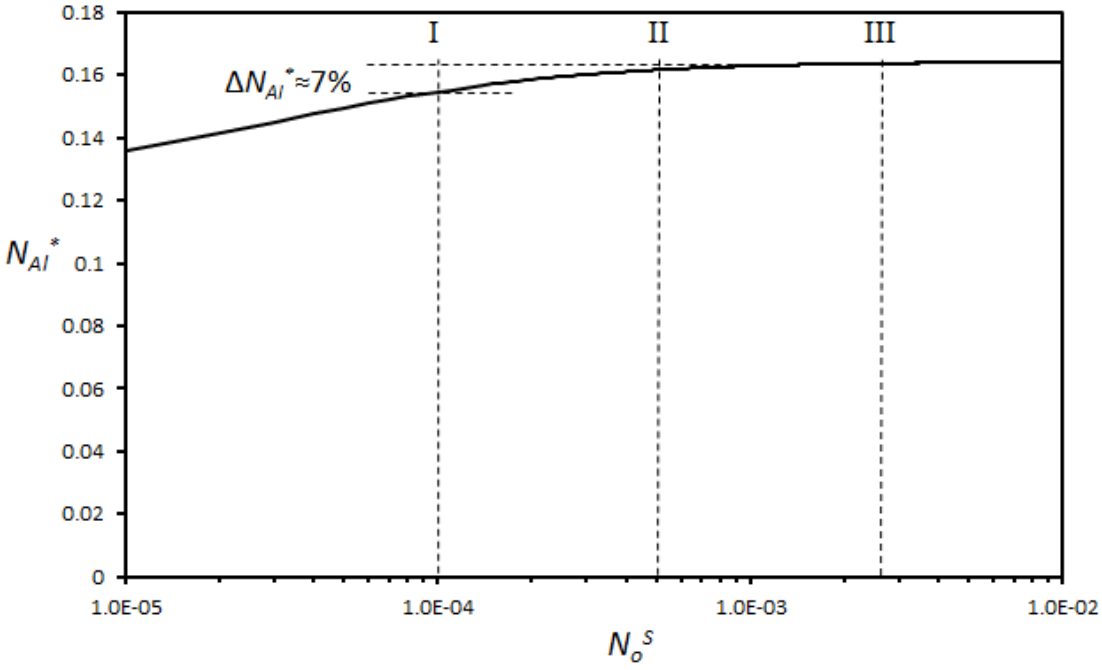

(b)

Figure 4.18 The critical concentration of Al versus $D_{o,eff}$ (a) and N_o^S (b). Dash line II corresponds to the $D_{o,eff}$ (a) and N_o^S (b) values used in the calculations. Dash line I and III corresponds to those values divided or multiplied by a factor of five.

From theoretical calculation, the three parameters $D_{o,eff}$, N_o^S and u cannot adequately increase N_{Al}^* to the levels corresponding with what was measured experimentally. Actually, those three parameters affect the critical concentration by affecting the enrichment factor α, which is defined in equation 4.6. Expressing N_{Al}^* in equation 4.12 as a function of the enrichment factor α gives:

$$N_{Al}^* = \frac{f_v^* \cdot V_{all}}{\alpha \cdot V_{AlO_{1.5}}} \tag{4.32}$$

In this equation, f_v^*, V_{all} and $V_{AlO1.5}$ are material parameters that are independent of the diffusion dynamics of oxygen or aluminum in the alloy. To make this point clear, the following example is presented: If there is no enrichment of aluminum in the IOZ (α=1), 1at% aluminum originally in the alloy before internal oxidation will convert to $V_{AlO1.5}/V_{all}$ x1at% =1.8vol% alumina in the region of internal oxidation. Therefore, a critical volume fraction f_v^*=0.3 corresponds to a N_{Al}^* value of around 0.16. By comparison, if aluminum is enriched in the IOZ, for example α=2, then 1at% aluminum in the alloy will convert to 3.6vol% alumina in the IOZ. As a result, for the same critical volume fraction f_v^*=0.3, the N_{Al}^* value is reduced to 0.08. Therefore, the diffusion dynamics of oxygen or aluminum, as reflected by oxygen permeability or NiO growth will affect the N_{Al}^* only if the enrichment factor α is affected. Qualitatively, increasing $D_{o,eff}$, N_o^S and u corresponds to increasing the permeability of oxygen into the alloy, which will have two consequences: (1) more aluminum supply from the base alloy it required since almost all the oxygen will react with aluminum to form alumina at the internal oxidation front, as shown in Figure 4.14; (2) the internal oxidation front will move faster. Meanwhile, the aluminum supply from base metal is limited by the diffusivity of Al and its concentration. Ultimately, a point will be reached at which a further increase in the oxygen permeability will only result in a faster moving internal oxidation front with no Al enrichment. State differently, since almost all the

aluminum supply to the internal oxidation front will form alumina, increasing the migration rate of the internal oxidation front will reduce the enrichment factor, as indicated in equation 4.7. Under this condition, increasing the oxygen supply rate will decrease the enrichment factor, which in turn, will increase the N_{Al}^{*}. However, the enrichment factor cannot be decreased to a value smaller than one. As a result, there will be a stage in which increasing the oxygen supply rate has no effect on the enrichment factor, and therefore, have no effect on the N_{Al}^{*}. Figure 4.19 shows the enrichment factor α as a function of $\gamma\varphi^{1/2}$, which increases with increasing $D_{o,eff}$, N_o^S and u. From our calculation, the $\gamma\varphi^{1/2}$ value for Ni-Al alloy oxidized at 1000^{o}C in dry air is 5.6, which is shown by the dash line in Figure 4.19. It is seen that changing $D_{o,eff}$, N_o^S and u cannot change the enrichment factor significantly, since α is already close to unity. Stott and Wood[95] also reported no Al enrichment in the IOZ in Ni-Al system, which is confirmed by this calculation. Therefore, changing $D_{o,eff}$, N_o^S and u values in dry or wet oxidizing conditions cannot change the enrichment factor, which in turn, cannot change the N_{Al}^{*} for the Al_2O_3-scale forming Ni-based system oxidized in these two conditions.

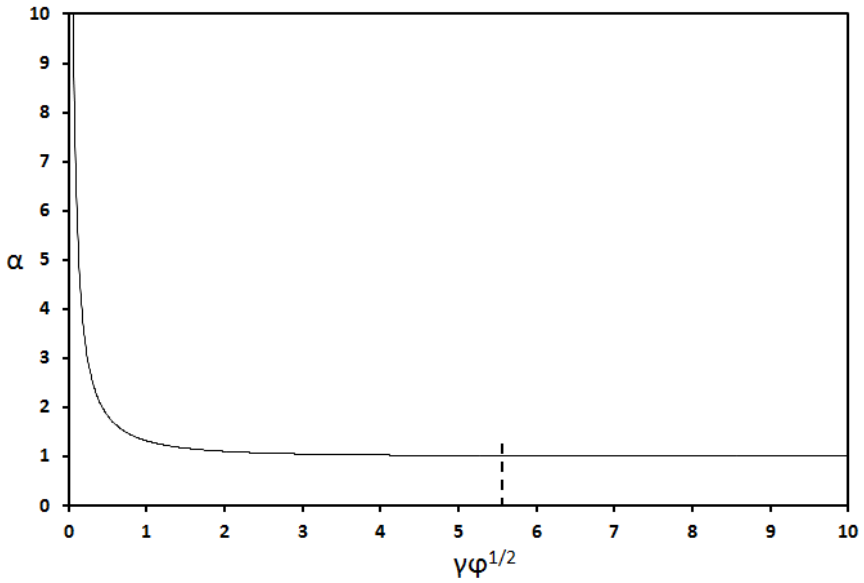

Figure 4.19 The enrichment factor α as a function of $\gamma\varphi^{1/2}$, which increases with increasing $D_{o,eff}$, N_o^S and u values.

Thus, based on this analysis, it is deduced that the only factor that can give the large change in the critical concentration is the critical volume fraction f_v^*. Although this factor is usually assumed to be a constant 0.3 and independent of the reacting conditions, a clear elucidation of this factor has not been established. Indeed, as indicated by Figure 4.20, the morphology of the internal oxides was changed by the presence of steam in terms of the number density, size and spacing of the precipitates. The morphology change can be quantified by drawing a line of a fixed length across an image and counting the number of precipitates that the line crosses. Table 4.1 shows the average number of precipitates on the three lines shown in Figure 4.20 and measured on at least three sets of different images.

Moreover, it was found by quantitative analysis of digitized images (Figure 4.21) that the area fraction of internal precipitates formed in the dry oxidizing condition is 30%(±2%), which is almost identical to the measurement of 29%(±2%) for the wet oxidizing condition. Based on those experimental observations, the average inter-precipitate distance can be estimated by the following model. The 3D morphology of the precipitates in the IOZ is assumed to be as shown in Figure 4.22 (a) and the 2D top view is assumed to be as in Figure 4.22 (b). Suppose that the dimension of the square shown in Figure 4.22 (b) is *L*, which is the width of the cross-sectional image shown in Figure 4.20, *r* the average radius of the precipitates, and *N* the number of precipitates on the line.

Table 4.1 Number of precipitates on a line going from the left to the right of the cross-sectional image of alloy #5 oxidized in dry air and air+30%H_2O at 1000^{o}C for 20h

Number	Top	Middle	Bottom
Dry Air	110±20	70±16	39±14
Air + 30% H_2O	40±10	32±9	21±9

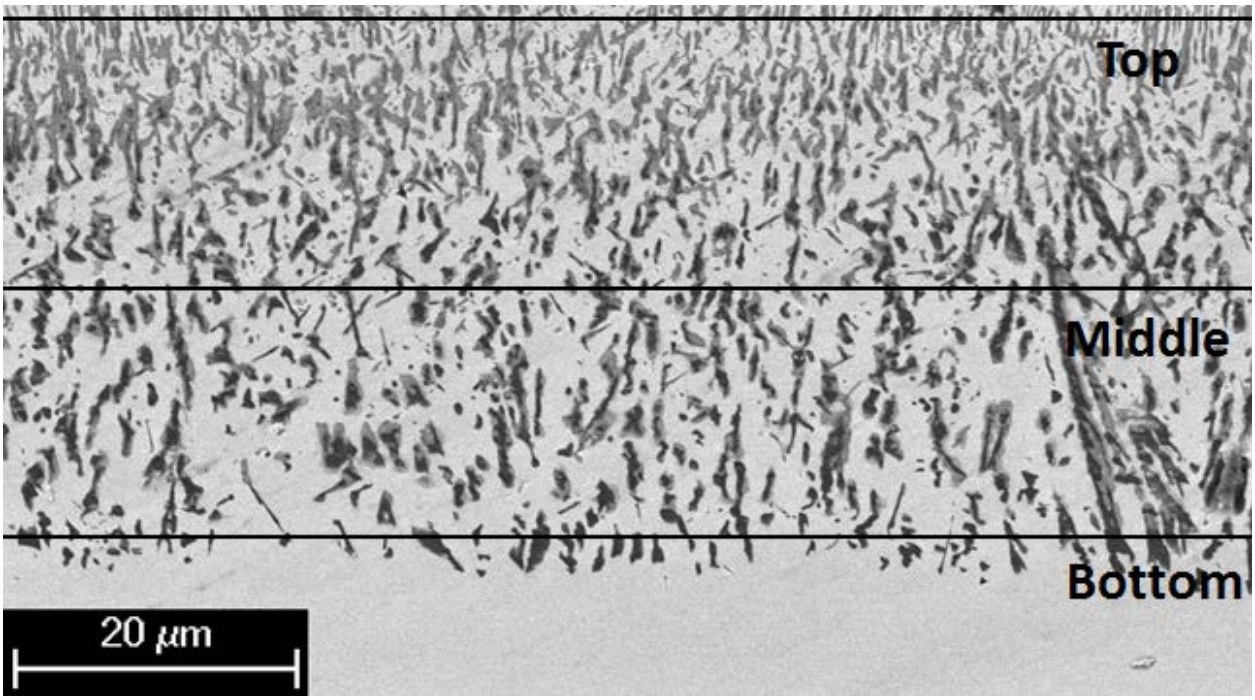

(a)

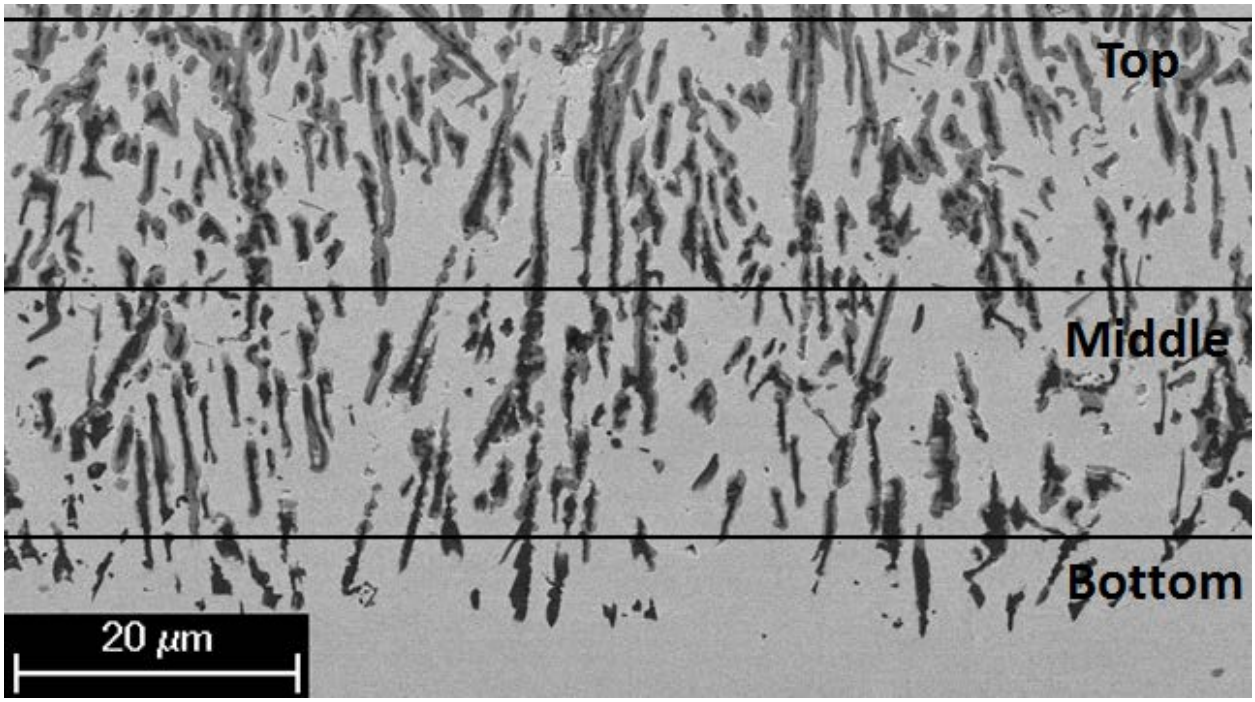

(b)

Figure 4.20 The morphology of the internal oxides formed on alloy #5 oxidized in (a) dry air and (b) air+30%H_2O at 1000^oC for 20h

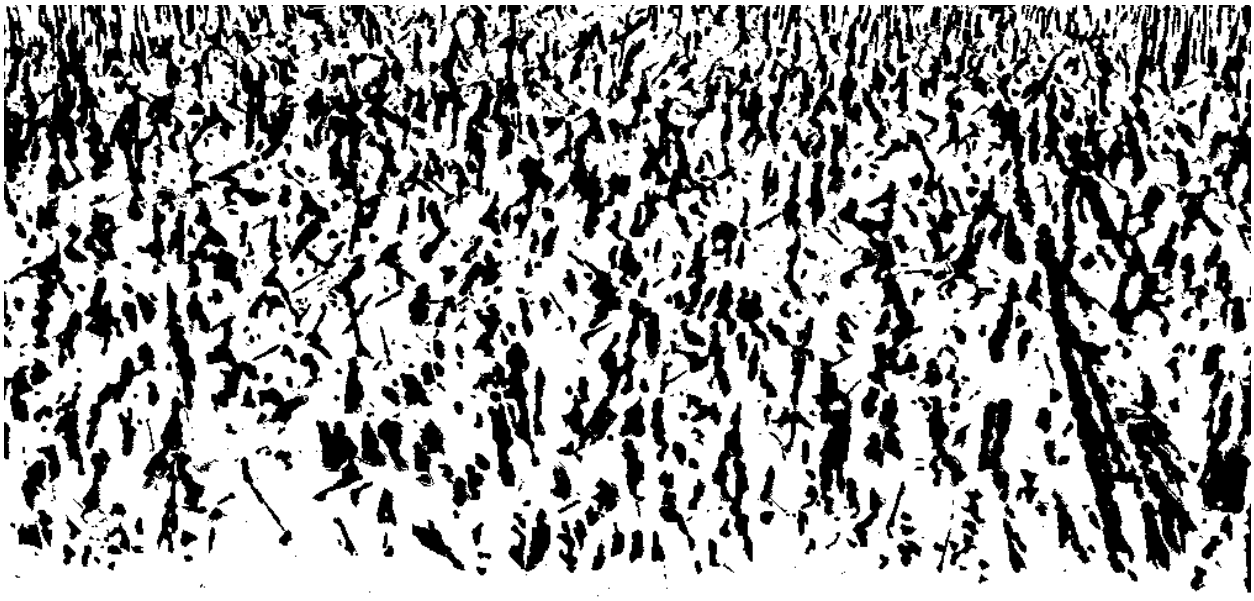

(a)

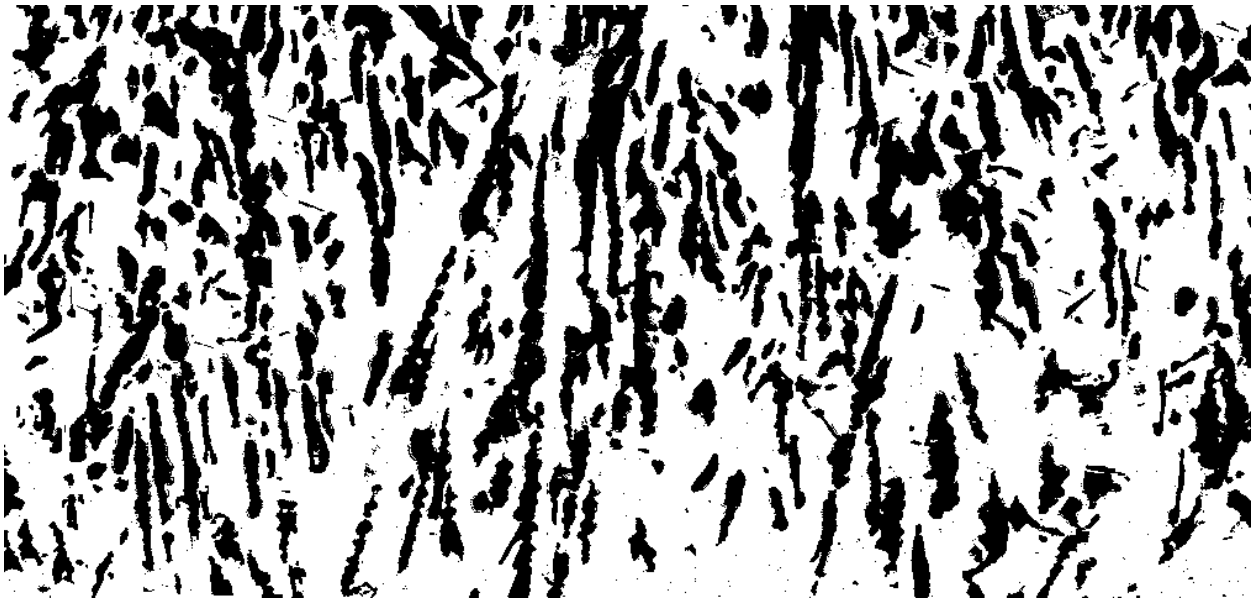

(b)

Figure 4.21 Digitized images from Figure 4.20 used to determine the area fraction of the internal oxidation precipitates

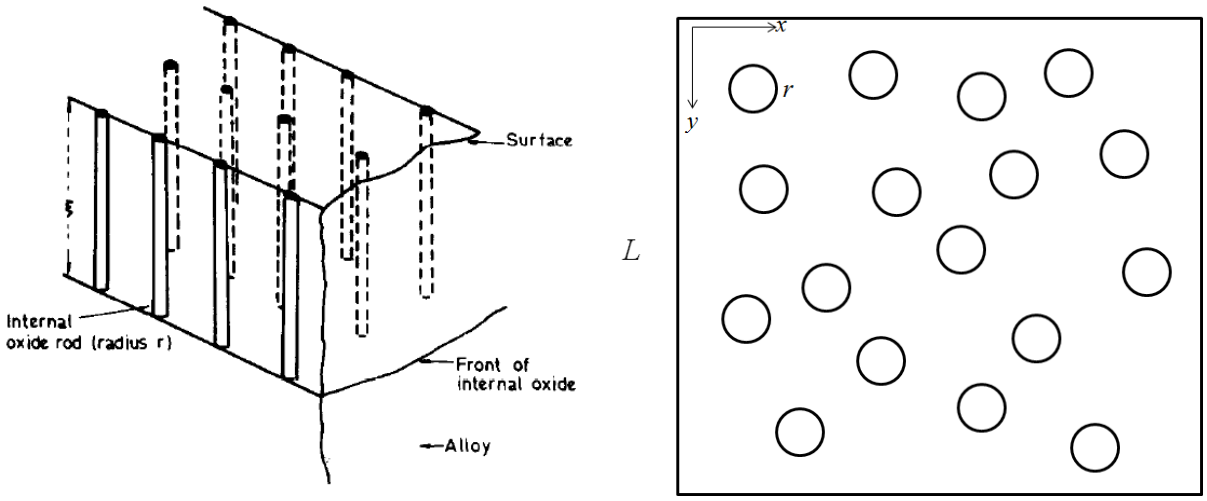

Figure 4.22 Schematic model to quantify the morphology of the internal oxidation precipitates. (a) 3D view[94] and (b) top view.

From the top view shown in Figure 4.22 (b) and if the distribution of the precipitates is completely random, the cross-sectional images should be equivalent in either the x or y directions. Therefore, if the number of precipitates on a line parallel to the x direction is *N*, this number should also be *N* along y direction. Thus, the total volume of precipitates for a unit thickness is:

$$V_p = N^2 \pi r^2 \tag{4.33}$$

Also, the total volume of the alloy for a unit thickness under the square shown in in Figure 4.22 (b) is:

$$V_{total} = L^2 \tag{4.34}$$

Therefore, the volume fraction of the precipitates is:

$$f_V = \frac{N^2 \pi r^2}{L^2} \tag{4.35}$$

where f_v is the volume fraction of the precipitates.

Based on the principles of quantitative microscopy[103], if the selection of cross-sectional images is completely "random", then the average area fraction on this cross-sectional image should be the same as the volume fraction, i.e.

$$\overline{A_A} = f_V \tag{4.36}$$

where $\overline{A_A}$ *i*s the average area fraction of precipitates. However, the definition of "random" selection is not straight-forward. It depends on the size, shape and distribution of the precipitates. In our case, the precipitates are rods extending from the original surface to the internal oxidation front. The cross-sectional images (Figure 4.21) contain a large amount of cross sections of this feature. Moreover, cross-sectional images taken at different positions on the same sample (Figure 4.23) show that the area fractions are statistically at the same level. This indicates that the "random" selection assumption is valid here. Therefore, the average area fractions measured from those images are taken to be equal to the volume fraction of the precipitates.

Substituting equation 4.36 into 4.35 yields:

$$r = \sqrt{\frac{\overline{A_A}}{\pi}} \cdot \frac{L}{N} \tag{4.37}$$

The average inter-precipitate distance *d* can be defined as:

$$d = \frac{L}{N} - 2r \tag{4.38}$$

Substituting equation 4.37 into 4.38, the inter-precipitate distance can be calculated by:

$$d = \left(1 - 2\sqrt{\frac{\overline{A_A}}{\pi}}\right)\frac{L}{N} \tag{4.39}$$

From equation 4.39, the inter-precipitate distance increases if *N* is decreased. Meanwhile, from the experimental observation shown in Table 4.1, despite the fact *N* changes at different

depths, it is clearly seen that the presence of steam significantly decreased the number of precipitates *N*. Table 4.2 shows the inter-precipitate distance for alloy #5 oxidized in dry air and air+30%H_2O at 1000°C for 20h. The inter-precipitate distances are significantly increased in the wet oxidizing conditions.

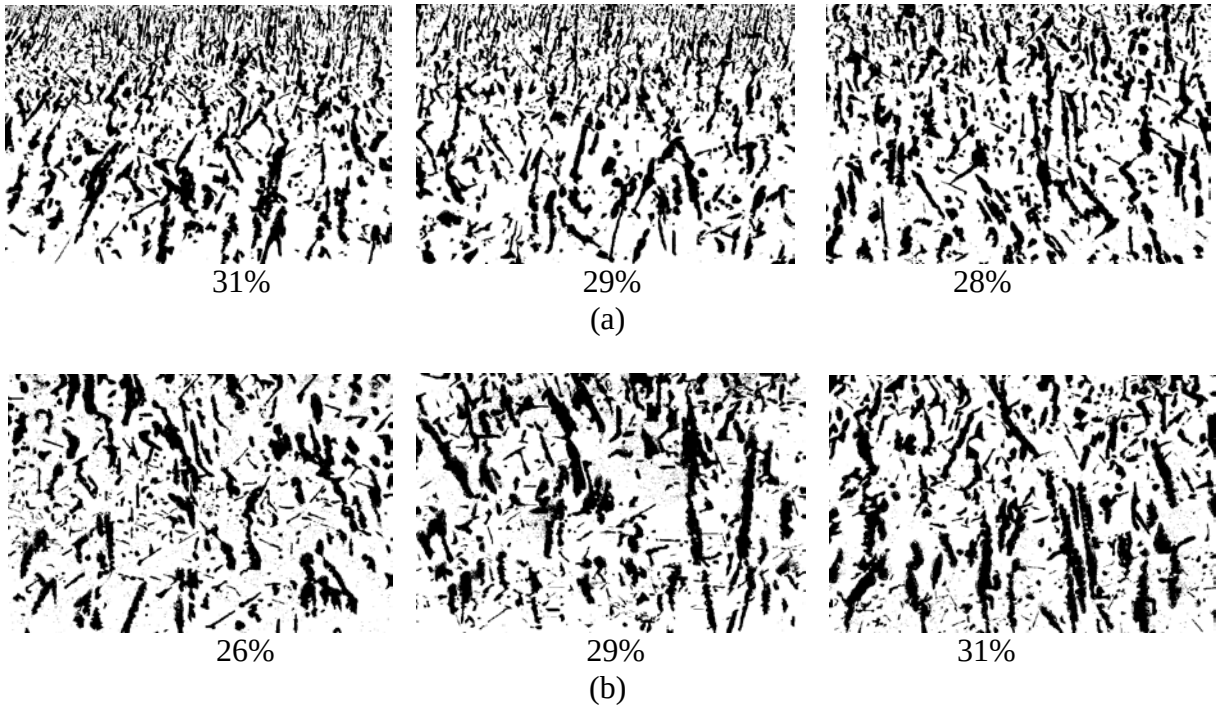

Figure 4.23 Digitized images of alloy #5 oxidized in (a) dry air and (b) air+30%H_2O at 1000°C for 20h. The numbers below the images are area fractions.

Table 4.2 Inter-precipitate distance for alloy #5 oxidized in dry air and air+30%H_2O at 1000°C for 20h

d (μm)	Top	Middle	Bottom
Dry Air	0.33	0.51	0.92
Air + 30% H_2O	0.92	1.2	1.7

In terms of the N_{Al}^*, greater inter-precipitate distance means that it is more difficult for the precipitates to grow laterally to form a continuous layer. In other words, for the rod-like precipitates formed in Al_2O_3-scale forming Ni-based alloys, it is the inter-precipitate distance

that actually dictates the transition from internal to external oxidation. This effect manifests itself as an increased critical volume fraction f_v^* in Wagner's theory for wet oxidizing conditions.

The reason for steam affecting the morphology of internal oxidation precipitates is not clear, but undoubtedly hydrogen is playing an important role. It has been found that hydrogen can diffuse rapidly into pure Ni at high temperatures[104]. Therefore, it is reasonable to expect that hydrogen can also diffuse rapidly into the Ni-based alloys considered in this study. There are several possible mechanisms for hydrogen to affect the internal oxidation behavior. For example, hydrogen can incorporate into the alloy as proton defects according to the reaction:

$$\frac{1}{2}H_2(g) + h^{\bullet} = H_i^{\bullet} \tag{4.40}$$

This may affect defect-related properties such as diffusion. Related to this, the hydrogen content may be at a sufficient level to be acting as a component, such that the thermodynamics of the system must be defined by Ni-Al-O-H equilibria rather than simply Ni-Al-O equilibria. This may have the effect of changing the diffusion path, which was shown in Figure 4.3, in a manner that the boundary conditions and, hence, driving force to form the oxides may be significantly changed. For example, N_o^S may be changed by the presence of hydrogen. Although this may not affect the N_{Al}^* directly, as shown in Figure 4.18 (b), it can change the oxygen concentration profile in the IOZ and thus affect the driving force for the internal oxide nucleation.

Another possibility is that hydrogen may segregate to the internal oxide/alloy interface. This, in turn, would lead to a different interfacial energy between the oxide and the alloy. Indeed, hydrogen segregation has been found in some metal/ceramic interfaces such as Ag/MgO[105,106], although these findings were limited to room temperature and 390˚C. Since the interface energy works as the barrier for nucleation, it could be inferred from the experimental observations that the Al_2O_3/alloy interfacial energy was increased in the presence of steam. By contrast, from a

strict thermodynamic point of view, the occurrence of hydrogen segregation to the interface would suggest a reduction of the interfacial energy. Thus, if the Al_2O_3/Ni interface favors hydrogen segregation at elevated temperatures, as may be indicated by the results reported for the Ag/MgO system, then it would be expected that internal oxidation is favored in the presence of hydrogen. However, such a result is a variance with what was found in this study. It is therefore inferred that the main reason for internal oxide nucleation being less favored in wet oxidizing conditions compared to dry oxidizing conditions is that hydrogen enters the system as a thermodynamic component which, in turn, acts to decrease the driving force for nucleation. This inference would require further validation, which is considered beyond the scope of the present study.

4.1.2 Surface instability of NiO scale in wet oxidizing conditions

4.1.2.1 Experimental observations

When the NiO-forming alloys were oxidized in wet oxidizing conditions, the surface of the NiO often became porous and non-uniform. Figure 4.24 shows two low-magnification images of the high-purity Ni oxidized isothermally in air+30%H_2O at 1000^{o}C for 98h. Some powders were formed on the surface and were poorly attached to the scale. During cooling, some powders invariably dropped into the container. A similar NiO formation behavior was recently reported by another research group[77].

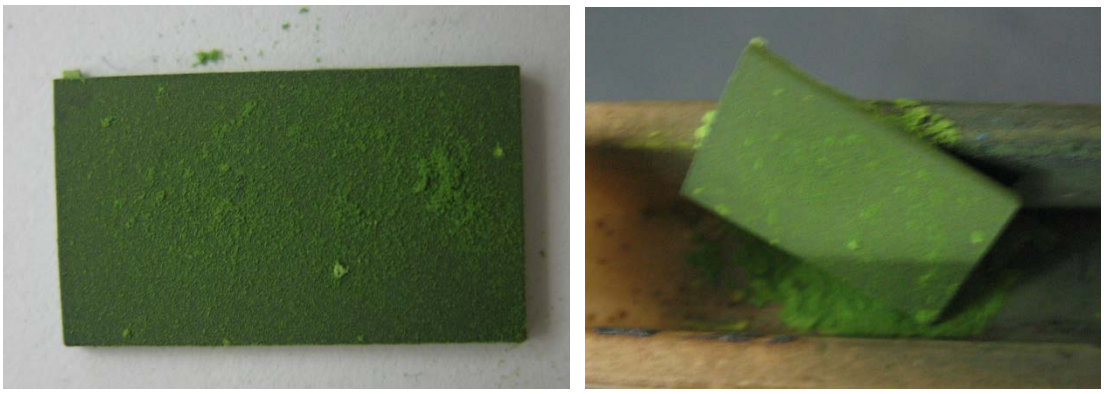

Figure 4.24 Photographs of powder formation on the surface of isothermal oxidized high purity Ni in air+30%H_2O at 1000^{o}C for 98h

To determine the condition for powder formation on the surface, tests were carried out on three different nickel samples of different purity levels: Ni 99.99%, Ni 99% and Ni200 (>98%). Oxidation was carried out at 1000^{o}C and 1100^{o}C in three steam levels of 6%, 20% and 30%. Figure 4.25 to Figure 4.27 show the surface morphology of samples oxidized in air+6%, +20% and +30% H_2O. Typically, when powders formed on the surface, the surface morphology was porous, which can be seen on samples oxidized in air+30%H_2O at 1000^{o}C shown in Figure 4.27. The samples shown in Figure 4.25 showed no porous morphology. The non-uniform structure formed on 99% Ni at 1000^{o}C might be related to an initial form of the porous structure, although no sign of powder could be found on this sample when analyzing using SEM. Therefore, the porous surface structure does not seem to form in air+6%H_2O. The samples oxidized at 1100^{o}C shown in Figure 4.26 show no porous structure either. By contrast, some fine and faceted particles can be found on the 99.99%Ni oxidized at 1000^{o}C. Meanwhile, some smaller particles were also formed on 99%Ni oxidized at 1000^{o}C. From the macroscope surface morphology, green powders were found on both of the samples. However, there was no porous structure formed on the Ni200 (>98%) oxidized at 1000^{o}C. In summary, (1) the porous structure starts to form in air+20%H_2O, (2) its formation of this structure is more apt to occur at a lower

temperature than at a higher temperature and (3) higher nickel purity appears to favor the formation of the porous structure. In Figure 4.27, no porous structure was formed on all samples oxidized at 1100^{o}C, similar to the observation in Figure 4.26. However, much more powders formed on samples oxidized at 1000^{o}C. In particular, the surface of Ni 99.99% was covered completely by such a porous structure. The trend that the formation of the porous structure is favored at lower temperature and higher purity level is also supported in these images. Besides this trend, it is clear that more powders were found after exposures to a higher steam content environment. However, even though the general trend for the formation of a non-uniform structure has been identified, the occurrence is not fully reproducible. Although the experimental conditions have been controlled to be the same for each test, there is no certainty of whether or how much powder can form on the sample. To precisely determine the condition for the surface non-uniformity to occur, even better control of the experimental conditions and better quality of samples may be required.

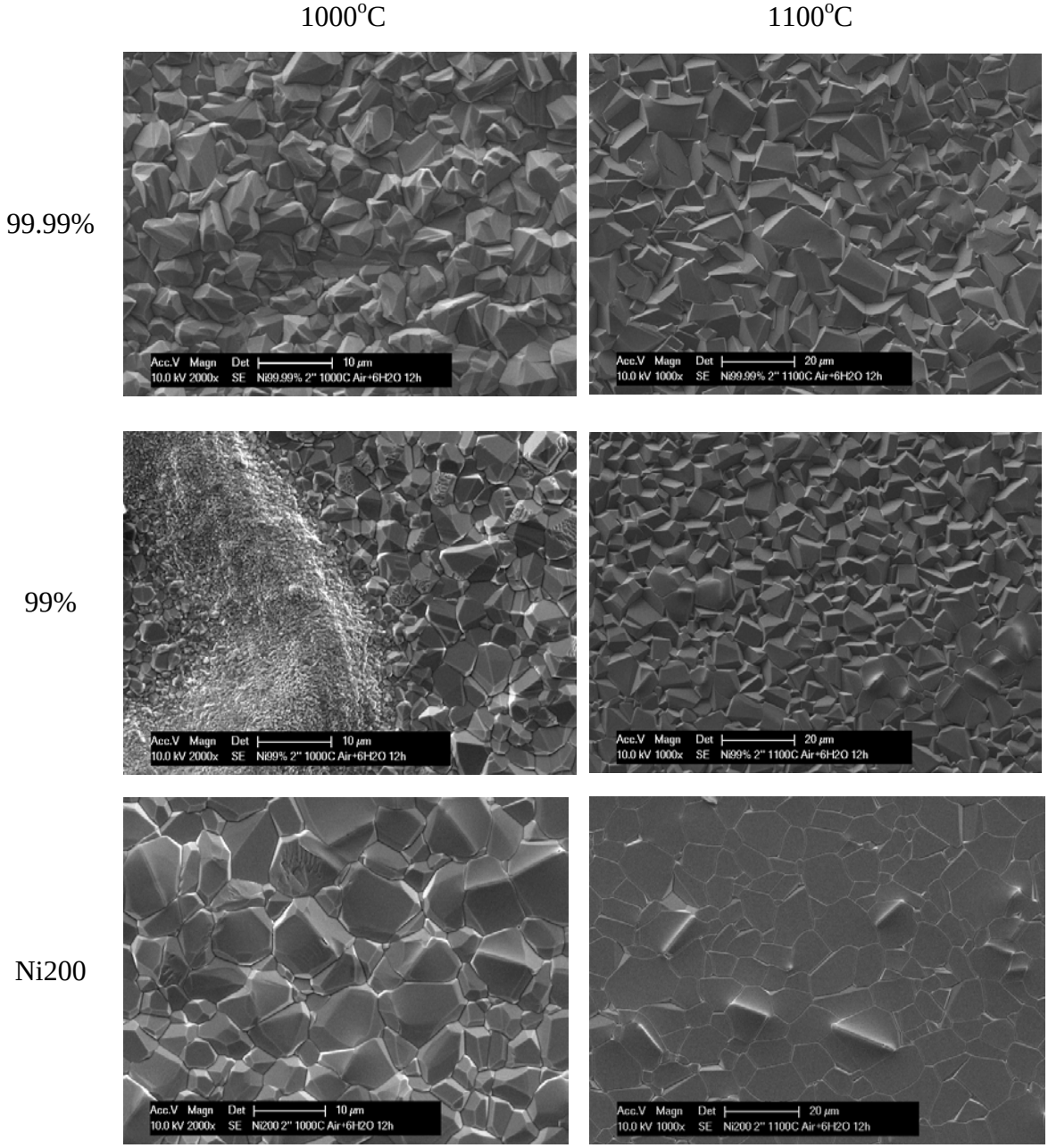

Figure 4.25 Surface morphology of samples oxidized in air+6%

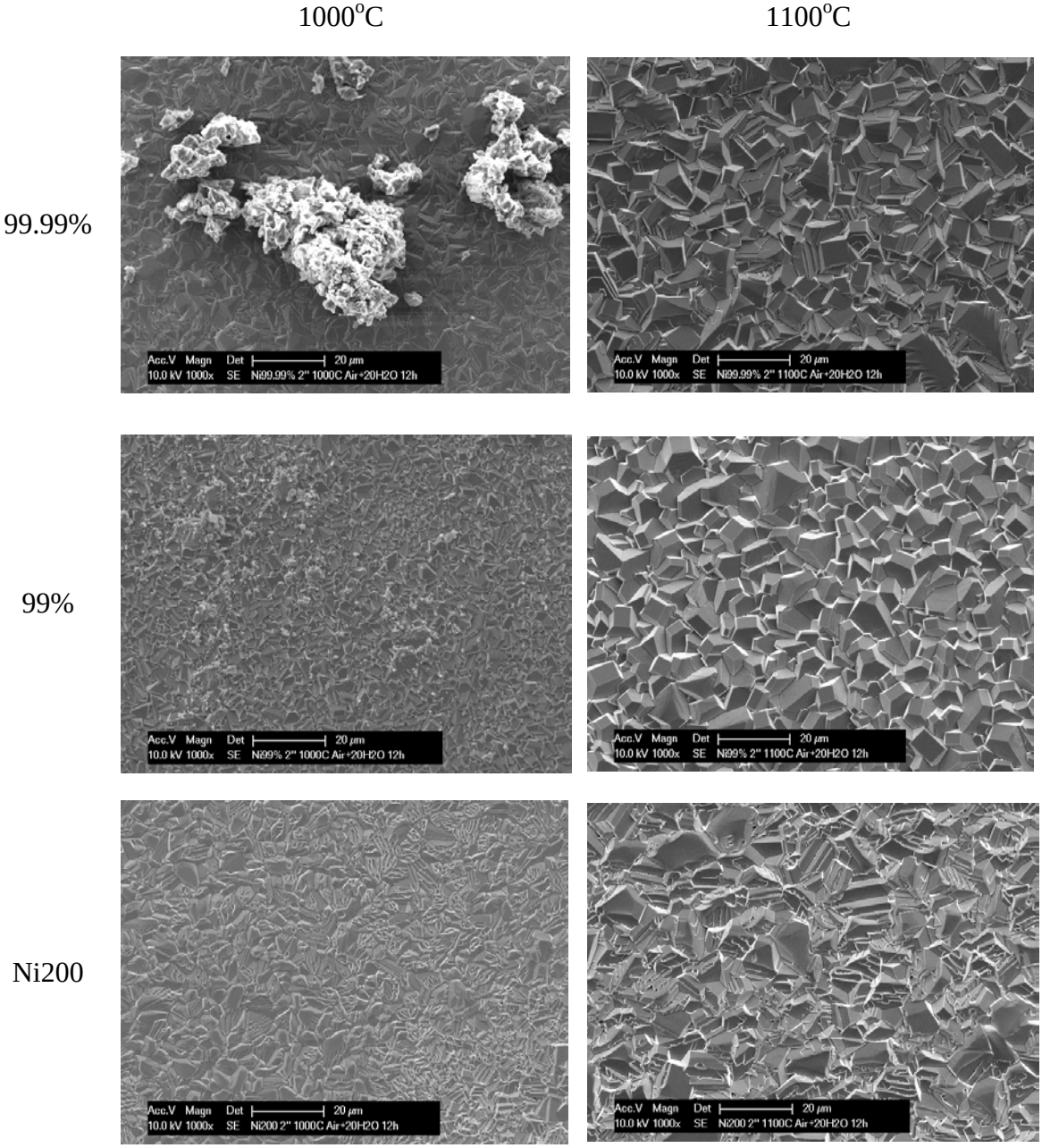

Figure 4.26 Surface morphology of samples oxidized in air+20%

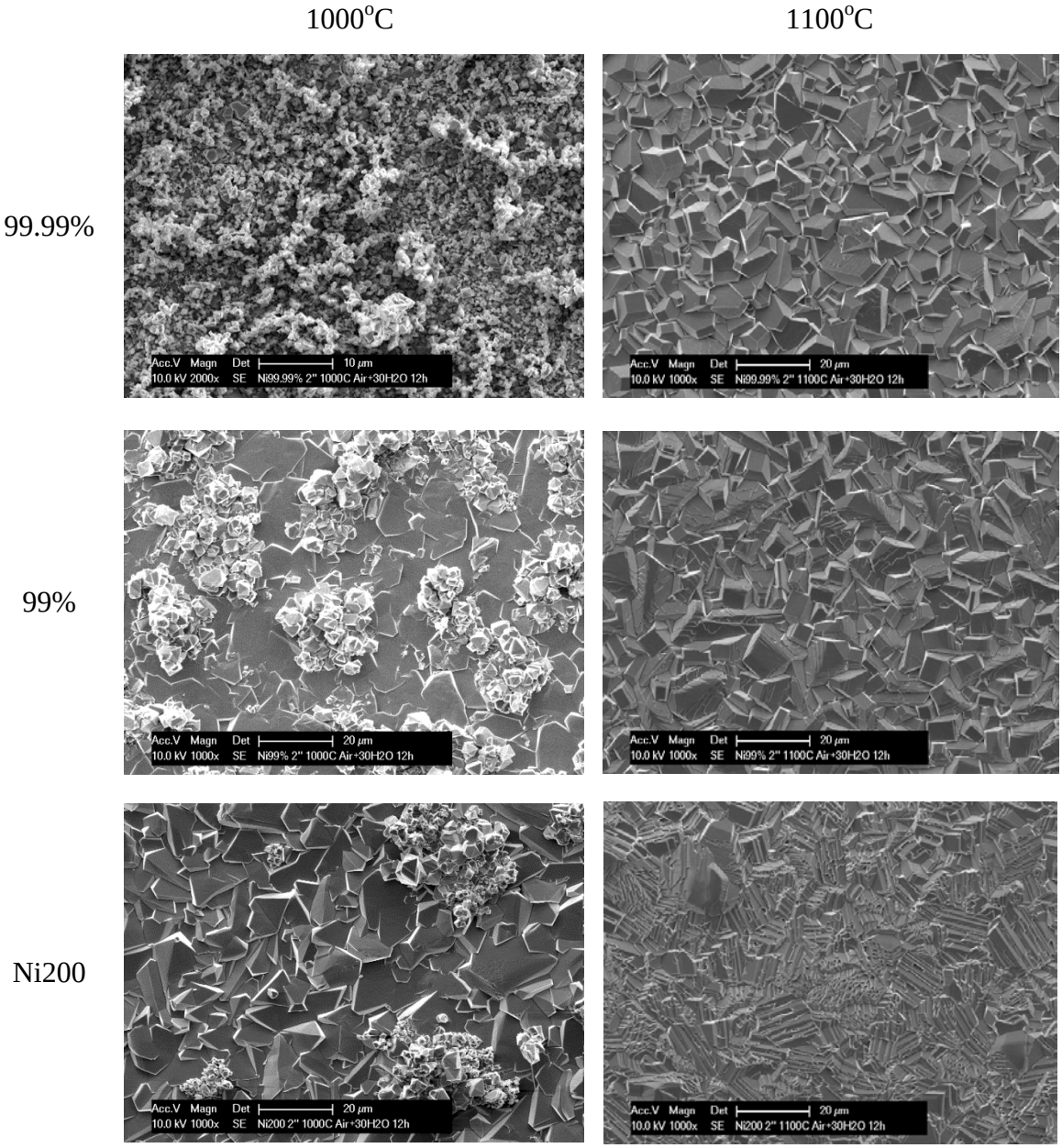

Figure 4.27 Surface morphology of samples oxidized in air+30%

The surface instability could also be found by oxidizing Ni-3at%Al in wet air, although this type of surface morphology was not exactly the same as the porous structure found on pure Ni. Figure 4.28 shows the cross-sectional images of Ni-3at%Al oxidizing in air with different steam content at 1000^{o}C. In no steam or air+10%H_2O environment, the surface was uniform and dense. However, the surface formed a less-dense, columnar structure (instability) if the sample was oxidized in air+30%H_2O. As shown in Figure 4.29, this less-dense, columnar structure was found to grow with increasing oxidation time. By increasing the oxidation time from 4 hours to 98 hours, the length of the columnar protrusions increased from ~8μm to ~40 μm. Similar to the case of the porous structure formed on pure Ni in air+30%H_2O at 1000^{o}C, this type of surface instability was not necessarily found on all samples oxidized under the same oxidation conditions.

The phase of the scale with the less-dense, columnar structure formed on Ni-3at%Al and the porous structure formed on pure Ni was identified to be NiO by standard X-ray diffraction. The XRD patterns for 99.99%Ni and Ni-3at%Al oxidized in air+30%H_2O at 1000^{o}C are shown in Figure 4.30. It is seen from the patterns that only NiO had formed. The XRD peaks marked by stars on the Ni-3at%Al oxidized for 1 hour were identified as Ni peaks, which were detected because the scale was thin and the X-ray beam had penetrated to the underlying Ni substrate. Therefore, during the oxidation, there was no species other than NiO that had formed. This result was confirmed by the EDS analysis. Further, by comparing the XRD patterns for Ni-3at%Al oxidized for 1 hour (fig. 4.29 c) and 98 hours (fig. 4.29 b), the relative intensities of the peaks were changed. Initially, the {220} peak predominates, while with increasing oxidation time, the {200} peak predominates. The change in the relative intensity indicates that there was a change in the preferred growth from {220} to {200} during the course of oxidation. The XRD patterns

for Ni 99.99% and Ni-3at%Al oxidized in dry air at 1000°C are shown in Figure 4.31. It is seen that the {200} peak predominates on both of the samples oxidized for 98 hours. This orientation is similar to the one found on the NiO scale formed on Ni-3at%Al after exposure in air+30%H_2O for 1 hour at 1000°C shown in Figure 4.30 (c). For the Ni-3at%Al oxidized in dry air, the relative intensities were not changed significantly going from 1 hour to 98 hours.

To confirm the change in preferred growth orientation of the outermost columnar grains of NiO formed in air+30%H_2O, the sample of Ni-3at%Al oxidized in air+30%H_2O at 1000°C for 98 hours was polished in a sequential manner. Each polishing step removed around 10μm of scale and at each step a XRD pattern was obtained. Figure 4.32 shows the XRD patterns obtained from this procedure. The patterns were scaled in the way that the intensity for {200} peaks are normalized to a hundred. The numbers near the {220} peaks indicate the relative intensity of this peak, which is marked by the arrow. The labels on the side of each spectrum indicate how much material was polished off from the surface and the image on the right shows the estimated positions within the scale from which the XRD spectra were collected. It is seen that the relative intensity for {220} peak increases with increasing amount of scale removed. This result confirms that the NiO scale formed in air+30%H_2O at 1000°C on Ni-3at%Al preferred the growth of {220} planes initially, and then switched to a {200} growth preference afterwards.

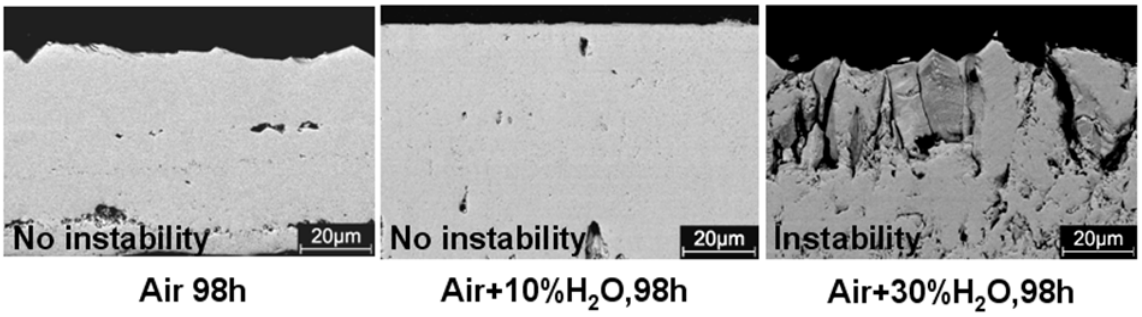

Figure 4.28 Surface morphology and instability formed on Ni-3at%Al oxidized at 1000°C

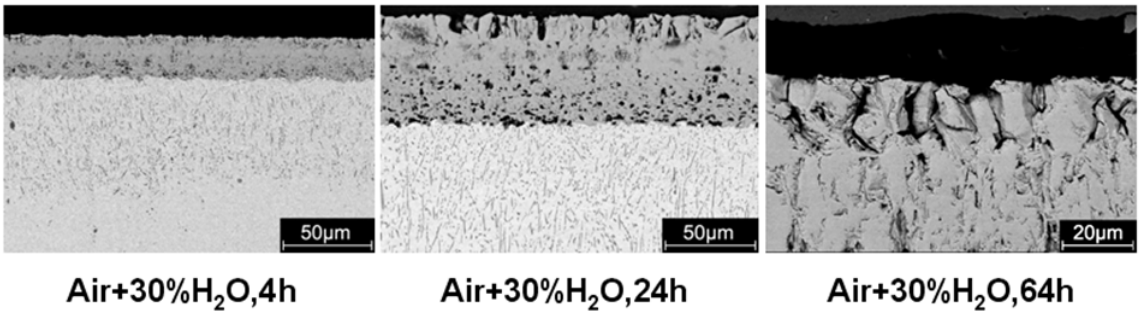

Figure 4.29 Surface instability formed on Ni-3at%Al oxidized at 1000oC for a series of time

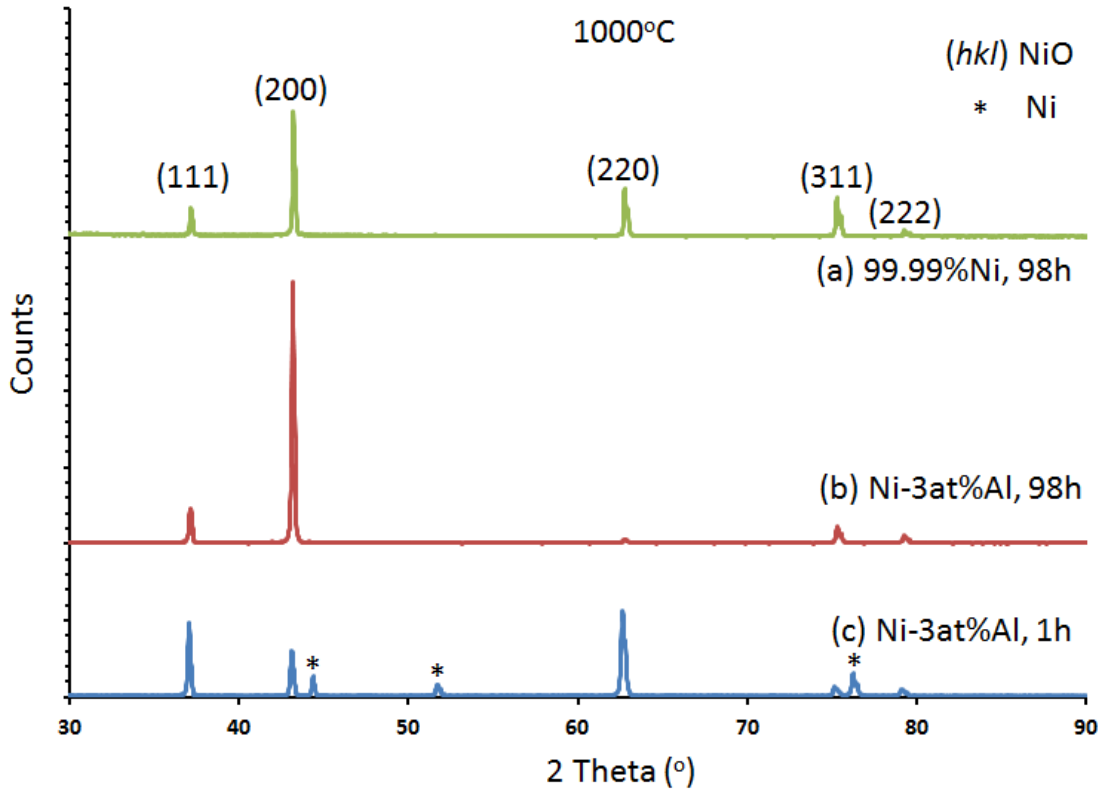

Figure 4.30 XRD patterns for samples oxidized in air+30%H_2O at 1000°C

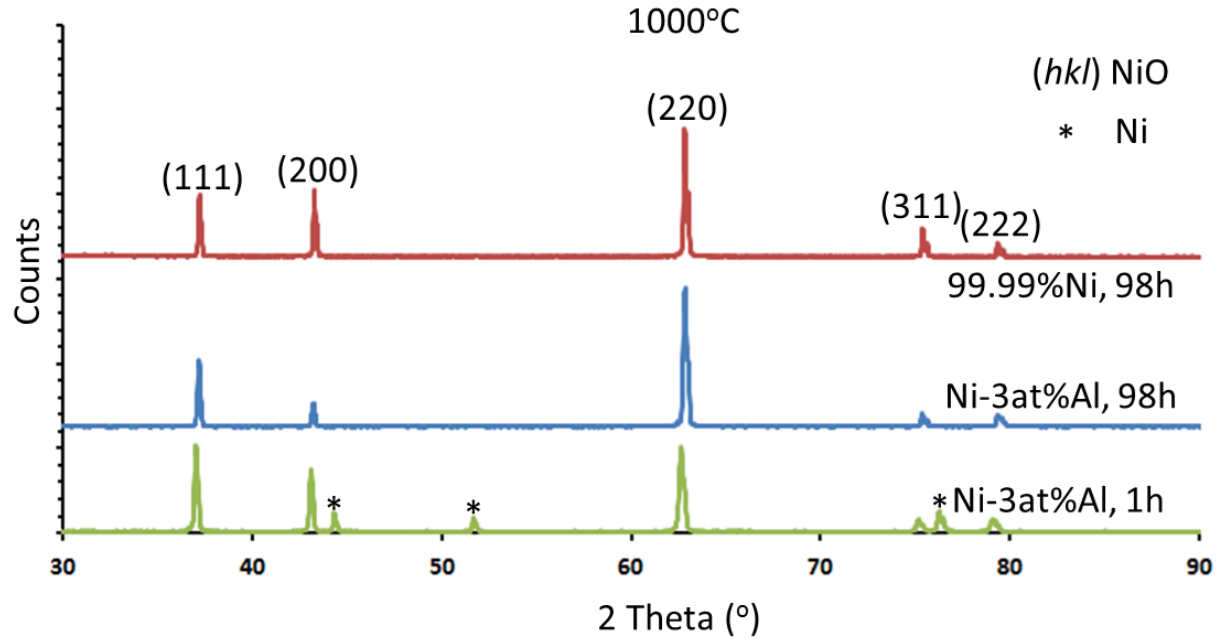

Figure 4.31 XRD patterns for samples oxidized in dry air at 1000°C

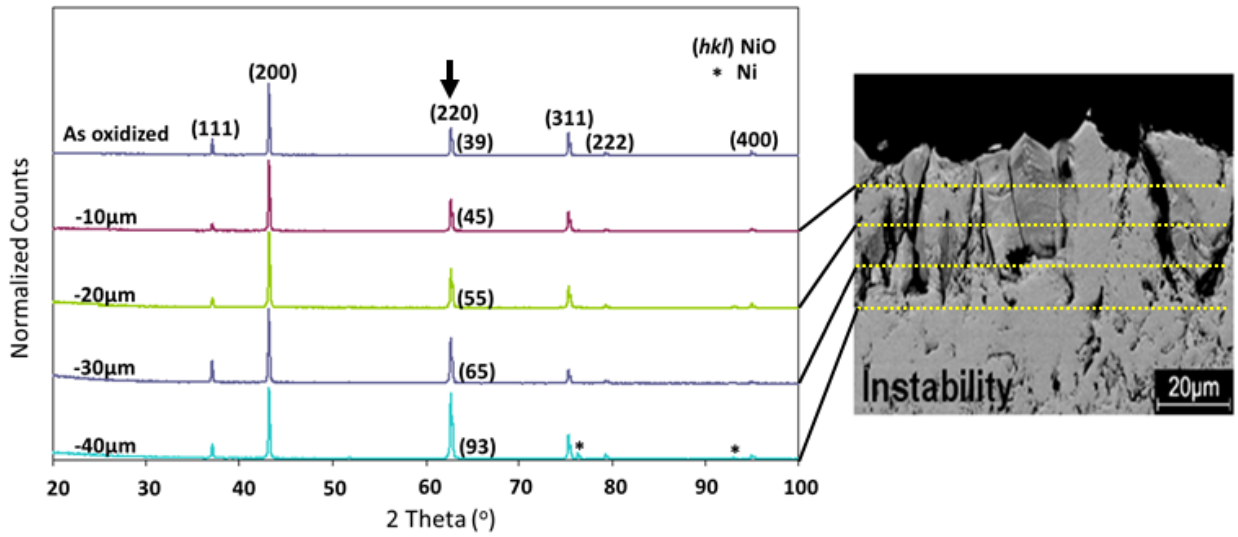

Figure 4.32 XRD patterns for a sample oxidized in air+30%H_2O at 1000°C for 98h and had been polishing off a series of thickness from the surface. The labels on the left-hand side of each curve indicate the depth of NiO scale polished off from the surface

4.1.2.2 Discussion on the mechanisms to form the surface instability

The porous structure of NiO formed on pure Ni and the less-dense columnar grains formed on Ni-3at%Al oxidized in wet oxidizing conditions at 1000^{o}C are very likely related. They both formed under high steam content (air+30%H_2O) and they only formed on the surface of the NiO scale. It is inferred that they both require direct contact with high steam content. Occasionally, a friable the porous structure would form at NiO surface during oxidation of Ni-3at%Al in air+30%H_2O. Due to the difficulty in reproducing the same result for each test, it is not yet possible to define the specific conditions that favor the growth of one morphology over another. Instead, several mechanisms to account for the formation of both surface instabilities (i.e. fine columnar or porous) are proposed based on the experimental observations.

The first possibility stems from the general issue that several metal oxides form volatile compounds by direct reaction with steam[41]. Indeed, the partial pressure of $Ni(OH)_2(g)$ produced in air+30%H_2O can be fairly high, to the extent that the evaporation of NiO cannot be neglected[107]. Therefore, the porous structure and gaps formed between the columnar grains might be due to the evaporation of $Ni(OH)_2(g)$.

The second possibility is based on the experimental observations from XRD patterns. The change in the preferred growth orientation found by XRD patterns in wet oxidizing conditions is schematically shown in Figure 4.33. Initially, the growth of grains with {200} planes parallel to the surface predominates, while after a certain time, the growth of the grains with {220} orientation parallel to the surface become predominant. For reasons that are not clear, steam apparently promote the growth of {220} orientation and inhibits the growth on all other planes. As a result, the surface may become faceted with only {220} orientations on the surface or the lateral growth of the columnar grains is so slow that the surface becomes less-dense.

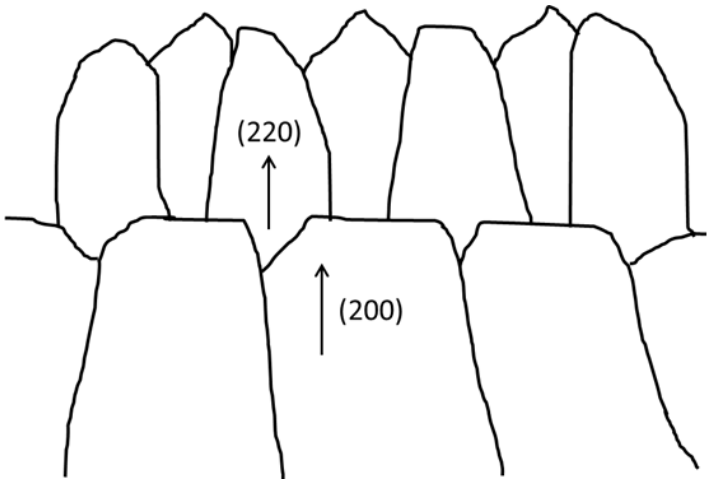

Figure 4.33 Schematic of changed preferred growth orientation in NiO formed on Ni-3at%Al oxidized in air+30%H_2O

The third possibility is based on the experimental observations that the surface instability tends to form at lower temperature (1000^{o}C). As shown by Figure 4.10, the diffusion mechanism in NiO is on the borderline to be controlled by lattice diffusion or by grain-boundary diffusion. Therefore, it is possible that steam (or maybe hydrogen) enhanced the grain-boundary diffusion of nickel in NiO to a large extent, so that much greater/faster growth of NiO occurred above those faster-diffusion paths, leading to the appearance of a surface instability.

In summary, the possible mechanisms to account for the formation of surface instabilities are:

1) enhanced evaporation of Ni-containing species
2) preferred growth along certain grain orientation
3) enhanced nickel diffusion along NiO grain boundaries.

To verify each possible mechanism, corresponding experiment and analysis were carried out.

Assessment of the enhanced evaporation of Ni-containing species

The evaporation rate of $Ni(OH)_2(g)$ can be estimated from the kinetics of gas-phase transport. Specifically, the flux of the evaporating species can be calculated by the mass-transfer

coefficient and the partial pressure of that species. The equilibrium partial pressures of volatile $Ni(OH)_2(g)$ can be calculated by the change of Gibbs free energy to form that species as well as the gas composition. The reaction to form volatile $Ni(OH)_{2\,(g)}$ species is:

$$NiO + H_2O_{(g)} = Ni(OH)_{2(g)} \tag{4.41}$$

The equilibrium constant $K_{4.41}$ for this reaction is given by:

$$K_{4.41} = \exp(-\frac{\Delta G_{4.41}}{RT}) \tag{4.42}$$

where $\Delta G_{4.41}$ is the Gibbs free energy change for the reaction 4.41 at the reaction temperature and it is determined from the Gibbs free energy of formation of the reactants and products as:

$$\Delta G_{4.41} = \Delta G_{f,Ni(OH)_2} - \Delta G_{f,NiO} - \Delta G_{f,H_2O(g)} \tag{4.43}$$

Further, and in accordance with the law of mass action,

$$K_{4.41} = \frac{P_{Ni(OH)_2}}{P_{H_2O}} \tag{4.44}$$

Here, the activity of the solid reactant (NiO) is assumed to be unity. Therefore, the equilibrium partial pressure of $Ni(OH)_{2\,(g)}$ is

$$P_{Ni(OH)_2} = P_{H_2O} \times \exp(-\frac{\Delta G_{f,Ni(OH)_2} - \Delta G_{f,NiO} - \Delta G_{f,H_2O(g)}}{RT}) \tag{4.45}$$

Thermodynamic data for those species can be obtained from the HSC Chemistry software database.

Figure 4.34 shows the equilibrium partial pressure of $Ni(OH)_2(g)$ as a function of temperature. Also included in this figure is variation in $P_{Ni(OH)}$ as a function of temperature. Table 4.1 compares the partial pressures of Ni(OH)(g) and $Ni(OH)_2(g)$ to those of the Al-containing species at 800°C-1200°C. It is seen that the most volatile species for Ni is $Ni(OH)_{2\,(g)}$ in wet air at 1000°C.

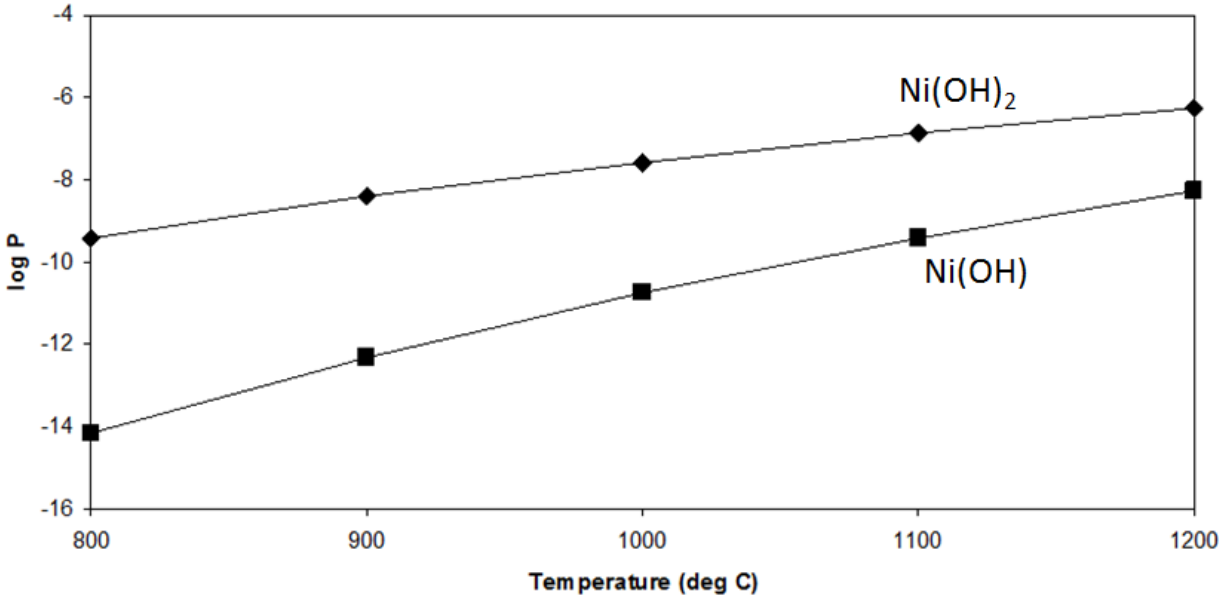

Figure 4.34 Vapor pressure of volatile Ni-containing species

Table 4.3 Partial Pressure of Ni and Al species in air+10% steam

Temperature (°C)	Partial Pressure (atm)					
	NiOH	$Ni(OH)_2$	AlO(OH)	AlOH	$Al(OH)_2$	$Al(OH)_3$
800	6.64×10^{-15}	3.90×10^{-10}	1.08×10^{-18}	8.35×10^{-29}	3.54×10^{-23}	1.05×10^{-11}
900	4.81×10^{-13}	3.81×10^{-9}	1.17×10^{-16}	1.26×10^{-25}	8.05×10^{-21}	6.47×10^{-11}
1000	1.76×10^{-11}	2.61×10^{-8}	6.04×10^{-15}	5.95×10^{-23}	7.76×10^{-19}	3.01×10^{-10}
1100	3.82×10^{-10}	1.35×10^{-7}	1.74×10^{-13}	1.13×10^{-20}	3.83×10^{-17}	1.13×10^{-9}
1200	5.41×10^{-9}	5.59×10^{-7}	3.14×10^{-12}	1.05×10^{-18}	1.11×10^{-15}	3.52×10^{-9}

When the reaction gas is assumed to flow slowly past the flat surfaces of oxidizing samples at atmospheric pressure, the resulting mass-transfer rate is calculated from gas transport theory in the viscous flow regime[41,108]. The molar flux, J, in a unit of mol/cm^{2}sec of a species is given by:

$$J = \frac{k_m}{RT}(P^i - P^o) \tag{4.46}$$

where k_m is the mass-transfer coefficient and P^i and P^o are the partial pressures of the gas species at the solid surface and in the bulk-gas, respectively. R is the gas constant and T the temperature in a unit of Kelvin. Generally, P^o is assumed to be zero to estimate the maximum mass flow.

The mass-transfer coefficient k_m is given by:

$$k_m = 0.664(\frac{D_{AB}^4}{\nu})^{\frac{1}{6}}(\frac{v_{gas}}{l})^{\frac{1}{2}} \tag{4.47}$$

where D_{AB} is the binary gas diffusion coefficient and ν the kinematic viscosity, v_{gas} the bulk-gas linear velocity and l the sample length along the flow direction. The binary gas diffusion coefficient D_{AB} can be calculated by Chapman-Enskog description:

$$D_{AB} = \frac{1.858\times10^{-3}\sqrt{T^3(1/M_A + 1/M_B)}}{P\sigma_{AB}^2\Omega_{D,AB}} \tag{4.48}$$

where M_i is molecular weight, P the total pressure and σ_{AB} the collision diameters of two gaseous species. $\Omega_{D,AB}$ is called collision integral, and the values are tabulated[108] as functions of kT/ε_{AB}, where k is Boltzmann's constant and ε_{AB} the characteristic energy of interaction between two molecules. The values of σ and ε vary with species and typical values for σ and ε/k are several angstroms and several hundreds, respectively. For two interacting molecules, the σ and ε can be calculated from:

$$\sigma_{AB} = \frac{\sigma_A + \sigma_B}{2} \tag{4.49}$$

$$\frac{\varepsilon_{AB}}{k} = \left(\frac{\varepsilon_A}{k} \cdot \frac{\varepsilon_B}{k} \right)^{1/2} \tag{4.50}$$

The kinematic viscosity v in equation 4.47 is given by

$$\nu = \eta / \rho \tag{4.51}$$

where ρ is the gas density in the unit of g/cm^3 and η is the viscosity of a gas mixture which is calculated from:

$$\eta_{mix} = \frac{\sum X_i \eta_i (M_i)^{1/2}}{\sum X_i (M_i)^{1/2}} \tag{4.52}$$

where X_i are mole fractions and η_i is given by

$$\eta_i = \frac{2.6693 \times 10^{-5} \sqrt{M_i T}}{{\sigma_i}^2 \Omega_i} \tag{4.53}$$

For equation 4.47 to reflect the real situation, the Schmidt number, which is defined as the ratio of kinematic viscosity to diffusion coefficient, Sc=ν/D, is required to be $0.6 \leq Sc \leq 50$.

Table 4.4 shows some key parameters for the calculation and the calculated evaporation rate of NiO as a function of temperature. From this table, the evaporation rate of NiO in air+30%H_2O at 1000^{o}C is 6.8x10^{-11}g/cm^{2}sec. For a 98-hour test, it corresponds to an NiO thickness loss of 3.6x10^{-3}μm. From the experimental observation shown in Figure 4.28, the affected thickness of NiO formed on Ni-3at%Al is around 40μm, which is three orders of magnitude higher than 3.6x10^{-3}μm due to evaporation. Therefore, the amount of NiO loss due to evaporation is negligible from a practical standpoint and it is concluded that the evaporation of $Ni(OH)_2(g)$ is not the reason for the surface instability formed in this condition.

Table 4.4 Calculated the loss of NiO as a function of temperature in air+30%H_2O

T (^oC)	$\Delta G_{4.41}$ (kJ)	P_{H2O} (atm)	$P_{Ni(OH)2}$ (atm)	v_{gas} cm/s	ρ_{air}	k_m	J_{NIO} g/cm^{2}sec
800	172.7461	0.3	1.17E-9	0.42	0.000353	0.100816	1.00E-13
900	166.6006	0.3	1.14E-08	0.42	0.000323	0.110945	9.85E-13
1000	160.4445	0.3	7.83E-08	0.42	0.000297	0.121038	6.78E-12
1100	154.2842	0.3	4.05E-07	0.42	0.000276	0.131083	3.52E-11

Assessment of the preferred growth along certain grain orientation

The evolution of grain structure in NiO scale formed in dry air was studied by Atkinson[84]. Figure 4.35 shows a schematic diagram of typical grain structure of NiO scale formed in dry air. A columnar structure tends to form with increasing scale thickness. In his study, the {220} orientation was found to be favored in NiO scale formed in dry air at 1000^{o}C, which agrees with the present experimental observation found by XRD analysis. Tinker[109] proposed a mechanism to account for the growth of such a columnar structure. When the oxide is forming relatively fast in the initial stage, the nucleation rate is high. As the oxide thickness increases, the nucleation rate at the oxide surface decreases (Figure 4.36). This can probably best be understood as a kinetic effect. As a result, the existing grains grow by extension of their lattices at the outer surface. Thus the grains are columnar. As this condition is approached, the grains become increasingly columnar although new grains may occasionally be nucleated. Texture tends to develop either because certain grain orientations have faces with relatively low energies or because those faces grow faster. Based on this mechanism, if the presence of steam can reduce the surface energy or increase the growth rate of {220} planes significantly, and at the same time inhibit the lateral growth of columnar grains to the extent that they cannot become continuous, the less-dense columnar structure can form on the surface.

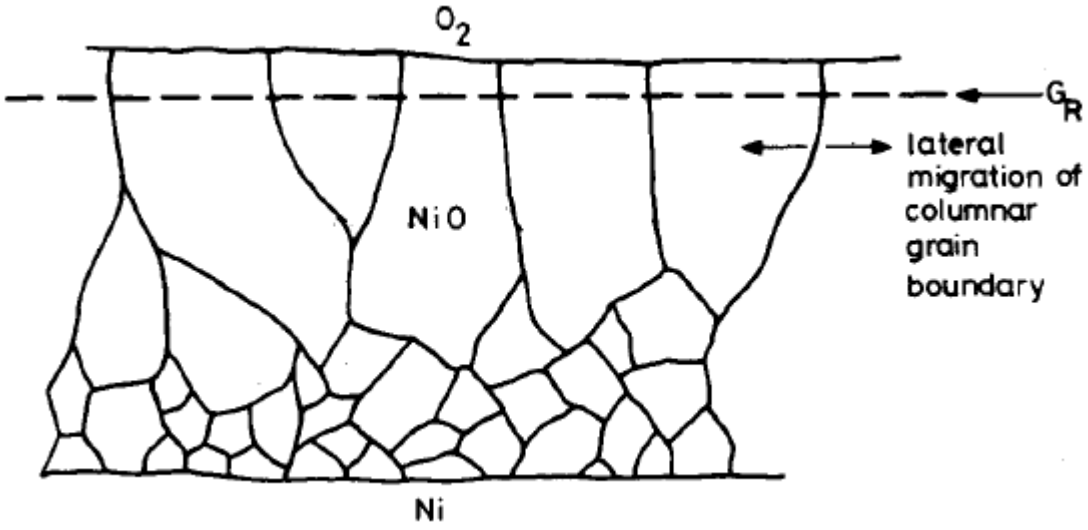

Figure 4.35 Schematic diagram of typical grain structure of NiO scale formed in dry air[84]

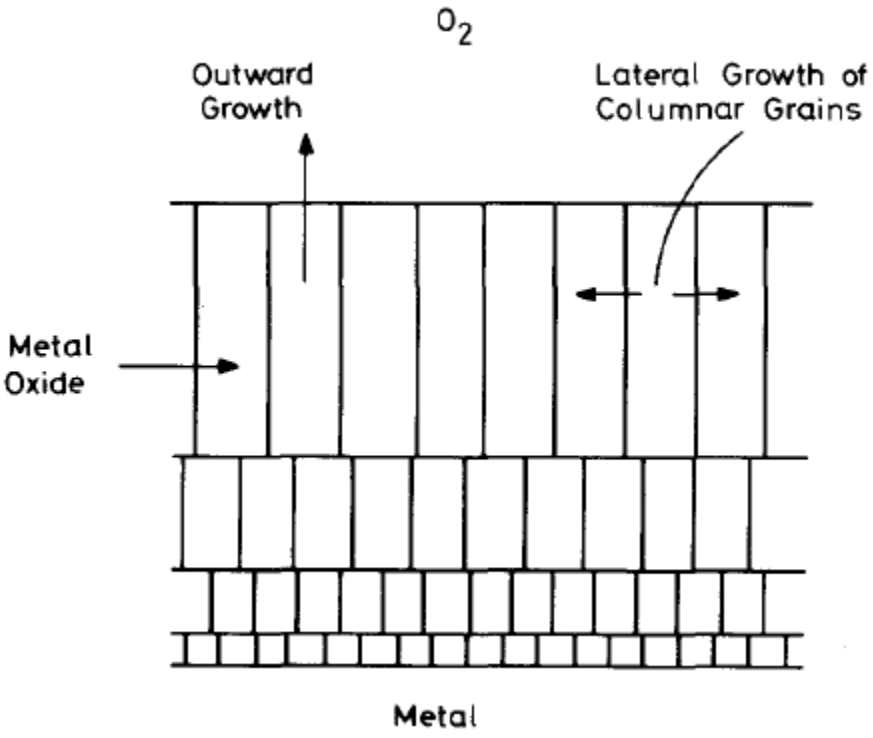

Figure 4.36 Columnar scale structure formed due to decreased nucleation rate[109]

To confirm the grain orientations and to determine more features of the grain orientation, EBSD mapping under SEM observation was employed. The cross-sections of the NiO scale formed in Ni-3at%Al oxidized in dry air and air+30%H_2O at 1000^oC for 98 hours were cut by focused ion beam (FIB) milling. However, due to severe spallation of NiO formed in dry air, it was practically impossible to obtain a complete through-thickness section of NiO. Therefore, only around the top 30μm of the NiO scale formed in dry air was assessed. Figure 4.37 shows the cross-sectional SEM image (a) and the corresponding EBSD map (b) for the top 30μm of the NiO scale formed in dry air. Since the sample was tilted, the SEM image is shown to illustrate the sample orientation in the chamber. The arrow next to the figure shows the growth direction of the scale. Figure 4.38 shows the cross-sectional SEM image (a) and the corresponding EBSD map (b) for the NiO scale formed in air+30%H_2O. It is seen that the grains formed in air+30%H_2O are much finer than those formed in dry air. The shape of the grains near the surface is columnar in air+30%H_2O; while it is comparatively equiaxed in dry air. Figure 4.29 shows the columnar grain structure near the top of the NiO scale formed in air+30%H_2O and its corresponding (001) pole figure. If there is a preferred growth direction, the pole figure should show a feature of zone axis. However, no feature is evident in figure 4.28 (b). It is worthwhile to note that the data points are probably too few to have a statistical result because of the preferred growth orientation. However, taking more EBSD images requires much more dedicated effort that was not feasible for this study nor clearly warranted. Therefore, no solid conclusion on steam affecting on the preferred growth in certain grain orientations can be clearly drawn.

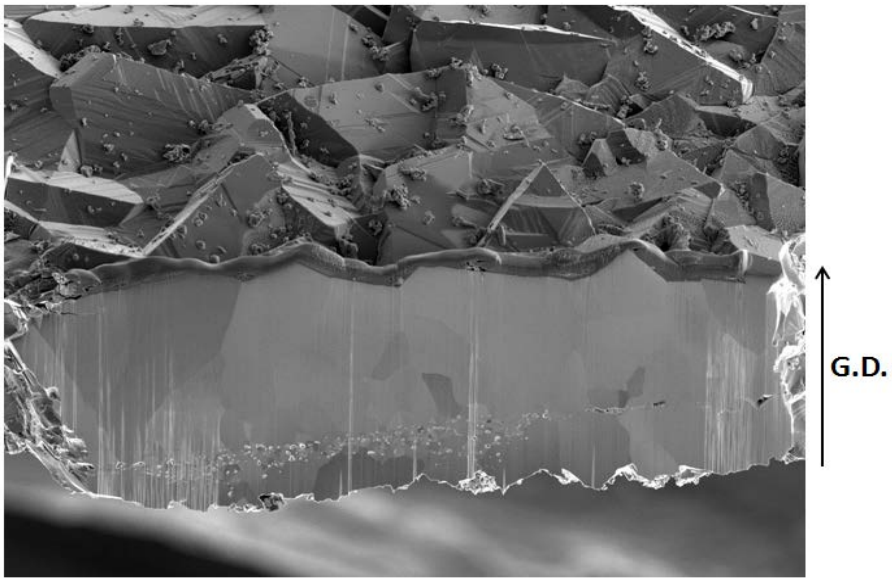

(a)

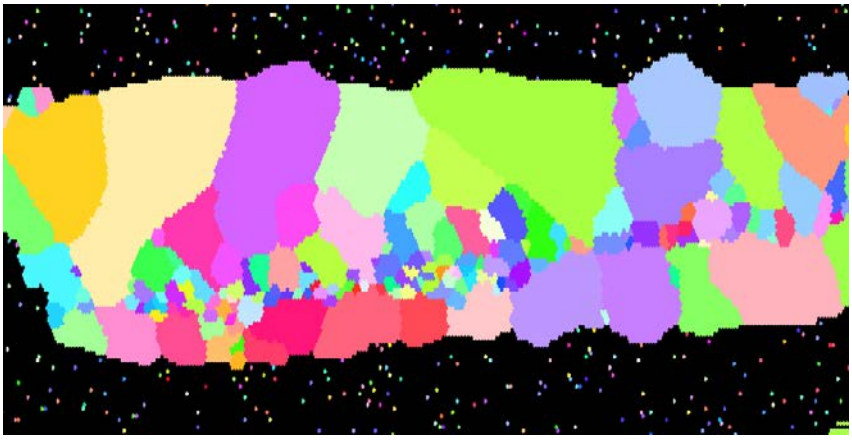

(b)

Figure 4.37 The cross-sectional SEM image (a) and the corresponding EBSD map (b) for the top 30μm of the NiO scale formed in dry air. Since the sample was tilted, the SEM image is shown to illustrate the orientation of the samples in the chamber. The arrow shows the growth direction of the scale

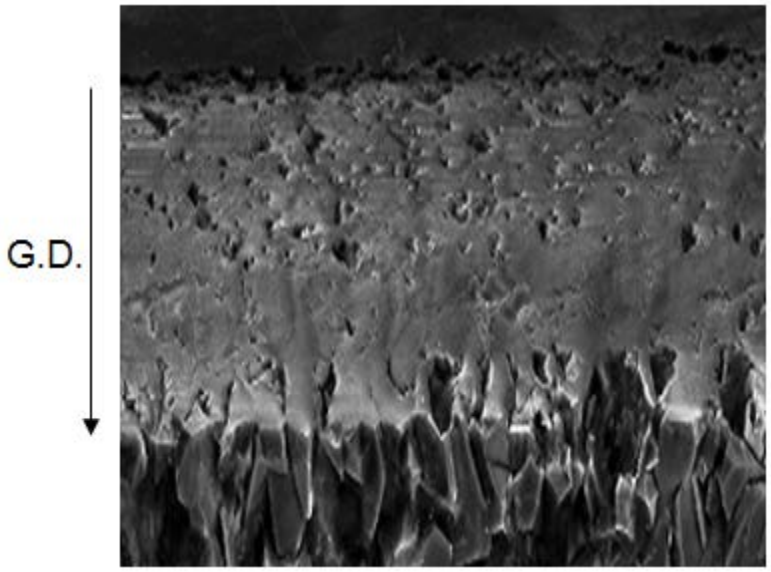

(a)

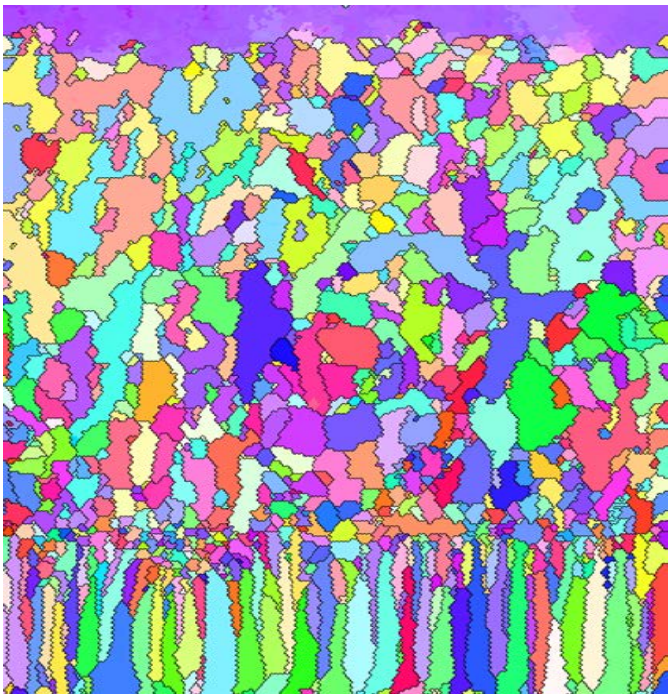

(b)

Figure 4.38 The cross-sectional SEM image (a) and the corresponding EBSD map (b) for the NiO scale formed in air+30%H_2O. Since the sample was tilted, the SEM image is shown to illustrate the orientation of the samples in the chamber. The arrow shows the growth direction of the scale

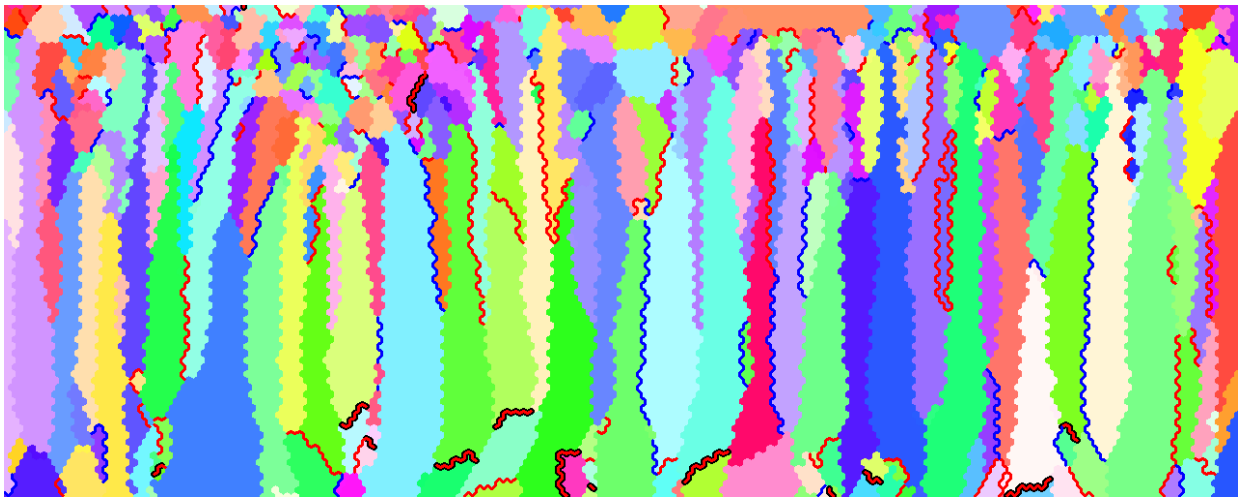

(a)

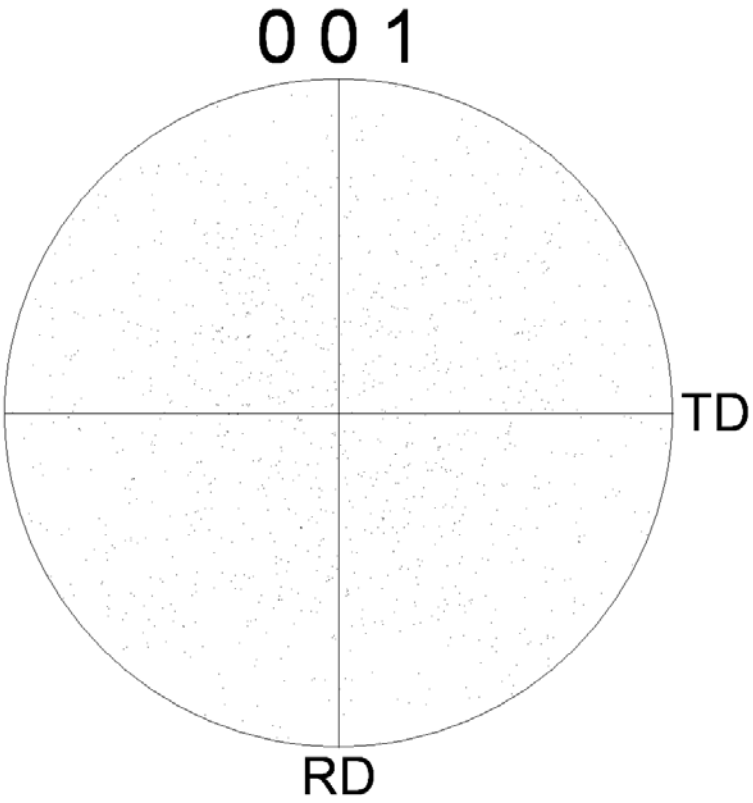

(b)

Figure 4.39 The columnar grain structure near the surface of the NiO scale formed in air+30%H_2O (a) and its corresponding (001) pole figure (b)

Assessment of enhanced diffusion through short-circuit paths

From the experimental observations of Auchi *et al.*[77], no surface instability could be observed by heating a pure NiO foil in air+30%H_2O environment. This result implies that the surface instability requires the outward diffusion of Ni to occur. Meanwhile, based on the experimental observation that the surface instability has never been found at 1100^oC and the Ni outward diffusion is clearly dominated by lattice diffusion at this temperature, it is deduced that the diffusion of Ni through short-circuit paths is involved for the formation of surface instability. Haugsrud[83] has reported that the outward diffusion of Ni through the lattice diffusion and through short-circuit paths in NiO formed in dry air at 1000^oC are at the same magnitude. This may explain the poor reproducibility of the instability, as the instability may only occur when diffusion through short-circuit paths is relatively more important. A comparison of Figure 4.37 to Figure 4.38 clearly shows that there are more grain boundaries in NiO scale formed in air+30%H_2O at 1000^oC. Another supporting factor is that the porous structure is apt to form on high purity Ni (99.99). Since the impurity concentration of these samples is low, few impurities can be adopted in the NiO scale. Therefore the lattice diffusion is less favored compared to short-circuit diffusion. This will improve the tendency for the porous structure to form on the surface. On the other hand, judging from Figure 4.27, not all the grain-boundary diffusion can result in surface instability; otherwise the porous structure would have formed on all the grain boundaries. Apparently, only high-diffusivity grain boundaries are involved. However, those short-circuit paths are not easy to characterize nor to be controlled. Although some relevant tests have been carried out, such as switching the sequence of oxidation in dry air and wet air, none of them revealed useful information due to poor reproducibility. Therefore, further interpretation of the surface instability is currently not possible.

In summary, it is confirmed that $Ni(OH)_2(g)$ evaporation is not the reason for the surface instability. Based on the XRD experiments, it is likely that preferred growth along {220} orientation can provide a mechanism for the less-dense columnar structure to form on the NiO scale formed on Ni-3at%Al oxidized in air+30%H_2O at 1000^{o}C. Meanwhile, enhanced short-circuit diffusion may be involved in the porous structure being formed on pure Ni oxidized in high steam content environment at 1000^{o}C. Finally, those mechanisms are not necessarily incompatible. They may work in a coordinated way for the surface instability to form in wet oxidizing conditions.

4.2 KINETICS ANALYSIS OF SCALING BEHAVIOR OF ALLOYS

4.2.1 Background on conventional way to determine oxidation kinetics

As introduced in section 1.4, there are several types of scaling growth kinetics for alloys. The growth kinetics are generally determined in two ways: measuring weight gain per unit area either periodically or continuously by a thermogravimetric technique or measuring scale thicknesses from cross-sectional images. Both of the methods have been employed by many researchers; although the thermogravimetric (TG) method generally provides more accurate measurement of the growth kinetics. Therefore, in our study, all the kinetics analysis will base on TG data.

If the growth kinetics are assumed to be parabolic, either in an simple form of equation 1.10 or in a more advanced form of equation 1.39 or 1.40 proposed by Peraggi[66], the way to determine the rate constant(s) from TG data is plotting the weight gain per unit area Δm versus the square root of time t, or the square of weight gain per unit area Δm versus time t. When the

later part of such a plot becomes a straight line, the parabolic growth rate constant k_p is calculated from the slope (or square of the slope for Δm-$t^{1/2}$ plot). Figure 4.40 shows a TG curve for isothermal oxidation of Ni-7.5Cr-20Al-3Si-3Pt-0.1Hf-0.05Y alloy in air at 1150^{o}C. Corresponding parabolic plots are shown in Figure 1.21.The growth rate constant k_p is $1.2x10^{-12}g^2/cm^4sec$ from Figure 1.21(a), while it is $0.6x10^{-12}g^2/cm^4sec$ from Figure 1.21 (b). It is clear that the method to determine k_p from these two plots is not consistent, as the two k_p values are not identical. Therefore, a more accurate method to determine the growth-rate constant is needed. It may be argued that if the TG test is long enough, the k_p values determined by the two conventional methods will become identical. Indeed, this argument should prove true so long as the testing time is enough. However, the two plots in Figure 1.21 are already exhibiting straight-line behavior at the longer time (i.e. t>4h). This means they are considered as being in the steady-state growth stage. If either of the two values is used in further analysis without careful consideration, it may lead to inaccurate conclusion. Therefore, the question is how long of a testing time is needed for the two methods to give an identical k_p values?

The dash lines in Figure 1.21 show where the curves become straight. Before the dash lines, the oxidation is in a so-called transient stage. The oxidation kinetics in the transient stage is quite complex and does not follow a simple parabolic law. Several methods have been introduced in section 1.5 to quantify the instantaneous oxidation kinetics within the initial stage. Among those methods, the analysis on the instantaneous values determined by equations 1.50 and 1.51 will be extended. Specifically, the limits and correct method to use these values will be studied.

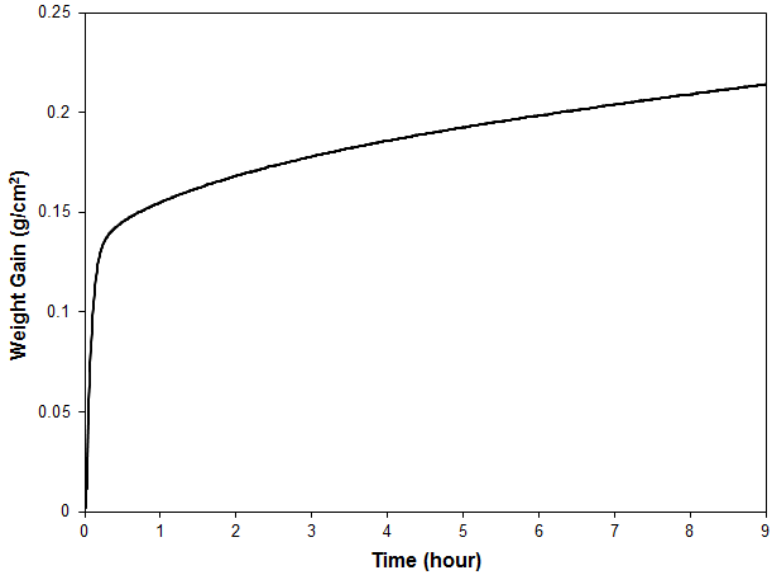

Figure 4.40 The TG curve for isothermal oxidation of Ni7.5Cr20Al3Si3Pt0.1Hf0.05Y alloy in air at 1150°C

Development of a modified method to determine steady-state oxidation kinetics

In this study, determination of the type of growth kinetics and calculation of a corresponding growth-rate constant are achieved by calculating instantaneous quantities. This method is based on the assumption that the overall growth kinetics follow the basic empirical rate law

$$\Delta m = kt^n \tag{4.54}$$

Here, Δm is the measured weight gain per unit area at time t, k is the rate constant, and n is the time exponent[110,111]. Accordingly, the *instantaneous time exponent n* (n^i for short) as a function of reaction time is calculated as:

$$n^i = \frac{\partial(\log \Delta m)}{\partial(\log t)} \tag{4.55}$$

The corresponding *instantaneous growth rate constant* k^i (k^i for short) is identified as:

$$k_1^{\ i} = \frac{\partial \Delta m^{1/n}}{\partial t} \tag{4.56}$$

$$k_2{}^i = \left(\frac{\partial \Delta m}{\partial t^n} \right)^{1/n} \tag{4.57}$$

This definition is different from the equation defined in equations 1.51, in the sense that equations 4.56 and 4.57 are not limited to parabolic growth which is implied in equation 1.51, and they become equivalent to equations 1.51 for ideal parabolic growth. It is also worthwhile to note that equation 4.56 and 4.57 infers that the overall growth rate kinetics follow:

$$\Delta m = \left(k \cdot t \right)^n \tag{4.58}$$

which is different from equation 4.54. Actually, equations 4.54 and 4.58 become equivalent when the calculated n^i and k^i values are true values corresponding to steady-state kinetics. When n^i and k^i are not the true values, they are not accurate because neither equation 4.54 nor 4.58 reflects the true kinetics at that moment.

Based on analysis by Tammann[62,63], Pilling and Bedworth[64] and Evans[65], the overall oxidation kinetics are usually found to be linear, parabolic or cubic, corresponding to the time exponent n value in equation 4.54 or 4.58 to be 1, 0.5 or 0.33. Figure 4.41 shows a schematic diagram of TG curves for those types of ideal growth kinetics. The corresponding n^i calculated by equation 4.55 as a function of time is shown in Figure 4.42 for each ideal rate law.

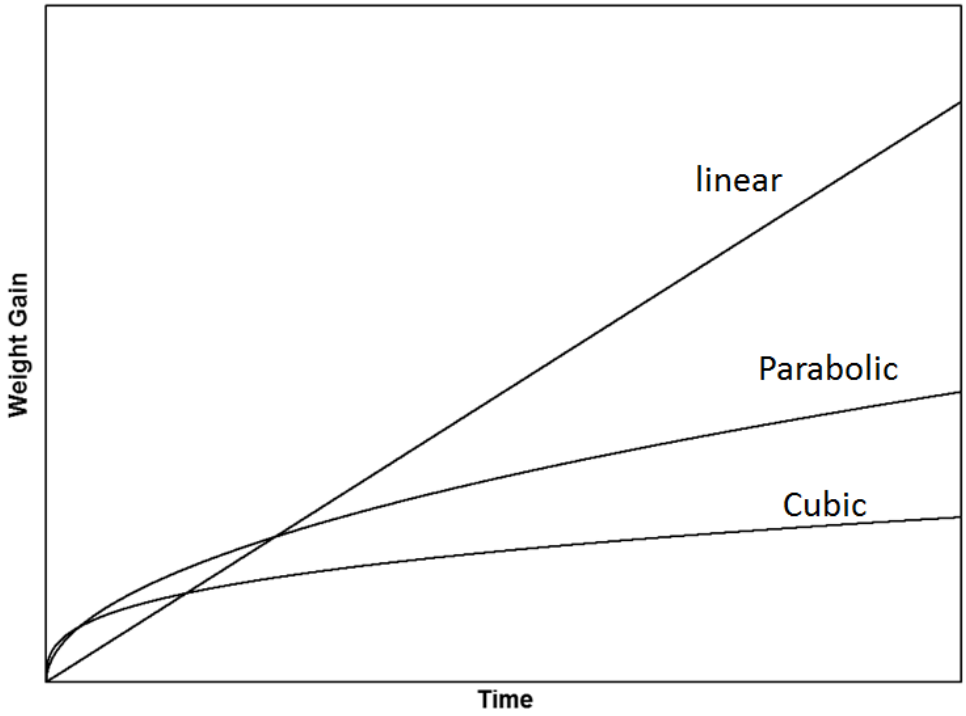

Figure 4.41 A schematic diagram of TG curves for different types of ideal growth kinetics

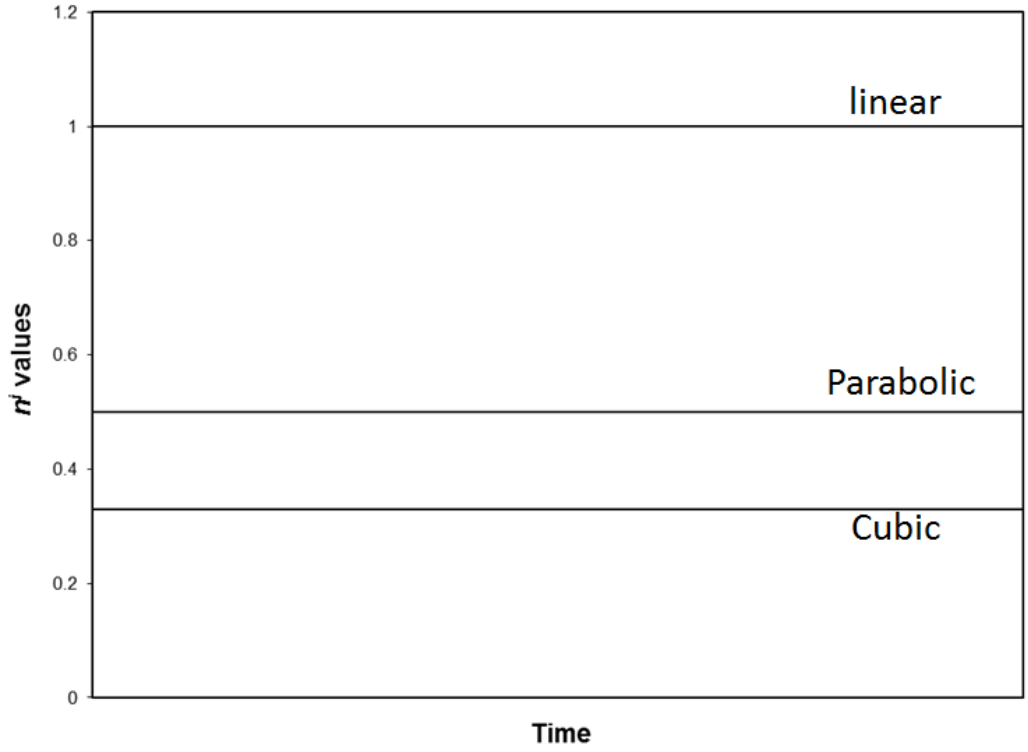

Figure 4.42 The corresponding n^i values for the ideal growth kinetics

It is seen in Figure 4.42 that, the calculated n^i values reflect the real type of growth kinetics if the growth kinetics are ideal. However, under conditions when the nature of the scale is dynamic, the parameters in equations 4.54 and 4.58 will vary with time. Correspondingly, n^i and k^i calculated by equations 4.55 to 4.57 cannot reflect the real growth kinetics immediately after the *k* and *n* are changed. This can be seen by an example of a simulated curve with changed growth kinetics shown in Figure 4.43. The curve was built by the way that the growth kinetics are changed from linear to parabolic at t = 1h. The equations to build this curve were:

$$\begin{cases} \Delta m = k_l \cdot t \ (t \le 1h) & (a) \\ \Delta m = k_p^{1/2} \cdot t^{1/2} + C \ (t \ge 1h) & (b) \end{cases} \tag{4.59}$$

For the sake of calculation, it was assumed that with k_l=5.6x10^{-7}g/cm^{2}sec, k_p=4.44x10^{-9}g^2/cm^{4}sec. It may be expected that by applying equation 4.55 to this curve, the n^i values are a constant value of 1 when t < 1h and a constant value of 0.5 when t > 1h. Further applying equations 4.56 and 4.57 to this curve, k^i values are expected to be 5.6x10^{-7} when t < 1h and 4.44x10^{-9} when t > 1h. However, Figure 4.44 (a) shows the calculated n^i values as a function of time. Before 1 hour, when the k and n values are time invariant, n^i values fixed at one. However, after 1 hour, the n^i values decrease gradually from one even though ideal parabolic (i.e. n=0.5) was inputted after t=1h. Figure 4.44 (b) shows that the n^i values will eventually be 0.5 after around 90 hours. There are two points raised by what is shown in Figure 4.44 (b). First, to accurately determine the type of growth kinetics by experiment for the sample kinetics here, the experiment have to be carried out as least 90 hours; second, so long as the experiment is long enough (>90h for this example), the correct type of growth kinetics can be determined by equation 4.54. Similarly, the plots in Figure 4.45 show the calculated k^i values as a function of time. In Figure 4.45 (a) k^i values calculated by equation 4.56 are correct before 1 hour with n=1

but they are quite different but approaching the correct value 4.44×10^{-9} with n=0.5 for t > 1h. From Figure 4.44 and Figure 4.45, it is clearly shown that the n^i and k^i values are not accurate immediately after the growth kinetics are changed (at t = 1h) from one rate law to another. Between t = 1h and 90h, n^i values do not have any physical meaning, while the trend of the change in n^i values during this time (n^i values are approaching 0.5) implies that the growth kinetics may be parabolic. For the n^i values to reflect the real kinetics, the test should be as long as 90 hours.

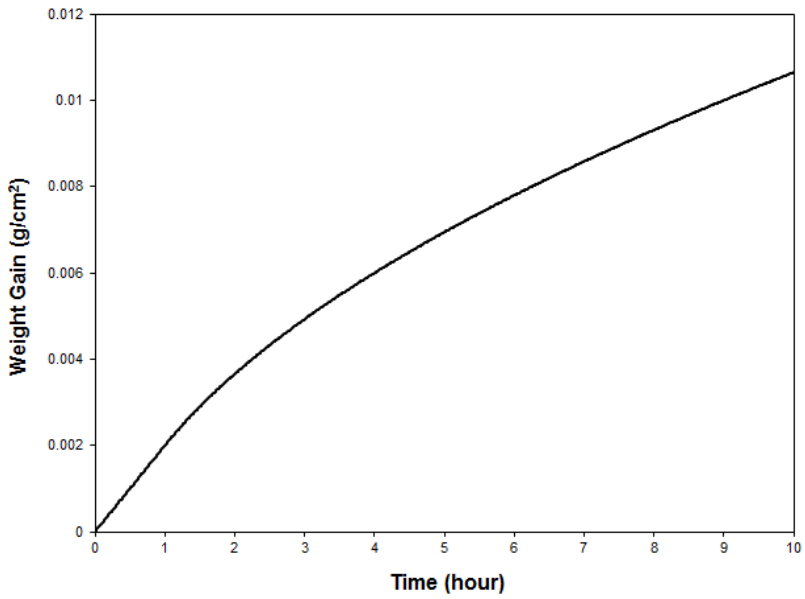

Figure 4.43 Simulated TG curve with growth kinetics changed from linear to parabolic growth at 1h

Although in Figure 4.45 (b), k^i values calculated by equation 4.57 show correct values ($k^i=5.6 \times 10^{-7}$ g/cm^{2}sec for t<1h and $k^i=4.44 \times 10^{-9}$ g^2/cm^{4}sec for t>1h), it does not necessarily mean that equation 4.57 always provides the correct k^i values. Equation 4.57 only works perfectly for the simulated case shown in equation 4.59. For more realistic growth kinetics, equation 4.57 cannot determine correct k^i values either.

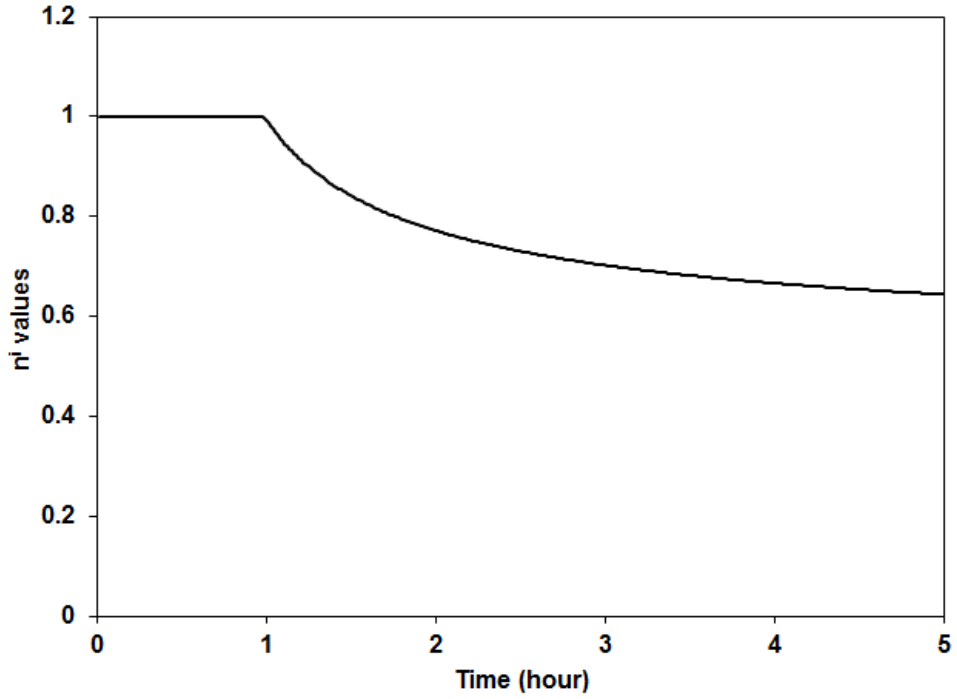

(a)

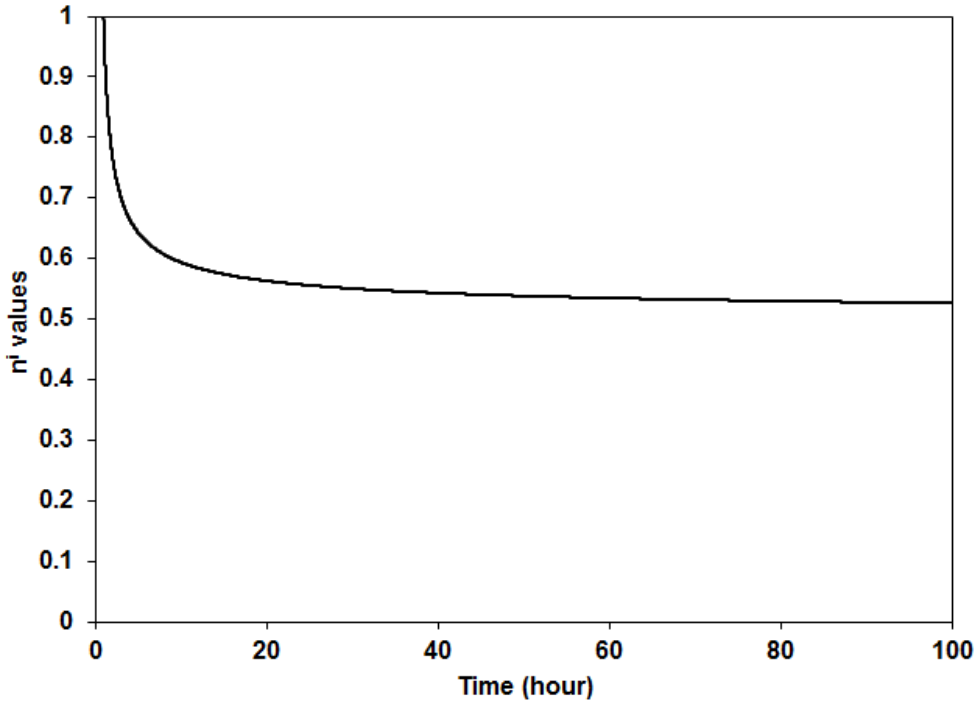

(b)

Figure 4.44 Calculated n^i values for TG curve shown in figure 4.33. In these figures, (a) and (b) are the same curve with different time range

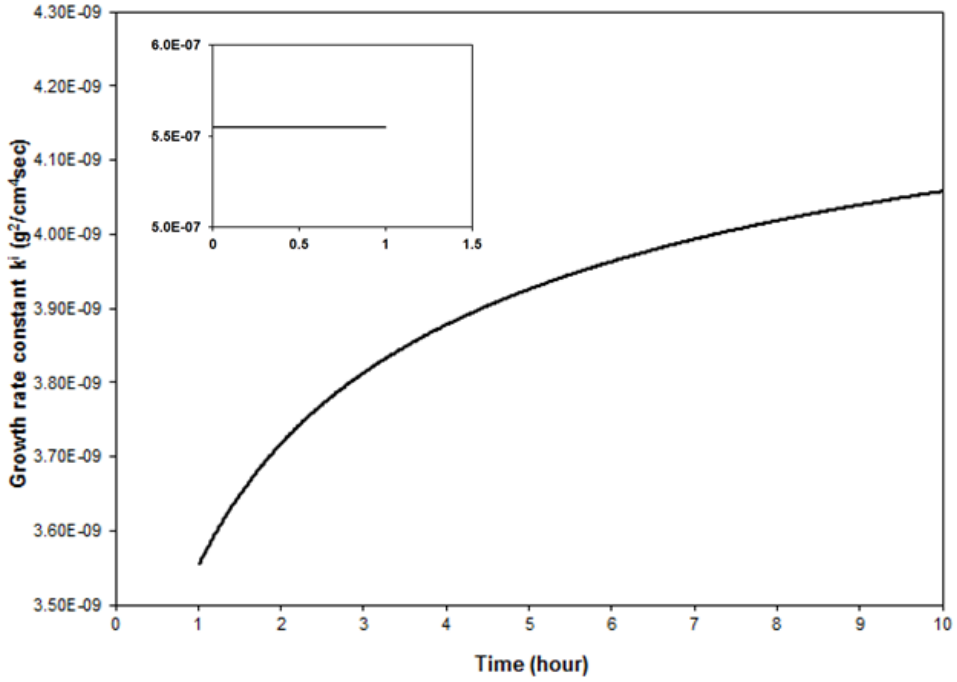

(a)

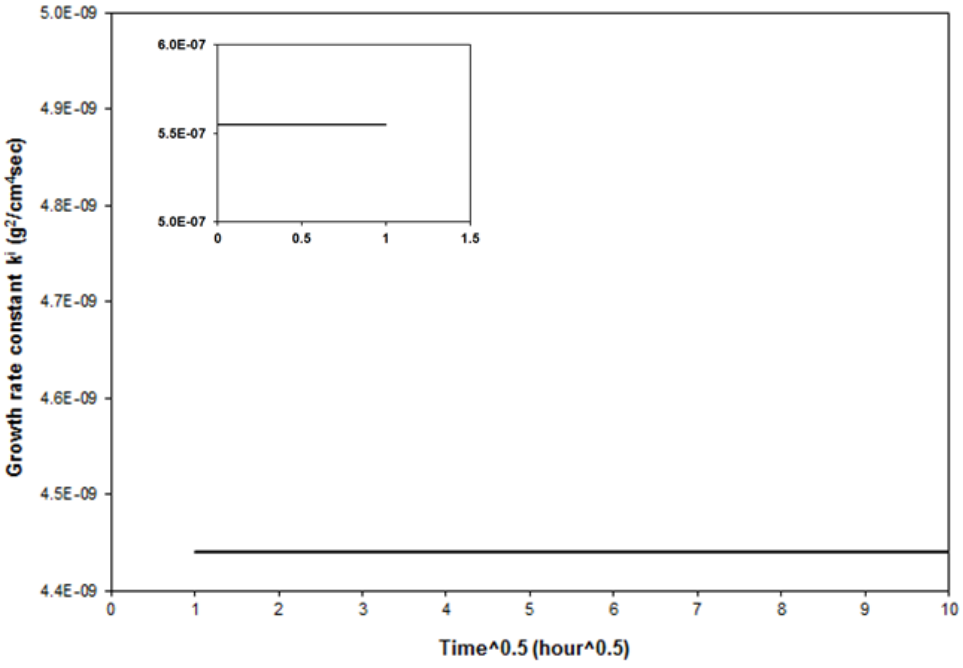

(b)

Figure 4.45 Instantaneous growth rate constant k^i for TG curve shown in figure 4.33. The inserted curves are used to show k^i for t<1h, when k^i is two orders of magnitude greater.

Study on instantaneous time exponent n^i values

Based on the example shown previously, the calculated n^i and k^i values are not accurate instantaneous values immediately after the growth kinetics have changed (i.e. n and k are changed), it is therefore worthwhile to study the n^i values more rigorously to determine the correct understanding of n^i values.

First of all, the reason that equation 4.55 can calculate the correct time exponent when k and n are time invariant is shown in the following. Taking equation 4.54 into equation 4.55 yields:

$$n^i = \frac{\partial(\log k \times t^n)}{\partial(\log t)} \tag{4.60}$$

$$n^i = \frac{\partial(n \log t + \log k)}{\partial(\log t)}$$

So,
$$n^i = n$$

However, if k and n change with time, the overall kinetics can be assumed to follow**Error! Bookmark not defined.**:

$$\Delta m = k \cdot t^n + \Delta m_i \ when \ t > t_i \tag{4.61}$$

where Δm_i is some initial weight gain per unit area after an initial time t_i. Substituting equation 4.61 into equation 4.55 gives:

$$n^i = \frac{\partial[\log(kt^n + \Delta m_i)]}{\partial(\log t)} \tag{4.62}$$

The logarithm in equation 4.62 cannot be expanded analytically. Therefore the calculated n^i values are not the true n values so long as Δm_i is not 0, which is shown in Figure 4.44 since equation 4.59 (b) is equivalent to equation 4.61 when n=0.5 and $\Delta m_i = C$.

Pieraggi[73] proposed another equation to calculate n^i values without using the logarithm; i.e.

$$n_2^{\,i} = \frac{1}{2}\frac{\left[\frac{\partial \Delta m}{\partial t^{1/2}}\right]^2}{\left[\frac{\partial \Delta m^2}{\partial t}\right]} \tag{4.63}$$

The subscript 2 in $n_2^{\,i}$ is used to differentiate the n^i values calculated by equation 4.63 from those calculated by equation 4.55. Figure 4.45 shows the calculated n^i and $n_2^{\,i}$ values for the curve shown in Figure 4.43. The open circles are calculated n^i values from equation 4.55 and the line represents calculated n^i values from equation 4.63. Despite the small difference at the very beginning, the two equations give exactly the same n^i values versus time. Indeed, the effect of the Δm_i on the n^i value shown by equation 4.62 also exists in equation 4.63 when calculating $\frac{\partial \Delta m^2}{\partial t}$. Therefore, equation 4.49 does not have an advantage to calculate more accurate n^i values.

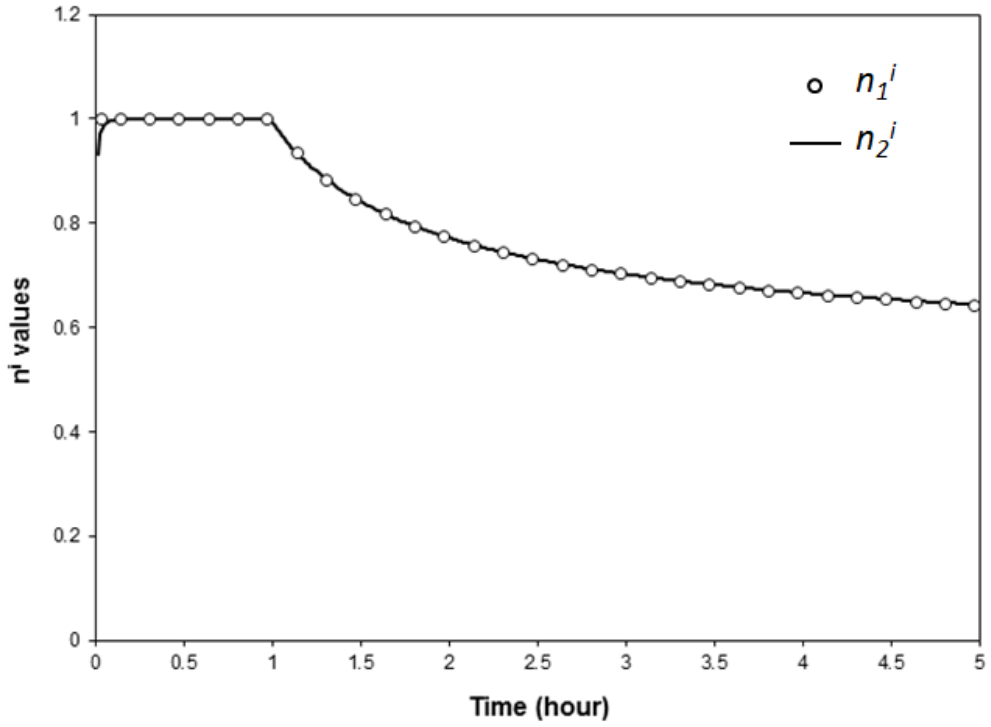

Figure 4.46 Calculated n^i values by the conventional definition ($n_1^{\,i}$) and Pieraggi's modification ($n_2^{\,i}$) [73]

So far, an example has been shown when the k and n changed in such a way that there is an initial weight gain Δm_i at $t = t_i$ but the growth kinetics are parabolic for $t > t_i$; however, the manner that k and n change is not limited to this. Graham et al.[112] reported that for the oxidation of pure Ni in 0.5 Torr at 700^{o}C, the parabolic rate constant calculated by equation 1.51 kept decreasing gradually from around $8.0x10^{-2}mg^2/cm^4h$ at 0.1h to as low as $8.3x10^{-3}mg^2/cm^4h$ at 20h (Figure 4.47). In our study, similar growth kinetics were also found for the oxidation of pure Ni in dry air at 900^{o}C, indicated by the decreasing n^i values shown in Figure 4.48. From 1h to 10h, the average n^i values decreased from 0.47 to 0.43. Based on the analysis shown in Figure 4.36, the decrease in growth kinetics should be due to the evolution of grain sizes. So long as the evolution persists, the growth kinetics will keep decreasing. This is an example that shows that the oxidation kinetics may not have a steady-state stage until after some extremely long oxidation time.

As a summary to this point, it has been shown that the growth-rate constants determined by conventional methods may not be accurate when the oxidation kinetics is more complex than ideal linear, parabolic or cubic. The reason that the calculated growth-rate constants are not accurate is that the test time is not long enough to the extent that the calculated growth-rate constants are influenced by the oxidation history. More importantly, even the later part of the kinetics plot (Δm^2 vs. time or Δm vs. time$^{1/2}$) becomes a straight line, it does not guarantee that the slope for the straight line reflects the true growth kinetics for steady state. In some cases, the oxidation process can reach a steady state in comparatively a short time (e.g. less than a hundred hours) while it is possible the oxidation kinetics will not reach a steady state for an extremely long oxidation time (e.g. thousands of hours). Therefore, a method that can identify whether the oxidation kinetics can reach a steady state during the test time is needed. One way to achieve this

goal is using the k^i and n^i values calculated by equations 4.55 to 4.57. Although, it has also been shown that k^i and n^i values are not true values immediately after the growth kinetics is changed from one ideal kinetics to another. Therefore, it is worthwhile to discuss how useful information on the growth kinetics can be derived from k^i- and n^i-value curves.

The first step to analyze a n^i-value curve is trying to find a steady-state stage. In particular, based on the fact that n^i values may not be the true values due to the oxidation history, if the n^i values become a constant value of 0.5, does this necessarily indicate a steady-state stage? The following mathematics derivation can be used to answer this question.

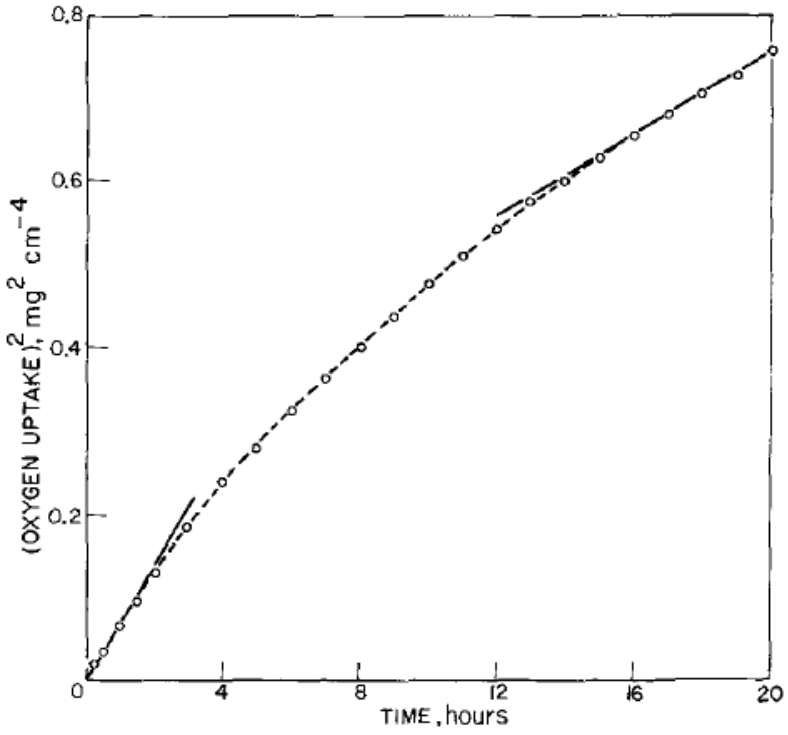

Figure 4.47 Plot of (oxygen uptaken)^2 vs. time at 700^{o}C, showing deviation from parabolic behavior

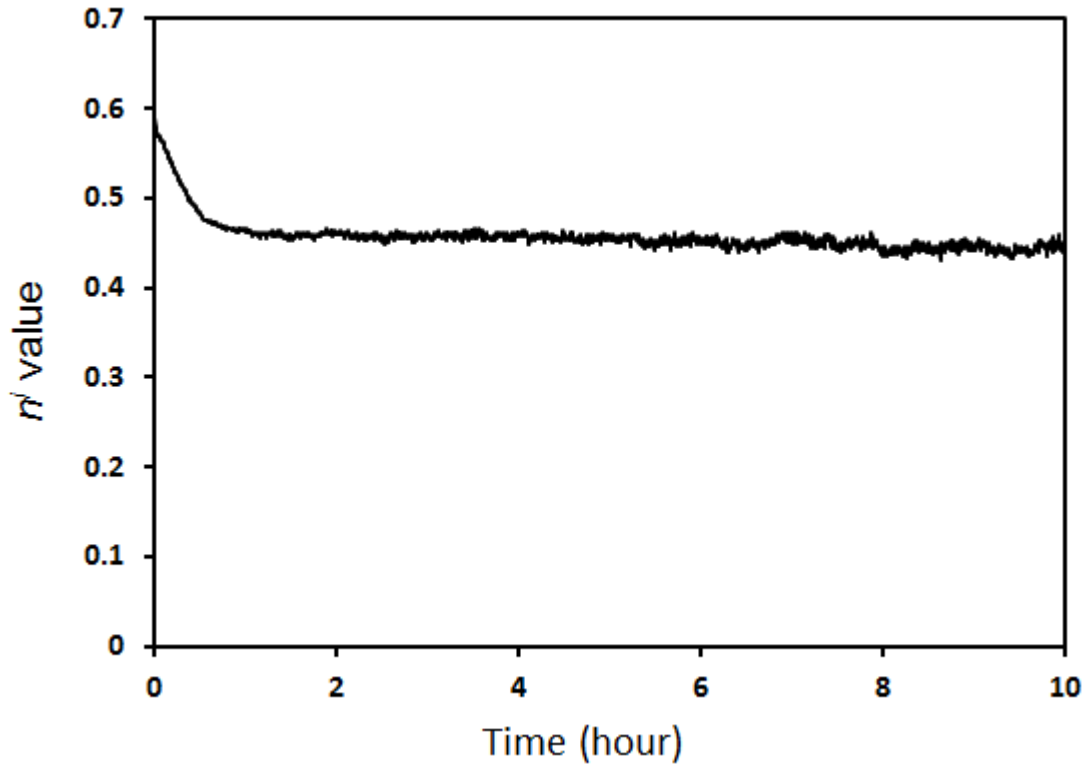

Figure 4.48 n^i values associated with TG data for oxidation of pure Ni at 900°C in dry air

Suppose the calculated n^i values become a constant value of 0.5 at the times beyond t_0, and at this time, the weight gain is Δm_0. Substituting $n^i = 0.5$ into equation 4.55 yields:

$$\frac{\partial \log(\Delta m)}{\partial \log t} = 0.5 \text{ for } t > t_0 \tag{4.64}$$

This gives:

$$\partial \log(\Delta m) = \partial \log t^{0.5} \tag{4.65}$$

Integrating both sides from $t = t_0$ to any time t after t_0 gives:

$$\int_{\log(\Delta m)\ at\ t=t_0}^{\log(\Delta m)\ at\ t=t} \partial \log(\Delta m) = \int_{\log t^C\ at\ t=t_0}^{\log t^C\ at\ t=t} \partial \log t^{0.5} \tag{4.66}$$

$$\log \Delta m - \log \Delta m_0 = \log t^{0.5} - \log t_0^{0.5} \tag{4.67}$$

$$\log \frac{\Delta m}{\Delta m_0} = \log \frac{t^{0.5}}{t_0^{0.5}} \tag{4.68}$$

$$\Delta m = \frac{\Delta m_0}{t_o^{0.5}} t^{0.5} \tag{4.69}$$

This derivation indicates that during the time that calculated n^i values become constant at a value of 0.5, the corresponding overall weight gain kinetics follow a form of equation 4.69. Since Δm_0 and t_0 are constants, the overall weight gain as a function of time (equation 4.69) corresponds to exactly the parabolic growth kinetics. Given that steady-state oxidation has not been quantitatively defined, we will state that "weight gain as a function can be written in the form of $\Delta m = k_p t^{0.5}$", (note there must be no Δm_i in this equation) is by far the most reliable criterion to identify a steady-state kinetics compared to the conventional kinetics plot and the local analysis method. Moreover, this constant value 0.5 can be replaced by 0.33 or 1 corresponding to cubic and linear kinetics.

After identifying the steady-state stage when the n^i values are constant, it is possible to identify the stages in which the steady-state has been established but not shown as constant n^i values. This is shown by Figure 4.44 (b). In that figure, a new steady-state has been established for t > 1h; however the calculated n^i values are not a constant value of 0.5 immediately after t = 1h. But, the trend for the n^i values after t = 1h is such that n^i values are monotonically approaching 0.5. Therefore, this example shows that steady-state oxidation is established first and then manifests as constant n^i values after a certain time. The duration of this time depends on real situation so that it is not easy to specify here. Moreover, is it also shown by Figure 4.44 (b) that when n^i values do not the values correspond to parabolic, cubic and linear kinetics (0.5, 0.33 and 1 respectively), they may not have any physical meaning. For example, after t=1h in Figure 4.44 (b), the real time exponent is n = 0.5 but the calculated n^i values are numbers between 1 and 0.5.

Finally, the change in the real kinetics always has some characteristic feature manifest on the n^i values curve. For example, if the overall kinetics are changed from a linear to a parabolic rate law (Figure 4.44), the n^i values always decreases gradually and monotonically from 1 to 0.5. However, the duration for n^i values to approach the new steady-state value (0.5) depends on the specific kinetics situation, such as the k_p for the parabolic kinetics and the total weight gain Δm_i at the end of the linear-growth stage. Moreover, for the case of oxidizing pure Ni in dry air at 900^{o}C (Figure 4.48), with the average grain size increasing with exposure time, the amount of grain boundary as faster-diffusion paths decreases[109] and the overall NiO growth rate keeps decreasing. This will lead to a feature on the n^i-value curve that n^i values keep decreasing. Indeed, the features on the n^i-value curve can be various. A detailed analysis on those features can be used to quantify the kinetics corresponding to the specific scaling behavior.

Study of the instantaneous growth rate constant k^i

The k^i values can also be used to establish a criterion to identify steady-state kinetics during oxidation. This is shown in the following way. Suppose the k^i values calculated by equation 4.56 and 4.57 are as an identical constant B for $t > t_0$, and the weight gain at this time is Δm_i, i.e.:

$$\frac{\partial \Delta m^{1/n}}{\partial t} = B \tag{4.70}$$

$$\left(\frac{\partial \Delta m}{\partial t^n}\right)^{1/n} = B \tag{4.71}$$

Integrating both equations from t=t_0 to any time t after t_0 gives:

$$\Delta m^{1/n} - \Delta m_0^{1/n} = B(t - t_0) \tag{4.72}$$

$$\Delta m - \Delta m_0 = B^n (t^n - t_0^n) \tag{4.73}$$

For parabolic growth kinetics, n=0.5. Substituting n=0.5 to equations 4.72 and 4.73 gives:

$$\Delta m^2 = Bt + C \tag{4.74}$$

$$\Delta m = B^{0.5} t^{0.5} + D \tag{4.75}$$

Here C and D are constants. Taking the square of equation (4.75) yields:

$$\Delta m^2 = \left(B^{0.5} t^{0.5} + D \right)^2 \tag{4.76}$$

$$\Delta m^2 = Bt + 2B^{0.5} t^{0.5} D + D^2 \tag{4.77}$$

Since equation 4.74 and 4.77 should equal to each other for all the time t after t_0, it requires the coefficient $B^{0.5}D=0$. Since the growth rate constant B cannot be zero, D has to be zero. Therefore, equation 4.63 becomes:

$$\Delta m^2 = Bt \tag{4.78}$$

Equation 4.78 is also equivalent to the form of $\Delta m=k_p t^{0.5}$, which is the definition of parabolic growth kinetics. Therefore, the constant B must be the real k_p. This derivation excluded the possibility that although the k^i values calculated from equations 4.56 and 4.57 are identical, they are identical to a value which is different from the real k_p.

It is seen that when identifying the steady-state kinetics during the course of oxidation, no matter if it is determined by the n^i values or k^i values, they both require that the overall growth kinetics follow an form equivalent to $\Delta m=k_p t^{0.5}$. This implies that the period for the steady-state determined by both n^i and k^i values should be identical. This point may appear to be obvious; however, it is actually not so obvious in the sense that the real steady-state was probably established earlier than the time predicted by the two ways. Therefore, to determine the steady-state either by analyzing n^i values or by k^i values provides a shorter period than the real kinetics. Even though, both of the criteria are still very useful because at least they can determine a period during which the growth kinetics are in steady state and the k^i values calculated in this period are

representative of the actual values of k_p. This can be shown by the following experimental example.

Figure 4.49 shows the experimental TG curve for oxidation of Ni-7.5Cr-20Al-3Si-3Pt-0.1Hf-0.05Y alloy oxidized in air at 1150°C for 100h. Figure 4.50 shows the n^i values associated to the TG curve. Figure 4.51 (a) and (b) show the corresponding k^i values curves calculated by equation 4.56 and 4.57. From the Figure 4.50, n^i values decrease to a value of around 0.17 at around 0.5h and then increase monotonically to 0.5 and becomes a constant value of 0.5 beyond 70 hours. Based on the analysis shown previously, this feature indicates a steady state was probably established between 0.5h and 70h. At the same time, the k^i values shown in Figure 4.51 become practically identical at $1.04 \times 10^{-12} g^2/cm^4 sec$ (Figure 4.51a) and $1.02 \times 10^{-12} g^2/cm^4 sec$ (Figure 4.51b) after 70h, which should be the real k_p under steady-state conditions. It is important to note that the standard deviation for the k^i values after 70h are $0.03 \times 10^{-12} g^2/cm^4 sec$ and $0.06 \times 10^{-12} g^2/cm^4 sec$, respectively. This means with accurate TG measurement, it is possible to use this method to determine the growth rate constant with 3 significant figures.

Actually, the data for the example shown in Figure 1.21 are from the first 9h in Figure 4.49. Therefore, those examples can be used to compare this method with existing methods. Based on the observation that the later parts of the Δm versus $t^{1/2}$ and Δm^2 versus t curves are already straight lines in Figure 1.21, without careful consideration, the k_p values may be taken as $1.2 \times 10^{-12} g^2/cm^4 sec$ or $0.6 \times 10^{-12} g^2/cm^4 sec$, as determined using equations 1.39 and 1.40 proposed by Pieraggi[66]. However, if the experiment is carried out long enough, (i.e. >70h), this method should be able to predict the real k_p value. Meanwhile, although Pieraggi[66] pointed out that for the case with a transient period of faster kinetics, a plot of Δm-$t^{1/2}$ is inherently superior to the Δm^2-t plot, this experiment shows a counter example for this. The initial growth rate for the first

0.5h is very fast, as shown Figure 4.49, however, the k_p determined by Δm^2-t plot is $0.6 \times 10^{-12} g^2/cm^4 sec$, which is further away from the true value $1.04 \times 10^{-12} g^2/cm^4 sec$.

The local analysis method proposed by Monceau and Pieraggi[70] was not carry out in this study. However, based on the fact that the essence of the local analysis method is no more than a polynomial fitting of a window of time rather than fitting of the whole later part of the kinetics plot, it is expected that this method cannot be accurate when the oxidation kinetics is more complex than what can be expressed by a polynomial. Moreover, the criterion used in the local analysis method to determine a steady-state stage is checking if the local k_p becomes a constant value. In some cases, this criterion is not accurate. For example, the calculated k_p in appear to be a constant of $0.6 \times 10^{-12} g^2/cm^4 sec$ for the first 16h in Figure 4.51b. However, this value is different from the value $1.0 \times 10^{-12} g^2/cm^4 sec$ determined at longer time (>70h). However, if the steady state is checked by the n^i values, the n^i values are different from a constant value of 0.5 for the first 16h. Therefore, it will not lead to an inaccurate conclusion that the k_p calculated for the first 16h is representative for the steady-state growth-rate constant.

In summary, two important points have been proven by the above analysis: (1) if the period for n^i values to be 0.5 or the period during which k^i values calculated by both equations 4.56 and 4.57 are identical, this period is at a steady state. The k^i values calculated during this period is representative for the steady-state growth-rate constant. (2) when the oxidation kinetics is more complex than what can be expressed by a polynomial, the features on n^i values can be used to quantify the real oxidation kinetics. Although in practice, several errors may affect the determined oxidation kinetics by n^i-value analysis. Therefore, the sensitivity of the n^i values to some practical issues needs to be checked.

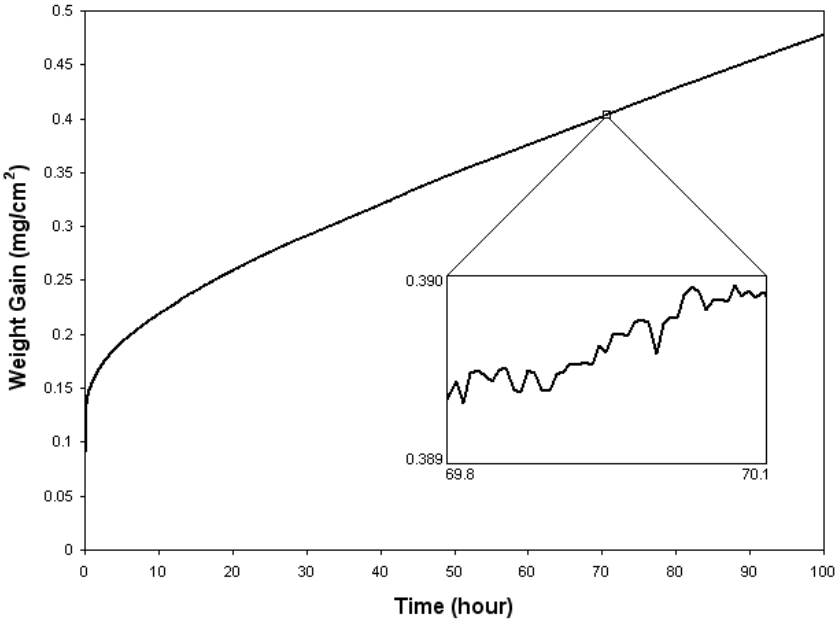

Figure 4.49 Experiment TG data of isothermal oxidation of the Ni7.5Cr20Al3Si3Pt0.1Hf0.05Y alloy in air at 1150^{o}C for 100h. The insert image shows the noise level of this test

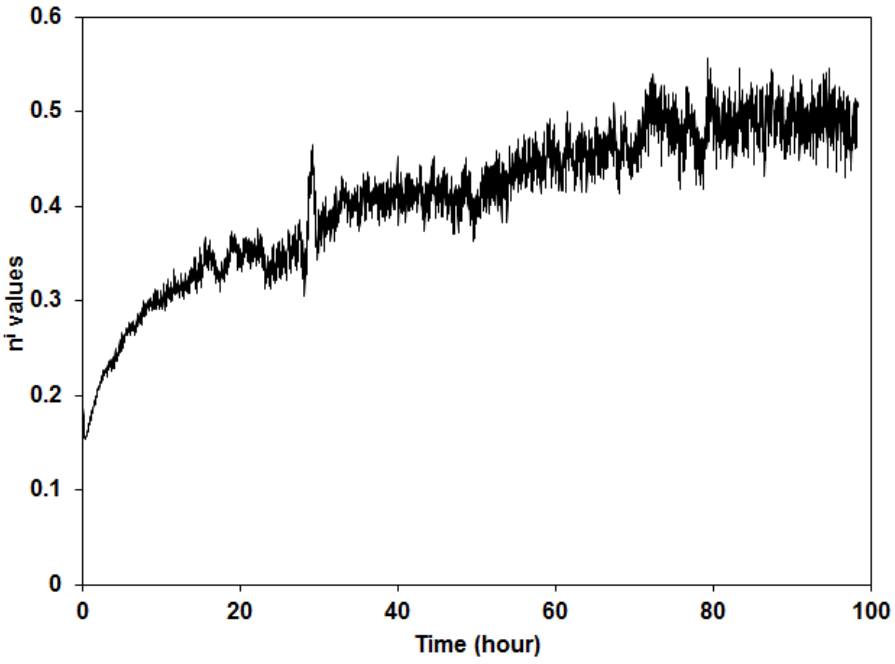

Figure 4.50 The corresponding n^i value curve for the TG curve shown in figure 4.38

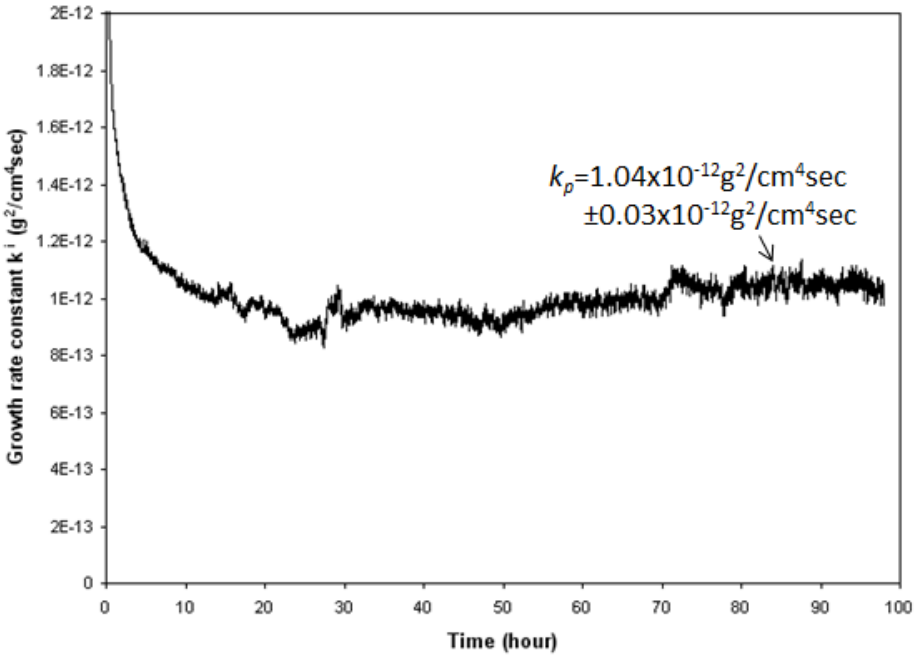

(a)

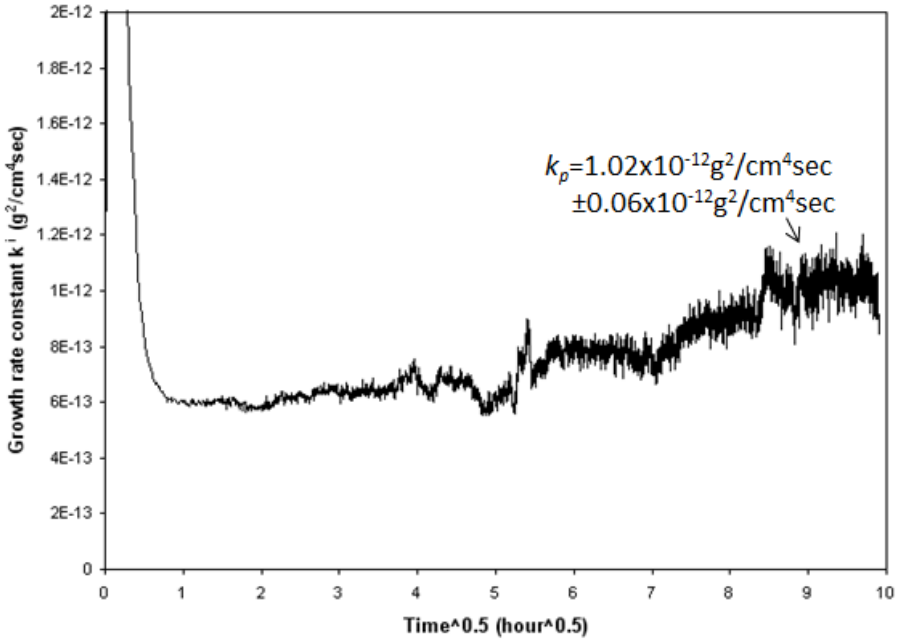

(b)

Figure 4.51 The k^i-value curve for the TG curve shown in figure 4.38. Curve (a) is calculated by equation 4.42 and Curve (b) is calculated by equation 4.43. The standard deviation for k_p calculated in figure (a) and (b) are $0.03\times10^{-12}g^2/cm^4sec$ and $0.06\times10^{-12}g^2/cm^4sec$ respectively

4.2.2 Practical issues to process TG data

The method to determine the growth kinetics by analyzing instantaneous values was presented in the last section. When applying this method to determine the growth kinetics, there are some practical issues that one must be careful with. Otherwise, significant error may be brought into the results. Those errors may not be completely eliminated, however if they are treated properly, they may be can be minimized to a negligible level.

The first type of error comes from the choosing of the differential interval when the differential values need to be calculated from discrete numbers. In a given TG experiment, the data are recorded as discrete numbers over a certain time interval. Therefore, the differentiations such as those in equations 4.55 to 4.57 are usually calculated in a way as:

$$\left.\frac{\partial Q}{\partial t}\right|_{t=t_1} = \frac{Q_2 - Q_1}{t_2 - t_1} \tag{4.79}$$

where Q_1 and Q_2 can be any quantities at the time t_1 and t_2 ($t_1<t_2$). As a consequence, the calculated differential values at a time (t_1) depend on the intervals between t_2 and t_1. Figure 4.52 shows the effect of the differential interval on the calculated n^i values for the experimental data shown in Figure 4.49. Three differential intervals Δt=10min, 30min and 1hour were chosen in this example. With increasing the interval, the scattering of the calculated data decreases. On the other hand, Figure 4.53 shows enlarged n^i values curves for the first 2 hours. With increasing the interval, the minimum value for the n^i values is shifted, and the curvature becomes larger (or more blunt), which means the details of the curve is being lost. Therefore, there is a balance to choosing the optimal interval. It needs to be able to reduce the noise level as well as maintain the details of the curve. The determination of the optimal interval is empirical, however, the same intervals should be used when two calculated differential values are compared.

Another type of error comes from the initial heating stage or gas-filling stage. In some studies, the sample is heated within the furnace to the target temperature in an inert gas environment. After reaching the target temperature, the gas is changed to the testing gas. However, the gas in the furnace cannot be replaced immediately. There must be an intermediate stage during which the oxidant partial pressure is high enough to start the reaction but lower compared to the target pressure. In such an experiment, it is difficult to avoid kinetics "artifacts" associated with the initial stage for heating or gas-filling. This stage may take several minutes or much longer. Taking the initial heating stage as an example, if this period is included in the analysis, it can change the shape of the n^{i} and k^{i} curves significantly. Figure 4.54 shows typical initial weight gain data from a real experiment when the sample was heated in air within the furnace from room temperature to the 1100^{o}C for around 10mins. Figure 4.55 shows calculated instantaneous n^{i} values with and without this initial period. It is seen that with the initial stage removed, the growth kinetics can be considered as a simple parabolic. However, if the initial stage is not removed, there is a huge effect on the calculated n^{i} values even up to 100 hours, even though the initial heating took only 10mins. Therefore, it is important to choose a proper starting point for the experimental curve. Usually, the starting point for a test with initial heating stage can be chosen at the time that the furnace temperature reaches the target temperature.

The third type of error comes from data smoothing when it is needed. In this study, the experimental TG data has very high signal-to-noise ratio, to the level that noise is less than 0.1% of the TG data, there was therefore no need to do any smoothing of the raw data. However, in certain cases data smoothing might be needed to help reduce the noise level. Depending on the smoothing method and intensity, the calculated instantaneous values are affected to different

extents. If possible, the data smoothing should be avoided to reduce any artifacts associated with the instantaneous values.

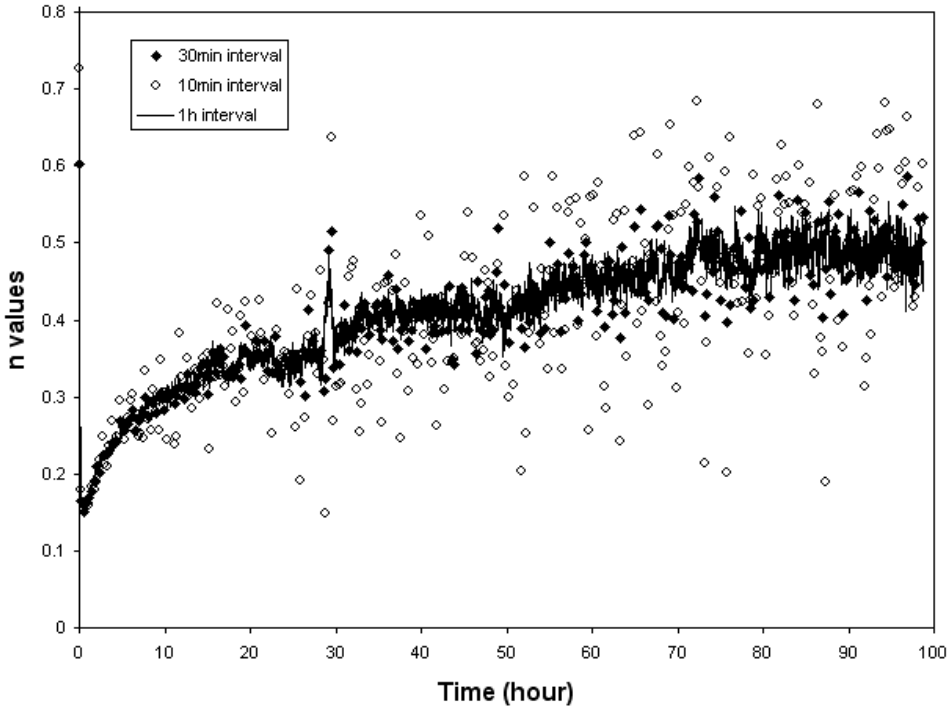

Figure 4.52 The effect of differential interval on the scattering of calculated n^i values

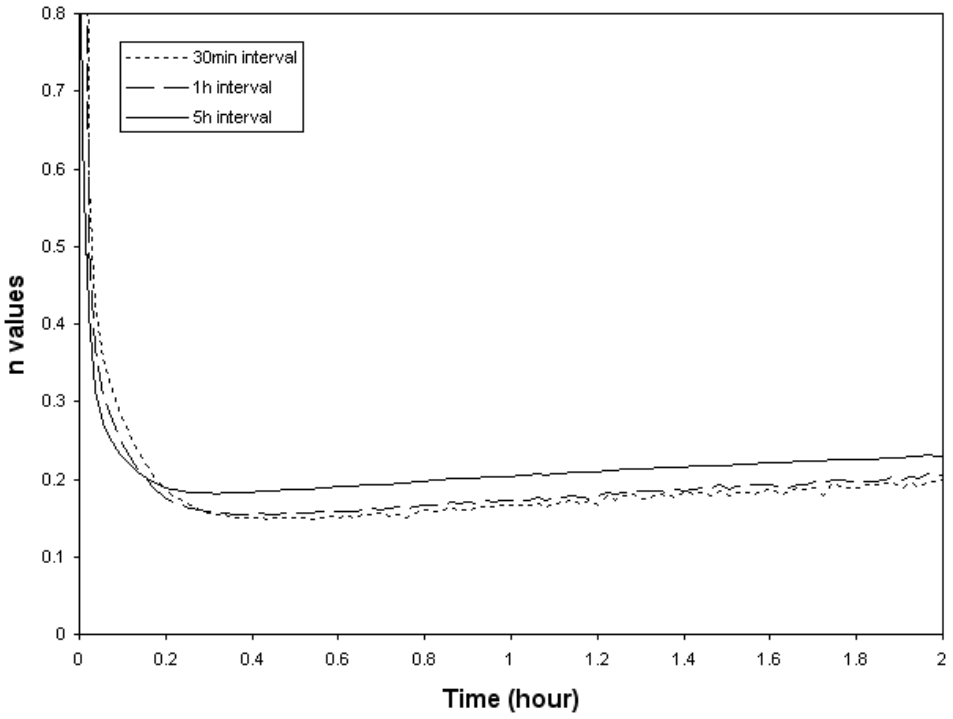

Figure 4.53 The effect of differential interval on the resolution of calculated n^i values

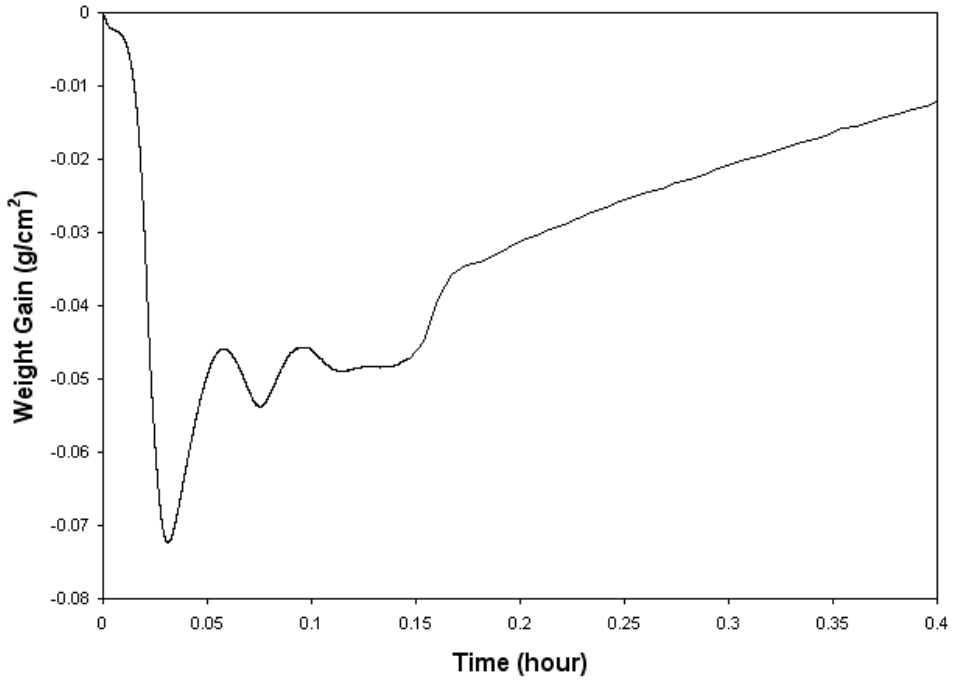

Figure 4.54 An example of the TG curve during the initial heating stage

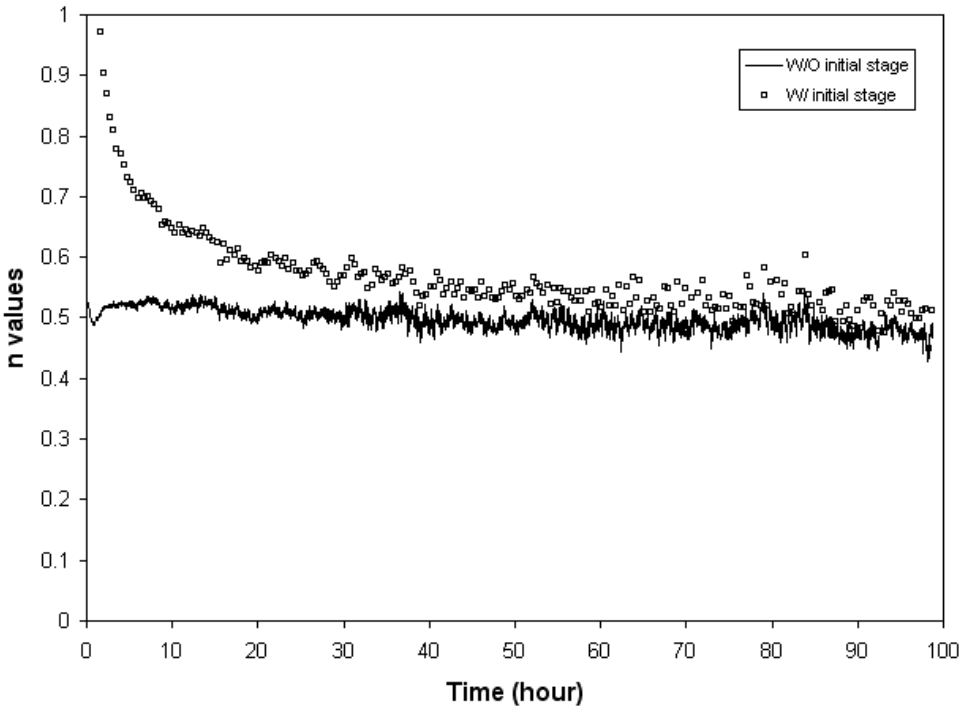

Figure 4.55 The effect of the initial heating stage on the calculated n^i values

4.2.3 A procedure to determine the evolving growth kinetics and accurate growth rate constant

Based on the previous analysis, a procedure to carry out a rigorous kinetics analysis of TG data will be developed in the following.

Step 1. Setting the starting point of the TG curve. The purpose of this step is to minimize the effect caused by the initial heating stage or other initial stages. Although the selection of this point depends on the specific experimental conditions, it is suggested that this point is set to a location close to the end of the heating stage and to where the weight-gain curve starts to show a continuous weight gain. This point is then set as the time zero and weight-gain zero.

Step 2. Calculating the n^i values by equation 4.55. This is done to have an idea of the rate law dictating growth kinetics. If the n^i values are found to be around a constant of 1, 0.5 or 0.33

throughout the testing time, it means that the growth kinetics are ideal linear, parabolic or cubic respectively. If the n^i values are approaching one of the three values and stabilizing to that constant value for an extended period, it indicates that the oxidation process has reached a steady state.

Step 3. Determination of growth kinetics (n = 1, 0.5 or 0.33). If the growth kinetics are simple one or the n^i values in step 2 maintain at a constant value for a period, the growth rate constant can be calculated by the average of the instantaneous values during the time that n^i values are constant:

(1) If n=1, the linear instantaneous rate constant k_l is $k_l^i = average\left(\frac{\partial \Delta m}{\partial t}\right)$

(2) If n=0.5, the parabolic instantaneous rate constant k_p is $k_p^i = average\left(\frac{\partial \Delta m^2}{\partial t}\right)$

(3) If n=0.33, the cubic instantaneous rate coefficient k_c is $k_c^i = average\left(\frac{\partial \Delta m^3}{\partial t}\right)$

Step 4. Determination of growth kinetics ($n \neq 1$, 0.5 or 0.33). If the n^i values are not a constant, but they are approaching a constant value such as 0.5, it probably means that the testing time was not long enough for the fully establishment of the steady state. Under this case, the best option is elongating the testing time until n^i values are stabilized. However, if the n^i-value curve shown a trend not approaching any steady state, it probably means the real growth kinetics are more complex. In this case, it is better to determine the additional factors that are contributing to the growth kinetics.

In comparison to the conventional Δm^2-t or Δm-$t^{1/2}$ plot, this procedure provides a criterion (step 2) to determine the period to reach steady-state growth. In the conventional way, even when the Δm^2-t or Δm-$t^{1/2}$ plot apparently becomes linear, the determined growth rate

constant can still have a large deviation, such as by a factor of two in the example shown in subsection 1.4.1. By contrast, by using the criterion in step 2, the period of steady-state growth can be determined and the growth-rate constant calculated for this period can have up to three significant digits as shown in Figure 4.51. Meanwhile, by analyzing the n^i-value curve, it is possible to see the complex growth kinetics to some extent, such as the example shown in subsection 4.2.3. In the next section, a more detailed kinetics analysis for quantifying the extent of $\theta \rightarrow \alpha$-$Al_2O_3$ transformation by analyzing the n^i-value curve will be shown. An accurate quantification of complex growth kinetics, especially during the transient stage, has not been presented in previous studies.

Both this procedure and the local analysis method shown in section 1.5 can be used to determine a more accurate growth-rate constant. One important advantage to use this procedure is that this procedure can be used to determine the period for steady-state growth more reliable. The reason that checking k_p to be a constant is not reliable is that k_p can change very slowly so that it "appear" to be a constant. After much longer time, k_p can still change significantly. By constant, checking n^i values to be 0.5 does not have such an issue. As long as the n^i values are close to 0.5 for a period, the oxidation kinetics for this period is close to a steady state. Additionally, n^i values are more stable for long-term testing. It is seen that the denominator has only Δt in it. Therefore the measurement error on the weight gain will not be amplified. Last but not least, it can be identified by this procedure when the real growth kinetics are more complex than linear, parabolic or cubic.

4.2.4 An example of kinetics analysis on the oxidation behavior of Ni-5Al-3Cr-1Si alloy

In the following example, the n^i value analysis will be combined with cross-sectional SEM images to characterize the oxidation behavior of a Ni-5Al-3Cr-1Si alloy oxidized in dry air at 1000^{o}C. The purpose to show this example is that by going through the procedure shown in subsection 4.2.3, it is possible to obtain information from the n^i value analysis which cannot be obtained from any other method. This information can be used for further quantification of the oxidation kinetics.

After setting the starting point of the experimental TG curve according to *step 1*, the TG data used for analysis is shown in Figure 4.56. Apparently, this curve has a nice parabolic shape; however, after calculating the n^i-value curve as shown in Figure 4.57 (*step 2*), it was found that there were three stages with different oxidation kinetics occurring in the following sequence: an initial stage before 10h; an apparent steady-state between around 10 to 50h; and a stage with decreasing n^i values after 50h. The calculated k^i values from this TG curve are shown in Figure 4.58. From around 10 to 50h, the n^i values are around 0.5; then, according to *step 3*, the growth-rate constant k_p in this period is an average of around $2.8 \times 10^{-9} g^2/cm^4 sec$. Other than the period between 10h and 50h, n^i values do not show ideal behavior. Therefore, based on the n^i-value analysis, it is deduced that, to have an accurate estimation of the weight gain during whole oxidation process, at least three distinct kinetic stages are required. The first stage corresponds to the weight gain during the first 10 hours. The second stage is the apparent steady state between 10h and 50h. The third stage is the period after 50h. Such detail about the oxidation kinetics cannot be obtained from other kinetics analysis method.

To interpret the physical meaning of the three stages, cross-sectional SEM images were taken from the alloy oxidized for 20h (Figure 4.59) and 100h (Figure 4.60). In Figure 4.59, it is

seen that NiO had formed on the surface of the sample. A zone of internal oxidation formed below the NiO scale, while an Al_2O_3 layer formed below this IOZ. By comparing the IOZs in Figure 4.59 and Figure 4.60, no internal oxidation precipitates formed below the Al_2O_3 layer and most of the base metal was oxidized above this layer at 100h.

These cross-sectional images, accompanied with the kinetics analysis in Figure 4.57, indicate that a continuous Al_2O_3 layer was probably established by 10 hours. From that time to around 50h, the base alloy above this layer was oxidized to form NiO. From around 50h and onward, most of the base alloy had been consumed. Therefore, the growth kinetics starts to decrease from this time. From the literature, the growth-rate constant $2.8x10^{-9}g^2/cm^4sec$ determined in Figure 4.57 corresponds to the reported growth rate constant of NiO, $3x10^{-9}g^2/cm^4sec$ at this temperature[83]. These results also indicate that although this alloy was not as protective as single Al_2O_3-scale forming alloy, it became protective after tens of hours.

Finally, the above analysis is not used to emphasize what had occurred during the course of oxidation of this alloy, but rather to demonstrate that about the oxidation kinetics that can be identified by the n^i-value analysis. The n^i-value analysis can be used as a tool to magnify the non-ideal behavior during the oxidation process.

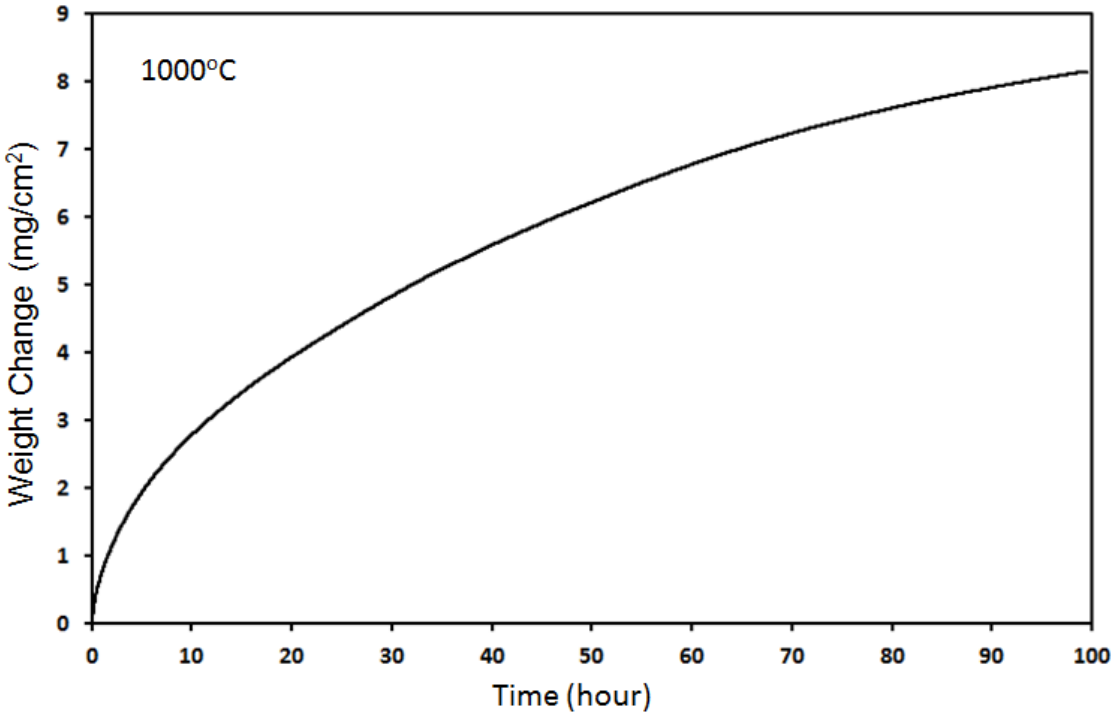

Figure 4.56 TG curve for Ni-5Al-3Cr-1Si alloy oxidized in dry air at 1000°C

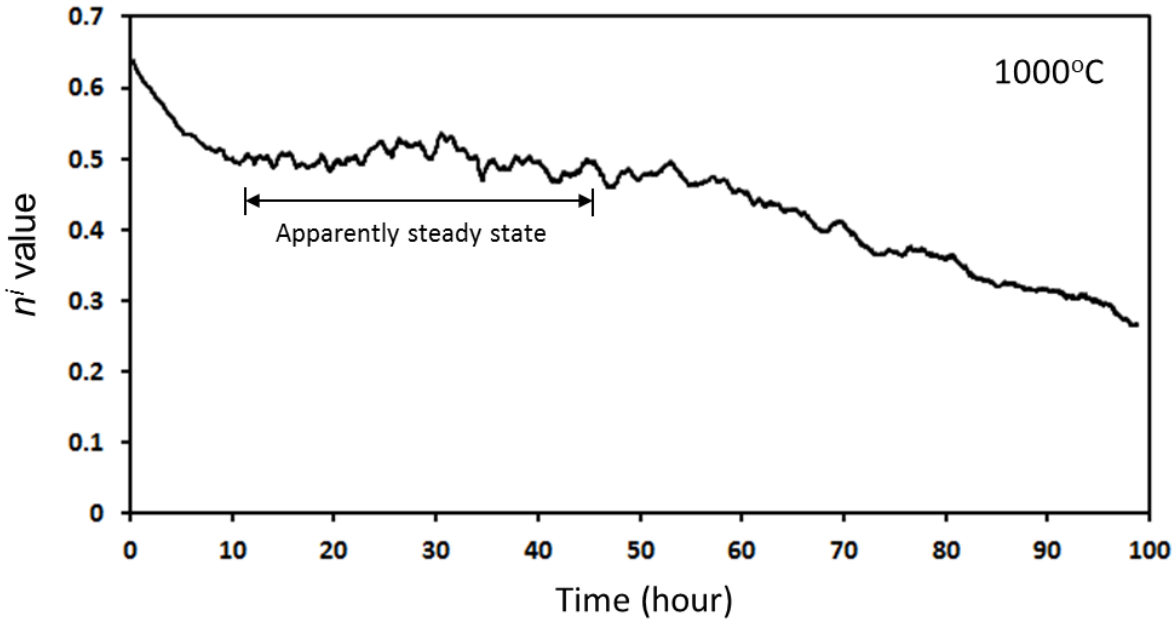

Figure 4.57 The associated n^i-value curve for the TG curves shown in figure 4.45. The n^i values are 0.5 from around 10h to 50h, which indicates the oxidation is in a steady state during this period

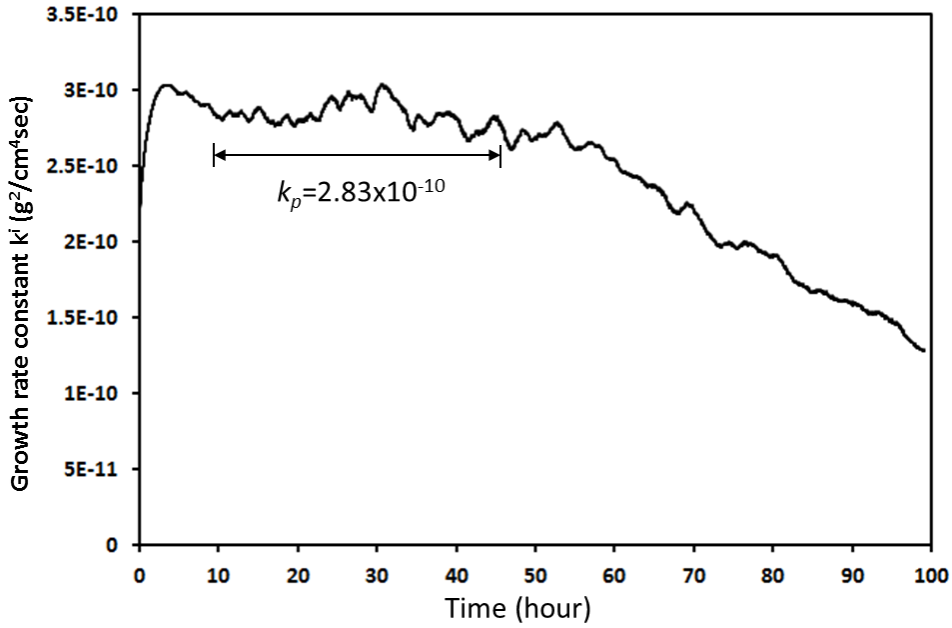

(a)

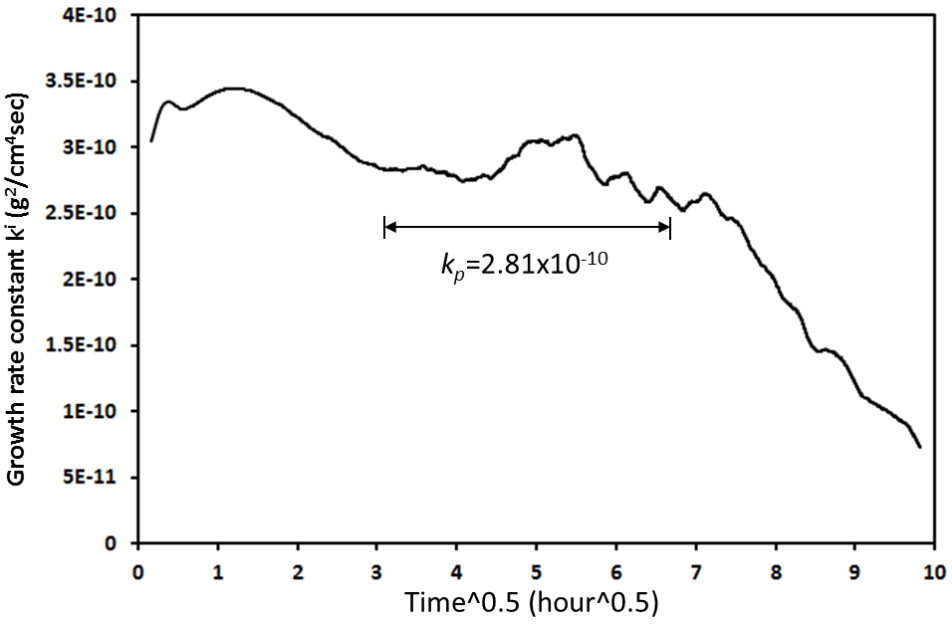

(b)

Figure 4.58 Calculated instantaneous growth rate constant k^i for Ni-5Al-3Cr-1Si alloy oxidized in dry air at 1000°C by equation 4.56 and 4.57. Both of the curve shows that the instantaneous growth rate constants k^i during around 10h to 50h are $2.8 \times 10^{-10} g^2/cm^4 sec$, which corresponds to the growth rate of NiO at this temperature.

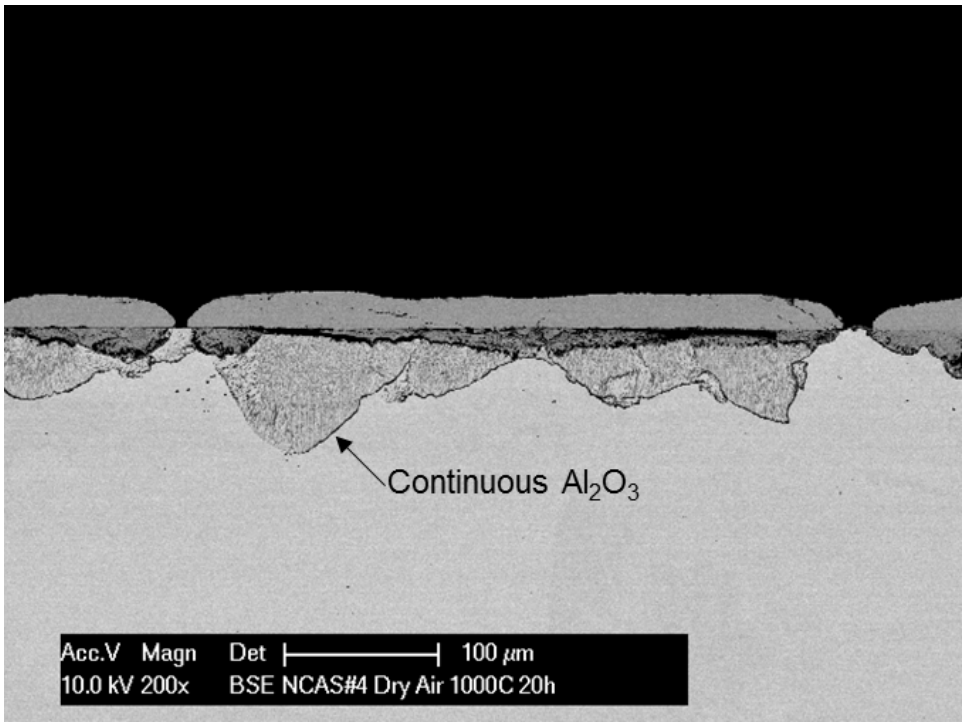

Figure 4.59 Cross-sectional SEM image of Ni-5Al-3Cr-1Si alloy oxidized in dry air at 1000^{o}C for 20h

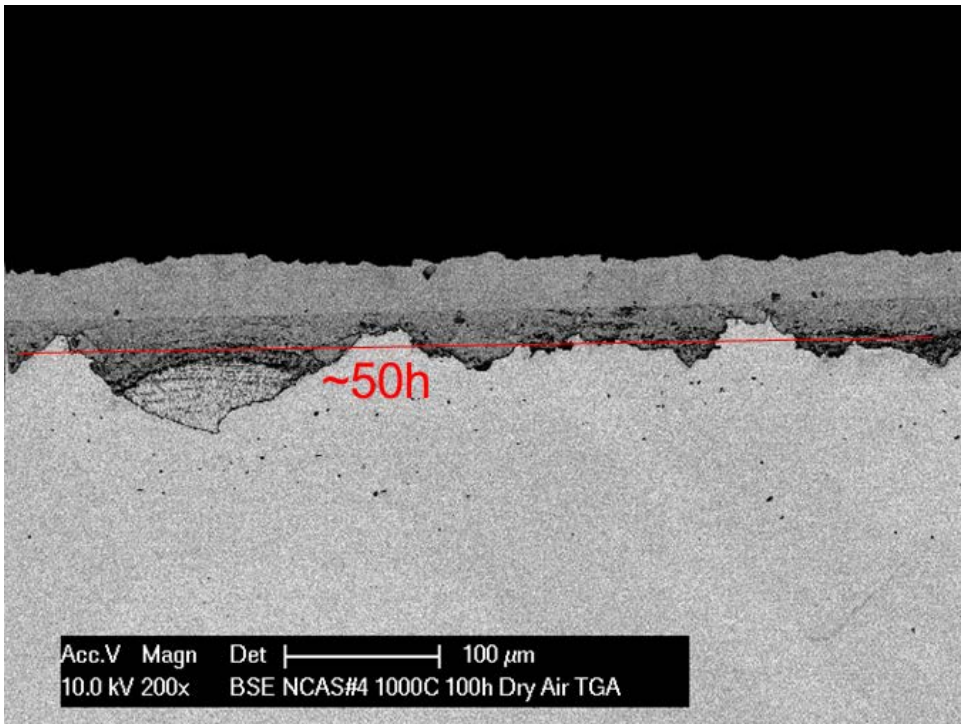

Figure 4.60 Cross-sectional SEM image of Ni-5Al-3Cr-1Si alloy oxidized in dry air at 1000^{o}C for 100h. The red line indicates that estimated thickness of NiO layer at 50h

4.2.5 Significance of the kinetics analysis by n^i-value analysis

Although the idea of using n^i values to analyze the growth kinetics are not new, this study provided a detailed investigation on several important aspects associated with the use of n^i-value analysis. The possible misunderstand of the meaning of instantaneous k^i value has been pointed out by Pieraggi[73]. In this study, it has been pointed out that although the n^i and k^i values are called the instantaneous time exponent and the instantaneous growth rate constant respectively, they are influenced by oxidation history. Therefore, analysis based solely on the determination of instantaneous kinetics parameters can lead to inaccurate conclusions.

Even so, n^i-value analysis can still be used with reasonable accuracy to confirm ideal growth kinetics. Specifically, if n^i values become a constant at 1, 0.5 or 0.33, it means the growth kinetics becomes linear, parabolic or cubic respectively. A procedure to use n^i-value analysis associated with a TG curve was summarized in subsection 4.2.4. By going through the procedure, the time for steady-state growth to be reached can be identified more reliably compared to the conventional kinetics plot and the local analysis method. Furthermore, it can also be identified by this procedure that the real growth kinetics may be more complex, i.e. the nature of the oxidation may change with time. In such a case, the n^i values will deviate from the ideal values of 1, 0.5 or 0.33. In the past, little study has paid attention to the non-ideal behaviors on the n^i-value curves. Therefore, one important contribution of this study is to emphasize that the non-ideal behavior of n^i values can be used to quantify the complex growth kinetics.

In this study, theoretical analysis and practical issues have been presented to investigate how to make use of the non-ideal behavior of n^i values to quantify the complex growth kinetics. This n^i-value analysis has been applied to several experimentally determined curves. Among

them, the most successful and thorough study was done on quantifying the extent of $\theta \rightarrow \alpha$ Al_2O_3 transformation, which will be shown in the next section.

Furthermore, to better understand the capability of the use n^i-value analysis, it is worthwhile to consider the n^i-value analysis to be a tool to draw more information from a TG curve. A n^i-value curve itself does not have any predictability unless the n^i values are ideal, such as 0.5. However, the n^i-value curve may be used to predict the "point of interest" during an oxidation process for further characterization (e.g. see subsection 4.2.3).

4.3 QUANTIFYING THE EXTENT OF $\theta \rightarrow \alpha$ TRANSFORMATION IN Al_2O_3 SCALES BY KINETICS ANALYSIS

4.3.1 Experimental Observations

From the literature[113], it is generally found that the formation of an alumina scale at 1100°C is initially dominated by the growth of θ-Al_2O_3. After some incubation period, α-Al_2O_3 growth commences such that there is $\theta + \alpha$ co-formation coupled with $\theta \rightarrow \alpha$ transformation. Eventually, all of the initially-formed θ-Al_2O_3 will transform to α-Al_2O_3, and α-Al_2O_3 will grow exclusively from that time on. Figure 4.61 shows a typical progress for this initial scale evolution[113], for the case of isothermal oxidation of (001) β-NiAl(Zr) at 1100°C in air. In this figure, the dark data points correspond to the total scale thickness; the purple and red points are the thickness of θ-Al_2O_3 and α-Al_2O_3 respectively. It is seen that there are three stages for the scale evolution in terms of the growth kinetics and phase constitution: in stage I, α-Al_2O_3 is nucleating and grows at the expense of θ-Al_2O_3. The overall growth kinetics are initially

dominated by θ-Al_2O_3 and then slowed by the transition from θ-Al_2O_3 to α-Al_2O_3. In stage II, α-Al_2O_3 phase become continuous and the overall growth kinetics are dictated by the slower-growing α-Al_2O_3. In stage III, all the scale is α-Al_2O_3 phase. The overall weight-gain kinetics correspond to the single α-Al_2O_3 growth. Stages I and II are separated by growth kinetics, while stages II and III are separated by phase constitution.

Figure 4.62 shows the distribution and morphology of the two phases (top view[114]) for isothermally oxidized (111) NiAl at 1100^{o}C from. The dark spots are rich in α-Al_2O_3. It is clear that α-Al_2O_3 is randomly nucleated and grows laterally. From a conventional TG experiment, the stages I and II can be easily distinguished. Figure 4.63 plots the weight-gain versus time for isothermal oxidation of Ni-20Al-5Cr-0.5Y-0.5Hf alloy at 1100^{o}C in air[113]. The weight gain is seen to increase rapidly for around the first two hours, which corresponds to stage I when θ-Al_2O_3 dominated the growth kinetics. After two hours, the rate of weight gain started to significantly slow. This corresponds to stages II and III when α-Al_2O_3 dominated the growth kinetics. Although the growth kinetics are characterized by thickness in Figure 4.61, the thickness is equivalent to the weight gain per unit area, which can be measured by the TG method. Therefore, the weight-gain kinetics in figure 4.47 is in good correspondence with the total thickness shown in figure 4.45. To study the instantaneous growth kinetics, equations 4.55 to 4.57 were employed.

Figure 4.64 shows the corresponding n^i-value derived using 4.55 on the curve for the weight-gain curve shown in Figure 4.63. Those n^i values are not a constant of 0.5 because the overall growth kinetics are not simple parabolic for a single phase. Rather, it decreases from around 0.5 to a minimum value of 0.15 and then tends to increase back to 0.5. This particular shape of the *n*-value curve is a result from the θ-Al_2O_3 → α-Al_2O_3 phase transformation.

Therefore, the kinetics of θ → α transformation can be extracted from this particular shape by applying a rigorous kinetics analysis.

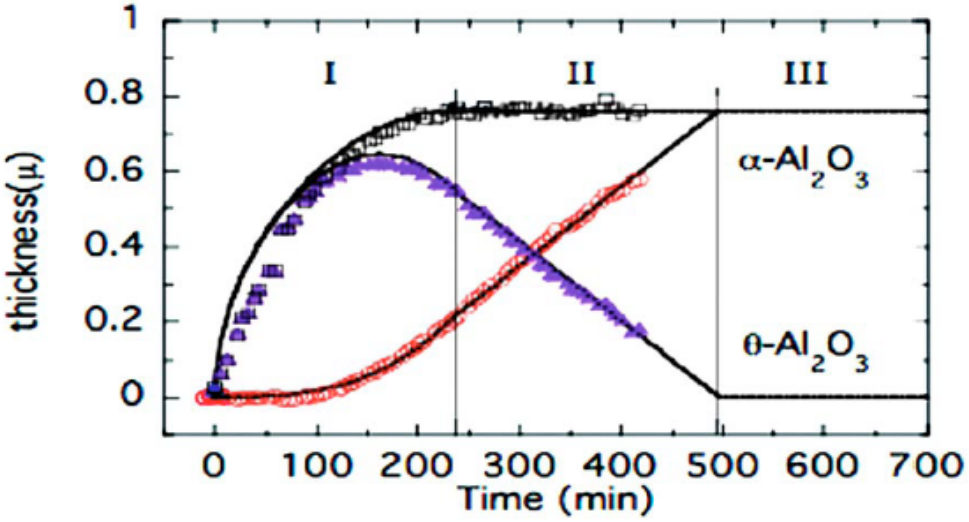

Figure 4.61 Thickness of θ-Al_2O_3 and α-Al_2O_3, grown on diamond polished 001-face of NiAl(Zr), as the oxides evolve at 1100°C[113]

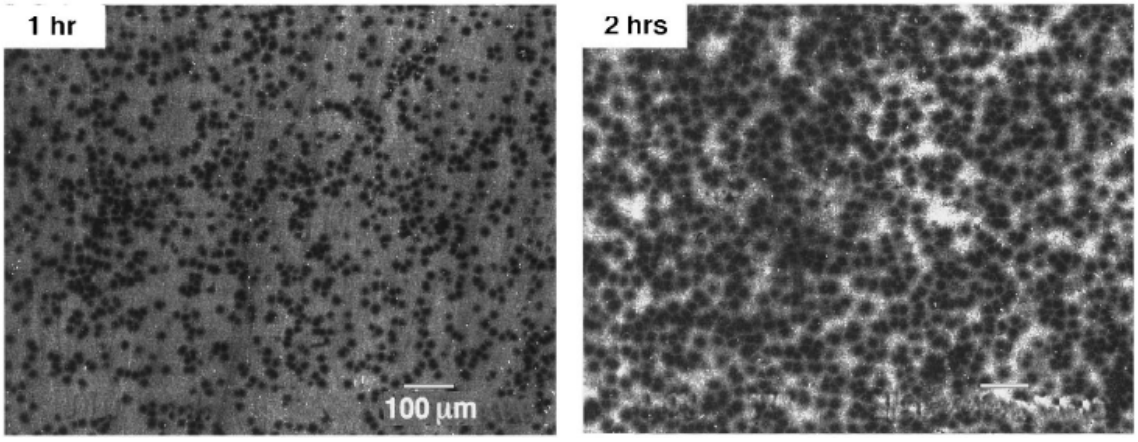

Figure 4.62 Secondary electron images of the oxide scale formed on 111-plane of NiAl at 1100°C. It was confirmed that the dark spots are α-Al_2O_3 and the matrix is θ-Al_2O_3 by a chromium luminescence spectroscopy[114]

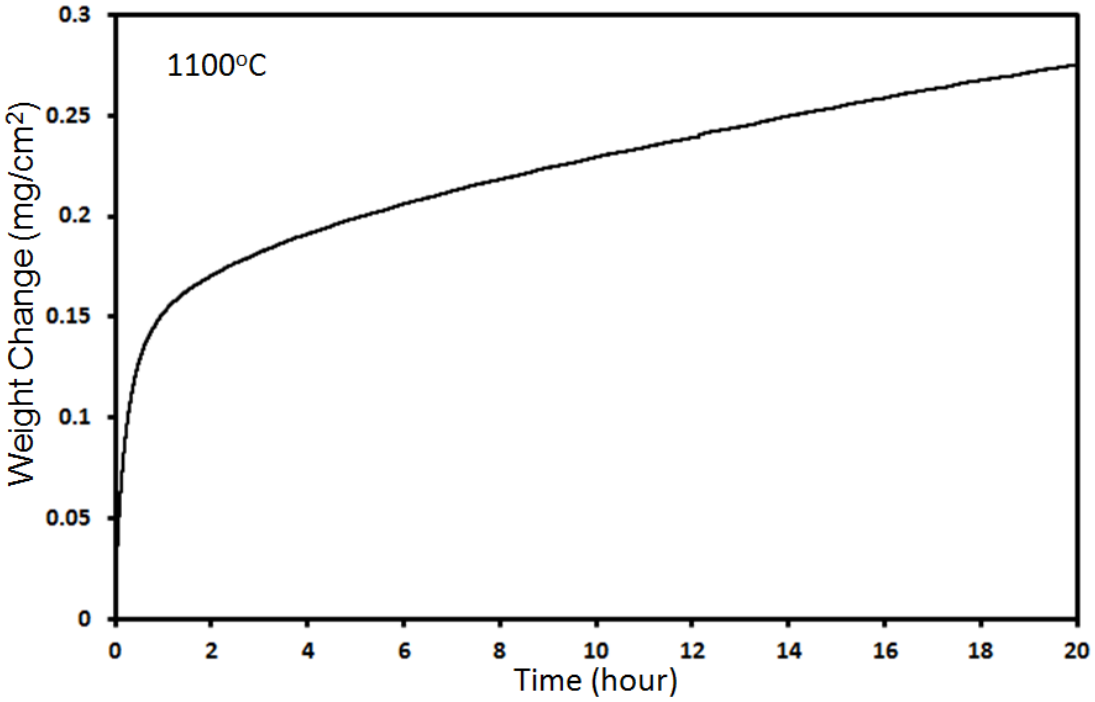

Figure 4.63 The TG data for Ni-20Al-5Cr-0.5Y-0.5Hf alloy oxidized at 1100°C in air

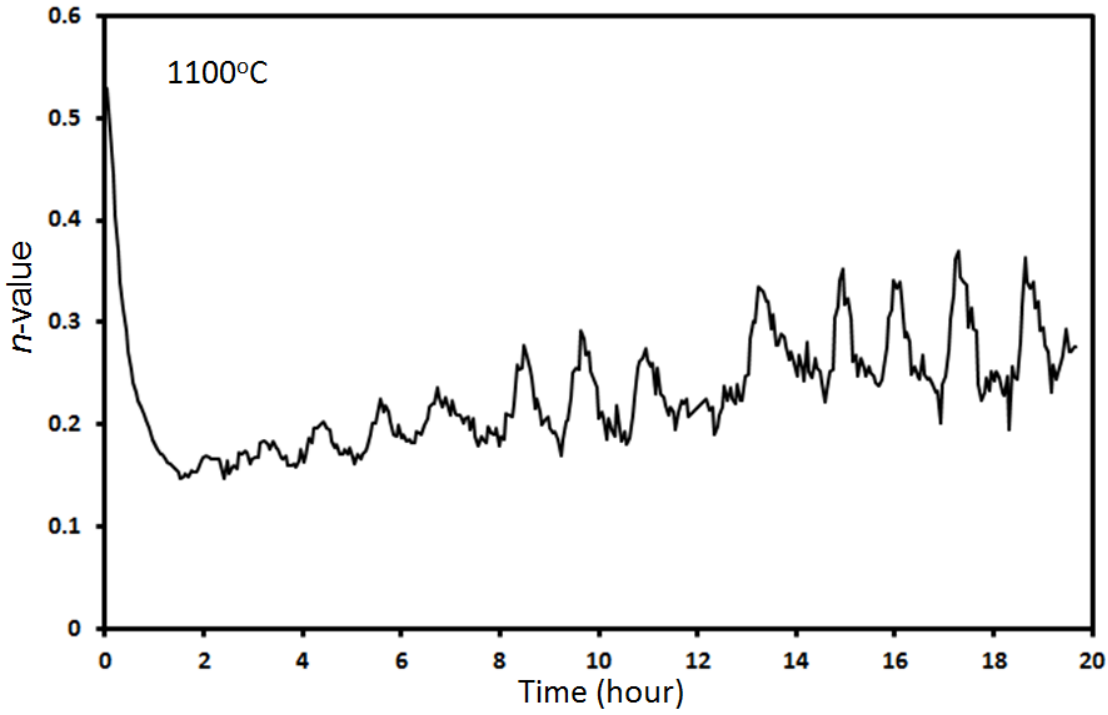

Figure 4.64 The corresponding n^i-value curve for the TG data in figure 4.47

4.3.2 Kinetics Analysis

The methodology to quantify the extent of the θ-Al_2O_3 → α-Al_2O_3 phase transformation from TG data is outlined in the following. As a starting point, it is necessary to establish a scenario model for the θ + α co-formation during the initial transient stage. Such a model must account for the θ → α transformation kinetics in order to accurately simulate the overall oxidation kinetics. Based on the experimental results, a schematic illustrating the three stages is shown by Figure 4.65. For the co-formation scenario, two important points should be noted: (1) The θ → α phase transformation itself does not cause weight change. It is the oxidation of the alloy, i.e. oxygen uptake, which causes the weight gain. (2) The overall oxidation kinetics are controlled by diffusion rates through θ and α phases. Based on the scenario shown in figure 4.49 stage I, as long as some area is covered by α-Al_2O_3, it significantly slows down the weight gain on this area, even of θ-Al_2O_3 is present above the α-Al_2O_3. Therefore, it is the lateral growth of α-Al_2O_3 that blocks the fast diffusion through θ-Al_2O_3 phase and reduces the instantaneous weight-gain kinetics. The lateral diffusion within θ-Al_2O_3 is neglected because it is a minor effect compared to blockage effect by lateral growth of α-Al_2O_3, which can reduce the growth rate by as much as two orders of magnitude[115].

In this study, it is assumed at any time during the θ + α co-formation, the weight-gain rate on the alloy/scale interface area covered by α-Al_2O_3 is the same as the growth rate of single α-Al_2O_3. The weight-gain rate on area covered by θ-Al_2O_3 is the same as the growth rate of single θ-Al_2O_3. Both θ-Al_2O_3 and α-Al_2O_3 are assumed to grow according the parabolic law:

$$\Delta m_i=(k_p^i t)^{1/2} \tag{4.80}$$

where Δm_i is weight gain per unit area, k_p^i is the parabolic rate constant of θ or α phase.

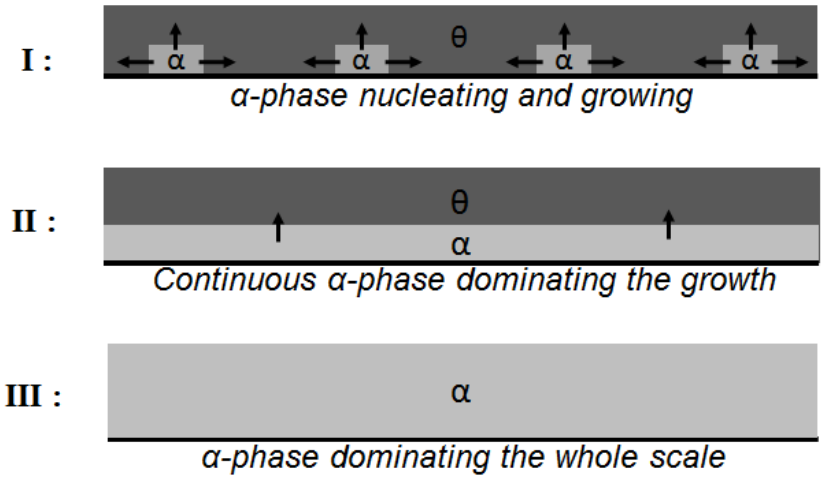

Figure 4.65 Schematic of three stages of alumina scale growth with initial θ- alumina formation

Since the area covered by θ and α phases are changing with time, a differential equation for the weight gain is needed. Taking the differential form of equation 4.80 gives:

$$dm_i=(k_p^i)^{1/2}dt^{1/2} \tag{4.81}$$

where dm_i has the unit of mass gain per unit area. Assuming that at any time, the area covered by α-Al_2O_3 is A_α and the area covered by θ-Al_2O_3 is A_θ, the differential of total weight gain at this time is the sum of weight gain by α and θ:

$$dm \cdot A_{total} = dm_\alpha \cdot A_\alpha + dm_\theta \cdot A_\theta \tag{4.82}$$

Dividing both sides of equation 4.82 by the total area gives:

$$dm = dm_\alpha \cdot \frac{A_\alpha}{A_{total}} + dm_\theta \cdot \frac{A_\theta}{\cdot A_{total}} \tag{4.83}$$

$$dm = dm_\alpha \cdot f_\alpha + dm_\theta \cdot f_\theta \tag{4.84}$$

where f_α and f_θ are the area fractions of α and θ with:

$$f_\alpha + f_\theta = 1 \tag{4.85}$$

Thus, substituting equation 4.81 and equation 4.85 into equation 4.84 gives:

$$dm = f_\alpha k_\alpha^{1/2} dt^{1/2} + (1 - f_\alpha) k_\theta^{1/2} dt^{1/2} \tag{4.86}$$

The total weight gain per unit area (Δm) at any time is the integral of equation 4.86 from time zero to that specific time:

$$\Delta m = \int_{t=0}^{t=t} \left[f_\alpha k_\alpha^{1/2} dt^{1/2} + (1 - f_\alpha) k_\theta^{1/2} dt^{1/2} \right] \tag{4.87}$$

In this equation, the area fraction of α-Al_2O_3 (f_α) is a function of time. After collecting terms, equation 4.87 can be written as:

$$\Delta m = (k_\theta^{1/2} - k_\alpha^{1/2}) \int_0^t (1 - f_\alpha) \cdot d(t^{1/2}) + k_\alpha^{1/2} t^{1/2} \tag{4.88}$$

The k_α and k_θ used in equation 4.77 are assumed to be the parabolic growth rate constants for single α-Al_2O_3 and θ-Al_2O_3; however, it should be realized that the k_α and k_θ conventionally determined from experimentally TG data plotting Δm^2 versus t or Δm versus $t^{1/2}$ plot are not exactly the same as the k_α and k_θ for single α-Al_2O_3 and θ-Al_2O_3. Specifically, when calculating k_θ from early-stage TG data, α-Al_2O_3 is present to some extent and that decreases the determined k_θ. When calculating k_α at a later time, the presence of faster-growing θ-Al_2O_3 during previous oxidation will also affect the calculated k_α. The k_α and k_θ determined directly from TG data should be expected to be slightly different from those determined using the present kinetics analysis method.

To calculate the total weight gain per unit area (Δm) as a function of time, an accurate expression for f_α is needed. From Figure 4.61, it is seen that the growth of α-Al_2O_3 has an incubation time at the beginning. It is very likely that the area fraction also has certain incubation time at the beginning. After that, α it has a relatively fast propagation stage and finally approaches fully transformation (f_α =1). Therefore, the area fraction of α-Al_2O_3 as a function of reaction time should have the general characteristics of any diffusion-controlled transformation.

Indeed, Bagwell et al.[116] reported that the θ → α transformation is diffusional in nature. Accordingly, the θ → α transformation should have a sigmoidal shape with respect to time, in accordance with the *Johnson-Mehl-Avrami* (JMA)[117] expression:

$$f_\alpha = 1 - \exp\left(-Kt^\omega\right) \tag{4.89}$$

where K and ω are two parameters characterizing the nature of the transformation. The time exponent ω value is usually written as n in Johnson-Mehl-Avrami model[117]. In our analysis, we use ω instead of n to differentiate it from the time exponent n in the kinetics of oxidation in equation 4.54.

With equations 4.88 and 4.89, the kinetics of phase transformation can be determined by fitting the simulated TG curve with that determined experimentally via TG analysis. There are a totally four parameters in these two equations: k_α, k_θ, K and ω. The parabolic growth rate constants k_α and k_θ can be found either from literature or calculated from the measured TG curve. The determination of K and ω can be achieved by simply fitting the weight-gain curve; however, the level of accuracy that can be reached by this fitting is not very high. This is because the weight gain is not very sensitive to the change in K and ω values. To improve the accuracy, the instantaneous n-value curve is employed (see previous section). A typical n^i-value curve for θ → α phase transformation is shown in Figure 4.64. The curve starts with some values close to 0.5. This must be because the θ-Al_2O_3 dominates the oxide at the very beginning while α-Al_2O_3 is in its incubation stage, as shown by stage I in Figure 4.61. During this period, the growth kinetics are close to those associated with single θ-Al_2O_3 phase. After the incubation period, the slower-growing α-Al_2O_3 starts to form, as shown by stage II in Figure 4.61. Hence the n^i values start to decrease. During the co-formation stage, the weight gain is expected to follow a complex form shown by equation 4.88. In the same stage, the calculated the n^i-value curve is found to a

concave shape shown in Figure 4.64. Indeed, this shape is dictated by the weight gain function shown by equation 4.88. Although it is difficult to find a definitive physical meaning of the minimum n^i value, the position of this minimum is inferred to be closely related with the kinetics of phase transformation and it is very sensitive to the change in K and ω values. This feature has a significant advantage to improve the level of accuracy of the fitting procedure. Eventually, the growth will be dominated by single α-Al_2O_3 as a steady-state stage, so the n^i values tend to increase back to 0.5 in Figure 4.64.

4.3.3 Determining the extent of $\theta \rightarrow \alpha$ phase transformation

The weight-gain curve for the oxidation of Ni-20Al-5Cr-0.5Y-0.5Hf in air at 1100^{o}C was shown in Figure 4.63. Its corresponding n^i-value curve was shown in Figure 4.64. To determine the kinetics of the $\theta \rightarrow \alpha$ phase transformation for this isothermal oxidation test, initial values for k_α, k_θ, K and ω are needed.

Figure 4.66 shows the conventional Δm-$t^{1/2}$ plot to determine k_α and k_θ. By calculating the slopes for the first 30min and after 6 hours, it was found that $k_\theta = 1.3\text{x}10^{-11}\text{g}^2/\text{cm}^4\text{sec}$ and $k_\alpha = 3.5\text{x}10^{-13}\text{g}^2/\text{cm}^4\text{sec}$. The time exponent ω in equation 4.89 has a value between 1 and 3 in most cases[117]. Under some special cases, this value can be greater than 4 or smaller than 1. In our analysis, the value for n is initially set to be 1.3. The parameter K is related with transformation rate. To have a reasonable initial value, K can be estimated by $K \approx 3/t_{tr}$, where t_{tr} is the time for the minimum point on n^i-value curve. Incorporating all those initial values into equations 4.88 and 4.89, a simulated weight-gain curve and its associated n^i-value curve can be obtained. Figure 4.67 shows the experimental and simulated weight-gain curve. Their corresponding n^i-value

curves are shown in Figure 4.68. Since the four initial parameters are reasonable, the simulated curves are not significantly different from the experimental curves.

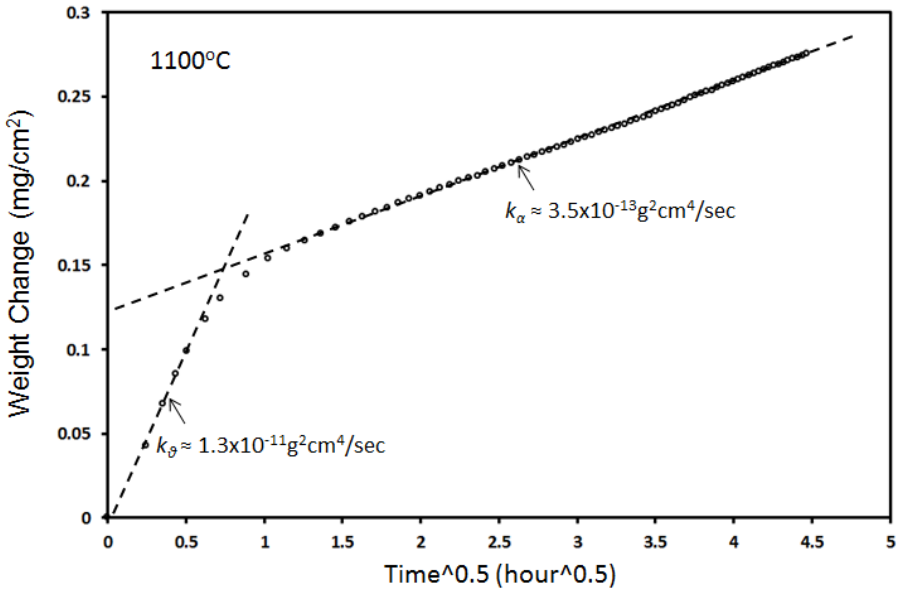

Figure 4.66 Determining k_α and k_θ by conventional $\Delta m\text{-}t^{1/2}$ plot. The circles are selected TG data from original 15,000 data points in an interval of 200 points

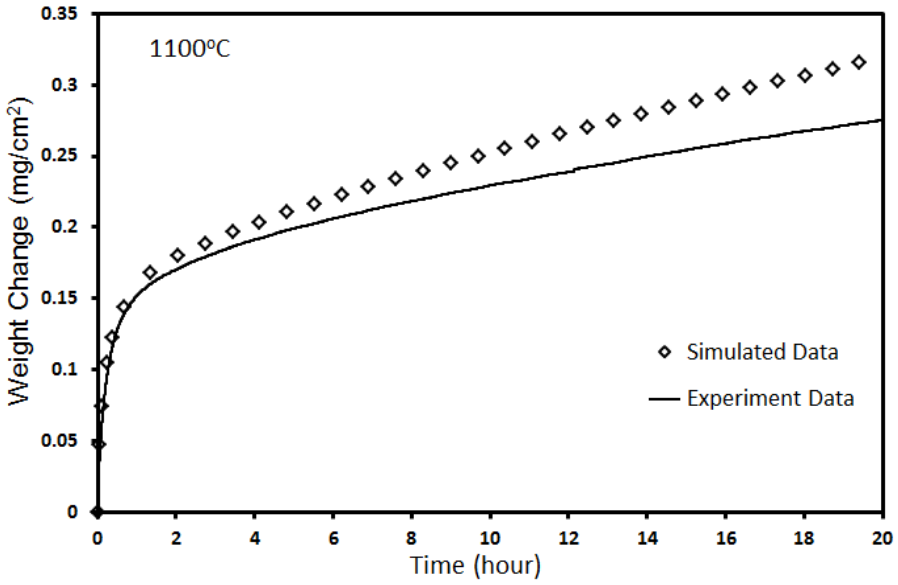

Figure 4.67 Experiment (solid line) and simulated (diamond) weight gain curve with initial values. The simulated data are shown as discrete points for the purpose of clarity. Those points are selected from 15000 data points corresponding to the experimental data as well

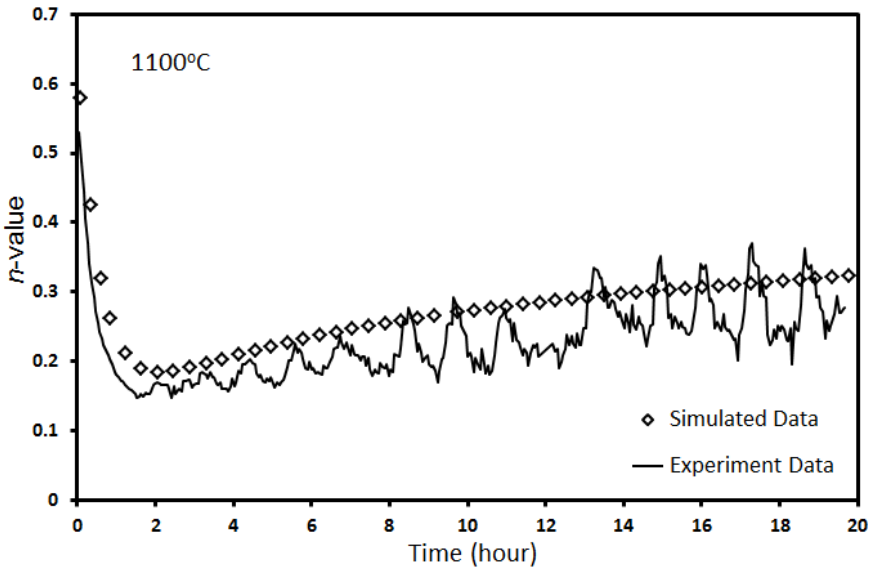

Figure 4.68 Experiment (solid line) and simulated (diamond) *n*-value curve with initial values. The approximate sinusoidal shape of *n*-value curve after 2 hour may come from noise or a physical procedure that are not related with this study

Before applying the simulation procedure, the sensitivity of simulated TG curve and its associated n^i-value curve to the change of K, ω, k_α and k_θ on have been investigated independently. This is done by checking the change of TG curve and its associated n^i-value curve by changing one parameter at a time and keep all other parameters constants. Those results are shown in Figure 4.69 to Figure 4.72. It is seen in Figure 4.69 and Figure 4.70 (b), the time corresponds to the minimum value on the n^i-value curve were not changed much with changing k_α and k_θ, although the n^i values changed significantly. Meanwhile, TG curves also changed significantly with changing k_α and k_θ. This is actually an example showing that when the overall kinetics are not in a steady-state, the n^i values have no physical meaning but depends on the specific kinetics.

From Figure 4.71 and Figure 4.72, n^i values are more sensitive to the changes of K and ω. Therefore, to determine the parameters for the $\theta \rightarrow \alpha$ transformation, K and ω are adjusted

mainly by matching the *n*-value curve while k_α and k_θ are adjusted by matching the weight gain curve. After an iterative process, K, ω, k_α, k_θ values are adjusted to arrive at a best fit.

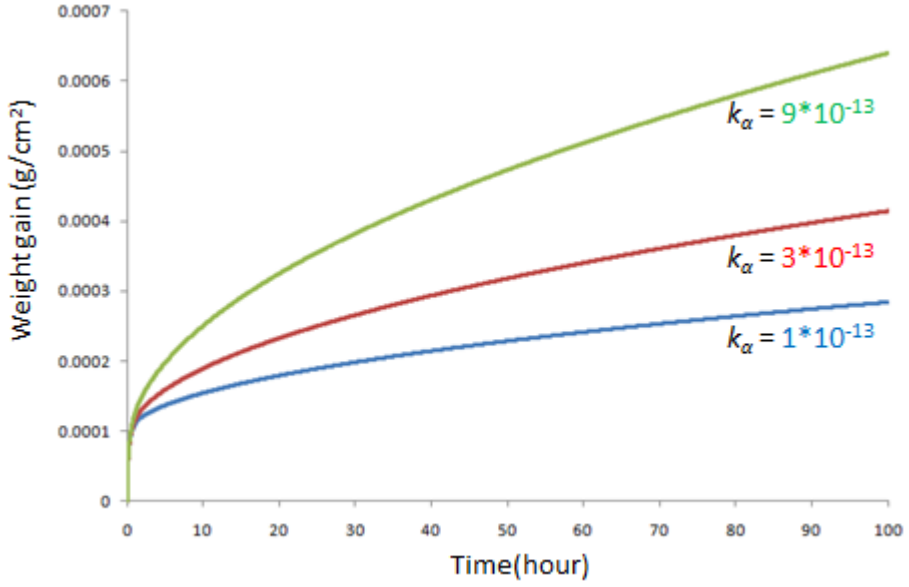

(a)

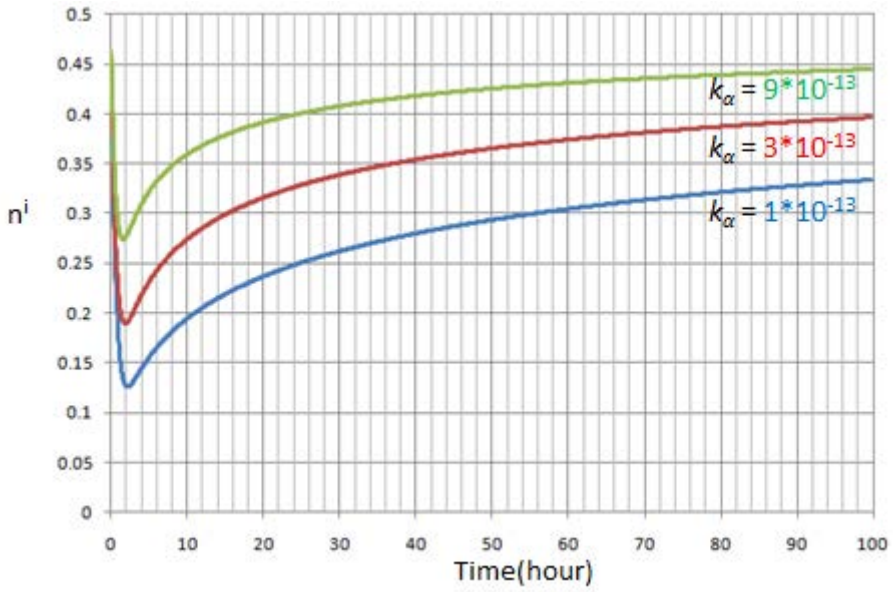

(b)

Figure 4.69 Sensitivity check of TG and its associated n^i-value curve to the change of k_α

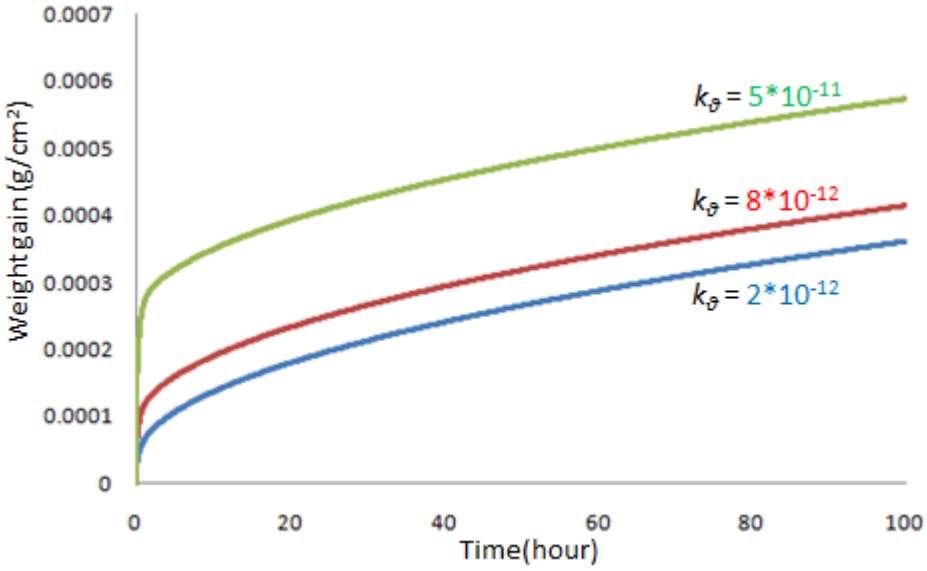

(a)

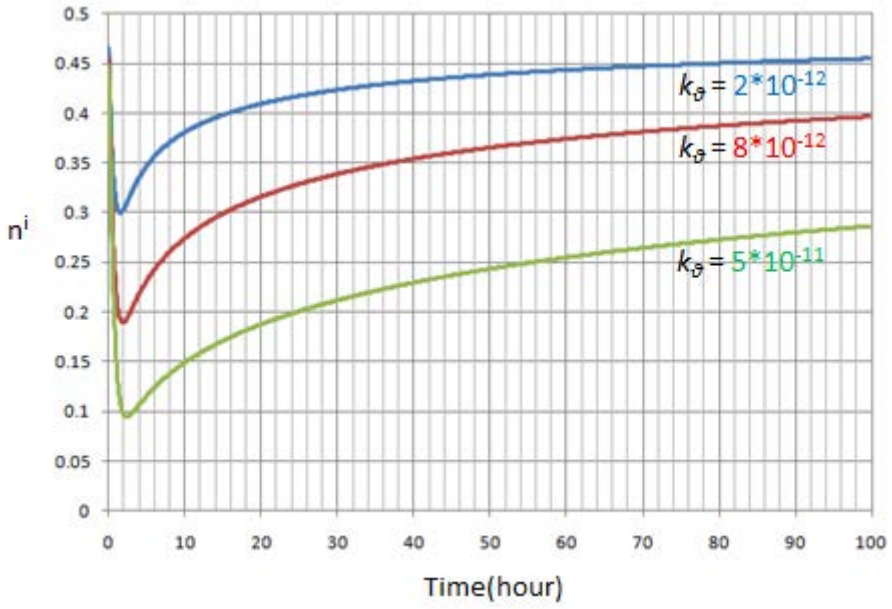

(b)

Figure 4.70 Sensitivity check of TG and its associated n^i-value curve to the change of k_0

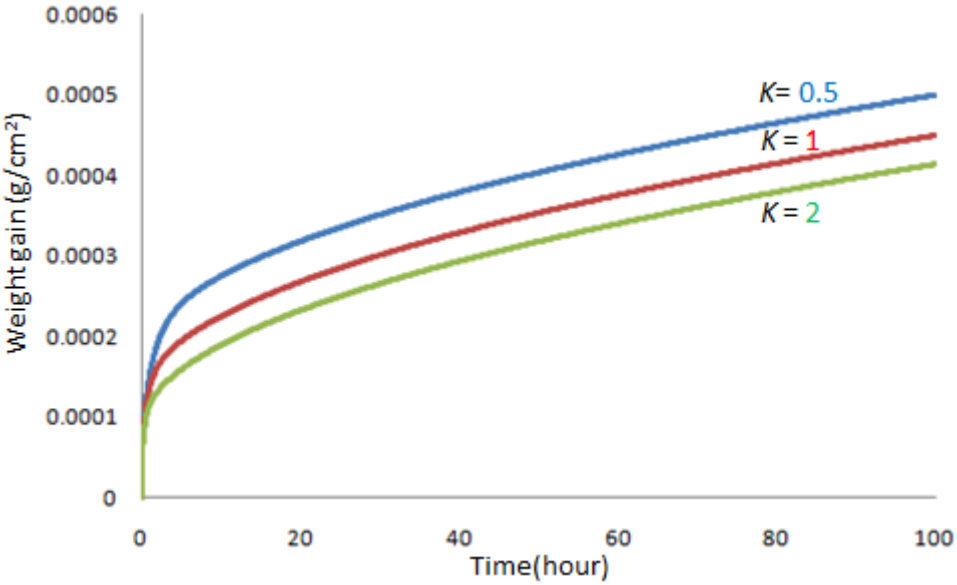

(a)

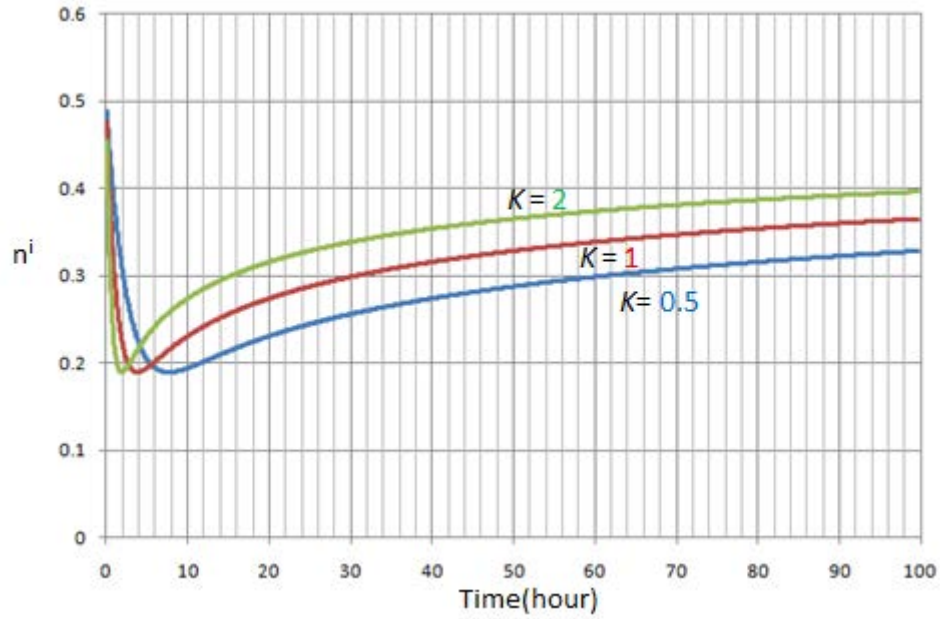

(b)

Figure 4.71 Sensitivity check of TG and its associated n^i-value curve to the change of K

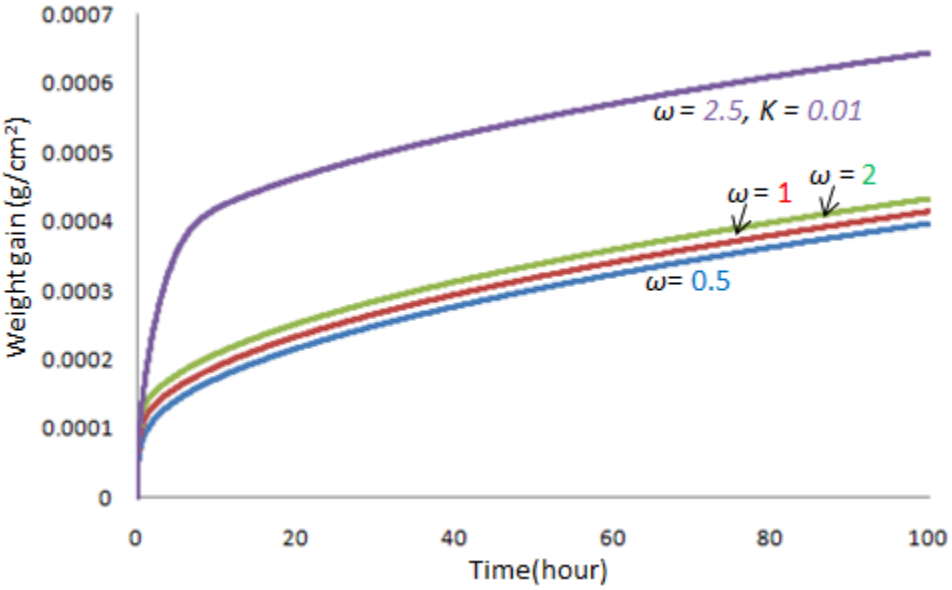

(a)

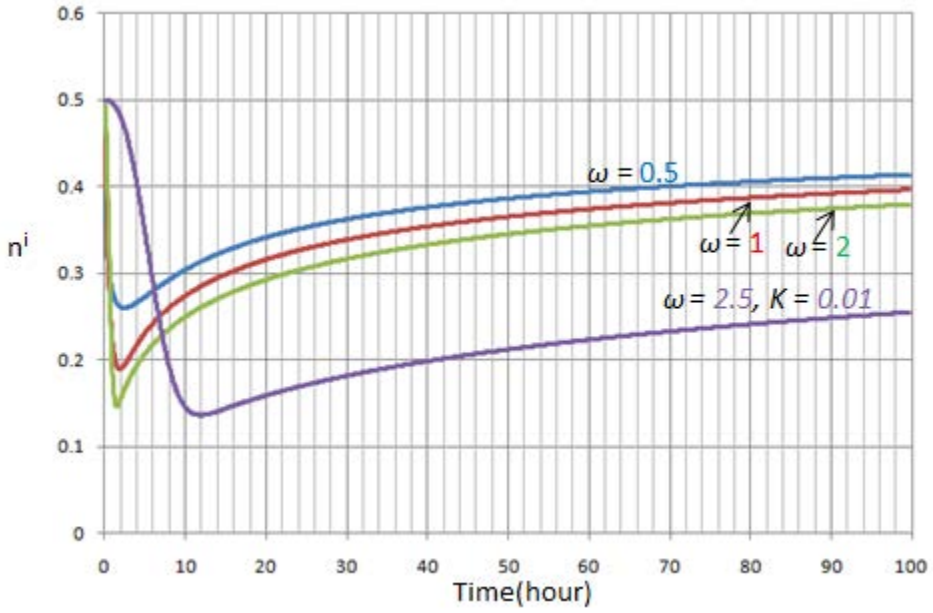

(b)

Figure 4.72 Sensitivity check of TG and its associated n^i-value curve to the change of ω. K value for ω=0.5, 1,2 are set to be 2. An sample of ω = 2.5 and K = 0.01 is shown to illustrate the effect by changing K and ω together

Figure 4.73 and Figure 4.74 show the experimental and simulated weight gain and n^i-value curves after best fitting. It is clear that actual kinetics are well simulated for both the initial and the steady-state stages. The final values to achieve the best fitting are: K=2.1, ω=1.0, $k_\alpha = 3.0\text{x}10^{-13}$ $g^2/cm^4 \cdot sec$ and $k_\theta = 1.5\text{x}10^{-11}$ $g^2/cm^4 \cdot sec$. Taking K and ω into equation 4.89, the fraction of α-Al_2O_3 as a function of time can be determined, which is shown by Figure 4.75. The fraction of α-Al_2O_3 calculated by glancing-angle XRD patterns of the same alloy are also shown for comparison. By comparing the time for the minimum point on n-value curve in Figure 4.74 and the fraction of α-Al_2O_3 corresponding to this time on Figure 4.75, the time for the minimum point is found to correspond to around 90% of α-Al_2O_3 was established.

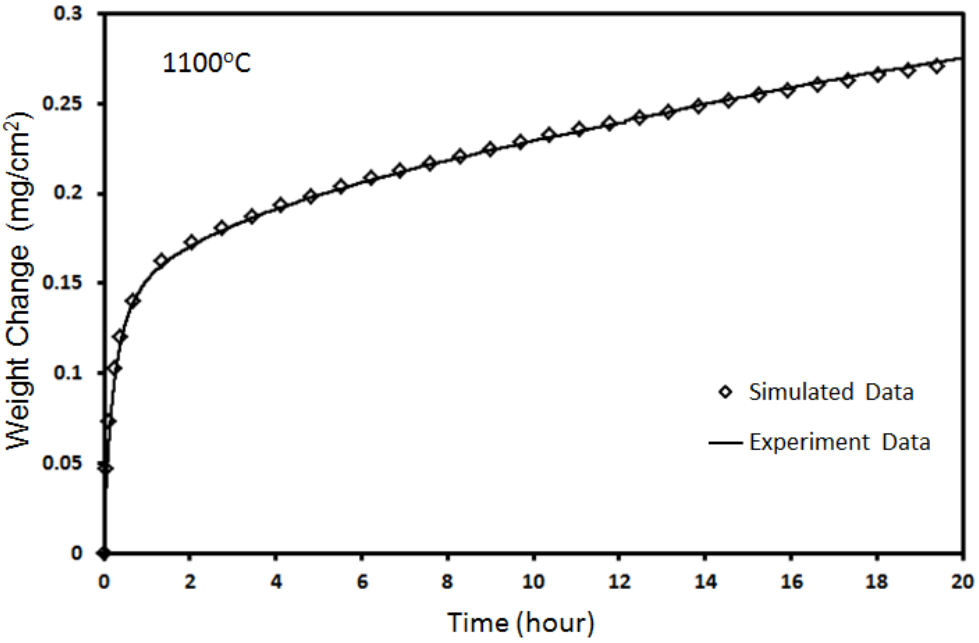

Figure 4.73 Experiment (solid line) and simulated (diamond) weight gain curve after best fitting. The merit of this figure is that weigh gain curve is well-simulated for both initial oxidation stage and the steady-state oxidation stage

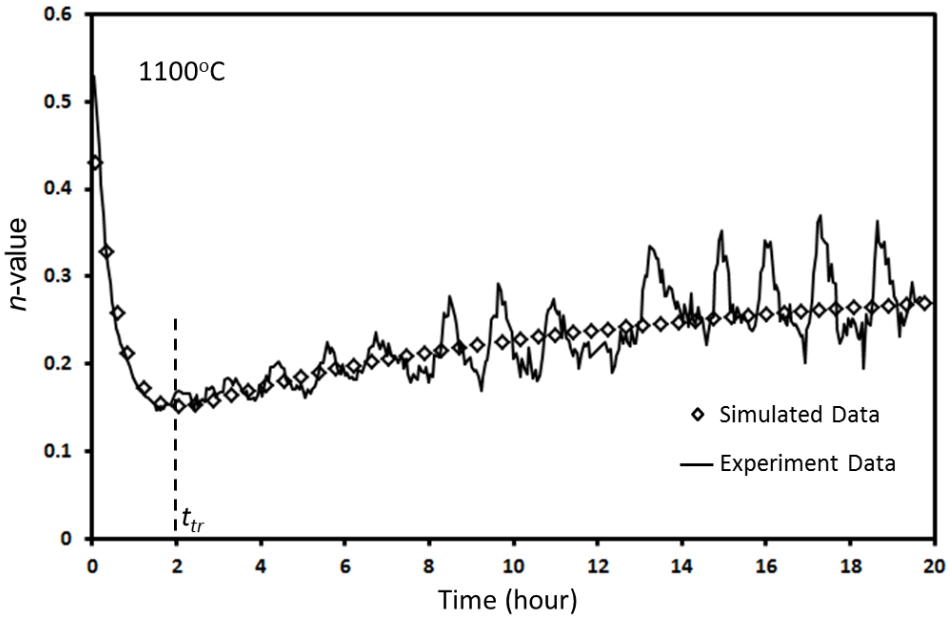

Figure 4.74 Experiment (solid line) and simulated (diamond) *n*-value curve after best fitting

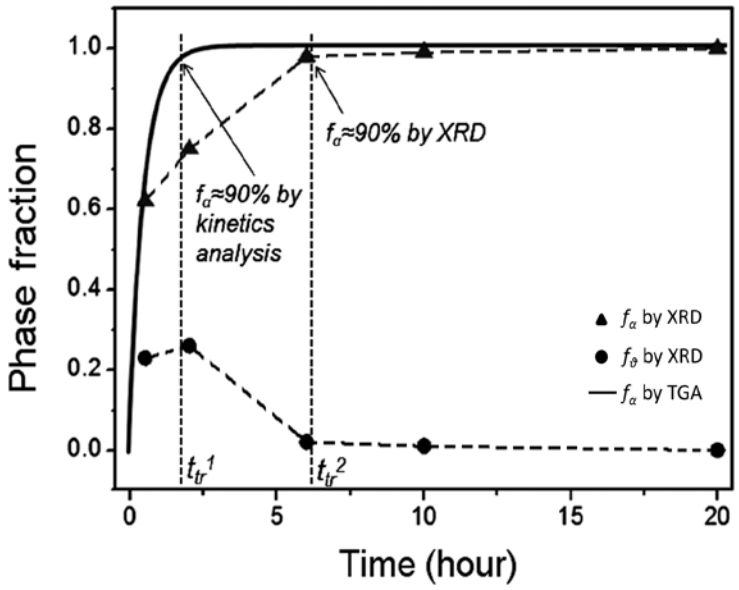

Figure 4.75 The fraction of α-Al_2O_3 determined by kinetics analysis method and glancing angel XRD method

4.3.4 Discussion on the physical meaning of determined parameters

The physical meaning of the minimum on n^i-value curve

It is seen that the time for the minimum value on the n^i-value curve corresponds to the time that around 90% of the scale/alloy interface is covered by α-Al_2O_3. This time can be defined as the transition time for the growth kinetics. For the isothermal oxidation of Ni-20Al-5Cr-0.5Y-0.5Hf in air at 1100^{o}C, this transition time was found to be around 2 hours. By comparing this transition time (t_{tr}^1) with the transition time (t_{tr}^2) determined by conventional X-ray diffraction shown in Figure 4.75, there is a difference in this two transition time. This is because the X-ray diffraction is a volumetric measurement, such that it measures the volume fraction of α-Al_2O_3 phase in the scale. In accordance with the scenario in Figure 4.65, transition time for growth kinetics (t_{tr}^1) corresponds to the time between stage I and II. However, transition time (t_{tr}^2) corresponds to the time between stage II and III. In terms of the oxidation of the alloys, since the

initial stage has orders of magnitude higher oxidation rate[115], it is always preferred to reduce this transition time or bypass this stage in order to reduce the aluminum consumption in the alloy. More importantly, the transition time (t_{tr}^{1}) determined by the minimum value on the n^{i}-value curve determines the time the overall growth kinetics are reduced. After this transition time, the remaining θ phase is just some remnant which will be consumed with time. Therefore, this transition time has a significant physical meaning in terms of the oxidation study. Because for the purpose of the protection of the alloy, it is always more important to know how fast the scale will grow and how much alloying element will be consumed.

The physical interpretation of determined parameters

The interpretation of the k_θ value determined by this kinetics analysis is straightforward. As discussed previously, the k_θ determined by this kinetics analysis is the growth rate constant for a single θ-Al_2O_3 phase, while, k_θ determined by conventional Δm-$t^{1/2}$ plot is growth rate constant for θ-Al_2O_3 phase accompanied by an increasing amount of the slower-growing α-Al_2O_3 phase. Therefore, it is not surprising to see that k_θ value determined by this kinetics analysis $1.5x10^{-11}$ g^2/cm^4·sec is a little higher than $k_\theta = 1.3x10^{-11} g^2/cm^4$sec determined by the conventional method shown in Figure 4.66.

The interpretation of the k_α value determined by the kinetics analysis is actually more complex than it might be expected. There are two important aspects that may influence the value of k_α, one is the influence of diffusion through θ-α phase boundaries and grain boundaries; the other is the θ → α phase transformation in the growth direction. The nucleation and growth of α-Al_2O_3 is accompanied by a large change of the amount of θ-α phase boundaries and grain boundaries present in the scale. Those boundaries are high diffusive paths and change in the amount of the boundaries will change the effective rate of reactant diffusing through the oxide

scale. This effect will vary the determined k_α value or K and ω values. However, it is important to realize that the θ → α transformation will decrease the overall growth kinetics by two orders of magnitude; while by considering the effective diffusion coefficient as $D_{eff} = f_{gb}D_{gb} + f_l D_l$, to increase the D_{eff} by two orders of magnitude, f_{gb} must also be increased by around two orders of magnitude as well. Careful characterization of the evolution of grain sizes in α-Al_2O_3 is required to estimate this effect. At this moment, the influence by the change in boundaries is expected to be negligible compared to the lateral growth of α-Al_2O_3.

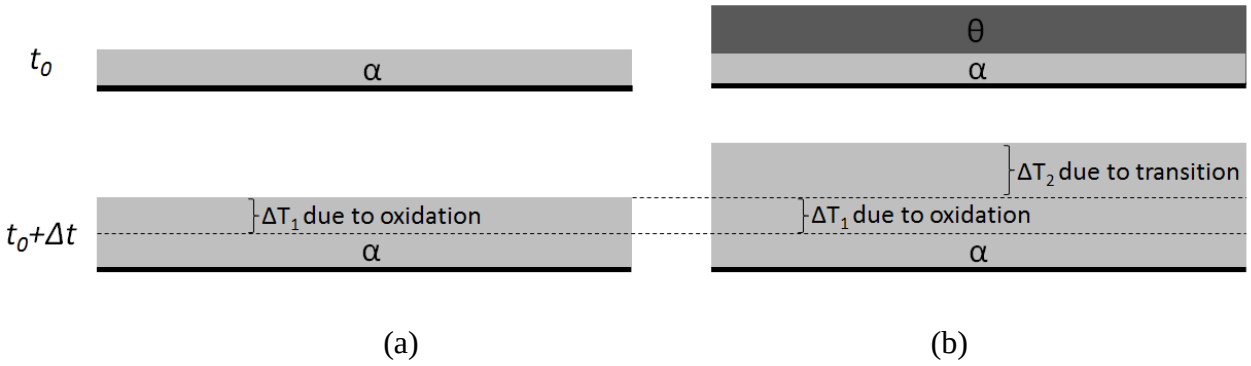

Figure 4.76 Schematic to show the influence by phase transition in the growth direction. In case (a), there is only growth due to oxidation. In case (b), the growth in Δt is due to both oxidation and phase transition. The extent of scale growth and phase transformation is exaggerated

The influence of the θ → α phase transformation in the growth direction is illustrated in the simplified schematic in Figure 4.76. Suppose there is only α-Al_2O_3 (Figure 4.76 a), after a small amount of time Δt after t_0, the thickness of the scale will be increased by ΔT_1 due to oxidation. Comparatively, if there is θ-Al_2O_3 above α-Al_2O_3 (Figure 4.76 b), after the small amount of time Δt, the thickness of the scale will be increased by ΔT_1 due to oxidation plus ΔT_2 due to phase transformation. Then, for the next Δt, since the scale with previous phase transformation is thicker, the diffusion distance is longer, so that the thickness increase due to oxidation is less.

Consequently, the weight gain during the second Δt is less, which corresponds to a reduced instantaneous growth rate at $t_0+2\Delta t$. This effect will invalidate the assumption that α-Al_2O_3 during the transition grows at the same rate as that for a single α-Al_2O_3 phase to some extent. Specially, $\theta \rightarrow \alpha$ phase transformation in the growth direction will decrease the calculated k_α and influence the determined K and ω. This effect persists even after the continuous α-Al_2O_3 layer is established. Accurate assessment of this effect during the transition is not straightforward, since the $\theta \rightarrow \alpha$ transformation rate in the growth direction is not known. However, this effect can be estimated by checking the k_α after the continuous α-Al_2O_3 layer is established. At this stage, f_α is a constant of 1. In equation 4.88, 1- f_α is a constant of 0. Therefore the integration term after this stage is actually a constant. The only parameter that dictates the weight gain kinetics are k_α. In Figure 4.73, it is clear that the experiment and simulated curves are in very good agreement after the transition time. Therefore, it can be deduced that the phase transformation in the growth direction does not affect the current kinetics analysis significantly. Qualitatively, if the initially formed θ-Al_2O_3 is thicker, this influence will be not negligible. Quantification of this effect may be complex, because if this effect is not negligible, due to the effect shown in Figure 4.76, the weight gain kinetics cannot be estimated by equation 4.88 anymore.

The interpretation of ω value is not straightforward either. This is mainly because in our case, the phase transformation is accompanied by alloy oxidation. The new alumina keeps forming from the oxidation of alloy. As a result, the total volume of alumina keeps increasing, not like the case that the total volume is conserved in Johnson-Mehl-Avrami model[117]. Despite this fact, ω value is directly related with the incubation time. For the same K value, the larger the ω value is, the longer the incubation time is. If assuming the incubation time is the result from

difficulty to nucleate, a larger ω value indicates that it is more difficult to nucleate the new phase. Meanwhile, the ω value determined in this example is around 1. In Johnson-Mehl-Avrami analysis, ω=1 corresponds to "grain boundary nucleation after saturation". This situation corresponds to "interface nucleation after saturation" in this study. There are two points for the physical interpretation of ω=1. The first one is that the nucleation should occur at the interface and the second one is that the nucleation sites are saturated, i.e. no more nucleation occurs. Figure 4.77 shows a SEM image of Al_2O_3 scale formed on Ni-55at%Al after oxidation at 1100^{o}C for 11min [118]. It is clearly shown that the α-Al_2O_3 nucleates at the scale/alloy interface. Meanwhile, as shown in Figure 4.62, all the dark spots (corresponds to α-Al_2O_3) have relatively a uniform size, which means there was no more nucleation occurred. In other words, if there was nucleation occurred, there should be some smaller spots with a series of sizes.

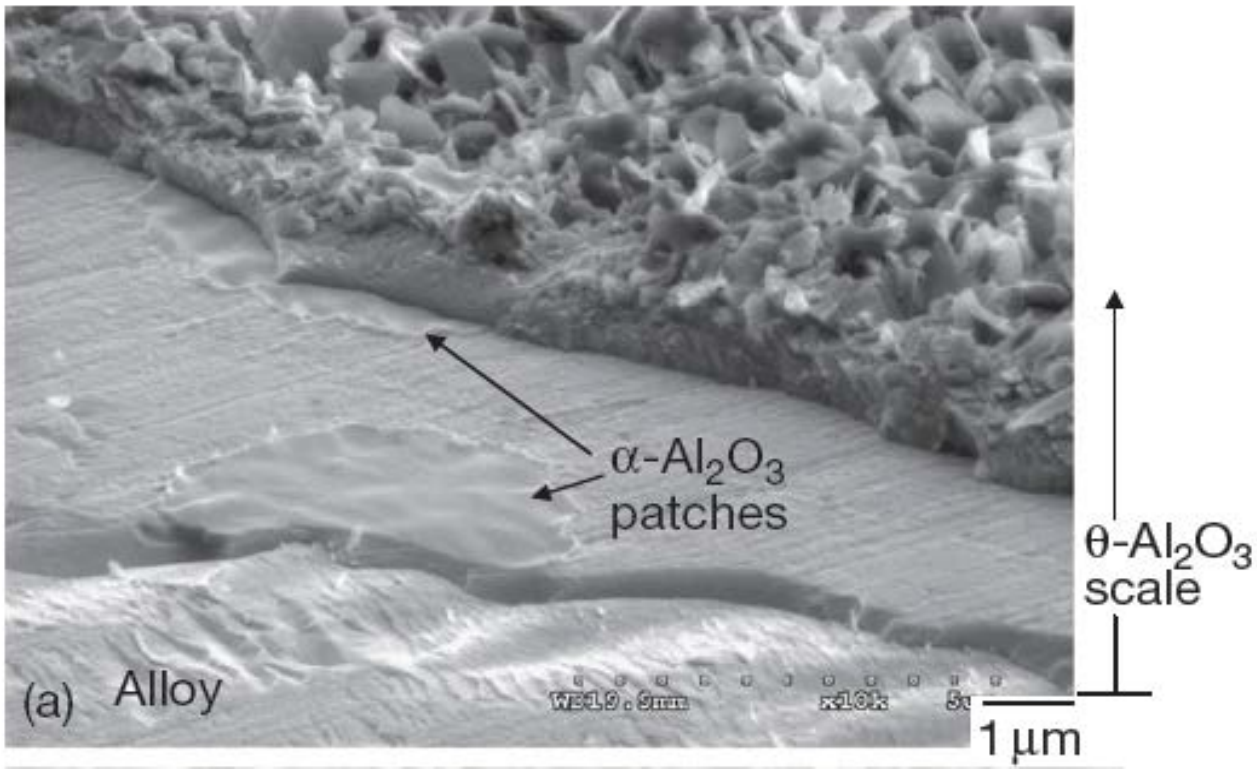

Figure 4.77 SEM image of Al_2O_3 scale formed on Ni-55at%Al after oxidation at 1100^{o}C for 11min[118]

The agreement between the experimental results and the physical interpretation of determined parameters indicates that the kinetics scenario reflects that real kinetics situation so that the determined parameters do have physical meanings.

Significance of kinetics analysis on $\theta \rightarrow \alpha$ transformation by n^i-value analysis

As indicated previously, since the initial stage has orders of magnitude higher oxidation rate[115], it is always preferred to reduce this transition time this stage in order to reduce the aluminum consumption in the alloy. Meanwhile, θ-Al_2O_3 has a less-dense monoclinic crystal structure compared to close-packed α-Al_2O_3 structure; the $\theta \rightarrow \alpha$ transformation is accompanied by ~9% volume shrinkage[119]. This volume change can be a source of scale cracking and even spallation. Therefore, it is of practical importance to either reduce the duration of this stage or even bypass it. This could be achieved through several ways such as adding alloy element[120] or by surface treatment[113]. It was found, yttrium has been found to accelerate the θ-$Al_2O_3 \rightarrow \alpha$-$Al_2O_3$ transformation on oxide-dispersion-strengthen (ODS) superalloys at 900^oC[120]. Similarly, Cr and Ti accelerate the transformation on a β-NiAl coating at 1050^oC[121]. By contrast, Zr[122], La and Hf[121] have been reported to delay the $\theta \rightarrow \alpha$ transformation. If fine particles of α-Al_2O_3 are applied to the surface of an alumina-scale forming alloy before oxidation, they can react as nucleation sites for thermally formed α and therefore greatly accelerate or even bypass the metastable $\rightarrow$ stable transformation[113]. However, most of the studies of the element effect[120, 121] are qualitative. There is a need to quantify the effect by those elements. Although this quantification can be achieved by a XRD[113] method, the transition time determined by XRD method is not directly related with oxidation kinetics. Therefore, the kinetics analysis method invented in this study is very useful for the purpose of studying the element effect on the $\theta \rightarrow \alpha$ transformation, which is related with the performance and life time of alloys. In the following, an

example of using the kinetics analysis method to quantify the Si effect on the θ → α transformation will be shown.

4.3.5 Quantification of Si effect on the θ → α phase transformation

The effect by Si on the θ → α phase transformation can be investigated by the kinetics analysis method developed in this study. The alloy investigated was Ni-20Al-5Cr-0.5Y-0.5Hf with and without 1% Si addition. Figure 4.78 compares the TG curve for Ni-20Al-5Cr-0.5Y-0.5Hf and Ni-20Al-5Cr-0.5Y-0.5Hf-1Si alloys oxidized in dry air at 1100°C. The corresponding n^i-value curves for the first 10 hours are shown in Figure 4.79 to compare where the minima occur. It is seen that the transition time is shifted to the right going from the Si-free alloy to the alloy with 1%Si. This means that the Si addition delayed the θ → α phase transformation at this temperature. This delayed transformation can be quantified by a simulating procedure. Figure 4.80 shows the experimental and simulated TG curve for the Si-containing alloy, while Figure 4.81 shows the corresponding n^i-value curves. After the simulation procedure, the parameters for the transformation kinetics were found to be K=0.6 and ω=2.2. Taking these two parameters into equation 4.78, the area fractions of α phase as functions of time for both of the alloys can be determined as shown in Figure 4.82. It is seen that not only was the overall transformation procedure delayed by Si, but also the incubation time for α phase formation was extended. Finally, the determined ω value may be used to infer information about the nucleation mechanism. For example, by adding 1%Si to the Ni-20Al-5Cr-0.05Hf-0.05Y, the ω value for the θ → α transformation in the scales formed on the alloys oxidized at 1100°C changed from 1.0 to 2.2. This change implies that the nucleation changed from “interface nucleation after saturation”

for ω=1 to some counterpart to "grain edge nucleation after saturation" for ω=2[117]. However, further experimental validation is needed to interpret the physical meaning of ω=2.2.

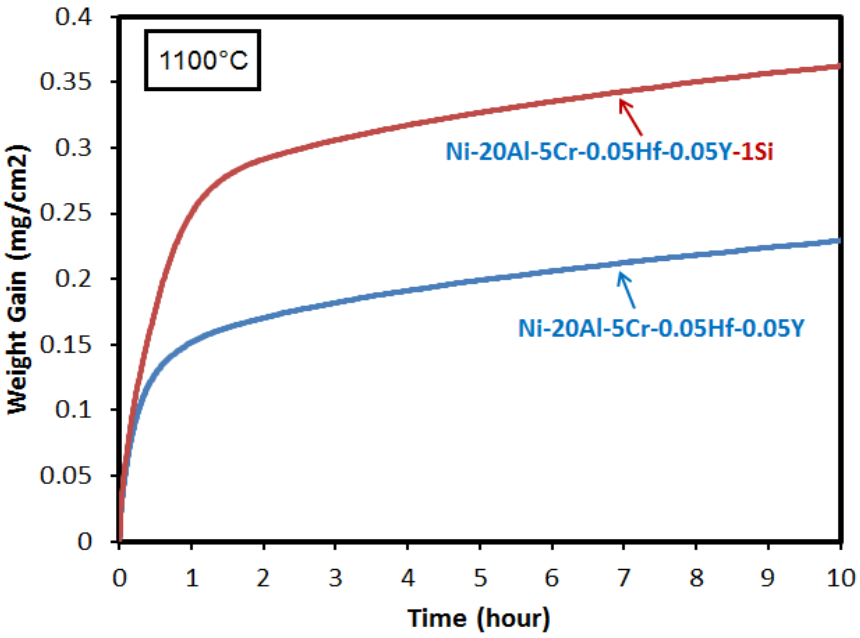

Figure 4.78 Comparison of TG curves for Ni-20Al-5Cr-0.05Hf-0.05Y and Ni-20Al-5Cr-0.05Hf-0.05Y-1Si alloys oxidized in dry air at 1100°C.

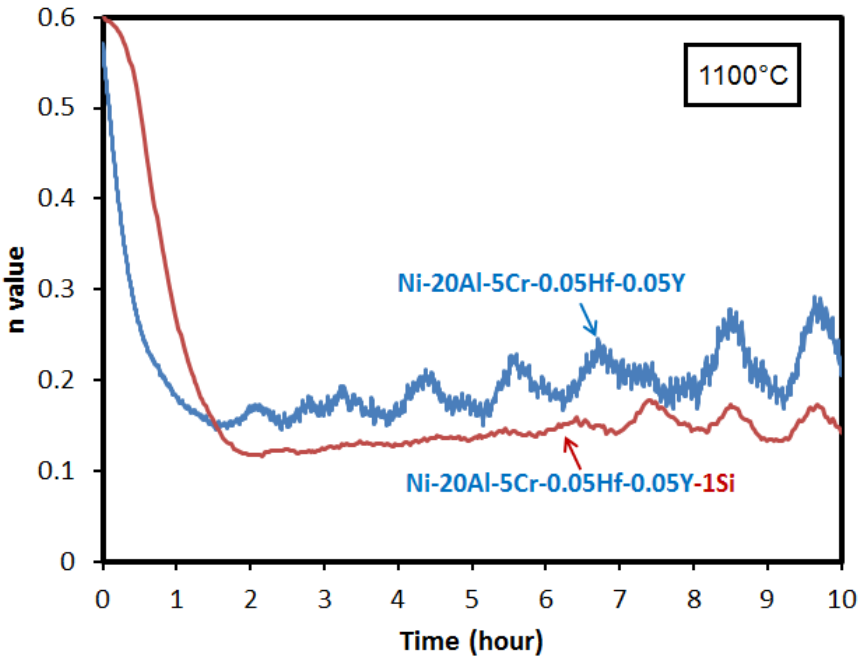

Figure 4.79 Comparison of associated n^i-value curve for the TG curves shown in Figure 4.78.

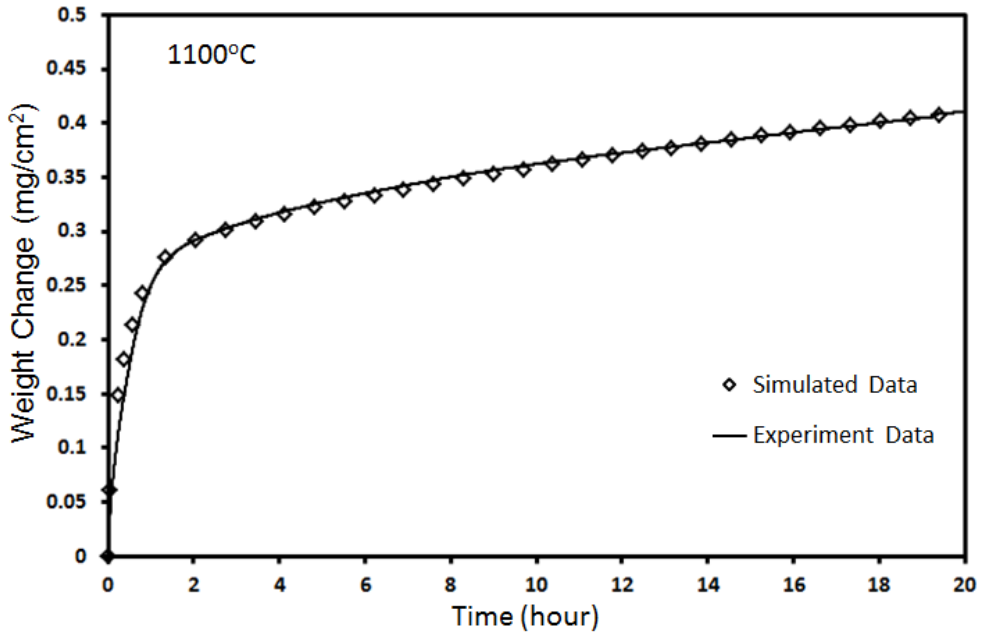

Figure 4.80 Experiment and Simulated TG curve for Ni-20Al-5Cr-0.05Hf-0.05Y-1Si alloys oxidized in dry air at 1100°C for 10h.

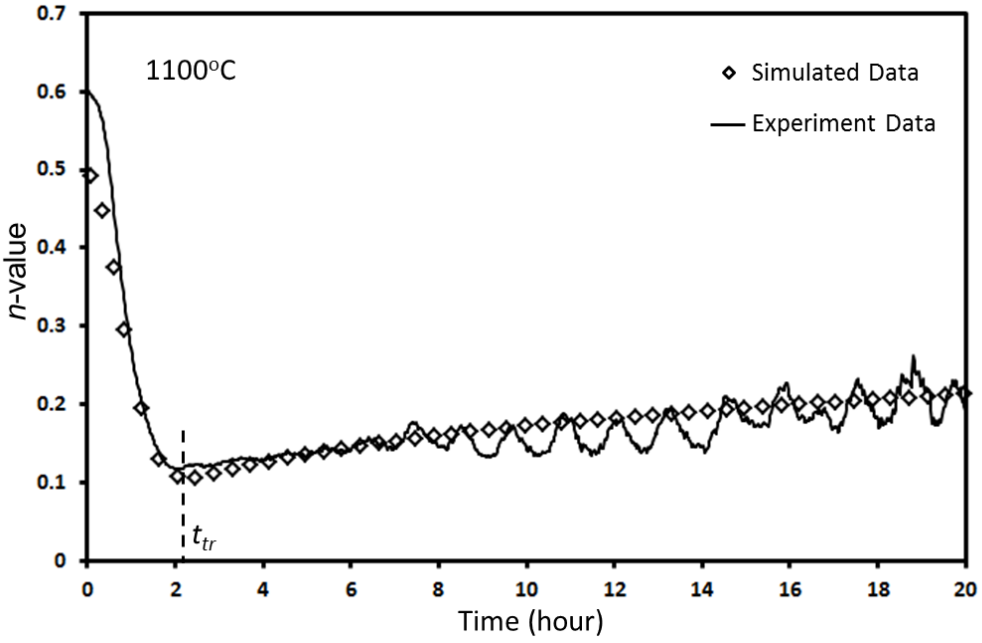

Figure 4.81 Experiment and Simulated n^i-value curve for Ni-20Al-5Cr-0.05Hf-0.05Y-1Si alloys oxidized in dry air at 1100°C for 10h. Figures 3 and 4 show that the simulation procedure can be repeatable on another case.

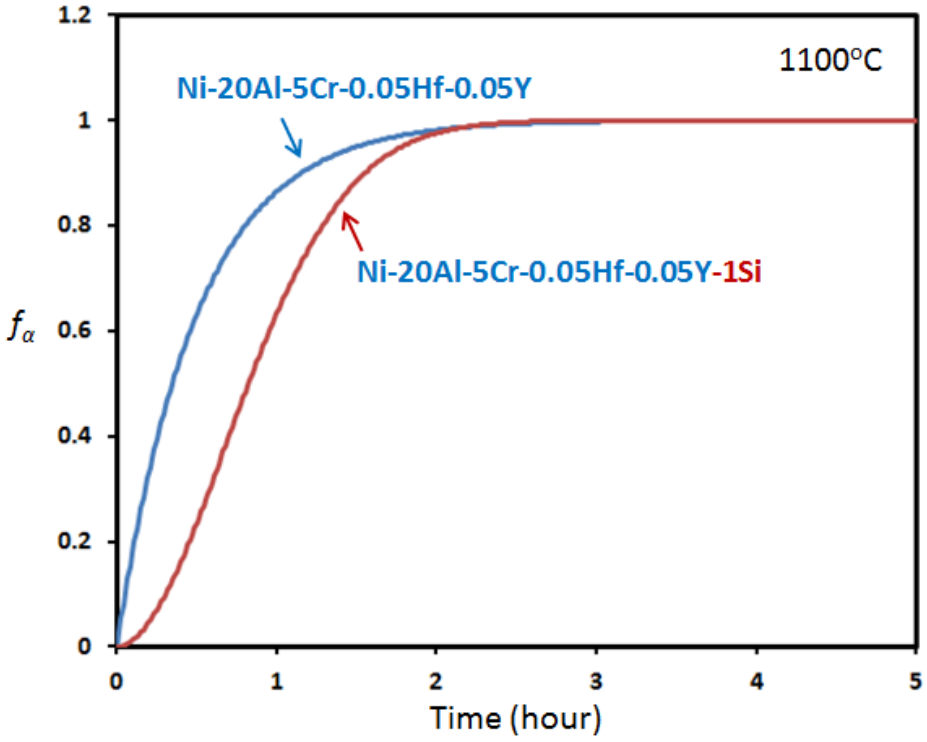

Figure 4.82 The area fractions of α phase as functions of time for Ni-20Al-5Cr-0.05Hf-0.05Y and Ni-20Al-5Cr-0.05Hf-0.05Y-1Si alloys oxidized in dry air at 1100°C

4.3.6 Significance of using n^i-value analysis to quantifying the extent of θ → α transformation

It was found that the variation with n^i values associated with a TG curve for Al_2O_3 scale formation with θ → α transformation always has a minimum. The time to reach this minimum corresponded to a transition time, which in turn, corresponded to significant establishment of a continuous α- Al_2O_3 layer. Therefore, after the transition time, the overall growth kinetics were significantly decreased. This transition time is very important in terms of the oxidation of the alloy, because it determines the duration it takes to establish fully protective the Al_2O_3-scale growth and how much aluminum is consumed from the base alloy. The extent of θ → α

transformation can also be determined by XRD method[113] or a confocal microscopy method[114]. However, both of these methods determine a time for all the θ-Al_2O_3 to transform to α-Al_2O_3. This transition time is always greater than the time necessary for the establishment of a continuous α-Al_2O_3 layer. This latter time is more relevant to the oxidation kinetics. This study is the first to report that n^i-value variation with time has such a feature and to make use of this feature for quantitative analysis.

By applying a kinetics scenario and assuming the transformation kinetics follow Johnson-Mehl-Avrami behavior, the transformation kinetics can be determined by a curve-fitting procedure. By fitting the TG curve as well as the associated n^i-value variation, the growth-rate constants for θ and α Al_2O_3 together with K and ω values used in Johnson-Mehl-Avrami equation for transformation kinetics, can be determined. With K and ω values, the area fraction of the α-Al_2O_3 can be determined, which, can then be used to quantitatively study the transformation phenomena such as element effect on the transformation.

5.0 CONCLUSIONS

5.1 STEAM EFFECTS ON OXIDATION BEHAVIOR OF AL_2O_3-SCALE FORMING Ni-BASED ALLOYS

The critical concentration of Al (N_{Al}^*) in NiCrAl alloys to form a continuous Al_2O_3 scale layer was found to increase when going from dry to wet oxidation conditions. In addition, enhanced NiO growth was found in wet oxidizing conditions, which may be due to accelerated oxygen ingress coming from direct molecular transport (O_2 and/or H_2O), ionic diffusive transport (*e.g.*, OH^-) of the oxygen-containing species, or some combination of these factors.

Using the results from a systematic experimental investigation, Maak's modification[2] of Wagner's theory[3] was successfully employed to predict N_{Al}^* in a dry oxidizing condition for the transition from internal to external Al_2O_3 scale formation. By assuming that this model can also be employed to determine the critical concentration in wet oxidizing conditions, the sensitivity of N_{Al}^* with respect to each input parameter in the model was checked. It was deduced that the only parameter which can give the necessarily large change in N_{Al}^* found in wet-air oxidation is f_v^*, a parameter that is usually assumed to be a constant and independent of the reacting conditions. Meanwhile, two types of surface instability were found by oxidizing pure Ni and Ni-3at%Al in wet oxidizing conditions. On pure Ni, a porous surface structure could be found above a dense NiO scale; while on Ni-3at%Al a layer of less-dense columnar protrusions were found. A

summary of the experimental observation indicated that the porous surface structure on pure Ni formed only in an environment with a steam content above 20%. This structure also tended to form at lower temperatures (1000^{o}C) and on Ni with higher purity. From a calculation based on gas-phase kinetics, it was concluded that the evaporation of Ni-containing species was not the reason for such an abnormal surface morphology to form. XRD patterns of the scale with surface finger-like protrusions tended to indicate that its formation is related to preferred growth along certain crystallographic directions. It was proposed that the formation of the surface instability may be related to enhanced diffusion through short-circuit paths.

5.2 KINETICS ANALYSIS OF COMPLEX SCALE EVOLUTION DURING ISOTHERMAL OXIDATION

It was shown that if the instantaneous growth kinetics are time dependent and that the growth-rate constant determined by conventional methods may not be accurate. Under the same condition, neither the calculated instantaneous growth rate constant k^i nor the time exponent n^i can reflect the true kinetics behavior. Therefore, a rigorous analysis of the conditions for which k^i and n^i can be employed to determine the real kinetics was determined. A standard procedure was summarized to determine the period for the steady-state oxidation. It was also indicated in this study that the non-ideal behavior of n^i values vs. time curve can be used to quantify the complex oxidation kinetics.

A novel kinetics analysis method was then developed for determining the scaling rates for the case in which two product phases are co-forming and the duration of the transition period during which a faster-growing transient phase is displaced by a slower-growing steady-state

phase. The analysis was successfully applied to the $\theta \rightarrow \alpha$ phase transition that occurs in Al_2O_3-scale growth at high temperature. This was achieved by simulating θ-Al_2O_3 and α-Al_2O_3 co-formation weight-gain kinetics and the associated instantaneous n^i values. The method developed can determine the growth-rate constants for each phase during the transient stage, and also determine the extent of lateral growth of α-Al_2O_3 due to phase transformation. Through a determination of n^i as a function of time, it was found that n^i establishes a minimum which corresponds to around 90% of the area on the interface being covered by the slower-growing α-phase. The analytical method developed proved to be an effective tool for quantifying the progression of the $\theta \rightarrow \alpha$ transition during scaling.

REFERENCES

[1] C. S. Giggins and F. S. Pettit, *J. Electrochem. Soc.,* Vol.118, p1782, 1971

[2] F. Maak, *Z. Metallkde.,* Vol.52, p545, 1961

[3] C. Wagner, *Z. Elektrochem.,* Vol.63, p772, 1959

[4] J. Robertson and M. I. Manning, *Mater. Sci. Technol.,* Vol. 4, p1064, 1988

[5] K. Akiba, M. Ueda, K. Kawamura and T. Maruyama *Mater. Trans.,* Vol.48, p2753, 2007

[6] N. Birks, G.H. Meier, and F.S. Pettit, in '*Introduction to High Temperature Oxidation of Metals*', Second Edition, Cambridge University Press, Cambridge, 2006

[7] J. Paidassi, *Rev. Met.* Vol.54, p569, 1957

[8] P. Kofstad, in '*High Temperature Corrosion*', Elsevier Applied Science, London, 1988

[9] K. Fueki and J.B. Wagner, *J. Electrochem. Soc.,* Vol.112, p384, 1965

[10] O. Kubaschewshi, O. van Goldbeck, *Z. Metallkunde.,* Vol.39, p158, 1948

[11] Y. Matsunaga, *Japan Nickel Rev.,* Vol.1, p347, 1933

[12] W. J. Moore, *J. Chem. Phys.,* Vol.19, p255, 1951

[13] E. A. Gulbransen and F. K. Andrew, *J. Electrochem. Soc.,* Vol.101, p128 1954

[14] W. Philips, *J. Electrochem. Soc.,* Vol.110, p1014, 1963

[15] H. J. Engell, *Archiv. Eisenuttenwesen,* Vol.28, p109, 1957

[16] H. J. Engell, *Acta Met.,* Vol.6, p439, 1958

[17] S. Mrowec and K. Przybylski, *Oxid. Met.,* Vol.3, p291, 1977

[18] S. Mrowec and T. Werber, in '*Gas Corrosion of Metals*' (Translated from Polish), Foreign Scientific Publications Department of the National Center for Scientific, Technical and Economic Information, Varsovie, 1978

[19] B. Gleeson, in '*High-Temperature Corrosion of Metallic Alloys and Coatings*', in Materials Science and Technology: A Comprehensive Treatment: Corrosion and Environmental Degradation, Volume I, Wiley-VCH Verlag GmbH, Weinheim, Germany, 2008

[20] V. R. Howes, *Corros. Sci*. Vol.8, p729, 1968

[21] B. Chattopadhyay and G.C. Wood, *Oxid. Met.*, Vol.2, p373, 1970

[22] F. Gesmundo, P. Castello, F. Viani and J. Philibert, *Oxid. Met.*, Vol.47, p91, 1997

[23] D. P. Whittle, G. C. Wood, D. J. Evans and D. B. Scully, *Acta Metall*., Vol.15, p1747, 1967

[24] C. Wagner, *J. Electrochem. Soc*., Vol.99, p369, 1952

[25] C. S. Giggins and F. S. Pettit, *Trans. Met. Soc. of AIME*, Vol. 245, p2495, 1969

[26] N. Birks and H. Rickert, *J. Inst. Met.*, Vol.91, p308, 1962/1963

[27] R. A. Rapp, *Acta met.*, Vol.9, p730, 1961

[28] G. R. Wallwork and A. Z. Hed, *Oxid. Met.*, Vol.3, p171, 1971

[29] H. R. Pickering, *J. Electrochem. Soc.*, Vol.119, p64, 1972

[30] C. Wagner, *Corr. Sci.*, Vol.5, p751, 1965

[31] G. H. Meier, *Mater. Sci. Eng. A*, Vol.120, p1, 1989

[32] F. H. Stott, G. C. Wood, and J. Stringer, *Oxid. Met.*, Vol.44, p113, 1995

[33] B. Gleeson, N. Mu, S. Hayashi, *J. Mater. Sci.*, Vol.44, p1704, 2009

[34] J. P. Sauer, R. A. Rapp, J. P. Hirth, *Oxid. Met.*, Vol.18, p285, 1982

[35] P. R. S. Jackson, G. R. Wallwork, *Oxid. Met.*, Vol.21, p135, 1984

[36] D.L Douglass, P. Kofstad, A. Rahmel and G.C. Wood, *Oxid. Met.*, Vol.45, p529, 1996

[37] D.J. Young, *Mater. Sci. Forum*, Vol.595, p1189, 2008

[38] O. Kubaschewski and C. B. Alcock, in '*Metallurgical thermochemistry*', Fifth edition, Pergamon Press, Oxford, 1979

[39] I. G. Wright and R. B. Dooley, *Int. Mater. Rev.*, Vol.55, p129, 2010

[40] E. J. Opila, D. L. Myers, N. S. Jacobson, I. M. B. Nielsen, D. F. Johnson, J. K. Olminsky and M. D. Allendorf, *J. Phys. Chem. A*, Vol.11, p1971, 2007

[41] D.J. Young and B.A. Pint, *Oxid. Met.*, Vol.66, 3/4, p137, 2006

[42] H. Buscail, S. Heinze, Ph. Dufour and J.P. Larpin, *Oxid. Met.*, Vol.47, p445, 1997

[43] E. Essuman, G.H. Meier, J. Zurek, M. Hansel and W.J. Quadakkers, *Oxid. Met.*, Vol.69, p143, 2008

[44] C.W. Tuck, M. Odgers and K. Sachs, *Corros. Sci.*, Vol.9, p271, 1969

[45] B. H. Kear, F. S. Pettit, D. E. Fornwalt, and L. P. Lemaire, *Oxid. Met.*, Vol.3, p557, 1971

[46] G. Hultquist, B. Tveten, and E. Hornlund, *Oxid. Met.*, Vol.54, p1, 2000

[47] S. Hayashi, S. Narita, T. Narita, *Oxid. Met.*, Vol.74, p33, 2010

[48] N. K. Othman, J. Zhang, D. J. Young, *Oxid. Met.*, Vol.73, p337, 2010

[49] A. Rahmel and T. Tobolshi, *Corros. Sci.*, Vol.5, p333, 1965

[50] A. Dravnieks and H. J. McDonald, *J. Electrochem. Soc.*, Vol.94, p139, 1948

[51] R. Peraldi and B. A. Pint, *Oxid. Met.*, Vol. 61, p463, 2004

[52] J. Ehlers, D. J. Young, E. J. Smaardijk, A. K. Tyagi, H. J. Penkella, L. Singheiser and W. J. Quadakkers, *Corros. Sci.*, Vol.48, p3428, 2006

[53] Y. Ikeda and K. Nii, *Transactions of National Research Institute for Metals*, Vol.26, p52, 1984

[54] A. Galerie, S. Henry, Y. Wouters, M. Mermoux, J. P. Petit and L. Anton, *Mater. High Temp.*, Vol.22, p105, 2005

[55] R. L. McCarron and J. W. Schultz, *Proc. Symp. High Temperature Gas-Metal Reactions in Mixed Environments, AIME*, Vol.114, p360, 1973

[56] H. Buscail, S. Heinze, Ph. Dufour, J.P. Larpin, *Oxid. Met.*, Vol.47, p445, 1997

[57] M. C. Maris-Sida, G. H. Meier and F. S. Pettit, *Met. Trans. A*, Vol.34, p2609, 2003

[58] R. Janakiraman, G. H. Meier and F. S. Pettit, *Metall. Mater. Trans. A.*, Vol.30, p2905, 1999

[59] J. F. Cullinan, *Master's Thesis*, University of Pittsburgh

[60] P. Kofstad: in '*Microscopy of Oxidation*', edited by M. J. Bennett and G. W. Lorimer, The Institue of Metals, London, 1991

[61] J. A. Sedriks,in '*Corrosion of Stainless Steels*', Second Edition, John Wiley & Sons, New York, 1996

[62] G. Tammann, *Z. Anorg. Allg. Chem.*, Vol.111, p78, 1920

[63] G. Tammann, W. Koster, *Z. Anorg. Allg. Chem.*, Vol.123, p196, 1922

[64] N. Pilling, R. Bedworth, *J. Inst. Met.*, Vol. 29, p529, 1923

[65] U. Evans, *Trans. Electrochem. Soc.*, Vol.46, p267, 1924

[66] B. Pieraggi, *Oxid. Met.*, Vol. 27, p177, 1987

[67] H.C. Yi., S.W. Guan, W.W. Smeltzer, A. Petric, *Acta Metall. Mater.*, Vol.42, p981, 1994

[68] W. J. Quadakkers, D. Naumenko, E. Wessel, V. Kochubey, L. Singheiser, *Oxid. Met.*, Vol.61, p17, 2004

[69] D. Naumenko, B. Gleeson, E. Wessel, L. Singheiser, W.J. Quadakkers, *Metall. Mater. Trans.A.*, Vol.38, p2974, 2007

[70] D. Monceau, B. Pieraggi, *Oxid. Met.*, Vol.50, p516, 1998

[71] M. J. Graham, D. Caplan, M. Cohen, *J. Electrochem. Soc.*, Vol.119, p1265, 1972

[72] D. Caplan, M.J. Graham, M. Cohen, *J. Electrochem. Soc.*, Vol.119, p1205, 1972

[73] B. Pieraggi, *Oxid. Met.*, Vol.64, p397, 2005

[74] A. Galerie, S. Henry, Y. Wouters, M. Mermoux, J.P. Petit and L. Anton, *Mater. High Temp.*, Vol.22, p105, 2005

[75] D.J. Young, *Mater. High Temp.*, Vol.595, p1189, 2008

[76] A. Rahmel, J. Tobolski, *Corros. Sci.,Vol.5, p 815, 1965*

[77] M. Auchi, S. Hayashi, K. Toyota, S. Ukai, Private discussion

[78] Y. Kitajima, S. Hayashi, T. Narita, *Materials Science Forum* Vol.522, p 103, 2006

[79] A. Atkinson and R.I. Taylor, *J. Mater. Sci.*, Vol.13, p427, 1978

[80] R. Herchl,, N.N. Khoi, T. Homma and W. W. Smeltzer, *Oxid. Met.*, Vol.4, p35, 1972

[81] R. Peraldi, D. Monceau and B. Pieraggi, *Oxid. Met.*, Vol.58, p275, 2002

[82] F.A. Elrefaie, A. Manolescu and W.W. Smeltzer, *J. Electrochem. Soc.*, Vol.132, p2489, 1985

[83] R. Haugsrud, *Corros. Sci.* Vol.45, p211, 2003

[84] H.V.Atkinson, *Mater. Sci. Technol.*, Vol.4, p1052, 1988

[85] S. Mrowec, *Proceedings JIMIS-3: High Temperature Corrosion, Transactions of Japan Institute of Metals*, Vol.69, 1983

[86] K. Fueki and J. B. Wagner, *J. Electrochem. Soc.*, Vol.112, p384, 1965

[87] J. Paidassi and L. Berry, C. R. *Acad. Sci. Paris.*, Vol.262, p1553, 1966

[88] D. L. Douglass, *Corros. Sci.*, Vol.8, p665, 1968

[89] A. Atkinson and R. I. Taylor, *Philos. Mag. A*, Vol.43, p979, 1981

[90] H. E. Evans *Mater. Sci. Technol.*,Vol.4, p1089, 1988

[91] M. C. Maris-Sida, *Ph.D thesis*, University of Pittsburgh, 2004

[92] F. Gesmundo, and F. Viani, *Oxid. Met.*, Vol.25, p269, 1986

[93] J. Park and C.J. Altstetter, *Metall. Trans. A*,Vol.18, p43, 1987

[94] F. H. Stott, G. C. Wood, D. P. Whittle, B. D. Bastow, Y. Shida and A. Martinez-Villafane, *Solid State Ionics*, Vol.12, p365, 1984

[95] F. H. Stott and G. C. Wood, *Mater. Sci. Technol.*, Vol.4, p1072, 1988

[96] F. A. Elrefaie and W. W. Smeltzer, *J. Electrochem. Soc.*, Vol.128, p2237, 1981

[97] K. P. Trumble and M. Ruhle, *Acta Metall. Mater.*, Vol.39, p1915, 1991

[98] W. Gust, H. B. Hintz, A. Lodding, H. Odelius and B. Predel, *Phys. Stat. Sol.*,Vol.64, p187, 1981

[99] A. Green and N. Swindells, *Mater. Sci. Technol.*, Vol.1, p101, 1985

[100] M. M. P. Janssen, *Metall. Trans.*, Vol.4, p1623, 1973

[101] J. L. Meijering, *Advances Mater. Res.*, Vol.5, p81, 1971

[102] J. Megusar and G. H. Meier, *Met. Trans. A*, Vol.7A, p1133, 1976

[103] R. T. DeHoff and F. N. Rhines, page 46, in '*Quantitative microscopy*', Herndon, Virginia, 1991

[104] E. Wimmer, W. Wolf, J. Sticht, P. Saxe, C. B. Geller, R. Najafabadi, and G. A. Young, *Phys. Rev. B*, Vol.77, 134305, 2008

[105] C. Kluthe, T. Al-Kassab, J. Barker, W. Pyckhout-Hintzen, R. Kirchheim, *Acta. Metall.*, Vol.52, p2701, 2004

[106] R. Kirchheim, A. Pundt, T. Al-Kassab, F.Wang, C. Kluthe, *Z. Metalkd.*, Vol.94, p266, 2003

[107] M. W. Chase, NIST-JANAF Thermochemical Tables, *J. Phys. Chem. Ref. Data*, Monograph No.9. Institute of Physics, Woodbury, New York, 1999

[108] D. R. Gaskell, in '*An Introduction to Transport Phenomena in Materials Engineering*', Macmillian, New York, 1992

[109] M. T. Tinker, *Ph.D. thesis*, Case Western Reserve University, 1984

[110] H. Al-Badairy, D. J. Prior, and G. J. Tatlock, *Mater. High Temp.*, Vol.22, p453, 2005

[111] D. Naumenko, B. Gleeson, E. Wessel, L. Singheiser and W. J. Quadakkers, *Metall. Trans. A.*, Vol.38, p2974, 2007

[112] M. J. Graham, G. I. Sproule, D. Caplan, M. Cohen, *J. Electrochem. Soc.*, Vol.119, p883, 1972

[113] B. W. Veal, A. P. Paulikas and R. C. Birtcher, *Appl. Phys. Lett.*, Vol.89, 161916, 2006

[114] D. M. Lipkin, H. Schaffer, *Appl. Phys. Lett.*, Vol.70, p2550, 1997

[115] M.W. Brumm and H.J. Grabke, *Corr. Sci.*, Vol.33, p1677, 1992

[116] R. B. Bagwell, G. L. Messing, P. R. Howell, *J. Mater. Sci.*, Vol.36, p1833, 2001

[117] J. W. Christian, in '*The Theory of Transformations in Metals and Alloys*', Pergamon Press, University of Oxford, 1965

[118] J. C. Yang, E. Schumann, I. Levin, M. Ruhle, *Acta. Metall.*, Vol.46, p2195, 1998

[119] D. M. Lipkin, D. R. Clarke, M. Hollatz, M. Bobeth, and W. Pompe, *Corr. Sci.*, Vol.39, p231, 1997

[120] A. Andoh, S. Taniguchi and T. Shibata, *Mater. Sci. Forum*, Vol.301, p369, 2001

[121] J. Dokychak and M. Ruhle, *Oxid. Met.*, Vol.32, p431, 1989

[122] P. Burtin, J. P. Brunelle, M. Pijolat and M. Soustelle, *Appl. Catal.*, Vol.34, p225, 1987